THE UNIVERSITY OF
WARWICK

University of Warwick institutional repository: http://go.warwick.ac.uk/wrap

A Thesis Submitted for the Degree of PhD at the University of Warwick

http://go.warwick.ac.uk/wrap/54103

This thesis is made available online and is protected by original copyright.

Please scroll down to view the document itself.

Please refer to the repository record for this item for information to help you to cite it. Our policy information is available from the repository home page.

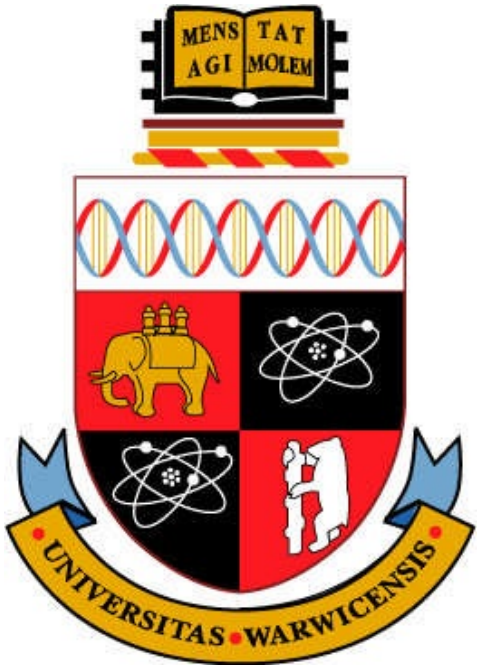

Jet Fuel Spray Characterisation Using Optical Methods:

an Experimental Study of High Speed Fuel Injection Systems in Small Rotary Engines

By:

Rami Zakaria

Thesis submitted in partial fulfilment of the requirements for admission to the degree of

Doctor of Philosophy in Engineering

School of Engineering

December 2011

THE UNIVERSITY OF WARWICK

Table of Contents

List of Figures

Abbreviations

AMD: arithmetic mean diameter

ASOI: after start of injection (time)

DI: direct injection

DC: direct current

DCT: discrete cosine transform

DOF: depth of focus

ECU: engine control unit

ESD: Equivalent Spherical Diameter

FOV: field of view

GDI: gasoline direct injection

IDI: indirect injection

LASER: Light Amplification by Stimulated Emission of Radiation

MMD: mass median diameter

Nd-YAG: neodymium-doped yttrium aluminium garnet

PIV: particle imaging velocimetry

3C-PIV: three components particle imaging velocimetry

PCA: principal component analysis

Q_i: absorbed heat (J)

Q_o: rejected heat (J)

Re: Reynolds number

RE: rotary engine

SLR: single-lens reflex

SMD: Sauter Mean Diameter

TDC: top dead centre (engine stroke)

UAV: unmanned aerial vehicle

We: Weber number

Acknowledgements

I would like to acknowledge and thank all those who have supported me in carrying out my research. My first thanks go to Professor Peter Bryanston-Cross, for his conscientious supervision and critical feedback. His encouragement and devotion have been very inspirational.

My gratitude goes to Optical Engineering Laboratory (OEL) staff members and Dr. Brenda Timmerman for the academic support, as well as to Dr David Hunter, Dr Jop Vlaskamp, Dr Daniel Claus, and Mr Paul Hackett.

Thanks also go to University of Warwick for funding my research and providing generous support that facilitated my studies; to Cubewano Limited, for financial and technical support; to QinateQ NTF team for supporting the experimental work; to my friends, who have helped me with this undertaking, sometimes in more obscure ways than they realized, in particular, Malek Zerkli, Yi Wang, Iman Sheeha, Yamen Rahwan, Naia Naser, Ahmed Al Makky, Siân Elizabeth Mitchell, Mahmoud Jeidani, Khalid Hathlool, Liz Hardiman, Vedita Cowaloosur, Rifkhan Anver, Abdul-Qadir Alyasin, and Khaled Alhaj-Husain for pleasant company during tea breaks and for their good humour.

Finally, it is to my family that I dedicate this work. Their belief in my abilities never ceased to motivate me and carried me through to the end. Each and every one of them has been an inspiration to me throughout this undertaking.

Declaration

I hereby declare that, except where otherwise indicated, this thesis contains the results of research undertaken by me in the School of Engineering at the University of Warwick. This thesis is entirely my own work, and that no part of it has been submitted for any other degree or qualification.

Rami A.K. Zakaria

The University of Warwick,

August 2012

Abstract

This thesis was initiated by the need to develop a stable low vibration engine with a high power to weight ratio. A new rotary (Wankel) engine was chosen to meet these requirements. A further operating criterion was that the engine was required to use JP8 (aviation fuel). The difficulty created by the use of JP8 is that its combustion temperature is higher than other conventional fuels, and preheating is necessary, especially in the case of cold start. Thus, the question posed was, could a more appropriate and efficient method of fuel delivery be devised?

This thesis presents the design and construction of a fluid spray visualisation system for investigating the macroscopic and microscopic characteristics of fuel sprays using low injection pressure up to 10 bar (1 MPa). Laser imaging techniques have been used for data acquisition. The thesis has been divided into several aspects.

Firstly, a background study of fluid sprays and fuel injection strategies was carried out. This has centred on the relationship between droplet size and the combustion process. It further investigated what differentiated the fuel delivery approach to Wankle from that to other engines.

Secondly, two families of fuel injector were tested and evaluated within the optical engineering laboratory using deionised water (DI) water for safety reasons. The first family involved conventional gasoline injectors with several nozzle arrangements. The second family involved medical nebulisers with several nozzle diameters. The evaluation of the fuel injectors required developing a fluid delivery circuit, and a specific ECU (Electronic Control Unit) for controlling pulse delivery and imaging instrument. The company associated with

the project then set up a test cell for performing experiments on JP8 fuel. The initial global visualisation of the jet spray was made using a conventional digital camera. This gave a measurement of the spray angle and penetration length. However, as the study moved to the more precise determination of the fuel spray particulate size, a specialised Nd:YAG laser based diagnostic was created combined with a long range diffraction limited microscope.

Microscopic characterisation of the fuel sprays was carried out using a backlight shadowgraph method. The microscopic shadowgraphy method was applied successfully to resolve droplets larger than 4 microns in diameter. The spray development process during an individual fuel injection cycle was investigated, presenting the frequency response effect of electronic fuel injectors (EFI) on the spray characteristics when operating at high injection frequencies (0.25 - 3.3 kHz). The velocity distribution during the different stages of an injection cycle was investigated using PIV. The influence of the injection pressure on the spray pattern and droplet size was also presented.

Novel fluid atomisation systems were investigated for the capability of generating an optimum particulate distribution under low pressure. Finally, it was found that a new electronic medical nebuliser (micro-dispenser) could be used to deliver the fuel supply with the relevant particle size distribution at low flow rate and high injection frequency. However, as yet it has not been possible to apply this approach to the engine; it is hoped that it will yield a more efficient method of cold starting the engine. The characteristics of this atomiser can be applied to provide a controllable fuel supply approach for all rotary engines to improve their fuel efficiency.

The second part of this research discusses the droplets-light interaction using Mie scattering for fluid droplets smaller than the microscope visualisation limit (4 microns). Mie

scattering theory was implemented into Three-Components Particle Image Velocimetry (3C-PIV) tests to address a number of problems associated with flow seeding using oil smoke. Mie curves were used to generate the scattering profile of the oil sub-micron droplets, and therefore the scattering efficiency can be calculated at different angles of observation. The results were used in jet flow PIV system for the determination of the optimum position of the two cameras to generate balanced brightness between the images pairs. The brightness balance between images is important for improving the correlation quality in the PIV calculations. The scattering efficiency and the correlation quality were investigated for different seeding materials and using different interrogation window sizes.

Chapter1. Introduction

1.1. Research Motivation

The investigation into the characteristics of fluid micro-mists is of importance to the fuel combustion application. Modern engine manufacturers worldwide have recently become focused on improving the efficiency of their engines, in order to produce more powerful engines that meet both the environmental and economic standards. Factors such as particle size distribution and injection-ignition timing play an important role in improving the thermal efficiency of the internal combustion (IC) engine. The mechanism of fluid disintegration and the impact of the different operational parameters are still not completely understood [Shao & Yan (2009)]. Therefore, the research on the dynamic behaviour of fuel sprays is crucial to the fuel injection systems.

The size of a fluid droplet produced by an atomiser is directly related to the design and quality of that atomiser; the more effective a fuel atomiser, the smaller droplets it produces. Increasing the overall surface area of a fuel improves the evaporation rate and the burning range, leading to higher rates of the released power during the combustion process and lower exhausted pollutant emissions.

The current study tackles the problem of fuel injection into a new small rotary engine design. The small physical dimensions of the engine introduce several requirements for undertaking an effective fuel injection strategy to improve the output energy of the engine.

These requirements are related to the fuel spray pattern, spray angle, fluid pressure, and flow rate, but more importantly, to the effective fuel atomisation in producing droplets within the microscopic range using low-pressure forces. For instance, it is required to produce droplets less than 5 μm in diameter in order to perform a cold start of the engine. These droplets are generated using an injection pressure less than 5 bar[1] to suit the high power-to-weight applications, such as unmanned aerial vehicles (UAVs). The current engine has further restrictions in terms of its size and the type of fuel (JP8 in this case) that requires preheating to achieve an internal combustion due to its low flash point.

Advancement in optical metrology provides the necessary tools for a better understanding of multiphase flows in engineering and industrial applications. Measurements on the size and velocity of a fluid droplet can be carried out by the light scattering methods. The light-droplet interaction is a complex process with a large number of parameters. Light scattering methods usually provide a point diagnosis rather than a global representation of the flow. Recent attempts have been made to allow droplet sizing using shadowgraph-imaging methods. These types of experiments, however, are usually reported for droplets larger than 30 microns in diameter, due to difficulties in producing well-contrasted images of high-speed micro-droplets at a high imaging resolution. The difficulty in the imaging based methodologies is to balance between the required spatial resolution and the area of view.

The analysis of light scattering images at the macroscopic range can provide adequate information about a spray jet geometry and development process in the time domain, while the application of the microscopic shadowgraphy allows the physical measurement of

[1] 1 bar=14.504 psi = 100 kPa

individual droplets. Both macroscopic and microscopic characteristics are used for the evaluation of the fuel injection systems.

It is also advantageous to an engine designer to evaluate the performance of a fuel injector against various operation parameters, such as fuel pressure and injection frequency. The accuracy in injection mechanism is more important in the case of high-speed engine (higher than 12,000 rpm), where the time for mixture formation, evaporation and combustion is extremely short. Spray development process can be investigated by calculating the jet tip velocity and also by applying particle imaging velocimetry (PIV).

Knowledge associated with the interaction between micro-particles and light-waves is also utilised in the stereoscopic particle imaging velocimetry (3C-PIV) topic, where changes in the angle of observation have a great impact on the amount of the received optical energy at an image sensor, and consequently on the correlation between the successive images of a flow.

1.2. Experimental Conditions

The experiments were conducted on the Jet A-1 (JP8) kerosene-grade, using a maximum of (10) bar injection pressure into an unpressurised ambient. The JP8 fuel is commonly used in turbine-engined aircrafts. The low injection-pressure condition was required by the engine manufacturer to reduce the operation energy, weight and vibration of the fuel delivery system. Two families of fuel injectors were tested during the experimental work. The first family (IWP series) included conventional 12V electronic gasoline injectors with different nozzle settings. This type of injector operates at a maximum injection frequency of 350 Hz. The second injector family was a micro-dispensing system (Lee VHS M/2) developed

by the Lee Company mainly for medical applications (drug delivery) that need micro-litre and nano-litre dispense volumes. The selection of this injector was based on the low power (500 milliwatts maximum), low weight and high frequency requirements. The top operation frequency of this injector is as high as 3.3 kHz. The pulse width of this injector could be accurately adjusted so that short injection pulses with a low flow-rate can be provided during the intake stroke. Another advantage of this injector was the ability of replacing the end-nozzle, which can be as small as 125 microns in diameter. Another advantage was

Spray images were acquired in dark environment; i.e. in an isolated cell where all devices were remotely controlled. Strict health and safety regulations were applied due to the explosive nature of the fuel and the risk of direct exposure to class-4 and class-3 laser beams.

1.3. Research Objectives

This research aims to contribute to the topic of fuel spray characterisation during the fluid atomisation process using optical methods. Experimental work is made possible by developing a visualisation system using digital imaging and laser sheets. The acquired data is used for the evaluation of different fuel injectors prior to application in a new design rotary (Wankel) engine. The light scattering theory is also applied on a 3C-PIV system, in order to address a number of practical problems associated with the seeding process.

The first objective is to assess the injectors' performance by developing a direct visualisation system and a programmable control system for injectors' pulse-width and frequency management.

The second objective is to develop a laser-sheet imaging system for the characterisation of the JP8 (kerosene) sprays and the frequency response of the injectors. The global fuel spray characteristics of interest include the spray pattern, angle, density distribution, overall area and penetration-velocity. The microscopic characteristics of interest include the droplet size and velocity.

Another objective is to study the formation process of the fuel mist in the time domain. Velocity vector maps of the fuel sprays can be generated in both macroscopic and microscopic ranges using PIV.

Finally, the investigation of the light scattering pattern and the Mie curves of the sub-micrometer droplets aims at estimating the light scattering efficiency of the oil smoke seeders used in stereoscopic-PIV tests, and comparing the PIV results of the oil seeder with other conventional solid seeding particles. The outcome of this study aims to improve the design of a jet-noise experimental rig by optimising the position of the PIV cameras with respect to the laser-sheet.

1.4. Thesis Structure

This thesis includes five main parts. The first part is a literature review of topics related to this research project. In chapter two a general review on the subject of fluid atomisation is presented. A description of the process of fluid droplet formation is provided and related definitions are clarified. Fuel injection strategies in IC engines are presented in chapter three, reviewing the up-to-date research conducted on rotary engines. An investigation into the evaporation rate of kerosene is carried out and discussed in terms of the current engine design. Optical diagnosis methodologies in fuel sprays are reviewed in chapter four,

including a general description of instrumentation commonly used in this type of measurement.

The second part (chapter 5) of the literature review comprises of a detailed study about the light-droplet interaction topic and light diffraction of small particles. Mie theory in light diffraction is applied in the study of the light-scattering efficiency against imaging angle for sub-micron oil smoke droplets.

Methodology, instrumentation, data acquisition and data processing are all included in the third part in chapter six, in which a detailed description is presented regarding the experimental work conducted on the fuel injection systems and the development of the experimental rig, illuminating the process of extracting the macroscopic and microscopic characteristics of the JP8 fuel sprays.

The last part presents results and discussions (chapter seven) about spray pattern, spray development process, flow rate, droplet size probability distribution, injector performance and droplet velocity (PIV). The results of the laser scattering angle effect on a 3C-PIV camera position and correlation quality are presented in this chapter too. The light scattering results are based on the application of Mie theory on jet flow seeding (oil) submicron-droplets for the experimental work during the jet noise test (in QinetiQ wind tunnel facilities). Finally, chapter eight concludes with recommendations for further work.

Chapter2. Fluid Atomisation

This chapter briefly reviews the physical aspect of fluid atomisation in producing various sprays, and the factors affecting spray characteristics. Fuel spray combustion is applied in automobile engines, jet engines, gas turbines and industrial furnaces. The investigation into fuel spray characteristics is critical to the internal combustion systems for the optimal utilisation of the fuel energy. The chapter contains key definitions in the spray characterisation topic, such as spray cone-angle, tip penetration and Sauter mean diameter (SMD). An empirical study is presented to determine the relationship between the SMD and the spray jet velocity based on experiments on the JP8 fuel. The analysis differentiates between the spray exit (discharge) velocity and the after-atomisation tip velocity.

Fluid spray characteristics of importance to the fuel combustion topic can be divided into two main categories:

a. Macroscopic characteristics: including spray jet pattern, tip penetration, global velocity and spray angle.

b. Microscopic characteristics: including droplet size distribution, droplet velocity distribution and droplet spatial density.

2.1. Fluid Disintegration Process

Fluid atomisation is the process in which a liquid volume is broken down into fine droplets. The device that performs the atomisation task is referred to as "**atomiser**". There are various ways in which sprays can be produced. However, the fundamental principle in all of them is to generate a sufficiently high relative velocity between the liquid and the ambient medium.

If no external forces are applied, the surface tension of a fluid shapes it out into a compact spherical form as this has the minimum surface energy. The disintegration of a fluid bulk occurs when the surface tension is disturbed by external forces. This can be practically produced by increasing the kinetic energy of the fluid by pressurising it through a narrow nozzle, or by providing mechanical energy using a high-speed rotor or vibrator.

The atomisation process goes through two main stages. A **primary atomisation** where a volume of liquid is disintegrated into smaller segments, and a **secondary atomisation** where fluid elements encounter further fragmentation due to interaction with the surrounding air and other droplets.

In the case of global spray imaging, the characteristics of interest include the spray cone-angle and the tip penetration against time. Figure 2.1 is an example of a fuel spray image showing the spray angle θ and the tip penetration $S(t)$ for a single injection pulse. The term "injection frequency" represents the switching frequency of an injector which is the number of spray pulses delivered per second.

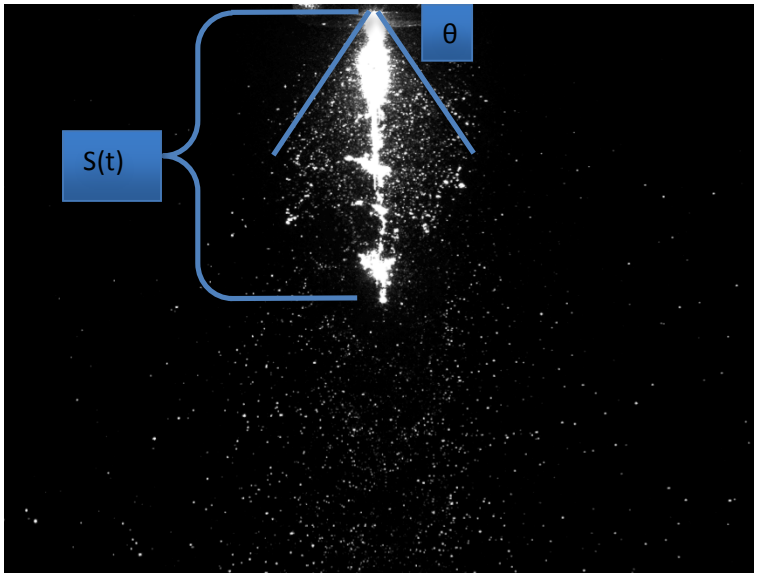

Figure 2.1 Fuel atomisation using plain orifice pressure atomiser at 5 bar injection pressure into unpressurised ambient; θ is the spray angle and S(t) is the tip penetration at the moment t.

2.2. Atomisers

The geometry of an atomiser and its operation mechanism play the main role in determining the macroscopic and microscopic characteristics of its spray. Beside the pressure atomisers, there is a wide range of fluid atomisers depending on the mechanism of producing the high velocity between the liquid phase and the gaseous phase such as rotary atomisers, air-assist atomisers, air-blast atomisers and other types [Watanawanyoo, *et al*. (2009); Chathcart, *et al*. (2005); Hoffman, *et al*. (1997); Lefebvre (1989)]. For example, in air-blast atomisers the fluid is injected using low pressure but into a high-velocity air stream [Kihm & Chigier (1991)]. The fuel injectors deployed in internal combustion engines are mostly pressure atomisers. The main principle of pressure atomisation is to convert the pressure into kinetic energy. Pressurised liquid jets travel faster when discharged into a relatively low-pressure medium. The sudden drop in pressure between the nozzle and the

ambient raises the fluid velocity (Bernoulli's principle)[1], giving it the required energy for breaking-up into a fluid mist. The exit velocity of a typical hydrocarbon fuel jet is proportional to the square root of the applied pressure.

$$U_e = const\sqrt{\Delta P} \tag{2-1}$$

There is a wide range of currently available pressure atomisers such as “plain orifice”, “simplex (pressure-swirl)”, “dual-orifice”, “duplex”, “fan- spray”, and “air-assist” Atomisers. Plain orifice and simplex atomisers are commonly used in automobile fuel injectors. Due to the relatively low viscosity of the automotive and jet fuels, it can be enough to pressurise the fuel through a circular nozzle into the combustion space in order to produce small fuel droplets. In this type of atomisers, spray particles have the highest velocity at the centre of the jet, which gradually decreases at the mist peripheries.

2.3. Factors Affecting Atomisation

The influence of the pressure differential between the fluid medium and the ambient has been investigated in several studies, mostly dealing with diesel engines. Due to the variation in injection system designs and the large number of variables involved in the spray characterisation, the relationship between the physical properties of an injector and the spray characteristics is usually determined by empirical modules relying on experimental measurements (or simulations in some cases). Some examples of these empirical modules will be later presented in this chapter.

[1] Daniel Bernoulli (1700 –1782) Dutch-Swiss mathematician.

Beside the injection technique, spray characteristics are also affected by the physical properties of the liquid and the surrounding air (or gas). The liquid viscosity, for instance, resists any change in the fluid shape, and therefore, liquids with smaller viscosities can be atomised at lower disruption energy. The high viscosity is associated with a small Reynolds number[1] which creates a time delay in the fluid breakup process.

Since hydrocarbon fuels show small differences in density (720- 810 kg/m^3), density has little influence on the atomisation process [Lefebvre (1989), Ch1]. The effect of the ambient gas density is reported several times in literature, where high values of ambient density negatively affect the spray penetration owing to its dissipation effect on the spray energy, but at the same time help producing wider cone-angles.

The surface tension, on the other hand, plays an important role in fluid atomisation. The surface area of all droplets together is larger than the surface area of the gathered liquid of the same volume. A spray with smaller particles has a bigger overall surface area. The surface tension of a liquid can be understood as the force that resists this increment in the liquid surface; meaning that liquids with higher surface tensions require higher energy levels to be atomised. Common petroleum derived fuels have surface tensions range between 23 and 32 mN/m at room temperature [Lefebvre (1989); Dormanb *et al*. (1951); NOAA; Dechoz & Rozé (2004)], which is considerably low in comparison with 71-73 mN/m for water at the same temperature. Liquids have smaller values of surface tension at higher temperatures [Berthier(2008), Ch.2], and for that reason, heating up a fluid before atomisation would help in producing sprays with smaller droplets for the same pressure level.

[1] The Reynolds number Re is a dimensionless parameter that represents the ratio of inertia to viscous force $\mathrm{Re} = \frac{\rho_l . U_l . r}{\mu}$

The atomisation phenomenon, therefore, occurs when the external forces represented by the fluid velocity and air density, overcome the internal forces represented by the surface tension. This can be mathematically described by the dimensionless "Weber number" [van Basshuysen (2009), Ch.3; Nigmatulin(1991),Ch.2] :

$$We = \frac{\rho_g U_l^2 D}{\sigma} \tag{2-2}$$

Where (D) is the diameter of the liquid drop, (U_L) is the liquid velocity, (ρ_g) is the air density and (σ) is the liquid surface tension. The atomisation of a hydrocarbon liquid fuel starts at Weber numbers bigger than 10-12.

Liquid instability and atomisation modes are mainly controlled by the Weber number[1] [Pai *et al.* (2009), Guildenbecher *et al.* (2011)], which estimates if fluid drops have sufficient kinetic energy to overcome the surface tension forces. At small Weber numbers, a drop starts splitting up into smaller droplets in a relatively slow manner until the new droplets reach a certain diameter where the Weber number is smaller than the critical value of fragmentation. At higher Weber numbers, the disintegration process becomes faster in a more explosive-like mode, producing much smaller droplets, as presented in Figure 2.2.

[1] Ohensorge number is also sometimes used in the qualitative fluid dynamic characterisation. It represents the ratio between the viscous forces and the surface tension; $Oh = \frac{\sqrt{We}}{\mathrm{Re}}$

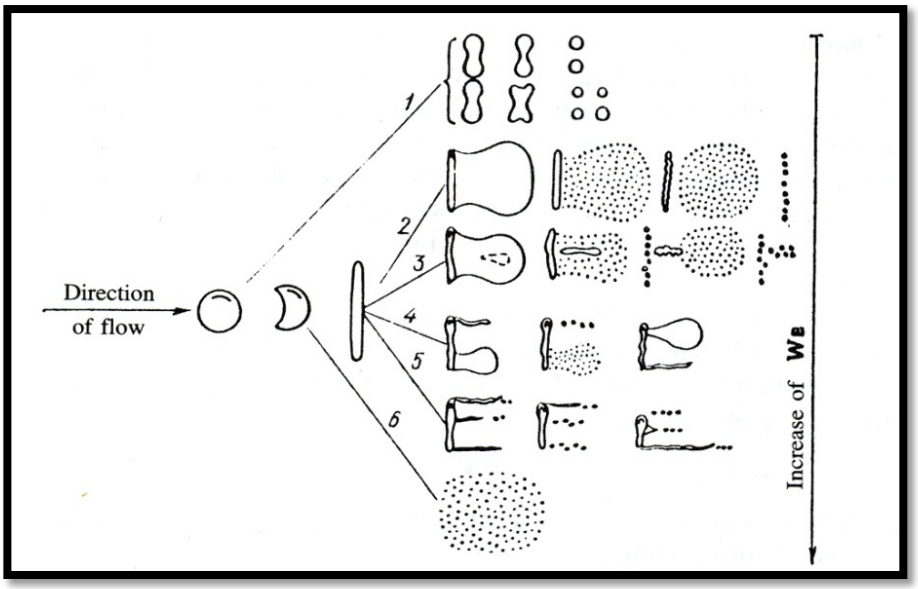

Figure 2.2 Different modes of fragmentation of a liquid drop interacting with gas flow, presenting the Weber number effect on atomisation [Nigmatulin(1991),P.158] ; (1) vibrational breakup (2) bag breakup (3) bag and stamen breakup (4) sheet stripping (5) wave crest stripping (6) catastrophic breakup.

Using a conventional gasoline injector with a nozzle exit 584 microns in diameter to atomise kerosene by applying 5 bar injection pressure, the measured fluid velocity at the moment of discharge was at the order of 40 m/s. The Weber number in this case is approximately 41.7 (Re=4730), which is almost four times larger than the critical Weber number, and this should be enough to produce an effective primary atomisation. The expected disintegration mode, in this case, takes a bag-like shape [Pilch & Erdman (1987)] during the first stage of atomisation, which agrees with the experimental results reported in [Berthoumieu et al.(1999)] and [Park et al. (2006)]. The jet tip velocity dropped down to around 28 m/s when measured 2 ms after the start of injection, making the critical diameter of fragmentation equals to 286 μm. The Weber number theoretical values for kerosene against the droplet velocity and diameter are presented in Figure 2.3.

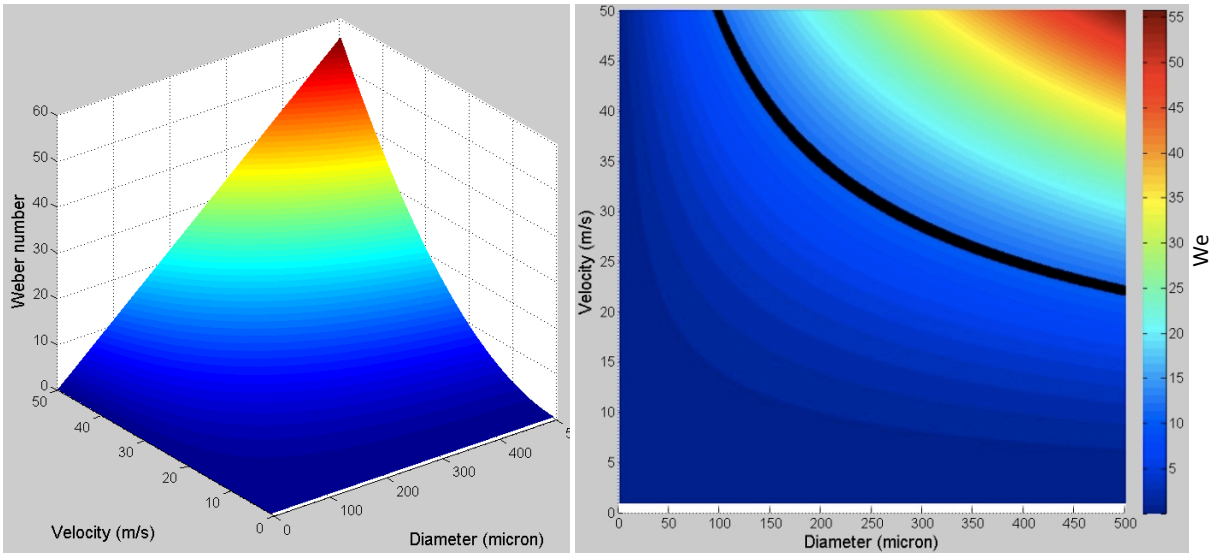

Figure 2.3. The Weber number for kerosene as a function of the droplet velocity and the diameter, marking the critical Weber number. Further fragmentation happens above the black mark (graphs are generated using Matlab code, see appendix 2.1).

2.4. Fluid Spray Characteristics

2.4.1. Droplet Size

2.4.1.1. Definitions

Fluid sprays contain droplets varying in size and shape. Depending on application, droplets size can be defined in different ways. Some important definitions include: linear mean droplet diameter, Sauter means droplet diameter, droplet diameter distribution, and mass-percentage diameter.

A simple way of describing a particle size in high-density fluid spray is by calculating the **linear mean** value of all diameters. The linear mean diameter is a useful parameter when comparing between different sprays. It is defined by the arithmetic mean value using the expression:

$$AMD(D_{10}) = \frac{\sum N_i D_i}{\sum N_i} \quad (2\text{-}3)$$

Sauter Mean Diameter (SMD or D_{32}) is a diameter of a single drop that has the same volume to surface ratio as the entire spray [Fleming *et al.* (2001)]. This diameter is used in fluid surface analysis and mass transfer, and it is important in combustion applications. The SMD is given by the expression:

$$SMD(D_{32}) = \frac{\sum N_i D_i^3}{\sum N_i D_i^2} \quad (2\text{-}4)$$

Droplet size distribution is calculated for a comprehensive view about the number of drops that fall within different size ranges. Sprays with a similar average diameter (or SMD) can have quite a different size distribution. The droplet size distribution is usually illustrated by plotting a histogram of the diameter probability distribution.

Another way to demonstrate droplet diameters is by defining (within the overall distribution) a diameter at which all smaller droplets together form a certain percentage of the total liquid volume. For example, $D_{0.1}$ refers to a diameter at which 10% of the total number of droplets have smaller diameter. Similarly, half of the particles have a smaller diameter than $D_{0.5}$ which is defined as **mass median diameter** (MMD).

2.4.1.2. Empirical Study

A mathematical module was suggested by [Merrington & Richardson (1947)] for calculating the mean droplet diameter in terms of viscosity and jet relative velocity. The fluid jet velocity was directly calculated from the measured pressure. The mean droplet size was defined as *"the size which is responsible for the greatest fraction of the total amount of*

liquid discharged". The droplets are collected on paper sheets located at a very high distance (around 15 m) from the nozzle, as high-speed imaging was not possible at that time. This experiment, therefore, investigated the breakup process in the central jet only, since the majority of the micro-particles spread at wide angles. Also, the change in liquid velocity with time was not considered in this case. This was a qualitative study where limited number of samples was used. However, it is worth comparing its results with those obtained by advanced imaging technologies; especially since the mathematical module of this result is still found in the modern literature of atomisation. In their experiments, Merrington and Richardson found that the mean diameter is inversely proportional to the liquid (relative) velocity U_L, as:

$$SMD = 500\frac{d^{1.2}\nu^{0.2}}{U_L} \tag{2-5}$$

Where (ν) is the fluid kinematic viscosity[1] (m^2/s).

Several empirical models were reported in the literature afterward, which usually have been very dependent on experiment conditions and measurement methodology; but what can be understood from all of them is the general relationship between a droplet diameter and various influencing factors.

In the experimental results of the current research on kerosene sprays, two aspects should be taken into account: the first is the relationship between the fluid velocity and the injection pressure; the second is the relationship between the droplet size and the fluid velocity. The exit velocity of a fluid (U_e) was found to be proportional to the square root of the applied pressure, which agrees with the equation 2-1. Using a single-nozzle (D_0=584

[1] Kinematic viscosity = Viscosity/ Density = (kg/s.m)/(kg/m^3)= m^2/s

μm), the ratio between the exit velocity and the pressure square root was almost constant at 17.5 on average (Table 2.1). This was noticed to be only true for the fluid exit velocity, as the ratio becomes incremental when calculated for the spray tip velocity after atomisation. The exit velocity was calculated at the moment (250 μs) after start of injection (ASOI), while the after atomisation velocity was taken around (2000 μs) ASOI. Therefore, the connection between the pressure and the jet velocity is defined, and now it should be associated with the particle sizing results.

Table 2.1: Fluid velocity, injection pressure, and SMD measurements on kerosene spray. Nozzle diameter is 0.584 mm, and $\nu_{kerosene}$=2.7 x10^{-6} m^2s^{-1} at 20° C (using data from test no.14 Table 6.3).

U_e (m/s)	U (m/s)	P (Bar)	SMD (μm)	U_e/SMD	$U_e/(P)^{0.5}$	$U/(P)^{0.5}$
At 0.25 ms ASOI	At 2 ms ASOI		(measured)			
39	28	5	52.06	0.75	17.441	12.522
35	22	4	61.92	0.57	17.500	11.000
29.5	16.5	3	71.24	0.41	17.032	9.526
24.5	12	2	86.31	0.28	17.324	8.485
18	8	1	106.31	0.17	18.000	8.000

Summarising the empirical results derived from different sources, particles mean diameter always decreases as the velocity of the fluid jet increases, which agrees with the formula (2-2) since increasing the velocity corresponding to higher Weber numbers and further fragmentation of the droplets; thus it is possible to write:

$$SMD = const U_L^{-x} \quad ; x \leq 1 \tag{2-6}$$

The constant (*const*) in the last relation is associated with the nozzle diameter and the fluid physical properties, and in more advanced studies the physical properties of the

ambient gas are included. In the previous example of Merrington and Richardson model, the mean diameter was inversely proportional to the jet velocity (x=1).

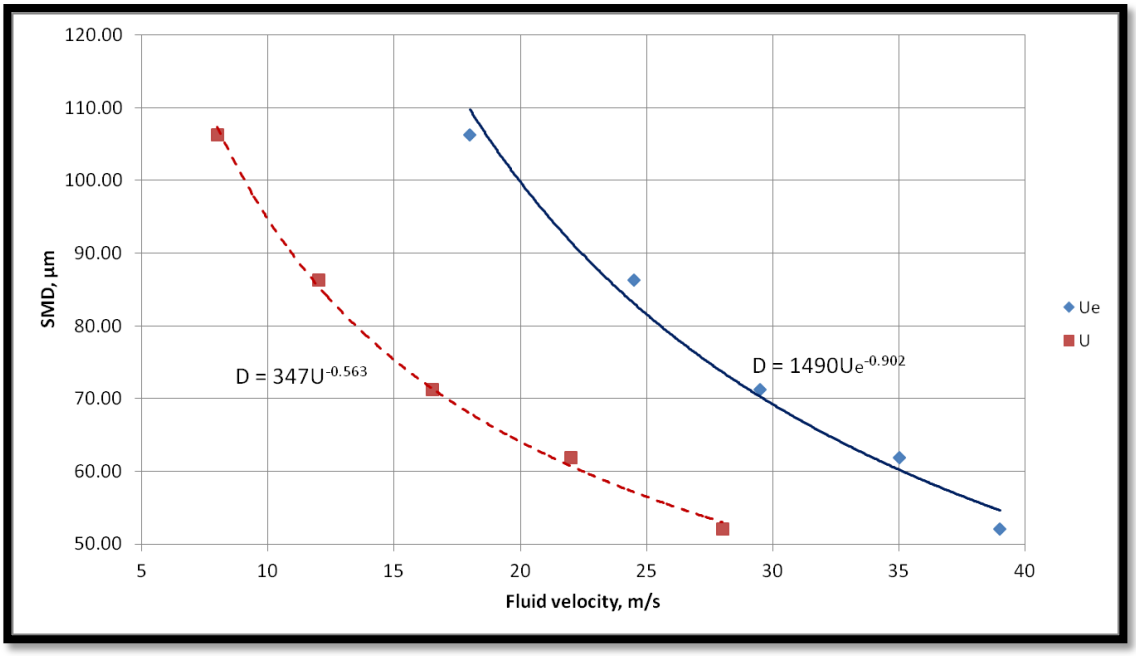

Figure 2.4 Measured SMD against fluid velocity for kerosene jet fuel. The fluid exit velocity (U_e) was measured at the moment 0.25 ms ASOI, while the after atomisation velocity was measured at the moment 2 ms ASOI.

By studying the kerosene data, the last relationship was almost accurate because (*x*) had a value of (0.902) only when dealing with the exit velocity. The factor (*x*) had a smaller value of (0.563) when calculating the velocity after (2000 µs) of injection, as shown in Figure 2.4.

2.4.2. Tip Penetration and Jet Velocity

The tip penetration of a spray is defined as the maximum distance that a fluid spray reaches when injected into a still ambient. It is physically understood that a fluid penetrates deeper as the kinetic energy of the jet increases, and therefore as the differential pressure increases (see the ambient pressure effect in [Lee et al. (2010)]). But it is more complicated in the practical applications as a higher fluid pressure leads to an early atomisation due to

the high Weber number, producing particles with smaller masses, and those lose their kinetic energy much faster. Jets with bigger droplets (or solid jets), therefore, penetrate further than the well-atomised sprays.

Several experiments have been conducted (mainly on diesel sprays) in order to find a mathematical relation linking the tip penetration to the differential pressure. Reported by [Naber & Siebers (1996)], this relationship was:

$$S \propto (\Delta P)^{0.25} \tag{2-7}$$

A similar result was reported by [Hiroyasu & Arai (1990)] and [Kennaird *et al*.(2002)], but with a connection to the density of the surrounding air as follows:

$$S \propto (\Delta P/\rho_a)^{0.25} \tag{2-8}$$

The penetration, therefore, decreases by increasing the air density of the injection space. High air density encourages the fast atomisation by increasing the pressure force on the fluid drops so that they overcome the surface tension force. This result was confirmed by [Iyer & Abraham (1997)] and [Arregle *et al*. (1999)]. The latter suggested that the relationship could be written as follows:

$$S \propto \left(\frac{\Delta P^{0.262}}{\rho_a^{0.406}} \right) \tag{2-9}$$

The tip penetration was a factor to be investigated independently of time in the early studies. The area of interest in this thesis is more related to the spray development process within the time frame, as it is important in this research to understand the changes the fluid jet velocity during the injection incident.

The shadowgraph method was applied by [Hwang *et al*. (2003)] for imaging the Dimethyl Ether (DME) fuel spray at a high injection pressure (350 bar). By adding the time factor to the formula, their results have shown that increasing the ambient pressure would increase the tip penetration (and the spray angle) through the empirical expression:

$$S = 0.39\left(\frac{\Delta P}{\rho_a}\right)^{0.25} t \qquad \text{For } t < t_b \qquad (2\text{-}10)$$

$$S = 2.95\left(\frac{\Delta P}{\rho_a}\right)^{0.25} (d_0 t)^{0.5} \qquad \text{For } t > t_b$$

Where t_b is an empirically calculated break up time of a droplet, and d_0 is the nozzle diameter.

The last formula also indicates that increasing the nozzle size results in an increase in the tip penetration. A similar formula can be found in [Kennaird *et al*.(2002)] for diesel, but with different constant values. Nevertheless, the image processing operations may lead to a difference in the results, especially with the disagreement about the greyscale threshold values that define the contour of the spray jet. This is because a fluid spray consists of small particles moving at different speeds, which cannot be treated as a single object.

The tip penetration of a fuel spray should be linked to the injection strategy in the engine; for example, a long-penetration can be desirable in direct injection engines, where fuel spray hits the hot walls of the chamber for a better vaporisation, but over-penetration could lead to a surface wetting of the combustion place. It becomes more essential to study the penetration velocity when the combustion chamber is relatively small.

2.4.3. Spray Cone Angle and Spray Pattern

Spray cone angle is affected by the same factors affecting the droplet size, such as surface tension, viscosity and pressure. A spray cone angle is connected to the spray scattering ability, which determines the spray pattern too. Sprays with a low penetration capacity and smaller particles tend to have wider angles. The empirical expressions of the spray angle differ from one study to another; yet there is an agreement that the cone angle generally increases as the surrounding air density increases and the liquid density decreases [Arregl, *et al.*(1999) ;Naber & Siebers(1996); Lefebvre (1989), CH7].

The same difficulties of calculating the tip penetration are also applicable to the cone angle since the fluid sprays have no smooth and clear contours when photographic methods are used. Furthermore, fluid sprays may have complex patterns (rather than a regular cone-like pattern), in which the angle calculation varies depending on the point of measurement. In literature, a spray cone angle can be measured at a distance $60D_0$ or $100D_0$ downstream of the nozzle exit. These two angles are referred to as “near- field angle” and “far- field angle”, respectively [Shao & Yan (2009), Lefebvre (1989), Ch7]. In [Iyer & Abraham (1997)], the spray angle was calculated in respect to the half penetration distance (S/2).

In the internal combustion application, the combustion efficiency and engine performance are affected by the distribution of the spray inside the combustion chamber and by the symmetry of its pattern. Experimental observations published by Louthan L. of AAI Corp. [Louthan(1993)] showed that the power output of a rotary engine improved when replacing a 30° fuel injector with a 60° one. This was explained by the less amount of unburned fuel in the case of larger spray angle.

Chapter3. Fuel Injection Systems

This Chapter briefly reviews the fuel combustion process, with the emphasis placed on the evaporation rate of kerosene droplets, and the relationship between the evaporation rate and droplet diameter. The time available for evaporation is extremely short in the case of high-speed rotary engines (typically 15,000 rpm) with small physical dimensions. This stresses the importance of the droplet size analysis of the fuel injection systems.

The second part of this chapter reviews the fuel injection strategies in current IC engines and explains the mechanism of electromagnetic fuel injectors (EFI). The focus of the current research is mainly on the gasoline indirect injection systems with sparkle-ignition setup due to the similarity with the one deployed in the new rotary engine subject of the study using kerosene (Jet-A1/JP8) jet fuel.

Finally, this chapter presents a literature review of the injection systems in modern rotary engines, including the effect of the injection-ignition timing on the output torque.

3.1. Introduction in Combustion Chemistry

Fuel combustion is a fast “exothermic” chain of hundreds or thousands of chemical reactions that transfer energy stored in the chemical bonds into heat. A general equation of the combustion of a hydrocarbon-air mixture for a certain air to fuel ratio (ϕ) can be given as follows [Ferguson & Kirkpatrick (2001), Ch3]:

$$C_\alpha H_\beta O_\gamma N_\delta + \frac{a_s}{\phi}(O_2 + 3.76N_2) \rightarrow n_1 CO_2 + n_2 H_2O + n_3 N_2 + n_4 O_2 + n_5 CO + n_6 H_2 + n_7 H + n_8 O + n_9 OH + n_{10} NO + n_{11} N + n_{12} C(s) + n_{13} NO_2 + n_{14} CH_4 \quad (3\text{-}1)$$

A hydrocarbon fuel is best thought of as a mixture of hydrocarbons rather than a fixed chemical formula. Kerosene, for instance, contains 9 to 13 carbon atoms [Dagaut & Cathonnet (2006)] in form of one n-dodecane, alkyl benzenes, and naphthalene derivatives. Kerosene is roughly represented in simplified chemical reaction expressions by its main n-dodecane molecular formula[1] ($C_{12}H_{26}$). The simplified oxidation reduction for Kerosene, therefore, could be written as:

$$C_{12}H_{26} + {}^{37}\!/_{2}\, O_2 \rightarrow 12CO_2 + 13H_2O \quad (3\text{-}2)$$

The heat realised by the reaction equals to ΔH= -7513 kJ (change in enthalpy), noting that the combustion heat energy released by 1 kg JP8 (kerosene) is approximately 42-46 MJ (42.8 MJ/kg in [Cookson *et al.* (1987)]).

An explosive reaction normally occurs at temperatures higher than 300-400°C and becomes faster by increasing the temperature. The primary fuel disappears shortly after ignition, producing unsaturated (lower-order) compounds and hydrogen with little energy release. The unsaturated hydrocarbons are oxidised to form carbon monoxide and hydrogen. The hydrogen oxidation increases gradually during the process to form water. Most of the energy is released afterwards when carbon monoxide is oxidised to form carbon dioxide [Glassman & Yetter (2008), Ch.3]. The combustion reaction characterisation including reaction speed, heat transfer and chemical species generated during the reaction,

[1] This is a general expression for different types of kerosene fuels. However, Jet-A fuel is given by the approximate formula $C_{12}H_{23}$ [Annamalai and Puri (2007), p.149] or $C_{11}H_{21}$ (JP8) [Dagaut and Cathonnet (2006)].

can be analysed by optical diagnostic of flame-fronts such as fibre optics spectrum analysis, high speed imaging [Wilson et al. (2002)] and mass spectrometry [Taatjes et al.(2008)].

Several researchers have been investigating the mechanism of single-drop combustion, and most of the effort in this topic has been made in form of experimental work. The time delay between introducing the fuel into a hot atmosphere and the ignition incident is called the ignition delay which can be divided into heating-up delay and evaporation delay [Satcunanathan (1971)].

3.1.1. Mass Transfer/Burning Rate

An isolated fuel drop in hot oxidizing atmosphere is a source for fuel vapour surrounding the droplet surface within a limited distance called the "flame reaction zone" [Krier & Wronkiewicz (1972)] or the flame radius. The reaction zone forms a flame envelope around each droplet where the fuel vapour defuses into the oxidant and reacts with it. In other words, the reaction zone is the "sink" where both the fuel substance and oxygen are consumed and turned into thermal energy [Annamalai & Puri (2007), Ch.16]. When a flame reaction zone is smaller than the distance between droplets, each droplet can be considered to be burning individually generating its own flame front [Brennen (2005), Ch.12]. Rapid reaction rates are connected with the large surface area between the micro-droplets and the hot oxidizer [Lu, et al. (1978)]. In the experiments of Lu, *et al.* the exploding "sensitivity" of the air-fuel mixture was found to increase as the fuel drop size decreases. Recent publications show strong relationship between the droplet size and the soot formation[1]. Large droplets do not completely burn, but turn into particulate matters (soot) to be later exhausted into the air. According to [Faiz et al.(1996), p.93], in order to have a "quick"

[1] See [Van Basshuysen (2009),pp. 67-70] for particle size and soot emissions at high fuel pressure values (200-600 Bar)

vaporisation (in gasoline engines), the SMD of the fuel droplets should be between 10 and 20 microns for direct injection, and around 100 microns for indirect injection.

The reduction in a fuel drop diameter with time is represented in the classic D^2-theory by the mass loss (evaporation) rate parameter (*k*) [Lawes M. (2007); Glassman & Yetter (2008), Ch.6; Annamalai & Puri (2007), Ch.10; Turns (2000), Ch.3]:

$$k = -\frac{d}{dt} D^2 \tag{3-3}$$

The mass loss rate is dependent on the fluid properties, and it increases as the temperature and pressure increase. It defines the speed in which a liquid fuel is turning into its gaseous phase. The temperature profile at the surface of a fuel drop, in the case of non-flamed evaporation, is different from the temperature profile of a burning droplet. In the first case, the temperature decreases by the heat absorption of the fluid drop; in the second case, the temperature gradually increases due to the chemical reactions during the combustion process. The evaporation rate during the combustion incident is sometimes referred to as “mass burning rate”, while the evaporation rate in the absence of combustion is called “mass transfer rate”.

Smaller droplets evaporate faster and mix better with the oxidant than larger drops due to their lower weight. The rapid mixture formation is essential in the IC engines especially those with a direct injection (DI) strategy since the time between the injection incident and the ignition spark is extremely short. Increasing the fuel velocity within the combustion chamber by applying a higher pressure behind the injector can improve the evaporation rate and the atomisation quality. This helps in performing a better heat transfer through the chamber walls and a better mixing with air in the induced vortexes [van

Basshuysen, 2009, Ch.3]. Additional velocity components can be gained when injecting the mixture during the compression stroke (either in piston or rotary engines). Beside the piston/rotor guidance of the flow, the high pressure reduces the vortexes diameter in the turbulent air, and therefore increasing the angular velocity.

In his experiments, Glassman [Glassman (1997), Ch6] has investigated the soot formation process during the fuel combustion (Figure 3.1-A). It is clear that the burning rate of a fuel drop decreases as the drop diameter increases for the same ambient temperature. The effect of increasing the ambient temperature is always positive on the evaporation rate (see: Appendix 3.3).

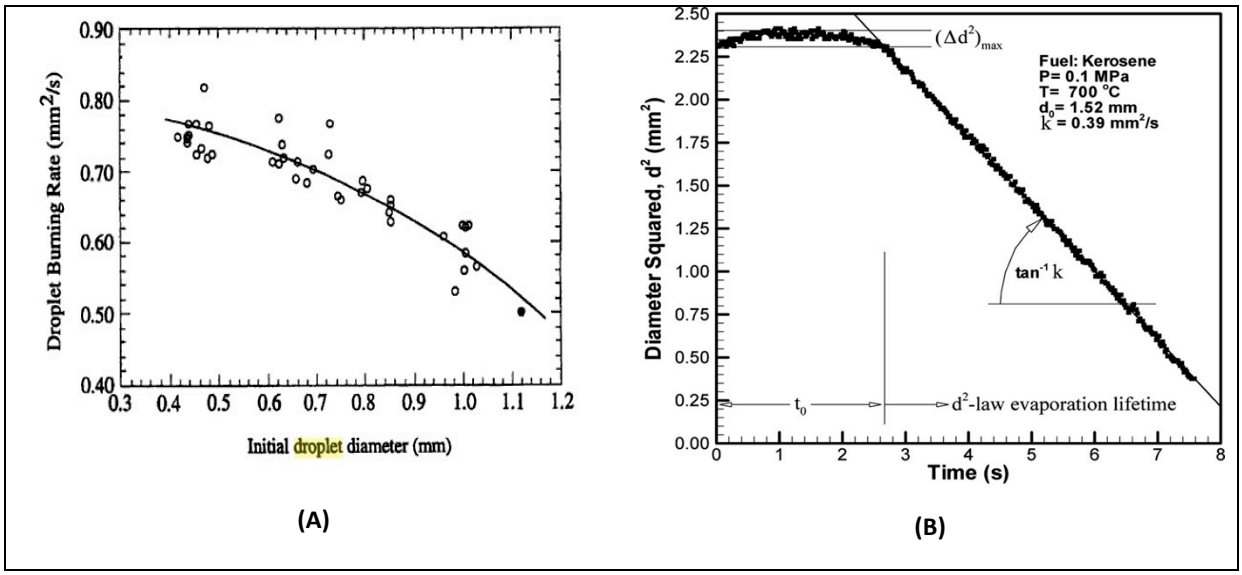

Figure 3.1 (A) Fuel drops (heptane) burning rate against Initial droplet diameter, source [Glassman (1997), Ch6]; (B) Changes in kerosene drop diameter squared against time. Initial diameter is 1.52mm at temperature of 700°C and pressure of 0.1 MPa (1 Bar). The calculated evaporation rate was 0.39 mm^2/s, source [Ghassemi *et al*. (2006)].

Related experiments were made by Ghassemi *et al*. [Ghassemi *et al*. (2006)] for kerosene drops. It was found that a kerosene drop in hot environment goes through two

stages during its lifetime, as shown in Figure 3.1 (B). In the first, changes in the squared diameter are nonlinear during a time interval (t_0) related to the initial diameter of the drop, the temperature of the surrounding gas and the chemical composition of the fuel. This time delay can be explained as the period needed for a drop to reach the boiling point where the evaporation during this period is unimportant. The diameter changes become linear afterward to follow the D^2-theory where the evaporation process becomes rapid. The evaporation of the JP8 jet fuel starts from the temperature of 165°C [Kutz (2006)].

The presented general behaviour of evaporation explains why increasing the ambient temperature has a very small effect on the spray area close to the injector nozzle but much more effect downstream from the nozzle. This agrees with the results reported in different resources with differences in time and rate values depending on the combination of the fuel itself. The effect on the pressure was found fluctuating between positive and negative in Ghassemi *et al*. study [Ghassemi *et al.* (2006)]. Chin and Lefebvre [Chin and Lefebvre (1931), in Lefebvre (1989), Ch8] defined the pressure influence more precisely: the evaporation rate for kerosene (JB-5) was found to increase as the pressure increases only for an ambient temperature higher than 800 K (around 527°C). For temperatures lower than 600 K (around 327°C), increasing the pressure was found to have a negative impact to the evaporation rate. Evaporation rate was independent of pressure between the two temperatures.

3.1.2. Discussion in light of the present project requirements

Using the above findings about the evaporation rate, it is possible to – roughly – estimate the time and conditions needed to maximise the evaporation of a kerosene droplet. From Ghassemi *et al.* study [Ghassemi *et al*. (2006)], the initial time delay for

heating up of fuel drop (t_0, where there is no change in diameter) can be calculated in respect to the drop initial diameter[1], and it has, for example, the value of: { $t_0 = 0.4\ D_0^2$ } at the 1000°C temperature and 1 MPa (10 Bar) ambient pressure. The evaporation rate under these conditions is equal to (K_v=1.88 mm^2/s). By going back to the D^2 law (equation 3-3), the drop diameter size (D) as function to time delay (t), can be plotted as shown in Figure 3.2.

The speed of the rotary engine under test is typically 15,000 rpm, which is equivalent to a period of 4 ms per revolution. If we consider that the intake and the compression strokes take half of the revolution period until the TDC when the ignition spark takes place, then the fuel droplets have around 2 ms only to evaporate.

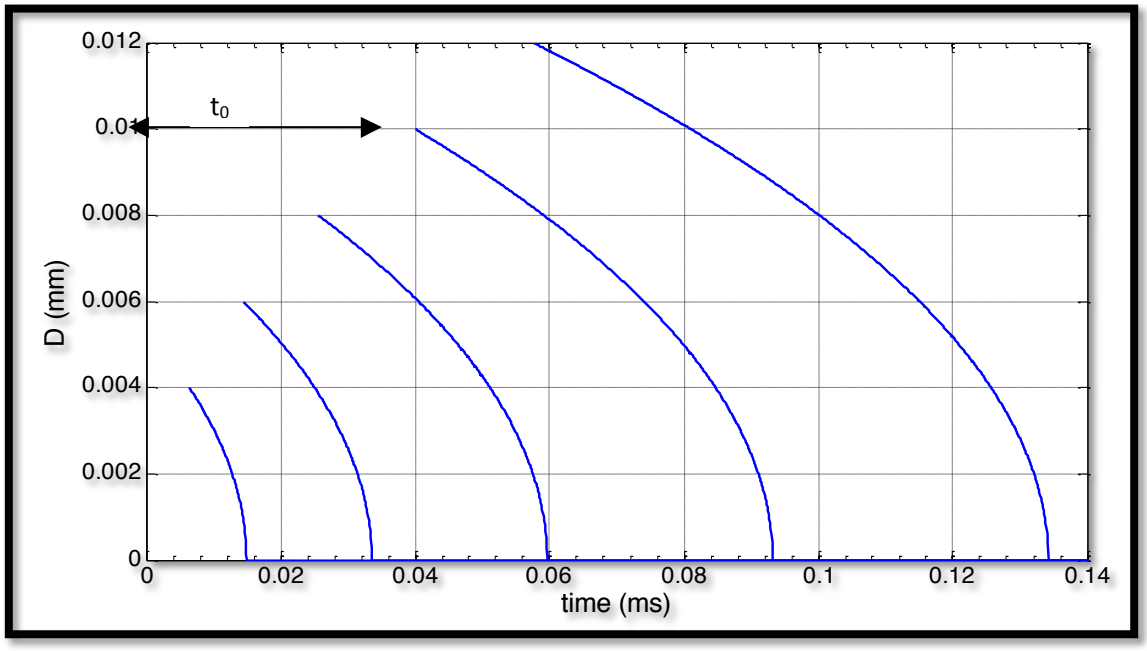

Figure 3.2 Changes in small droplet diameter against time for kerosene at T= 1000°C, P=1 MPa.

The temperature and pressure profiles inside the combustion engine cavity are always gradual. During a 2 ms spray life time, for example, most of the compression (and

[1] See Figure 3 in the same reference.

the heating up) is happening during the last 0.7 ms. From Figure 3.3, it can be seen that droplets larger than 36 µm in diameter will have no chance to completely evaporate before ignition, even with a high temperature as 1000°C. Moreover, larger fuel drops will not be able to reach the boiling point within the available time at such a high speed.

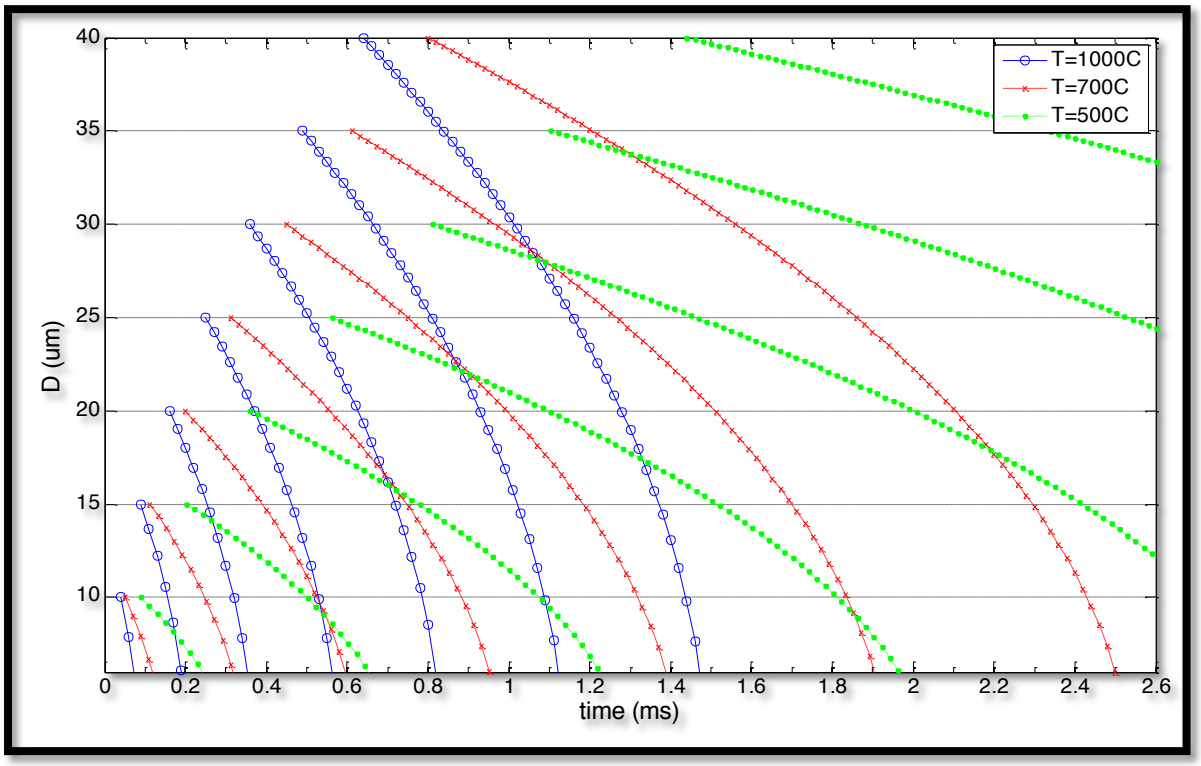

Figure 3.3 Changes in drops diameter against time for Kerosene Jet fuel at T= (1000, 700, 500)°C, P=1 MPa.

When an engine is operating at a relatively low temperature environment and with no preheating of the fuel, less evaporation during the intake stroke will take place, and the time for the fuel evaporation during the compression stroke is extremely small. In the indirect injection method, fuel droplets have much longer time to evaporate inside the intake manifold. Under a temperature of 500°C, particles with 15 µm diameter will take around 0.7 ms to completely evaporate. For the same droplet, around 1.6 ms is the

estimated evaporation time at 300°C; which shows the importance of the ambient temperature on the evaporation process[1].

3.2. Fuel Injectors

A fuel injector provides the fuel mixture into the combustion chamber during the intake stroke in the form of individual pulses at the system pressure. Fuel injectors are used in gasoline, diesel, heavy fuel, hydrogen and Liquefied petroleum gas (LPG) systems, and they have broadly replaced the old carburettor system in the automobile industry. Fuel injectors regulate the flow rate of the fuel mixture in the internal combustion system and increase the total fuel surface area, and thus, improve the heat transfer from the surrounding ambient to the fuel droplets which consequently speeds up the mixture formation leading to a more efficient chemical reaction [van Basshuysen (2009), Ch.3; Lefebvre(1989), Ch8].

Conventional fuel injectors (Figure 3.4) are electrically controlled by an electronic engine control unit (ECU). The electric current through an induction coil governs the movement of the valve arm, allowing the pressurised fluid to periodically pass into the final orifice disk. This type of injector is called “Electromagnetic Fuel Injector” or “Electrical Fuel Injector” (EFI). The pressure power comes from an external fuel pump rather than from the injector itself. The orifice disk contains a singular or multiple outlet holes where fuel is discharged at high velocity. The accurate control of the injection pulse-width, the frequency

[1] For evaporation rate at different ambient pressure and temperature values, see [Ghassemi et al (2006); Harstad & Bellan (2004)] for kerosene jet fuels, and [Anderson *et al.* (1996), in Van Basshuysen (2009), P.39] for gasoline.

response, the reliability and the durability are important characteristics of practical fuel injectors.

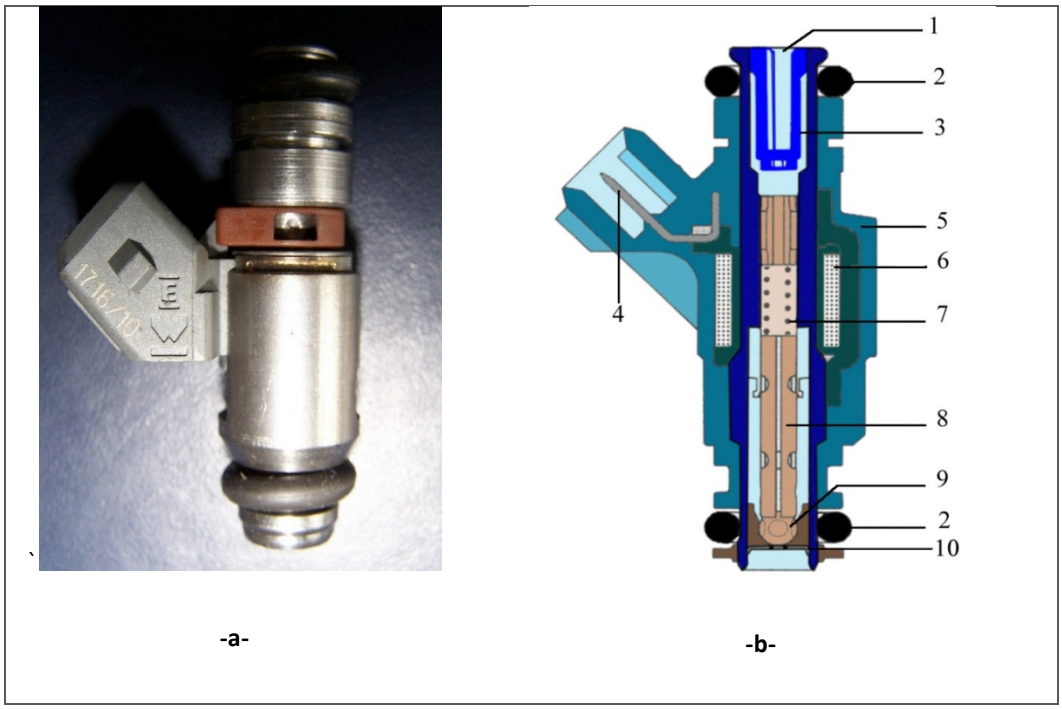

Figure 3.4 Conventional electromagnetic fuel injector (EFI); (a) IWP gasoline electromagnetic injector (b) Cross section in gasoline injector [adapted from Robert Bosch GmbH (2006)]. 1. Fuel inlet; 2. Rubber O-rings; 3. Filter; 4; Electrical Power plug; 5. Housing case; 6. Electromagnetic coil; 7. Return spring; 8. Valve arm; 9. Valve ball; 10. Orifice end disk.

The injector is attached to the engine's throttle body, where a throttle valve regulates the air mass entering to the engine's cavity. Large engines with multiple cylinders include several fuel injectors connected with the fuel delivery system through a common rail. The purpose of the injector is to generate fuel droplets as small as possible so that a better mixing with the air is performed.

Emission control in IC engines is related to the accuracy in the injection timing, which is possible by using adaptive closed-loop electronic controllers that can detect any deviation from the optimum combustion and correct it, rather than operating under predefined

parameters or with a mechanical intervention from the engine. A set of sensors, such as air-flow, engine speed, and temperature sensors, continuously reports information about the engine operation conditions and requirements to the ECU; for example, starting an engine from cold needs higher amount of fuel supply than normal.

The switching mechanism of an injector is limited to the time needed for the electric current to develop the required electromagnetic force in the coil in order to oppose the spring force, and therefore, to move the valve arm. This causes an offset time between the pulse trigger and the flow lift-off point; thus, the fuel delivery rate increases gradually during the injection event. The ratio of the maximum to minimum duration of injection is called the *dynamic range* of an injector, where the maximum duration is determined by the rotational speed of the engine and the minimum duration is connected to the injector design [Garrett (1991), ch.11].

3.3. Fuel Injection Strategy

There are two main strategies in how the liquid fuel is introduced into an engine's combustion place; namely, direct injection and indirect injection (Figure 5.3).

In the **direct injection (DI)** strategy, fuel is injected directly into the combustion chamber early during the intake stroke in order to maintain enough time for a homogeneous air-fuel mixture formation. The fuel spray, in this case, can be either self-directed by the external pressure only, or directed by the wall/piston surface where the micro-mist bounce off the surface toward the ignition plug, giving more time for mixing with air.

The indirect injection (IDI), also called **manifold injection** or **port injection,** can be achieved by injecting the fuel into a manifold where it is mixed with air and stored until the intake valve is open, and then drawn into the cylinder (in piston engines). Depending on the engine design, fuel is injected either before opening the intake valve where fuel spray strikes the walls of the manifold (and the valve), or while the valve is still open.

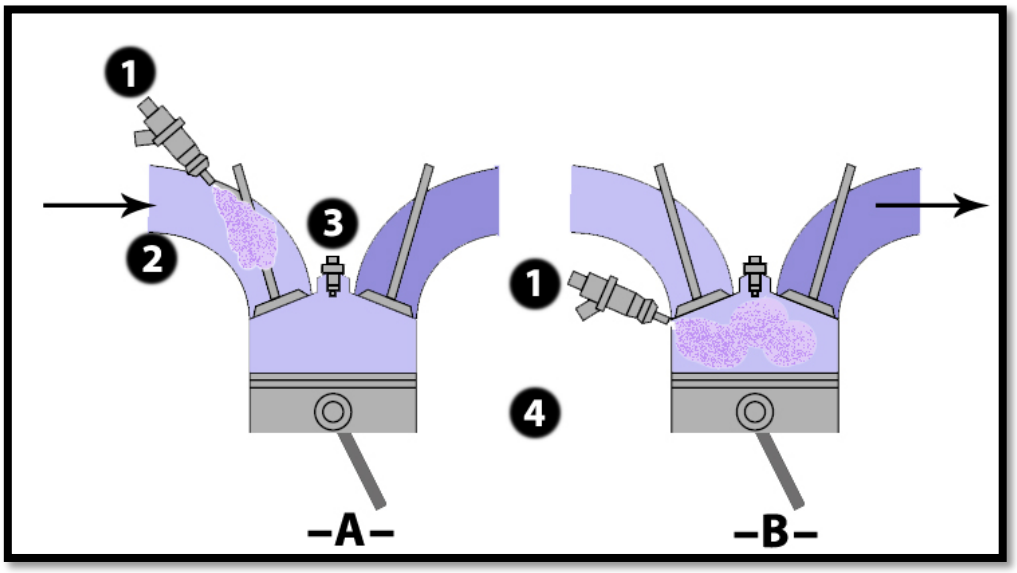

Figure 3.5: (A) indirect injection (IDI) strategy and (B) direct injection (DI) strategy in IC engines. 1. Electrical fuel injector (EFI), 2. Mixture intake port, 3. Spark plug, 4. Cylinder.

In piston engines with multiple injectors, the sequence of the injection pulses should be considered in relation to the position of the crank shaft for each cylinder during the engine revolution. The calculation of the pulse duration depends mainly on the injector switching profile, the pressure difference between the fuel and the manifold, and the amount of air allowed by the throttle, aiming to produce a homogeneous fuel-air mixture before the ignition spark [Robert Bosch GmbH (2006)]. It is worth mentioning here that the air-flow ratio and the injection duration should be connected with an engine temperature to

avoid increasing the amount of untreated emissions, especially in the cold start case, as most of the vaporisation occurs in the intake manifold.

Direct injection (DI) engines are proven to have a higher degree of freedom in injection timing control, which increases the compression ratio (high-power per cycle) and improves fuel economy and thermal efficiency [Osuga M, et al. (2004); Ferguson & Kirkpatrick (2001), Ch1]. The reaction time in the injector mechanism should be extremely short in the DI case, which could be difficult to achieve at high fluid pressures using electromagnetic injectors, so high-frequency high-pressure piezoelectric injectors are applied instead [Van Basshuysen (2009), Ch.4]. In comparison to indirect injection, the direct fuel injection into hot walls has an advantage of faster evaporation, and another advantage of cooling down the walls, which allows operating at lower temperatures. The mixture, therefore, will contain more air and less fuel to generate the same output of mechanical energy. But on the other hand, this increases the wall wetting, and thus, the unburned hydrocarbons.

By avoiding the direct injection into the combustion chamber, less energy is needed to overcome the compression pressure in the cylinder, and longer time will be available for a fuel spray to develop, evaporate, mix with air and combust [Poulton (1994), Ch.2; Garrett (1991), Ch.11]; a better atomisation, therefore, is required in direct injection strategy by using a very high fuel pressurising. In diesel engines with indirect injection (IDI), diesel is supplied at a pressure of 100 - 400 bar. Higher pressure is needed in the case of direct

injection (DI) which could exceed 1500 bar[1] [Morgan R, et al. (2001); Garrett (1994), ch.5]; such a pressure is built-up using multiple pumping stages.

3.4. Rotary Engine Review

A rotary engine (RE), often called Wankel engine[2], is an internal combustion engine with rotary movement of the piston, replacing the reciprocating movement in the ordinary cylinder engine. The piston in this case is called 'the rotor' which typically has a Reuleaux-like triangle shape (with flatter sides) forming three cavities inside the engine (Figure. 3.6). The volume of each cavity varies depending on the rotor angle. Another difference between piston and rotary engines is that the latter has no valves at the intake and the exhaust ports since they are controlled by the rotor motion itself [Poulton (1994)]. However, the power generation mechanism is still unchanged as the power cycle in the rotary engine involves the same four strokes of the conventional engine, namely: intake, compression, expansion (ignition), and exhaust, as shown in Figure 3.7. While the four strokes take place inside a single cylinder for the reciprocating engine, they occur in several places in the internal cavity of the rotary engine. The localised combustion in the rotary engine case, on one side, have advantages of decreasing the heat and the unburned fuel losses, as well as making the rotary engine more suitable for fuels with a quicker explosion potentiality such as **low octane-number gasoline** and **hydrogen.** The relatively long time available for mixing the fuel charge reduces the pre-detonation and engine-knock problems, which are common in reciprocating engines. On the other side, the localised combustion leads to an uneven

[1] Up to 2500 bar fuel pressure is reported for some recently developed diesel injectors.
[2] After Felix Wankel (1902-1988), a German engineer.

thermal distribution over the engine body. Rotary engines could be either air-cooled or liquid-cooled.

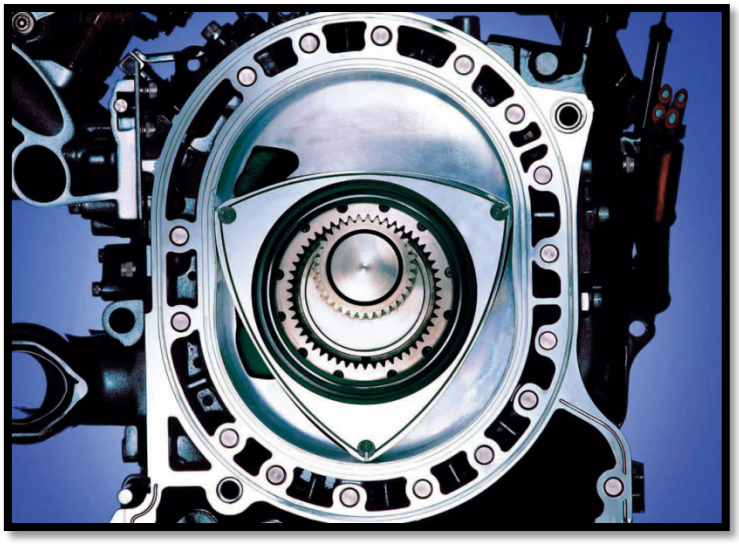

Figure 3.6 Mazda rotary engine for Mazda RX-8 sports car [Mazda website].

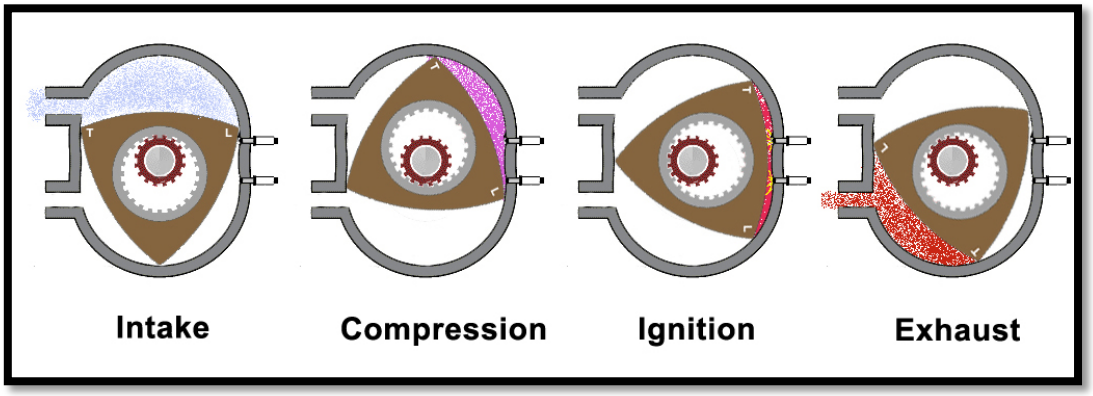

Figure 3.7 The power cycle of a rotary engine.

One important advantage of the rotary engine is that it has less moving parts than the conventional engines, and consequently, less: (1) friction losses, (2) complexity, (3) vibration, and (4) noise [Ansdale (1968)]. Moreover, the rotary engine needs only one combustion incident per revolution, compared to two per revolution for the reciprocating

engine [Poulton (1994)]. This allows building either more powerful engines or smaller in size and weight, which has recently made the rotary engine more attractive to the industry of racing cars and motorcycles, as well as aircrafts engines, where high power to weight ratio, low fuel consumption and low vibration are highly required. The rotary engine is considered as a smooth engine due to the sustained power delivery, unlike the uneven power delivery of the piston engine.

3.4.1. Fuel Injection in Rotary Engines

The fuel-air mixture is introduced to the intake chamber by the reduction in pressure (suction) created by the movement of the rotor [Ansdale (1968), Ch.8]. The air share in a fuel mixture is regulated by the opening time of the throttle and the area of the intake port. The fuel injector directly determines the amount of fuel introduced into the engine. The rotary engine is believed to have a quicker response to the throttle changes than the cylinder engine. In addition, it is easier to apply the direct injection strategy in the rotary engine case, owing to the relatively long time available for the fuel-air mixing process, beside the ability to avoid the direct exposure of the injector to the excessive heat.

Carried out by Hasegawa and Yamaguchi [Hasegawa & Yamaguchi (1993)] on a stratified charge single-rotor engine, the visualisation of the fuel mixture flow and the combustion analysis show that, at a low intake pressure (0.6-1 Bar), Vortices are formed at the leading and the trailing edges of the rotor. In the case of an engine rotating in a clockwise direction, a "*clockwise vortex driven by rotor motion becomes the main flow at low intake pressure",* gradually moving toward the leading edge of the rotor. By increasing the intake pressure a counter-clockwise vortex is formed at the leading edge of the rotor beside the clockwise vortex. The new vortex grows toward the leading edge as the rotor

moves due to the increasing pressure at the leading end. The counter-clockwise vortex eventually dominates the flow and weakens the other clockwise vortex in the trailing end. Therefore, by supplying the fuel to the dominating counter-clockwise vortex, it is possible to hold the stratification state of the charge as late as possible in the compression stroke before the combustion stage.

3.4.2. Injection-Ignition Timing

Optimum ignition timing is usually calculated so that the maximum possible torque is obtained. The ignition timing is defined with respect to the crank angle and is dependent upon speed and load. If a mixture is ignited too early during the compression stroke, the combustion pressure pushes the piston/rotor backward as it is approaching the top dead centre (TDC), and therefore, reducing the torque output. Likewise, a too late ignition leads to a smaller flame area [Babajimopoulos *et al.* (2003)], so the pressure work decreases in this case.

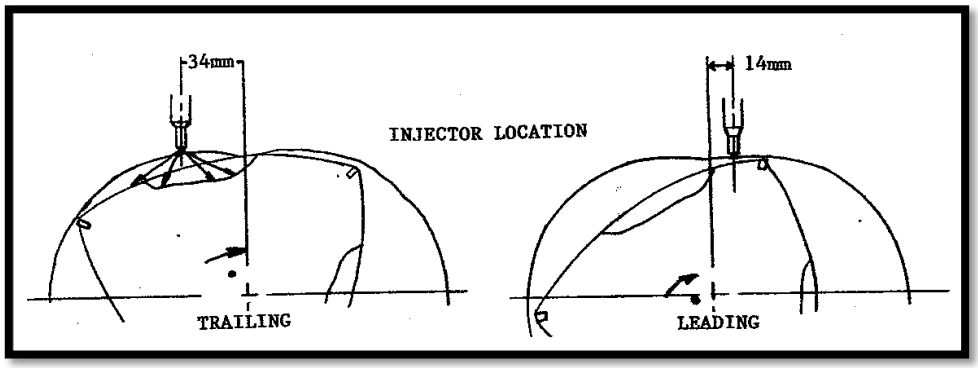

Figure 3.8 Trailing and leading injection. Changes in the location of the injector [Kamo *et al.* (1987)]; Injection time=35°BTDC.

In the case of direct injection, combustion quality is also influenced by the position of the main injector. It was found [in Kagawa *et al*. (1993) and [Louthan (1993)] that the main spray should be injected upstream of the flow (trailing injection) into a narrow, long,

combustion cavity by installing the injector well before the TDC. This provided a better distribution of the mixture and reduced the effect of the chamber high pressure on the injector. Figure 3.8 shows trailing and leading injection methods in a rotary engine.

3.4.3. Ignition Arrangement in Rotary Engines

Flames propagate at the flow direction, which also agrees with the rotor direction. However, flames could slightly propagate in the reverse direction of the rotor causing undesirable knocking phenomenon [Muroki et al. (1986)]. The position of the spark plug and the ignition timing play a main role in controlling the flame propagation and preventing the back flames.

One important study on rotary engine efficiency was published by Kagawa et al. of Mazda Motor [Kagawa *et al*. (1993)]; with the main goal of enhancing the ignition stability. In ignition methods, which use a single spark plug, the combustion could become unstable, especially when running on lean mixtures. A new approach suggested that deploying the spark plug inside a small cavity could hold a small amount of the ignitable vapour around it; this method was called the “sub-chamber ignition system”. The sub-chamber was opened and throttled against the injector, allowing most of the fuel sprays to flow into the main chamber (Figure 3.9). The only task of this arrangement is igniting the mixture while another main injector provides the major amount of the fuel spray which is burned by the flames from the sub-chamber. When air density in the main chamber is low, more fuel is ‘dragged out’ of the sub-chamber, and in opposition when air density is high most of the fuel in the sub-chamber is held there for re-circulation. Therefore, a continuous stable ignition could be produced where the air-fuel ratio around the plug is largely independent of the intake pressure and the throttled air. The published results [Kagawa *et al*. (1993)] showed an

improvement in fuel consumption and exhaust emissions when applying the sub-chamber ignition technique with the upstream direct fuel injection.

The sub-chamber idea is only a modification in principle of the previously developed 'pilot injector' ignition technique. In the pilot injection systems, a relatively small amount of fuel is injected toward a glow plug by a pilot injector. The produced flames increase the temperature and the pressure inside the combustion chamber, creating a suitable environment for the combustion of the (main) spray injected by a primary fuel injector [Louthan (1993)]. The pilot injection method is very useful in engines with low compression ratio or with lean mixture in decreasing the misfires effect.

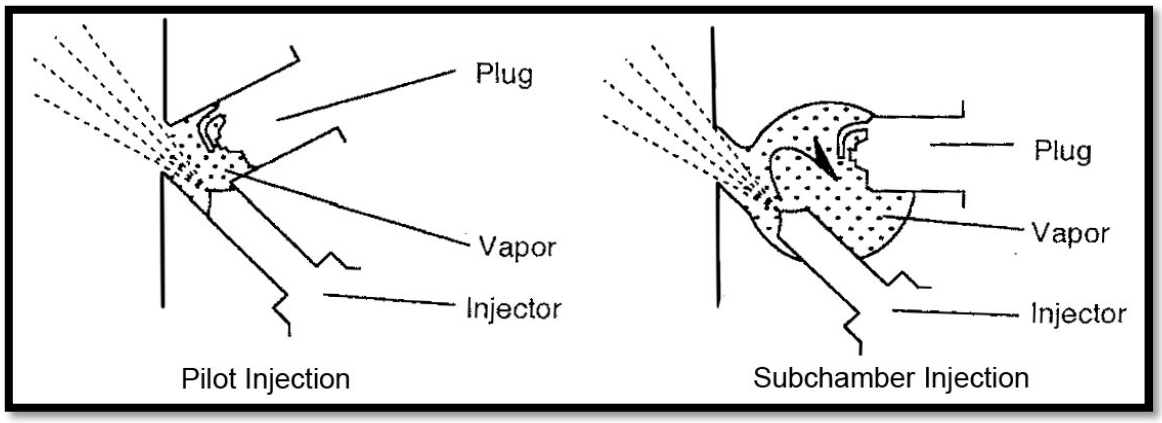

Figure 3.9 Sub-chamber ignition system with secondary fuel injector [Kagawa *et al*.(1993)].

Due to slow combustion, rotary engines emit lower concentrations of NOx but much more hydrocarbons (less economic). The slow combustion is a result of the low turbulence diffusivity caused by a relatively long time between the intake and the peak compression points [Abraham, *et al*. (1988)]. Two spark plugs (twin-spark) can be used in order to speed up the combustion and reduce the late explosion effect.

A recent study by Mazda Motor [OKui *et al*. (2009)] on an indirect injection optical rotary engine shows that the flames propagate only in the rotation direction and in a very

high-speed[1], so that a small amount of fuel vapour in the upstream remains unburned until a late stage of combustion. The first stage of combustion is the main combustion incident in which more heat is generated than in the late combustion period. The late combustion phenomenon reduces the efficiency of the rotary engine. In order to reduce the heat release during the late combustion, different spark plug arrangements were tested [in OKui *et al*. (2009)]. The trailing plug (above the short-axis of housing) was named the T-plug, while the leading plug (below the short-axis) was named the L-plug. The results of that research concluded that moving the T-plug in the upstream direction would reduce the late combustion phenomenon, and consequently, improve the thermal efficiency. Another modification was made to their engine by using two parallel leading spark plugs instead of one; the reason being that the flow at the rotor width direction is very weak, and two plugs at the leading end would improve the flame propagation at that direction. The heat release analysis showed the best possible efficiency was produced by using two L- plugs and one T-plug with a long distance between them, as presented in Figure 3.10.

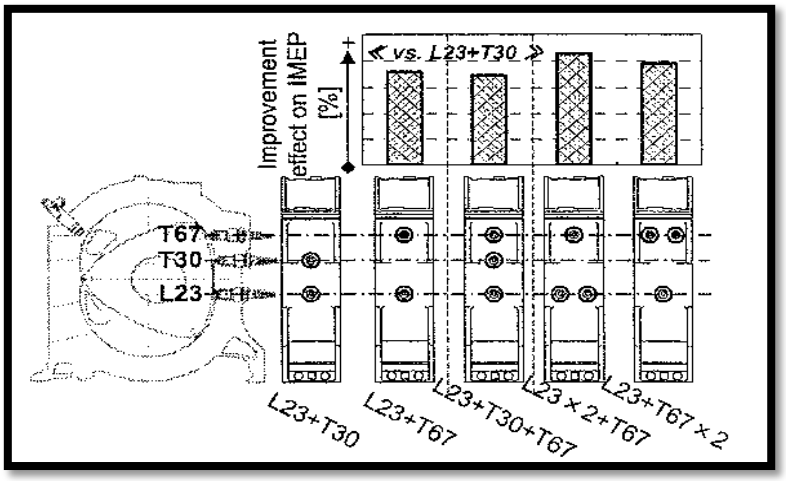

Figure 3.10 Different spark plug arrangements and their influence on the indicated mean effective pressure (IMEP) [OKui *et al*. (2009)]. Positioning numbers are in millimetres.

[1] The unidirectional, fast and low turbulent flow inside the combustion space leads to non-uniform pressure gradient which negatively affects the engine efficiency [Abraham, et al.(1988)].

Chapter4. Optical Diagnostics in Multiphase Flows; Available Tools and Related Works

This chapter reviews optical methodologies and recent experiments related to the visualisation and analysis of fluid sprays. The chapter starts with a brief introduction to laser technology and its application in multiphase flow diagnosis. This includes non-imaging diagnosis, such as LDA and LDV, and imaging techniques, such as PIV and shadowgraphy. Both direct imaging and laser-sheet imaging techniques are reviewed in this chapter since these methods are applied in our experimental work on the jet fuel sprays. Microscopic shadowgraphy is used for droplet sizing, which allows measuring non-spherical droplets as an advantage over the light scattering (diffraction) methods.

4.1. Introduction

Multiphase flow information can be extracted using mechanical or optical techniques. The mechanical techniques use sampling and microscopic inspection, while the optical methods are generally based on imaging and particle-light interaction analysis. Particle sizing is possible both by the mechanical and the optical methods, while velocity measurements are usually performed by optical methods such as PIV (Particle Image Velocimetry) , which is an imaging technique based on the successive imaging and image-

correlation [Crowe *et al.* (1998), Ch.9], or LDV, which is a light-scattering point measurement technique.

Mechanical methods are more popular in the case of solid particles (powder) than in fluid sprays. In mechanical patternators, samples are collected from the moving phase through containers divided into sections or buckets. A representation of the solid/fluid phase distribution within the gaseous phase can be obtained by calculating the mass of each sample. Another sampling method is by the quick exposure of a multi-phase flow to a microscope slide, in order to collect the moving particles, followed by their observation using an ordinary microscope. The limited spatial resolution of the mechanical methods leads to a lack of accuracy, besides the relatively slow process of data acquisition and examination. Moreover, the mechanical methods generally interrupt the flow pattern.

Optical methods, on the other hand, are widely used for fluid spray measurement due to their non-intrusive nature and the high spatial and temporal sampling accuracy. The physical principle of the optical diagnosis generally relies on the interaction between the moving particles and the light waves, and monitoring the changes in the waves' properties using photo-sensors. Light attenuation method, for example, uses the intensity difference between the emitted and the received optical energy in order to estimate the particle density when a light beam travels a particular distance through a multi-phase stream. The particle size in this method should be accurately identified (mono-size) in order to calculate the particle concentration, which is not applicable in the case of fluid sprays due to the wide spectrum of diameters involved.

Non-imaging light scattering methods, such as LDA and PDA, are point diagnosis techniques that can perform measurements on a certain point of a multiphase flow by

averaging out the effect of the particles on a laser beam. The light diffraction methods rely on the calculation of the intensity of a scattered laser beam at different angles after interacting with a multiphase flow. Instruments based on the light diffraction technology (such as Malvern) are high in cost and need a careful calibration using particles with accurately known diameter and refractive index. Also, all light scattering methods assumes that particles are perfectly spherical, which is not always an acceptable assumption for the high-speed sprays.

In the imaging methods, images are usually taken by a camera and then enhanced and processed in order to obtain the 2D information about the particles (size and distribution). Double-frame or high-speed imaging can be used to calculate the particles' velocity. Laser is the preferable light source in the imaging technique, although other artificial light sources are still in use for some applications. At the microscopic range, light scattering methods can be used to measure a droplet size through its diffraction pattern. Alternatively microscopic shadowgraphy can be applied so that micro-droplets images can be taken, with the added advantage of being able to detect particles with different shapes. Different approaches have been applied in approximating an irregular shape of a droplet into the corresponding spherical shape. A particle diameter could be represented by the size of the longest axis or by the average diameter at different axes. The Equivalent Spherical Diameter (ESD) method can provide a better representation of a droplet size [Kashdan *et al.* (2007)] where a particle volume is measured through its cross-section area and then linked to a sphere diameter of the same volume.

4.2. Lasers Application in Multiphase Flow Characterisation

4.2.1. Laser Overview

Laser (Light Amplification by Stimulated Emission of Radiation) is a special type of artificial light source which has a near-instantaneous intensity and a narrower frequency distribution than the other sources. Laser technology has widely been used for illumination in flow visualisation, fluid diagnosis, PIV, and LDV applications, due to its capability to produce high-power, highly-directional, mono-chromomeric, ultra-short pulses of light. Today, there are various types of lasers covering a wide range of the frequency spectrum from the far infrared to the soft X-ray region.

Solid-state lasers that use Neodymium-doped Yttrium Aluminium Garnet as a gain medium are called Nd:YAG lasers. The rare-earth neodymium ions (Nd^{3+}) are used as dopant ions by implanting them into the YAG material.

Q-Switching technique is commonly used for the amplification and the stabilisation of the laser pulses amplitude in the YAG lasers. Once the pumping begins, the laser medium gradually moves towards a certain population inversion density, and the laser beam begins to "grow up" during a period of time until the population reaches its saturation intensity (I_s). The optical feedback from a rear mirror adds more photons to the laser medium, stimulating new ions, which consequently reduces the upper-level lifetime (τ_u).The Q-switching extends the upper-level lifetime (τ_u) so that a longer pumping duration is obtained, and thus, more energy is pumped into the laser cavity. The Q-switch device is

simply an adjustable attenuator placed between the rear mirror and the lasing rod, temporarily preventing the optical feedback until the laser reaches its highest possible gain, and then suddenly the attenuation is removed producing a giant fast laser pulse. While the (Q) here refers to the cavity quality factor, the Q-switching term refers to the rapid change from a low Q-factor (intra-mirror losses are high) to a high Q-factor (intra-mirror losses are low) [Chang (2005), ch.6].

Flashlamp-pumped Q-Switched Nd:YAG Lasers are the most commonly used lasers in the flow visualisation and the fluid diagnosis applications due to its capability to produce high power beams at short pulse duration (5-25 ns). Most of the practical solid-state lasers are **optically pumped** [Malacara & Thompson (2001), Ch.20] using either flash-lamps or diode lasers. Figure 4.1 illustrates a simplified schematic of a flashlamp-pumped Q-switched laser cavity. The system typically consists of: two elliptical flash-lamps (gas discharge lamps), an Nd:YAG laser rod, a Pockels cell electro-optic shutter Q-switch, reflective walls, and a cooling (water) system. Table 4.1 shows the parameters on a typical Nd:YAG laser.

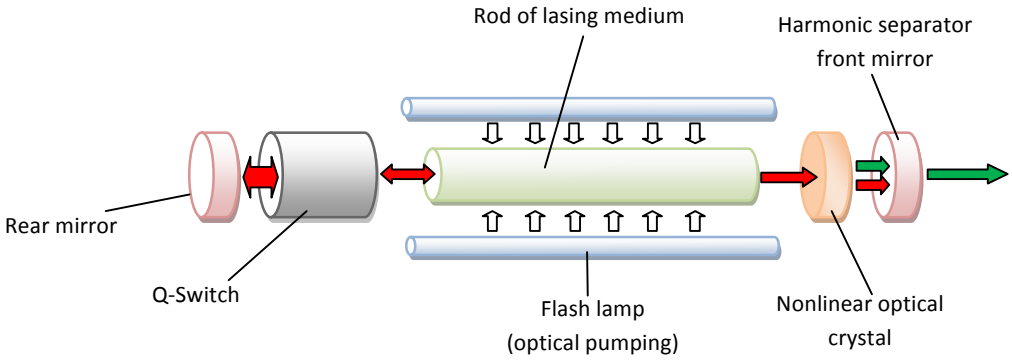

Figure 4.1 Q-Switched Nd:YAG laser cavity.

Table 4.1: Typical Nd:YAG Laser Parameters.

Wavelength[1] (λ)	**1064 nm (532 nm)**
Upper-state life-time(τ_u)	230 μs
Gain-medium length (L)	10- 15 cm
Doping density	1.4 x 10^{26} m^{-3}
Energy of lower level (E_1)	857 cm^{-1}
Inversion density (ΔN_{ul})	1.6 x 10^{23} m^{-3}
Output power [2]	100- 1000 J/ pulse
Pulse duration	5 – 25 ns
Refractive index at 1064nm	1.82
Repetition rate	Up to 200 Hz

4.2.2. Reflecting Mirrors

Mirrors are used to redirect laser beams. Depending on their coating substance, laser mirrors can be either metallic or dielectric. The metallic mirrors are easier to produce and lower priced, but their applications are limited to the low optical flux (less than 100 W/cm^2), as the absorbed radiation can damage the coating at higher energy. The dielectric mirrors on the other hand have a better reflectivity and absorb less energy than the metal coated mirrors [Malacara & Thompson (2001), Ch.13], so that the damage threshold is usually higher in the case of the dielectric mirrors [Laufer (1996), Ch.2]. The dielectric mirrors can be produced with a reflectivity as good as 99.9% for a monochromatic light source, in comparison with less than 95% reflectivity for the metallic mirrors.

[1] Emission could also be produced at wavelengths: 532, 946, 1319, and 1338.
[2] This is a significantly high output power. If we assumed laser pulse duration of 20 ns, then a 1 J pulse carries an optical power equal to 50 MW.

4.2.3. Laser Doppler and Phase Doppler Techniques

Doppler shift phenomenon[1] explains the slight change in frequency of an incident electromagnetic wave (beam) when interfering with a moving object. The measurement of the frequency shift is important in calculating an objects' speed. This phenomenon inspired scientists to develop the Laser Doppler Anemometry (LDA)[2] systems, originally used to calculate the fluid/particles velocity only. The principle of the laser Doppler effect was later extended to the measurements of particle size and concentration by developing the Phase-Doppler Anemometry (PDA) method [Crowe, *et al.* (1998)]. The frequency shift (Doppler signal) is detected by photo-detectors which can be solid-state-sensors or photo-multipliers connected to a high resolution optical spectrum analyser.

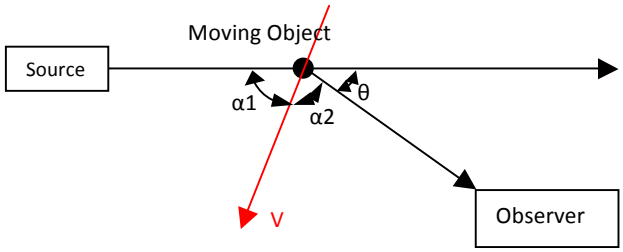

Figure 4.2 The LDA method in calculating the velocity of a moving object.

LDA can be conducted by using a single illumination source; the method is called "reference beam" LDA in this case (Figure 4.2), where the frequency shift (Doppler frequency) is directly connected to the particle velocity and the angle between the velocity vector and the direction of the light beam, as follows [Crowe, *et al.* (1998); Laufer (1996), Ch.6 ; Drain (1980), Ch.3]:

[1] Proposed by Austrian physicist Christian Doppler in 1842 [Drain (1980), Ch.1]
[2] Sometimes referred to as Laser Doppler Velocimetery (LDV)

$$\Delta f_D = f_r - f_e = \frac{V}{\lambda}(\cos\alpha_1 + \cos\alpha_2) \qquad V<< c \qquad (4\text{-}1)$$

or :

$$\Delta f_D = \frac{2V}{\lambda}\sin\frac{\theta}{2}\cos\frac{\Delta\alpha}{2} \qquad (4\text{-}2)$$

Where (V) is the particle velocity, (θ) is the angle between the laser beam and the observer, and $\Delta\alpha = \alpha_1 - \alpha_2$.

In contrast, the differential Doppler method uses the principle of frequency beating (modulation) in two signals' interference [Drain (1980), Ch.5; Malacara & Thompson (2001)] where the resulting signal contains the frequency of the difference between the two original signals. The final difference in frequency is between the two Doppler shifts generated by the two beams emitted at different angles (Figure 4.3). Doppler shift formula can be derived from equation (4-1) as follows:

$$\Delta f_D = \frac{V}{\lambda}(\cos\alpha_1 + \cos\alpha_2)$$
$$\Delta f_D^{'} = \frac{V}{\lambda}(\cos\alpha_1^{'} + \cos\alpha_2) \qquad (4\text{-}3)$$

Hence, the total frequency shift:

$$f = \Delta f_D - \Delta f_D^{'} = \frac{V}{\lambda}(\cos\alpha_1 - \cos\alpha_1^{'}) \qquad (4\text{-}4)$$

and:

$$f = \frac{2V\cos\beta}{\lambda}\sin\frac{\theta}{2} \tag{4-5}$$

Where $\theta = \alpha_1 - \alpha_1^{'}$ is the angle between the two beams, and $\beta = \frac{\alpha_1 + \alpha_1^{'} - \pi}{2}$ is the angle between the velocity vector and the normal at the beams' interference section, as shown in Figure 4.4. The last relation (4-5) shows that the frequency shift is independent of the angle between the velocity vector and the observer (α_2). Another useful advantage of the differential Doppler method over the reference beam method is that light is collected by a wider aperture in this case, allowing performing measurements with lower particle concentrations [Drain (1980), Ch.1].

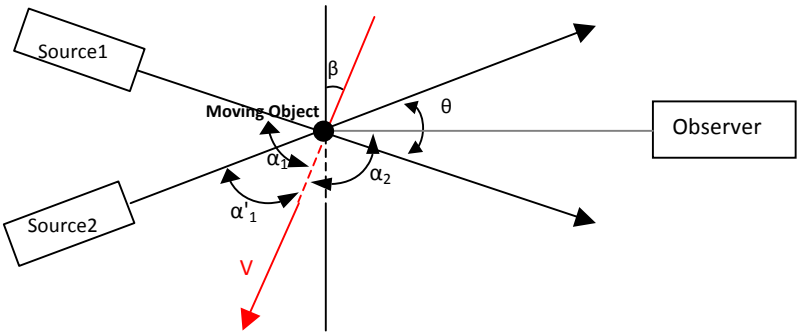

Figure 4.3 The differential LDA method in calculating the velocity of a moving object.

In the case of light interaction with fluid (or solid) particles in the air, light diffraction is always the dominating phenomena rather than reflection. In order to calculate the (average) particle size, beside the velocity, the light scattering angle with respect to the incident light beam should be calculated. The phase dependency on the particle size and the light scattering pattern can be explained by Mie approximation in light diffraction. However, when particles are very small compared to the wavelength the light intensity shows too much fluctuation, making measurements much difficult, and larger number of optical sensors are needed. Although phase Doppler method can provide the velocity information

of liquid droplets, it is insufficient in generating a global measurement of the velocity over the whole field of the flow. The spatial distribution of velocity can be investigated by applying PIV [Lee et al.(2001)].

PDA needs a very accurate calibration [Crowe, *et al.* (1998)] using particles with known dimensions and refractive index, and a very accurate alignment to optimise the accuracy of the system [Kashdan et al. (2007)]. Also, PDA is a point technique, so it does not provide information about the spatial structure of the spray. The PDA strictly considers that the measured droplets are perfectly spherical, compared to the imaging techniques, which can handle various shapes (see appendix 4.1 for samples of kerosene drops). The dependency to light intensity in this type of measurements makes the Gaussian profile of the light beam problematic since the received intensity is dependent on the particle position within the light beam in this case. Another limitation of light scattering-based sizing techniques is the effect of multiple scatters. The light-particle interaction and Mie theory will be explained in detail in the next chapter. Photo-Multiplier-tubes (PMTs) and photo-diodes are used for light detection in the LDA and PDA techniques.

4.2.4. Particle Image Velocimetry (PIV)

Velocity measurements in complex flows are made possible by the advancements in the PIV techniques. PIV is achieved by producing a relatively thin laser sheet to illuminate a particular cross-section in a multi-phase mixture. PIV has become an important method for flow measurements, due to its non-intrusive nature and good accuracy.

Images for the field of view are taken at each laser pulse. The time delay between pulses determines the temporal resolution of the system. The exposure time controls the amount of data acquired in a single image frame, while the laser pulse-width determines the

speed of an individual imaging incident, i.e. the ability to capture sharp images in high speed flows. In turbulent flows, the best PIV system which can accurately generate a high temporal resolution velocity map would consist of a high-speed camera and a high rate laser. In practical applications, this is a very expensive system with a very short recording time. If a high-speed camera is used for spray images, only a few shots can be taken before the spray arrives a relatively long distance [Klein-Douwel, *et al*. (2007)]. Alternatively, double-pulsed lasers are widely used in PIV tests in order to generate double images with a relatively short time delay between them. The double images are recorded either on a single frame or on two separated frames [Crua (2002), Ch.2] (see appendix 4.2 for examples from the kerosene data).

In the **single-frame double-pulse method** (exposure overlapping): images are recorded several times on the same image frame during single exposure period but for different laser pulses, using a predetermined time separation between them. The disadvantage in this case is that the direction of the particle motion cannot be identified by the image.

The **double-frame double pulse** is the most popular method in PIV. Advanced camera systems have the ability of grabbing two separated frames with a very short delay between them. The image grabbing mechanism should be accurately synchronised with the laser pulses. The main image processing steps for resolving a velocity vector field are:

1. Pre-processing (mainly noise and background removal and contrast enhancement).

2. Image cross-correlation between each two successive images (auto-correlation in the case of single-frame).

3. Displacement calculation of particles during the time gap between double-frames.

4. Post-processing (removing the out of range vectors).

4.2.4.1. Cross-Correlation in Image Processing

Cross-correlation techniques are used for the calculation of an object velocity by using one sensor arrangement with a determined sampling time window (t), or by setting up two sensor arrangements with a known distance between them (L) [Crowe, *et al.* (1998)]. The average velocity in both cases is the ratio of the distance to the time needed to travel that distance. The system accuracy can be improved by using short time steps.

In image processing, the brightness of the correlated frames can vary due to lighting conditions (differences in the output optical power between pulses) and the exposure mechanism of the camera. For that reason the images are first normalised by subtracting the mean image and then dividing the result by the standard deviation. The normalised cross-correlation of two interrogation windows f1 and f2 is given by the equation:

$$F(x,y) = \sum_{x,y} \frac{(f_1(x,y) - \bar{f}_1)(f_2(x,y) - \bar{f}_2)}{\sigma_1 \sigma_2} \qquad (4\text{-}6)$$

Where $\bar{f}$ and σ are the mean image and the standard deviation, respectively.

A high particle concentration is required in the PIV analysis in order to produce an effective correlation between images. Lack of particles within the correlation window can

lead to a wrong estimation of velocity and direction. The resolution of the results increases as the correlation window size decreases. Smaller windows, however, need a higher particle concentration in the area unit.

4.3. Direct Imaging Technique

The direct imaging technique in fluid spray diagnosis is a simple approach which can be achieved by the direct photography of a spray jet using a digital camera and a flash light source. The pulse duration of a typical electronic flashgun is around 50 μs, in comparison with a few nanoseconds for a laser pulse. The relatively long illumination time of the flash-based systems restricts their ability of providing information about high speed flows in the time domain. Furthermore, imaging fluid droplets at the microscopic scale requires a high-power highly-directional light beam, which is only available in lasers. However, direct imaging techniques have been used in the visualisation of spray jets, and in the extraction of general macroscopic characteristics such as spray cone-angle, spray symmetry and jet penetration.

Global spray photography can be achieved in two ways depending on the method of illumination. Light scattering images are produced using front or side illumination. Shadowgraph images are produced when backlighting is used. Although no significant differences in results between the two methods have been reported in literature, shadowgraphs were found to (be able to) distinguish the spray borders from the surrounding gas much easier [Ochoterena *et al.* (2010)]. The light scattering technique, alternatively, can provide statistical information about the distribution of the fluid volume over the spray pattern, due to the connection between volume and scattered light intensity.

4.3.1. Related Work

A qualitative study on diesel spray was presented by Shao and Yan [Shao & Yan (2006, 2009)] using a direct imaging technique. Images were captured by a CCD camera and a flash light source. The images were processed for the extraction of the macroscopic characteristics of the spray jet, including the tip penetration, the near-field angle, the far-field angle, and the average spray-tip velocity, at an injection pressure of 600-1400 bar. Their experiments were made on a common rail fuel injection system in a pressurised non-evaporating environment, discussing the effect of pressure on the spray macroscopic characteristics. A variation in luminous intensity from one image to another was observed, which could lead to errors in extracting the spray contours. The fluctuation in the light intensity is expected when using long exposure periods, as pixels can be saturated at the high density regions, and this becomes less controllable in highly turbulent flows. Shao and Yan results showed that diesel sprays penetrate faster, deeper, and with wider angles at higher pressure values, which agrees with the previous discussion (chapter.2).

The common rail diesel system was also investigated by Seneschal *et al.,* [Seneschal, *et al.* (2003)], using direct illumination from a set of halogen lights located around a multi-hole diesel injector operating at 800 bar fluid pressure. The shortest imaging time in this case was 0.5 μs which is the minimum exposure time of the employed camera. A similar system was tested by Hwang *et al*. [Hwang, *et al*. (2003)], for Dimethyl Ether (DME)[1] sprays. In this case, the spray pattern was determined by averaging out 30 shadowgraph images for each experimental condition. A threshold of 80% was used for extracting the spray image, although a higher threshold value can be used when the contrast between the background

[1] *"Dimethyl Ether (DME) is an alternative fuel that provides lower particulate matter (PM) than diesel fuel under the same engine operation conditions."* [Hwang, *et al*.(2003)]

and the spray in the foreground is higher. Their results showed that increasing the differential pressure increases the spray angle and tip penetration (formula 2-10); further increasing the nozzle size in this case has increased the tip penetration.

The low temporal resolution and the very low number of samples used in each condition can lead to errors in the spray progression estimation, or in any other time related characteristic. Only 6 images per test condition were used by Shao and Yan [Shao & Yan (2006, 2009)], and 30 images by Hwang *et al*. [Hwang, *et al*. (2003)]. The number of samples is important in the image processing of fluid sprays for reducing the margin of error, but it is limited by the memory size, the computing capacity and the system speed.

Another research on diesel sprays at high fluid pressure[1] was conducted by Morgan *et al.* [Morgan *et al.* (2001)] and Kennaird *et al.* [Kennaird *et al.* (2002)] of the University of Brighton (UK). A back-lighting technique was applied using an argon flash lamp with a lighting duration of about 3 μs. Kodak 400 digital camera was used for still imaging. Another video CCD system (Kodak Ektapro HS Motion Analyzer) was employed for high speed imaging, with a maximum frame rate of 4500 *fps* at the full resolution (256 by 256 pixels). The tip penetration and the cone angle of the sprays were calculated directly from the processed images. The images in the background were removed using a manually defined threshold. The tip of the nozzle and the primary spray were out of the camera field of view, which may lead to an error in angle calculation. The effect of the injection pressure on penetration has been carried out by Karimi K. *et al.* [Karimi K.; et al. (2006)] using a Phantom V7.1 high-speed camera. High-speed shadowgraphy is a well known approach in spray progression analysis, investigated by recent studies such as Ochoterena, *et al.* of Chalmers

[1] Pressure= 1600 Bar, injection duration= 3.5 ms in Morgan *et al.*

University, Sweden [Ochoterena R., *et al.* (2010)] and Klein-Douwel, *et al.* of Eindhoven University of Technology [Klein-Douwel, *et al*.(2007)].

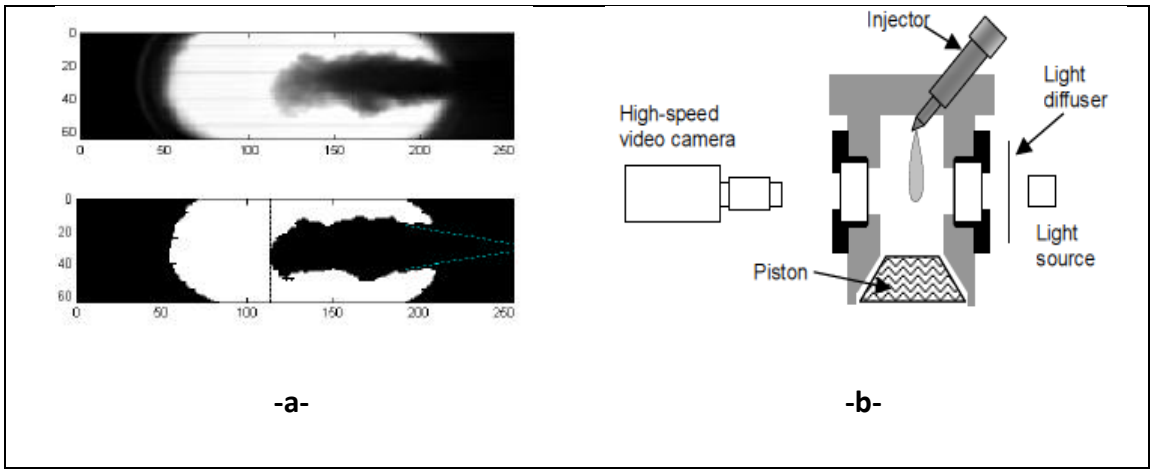

Figure 4.4 : a. Raw and binary images of the diesel spray (penetration study) [Morgan *et al.* (2001)]; b. Setup of a high-speed recording with backlight illumination [Kennaird *et al.*(2002)].

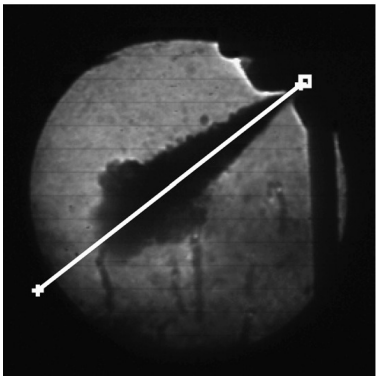

Figure 4.5: Image of diesel spray taken by Klein-Douwel, *et al.* at 1500 bar fluid pressure behind the nozzle. The high-speed imaging system has a temporal resolution of 222 µs [Klein-Douwel, *et al*. (2007)].

4.3.2. Discussion

The direct imaging technique is a popular low-cost choice for liquid sprays visualisation. Most of the available resources in literature are focused on the diesel grades at high injection pressures (400-1600 Bar). Both the scattering and the shadowgraph images can be used in this case. Spray contours can be extracted by binarising the raw images via a suitable threshold. Since producing (thin) light sheets is not possible in the conventional flash light

sources, this method can only provide an overall view of the spray pattern rather than detailed information about the fluid mass distribution in the gaseous phase. The direct imaging can be very useful in the extraction of spray angle, general spray pattern, and spray tip penetration, when a large number of samples are used. However, the temporal analysis of the spray formation process needs a higher temporal resolution and a far shorter illumination period than that of flash lights, as well as the need for a higher optical energy for the droplet size investigation at the microscopic scale (1-10 μm), which emphasises the importance of using laser beams in similar tests.

4.4. Laser Imaging Technique

Similar to the direct imaging techniques, the laser imaging can be achieved by both the light scattering and the shadowgraphy. The monochromaticity of the laser beam with a wavelength at the micrometer scale allows performing the particle size measurements by investigating the particle-wave interaction. In addition, the high directionality of the laser is important in producing light sheets that perform regional illumination in the spray. In the fluid droplets particularly, a high power light source is required as they have less reflectivity than the solid seeding particles used in the air flow measurements (such as TiO_2). The short time pulse is a key element in the multiphase flows characterisation because sharp instant images are required for both the particle sizing and the PIV.

4.4.1. Related Work

In-cylinder flow analysis was carried out by Towers D. P. and Towers C. E. [Towers & Towers (2004, 2001)] on a GDI engine, with the objective of investigating the cycle to cycle variations in the air flow. A high-speed PIV system was developed in this case using a copper

vapour laser (CVL, 2–3 mJ/pulse) and a Kodak 4540 camera with a 50 mm (focal length) lens (*F* #1.2) for imaging. The imaging speed was 13,500 fps for a spatial resolution of 128 × 128 pixels, representing around a 1° crank angle resolution at an engine speed up to 2000 rpm. Because of the relatively low power illumination source, the flow was seeded with Acrylonitrile microballoons (hollow particles) 35 µm in average diameter[1]. Figure 4.6 shows an example of a PIV vector field generated for the gasoline fuel mixture. A similar type of engine was tested by Lee *et al.* [Lee *et al.* (2001)] using phase Doppler particle analyser (PDPA) and an Nd:YAG laser PIV system. Spray visualisation was produced by a laser scattering method using a CCD camera. The experiments on a pressure-swirl nozzle showed that a ring shape vortex is formed at the upstream of the spray. It was believed that the ring vortex promotes the secondary atomisation of the fuel droplets.

Wu *et al.* [Wu *et al.* (2006)] have used an Nd:YAG laser for visualising diesel and other oxygenated fuels sprays. The experimental observations showed changes in the spray characteristics between different type of fuels, showing the correlation between the fuel physical properties and the atomisation quality. The spray images acquired by the author were over-saturated, due to either the high optical energy or the long exposure time, which normally prevents obtaining detailed information about the droplets distribution. The bulk spray velocity for diesel was 142 m/s at 400 bar injection pressure (pulse duration = 3.84 ms) into unpressurised ambient.

[1] According to the authors, Acrylonitrile microballoons provide ~100 times the light scattering efficiency of 2- 3 µm sized fuel droplets. In the current project, the maximum output power of the Nd:YAG laser used in most experiments was 200 mJ, allowing performing a PIV analysis without seeding.

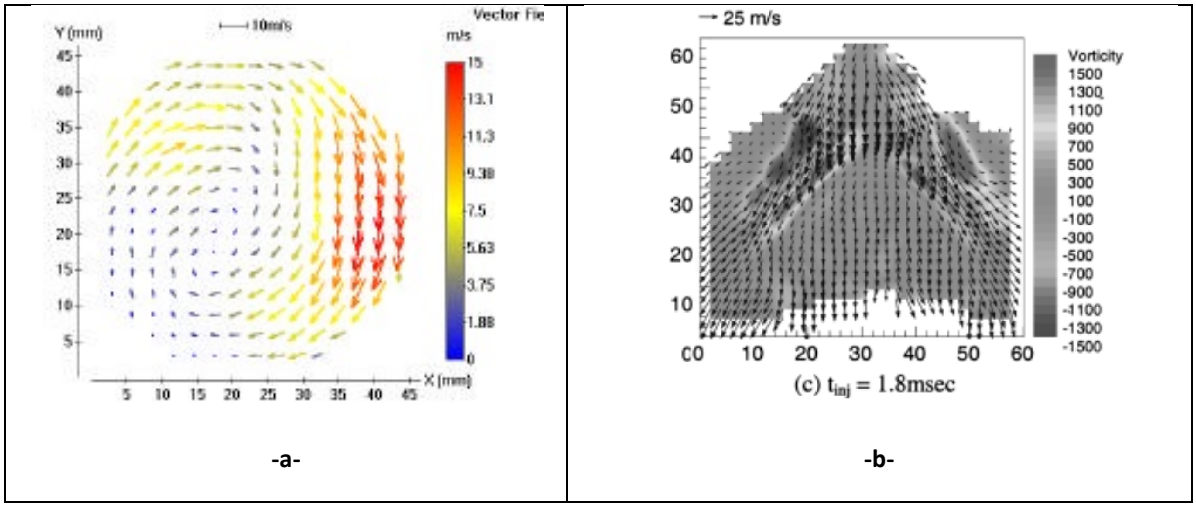

Figure 4.6: a. Part of Towers D. P. and Towers C. E. PIV results at 320° crank angle [Towers & Towers (2004)]; b. Spray velocity map at 1.8 ms ASOI and 5 MPa fluid pressure in GDI engine [Lee et al. (2001)].

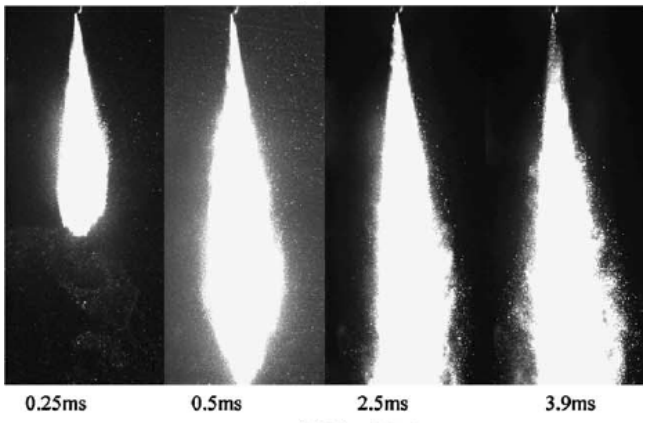

Figure 4.7 Diesel spray by light scattering method [Wu et al. (2006)].

Highly pressurised diesel spray was also investigated by Bae *et al.* [Bae *et al.* (2002)] using different nozzle designs. Both Mie-scattering and shadowgraphy imaging were used for the visualisation of the spray droplets. Spray images were acquired with CCD using 100 ns light pulse. Shadowgraph technique was also applied using Ar-ion laser[1] (backlighting) and ICCD camera and long range microscope. Their results included calculations of tip penetration and spray angle. Spray development process was closely observed too. The atomisation performance was evaluated by calculating the droplet SMD from the

[1] Ar-ion lasers (4W) are also used in the investigation of the symmetry and distribution of a test fluid spray by [Lee, et al.(1999)], with a Kodak (DCS 460) CCD camera for imaging.

microscopic images. The difficulty in the long distance microscopic shadowgraphy is in obtaining fully focused images with well contrasted particles to be resolved from the background (figure 4.8.b) because of the depth of focus (DOF) of the imaging systems [Fdida & Blaisot (2010)], and for this reason, the shadowgraph imaging was not widely applied in microscopic analysis comparing with other sizing methods such as PDA [Choi *et al.* (2000)]. A similar method was used attempting to resolve individual micro-droplets in [Jiang, *et al.* (2010)], [Esmail, *et al.* (2010)], and [Berthoumieu *et al.* (1999)], obtaining a maximum spatial resolution of 16.5, 7.1, and 5.6 µm/pixel respectively. In [Jiang *et al.* (2010)], the shadowgraph method was used to resolve water droplets using LED arrays, within a field of view FOV=10.6 x 7.9 mm, DOF= 2.6 mm. Image processing droplet sizing studies have generally been conducted on low velocity flows where the droplets are of the order of 100 microns and above [Kashdan *et al.* (2007)].

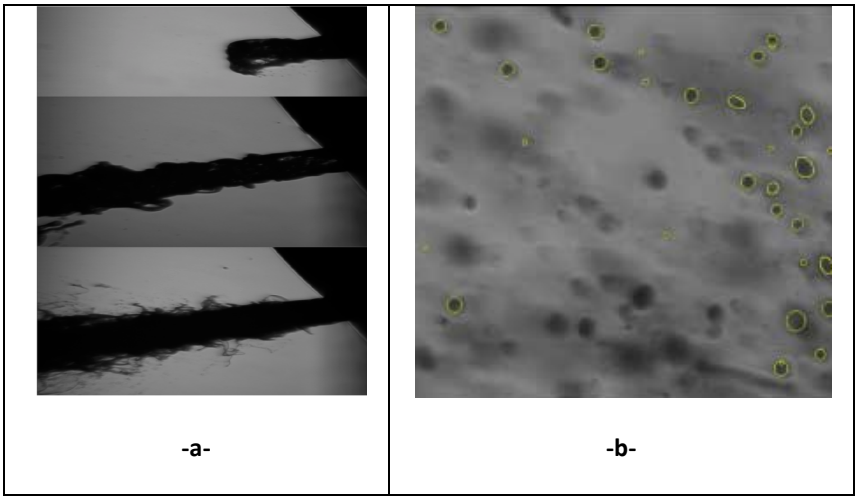

Figure 4.8: a. Early spray development (shadowgraph); b. (Part of) a processed image (1.23mm×0.98mm) with tracked particles [Bae *et al.*(2002)].

A remarkable study about microscopic shadowgraphy was published by Parks *et al* [Parks, *et al.*(2006)] about single diesel drop breakup process due to cross-flow at a Weber number varies between 52 and 538, showing a successful attempt to visualise moving

droplets (Figure 4.9) using an Nd:YAG laser and a CCD camera. Diesel droplets approximately 185 µm in diameter were produced using a mono-dispersed droplets generator. The effects of Weber number (relative velocity) and travelling distance from the nozzle orifice were presented.[1] Although this type of test on individual mono-sized droplets can provide a good contribution into the knowledge of the fluid breakup mechanism due to the external forces, there is still a need for more work in order to move the microscopic shadowgraphy into the practical level of the fluid injection applications, where the sprays are higher in density and the particles are much smaller and travel much faster (see also [Okuda *et al.* (2009)] for a similar study).

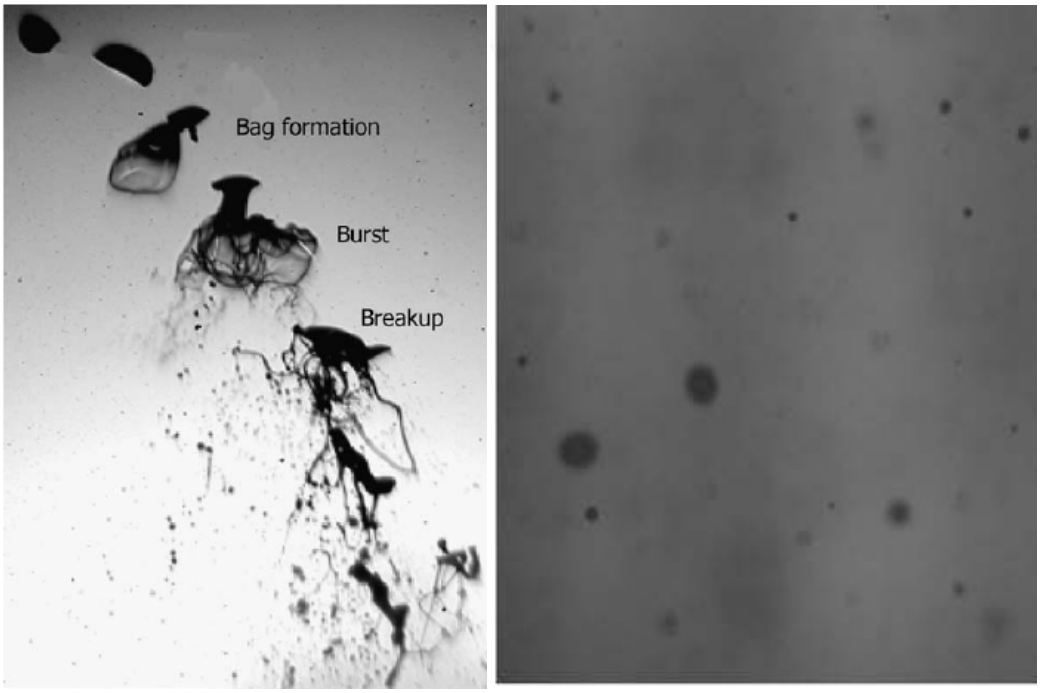

-a- **-b-**

Figure 4.9: (a) Microscopic shadowgraph of one diesel droplet breakup (We=68) [Parks, *et al.*(2006)]. (b) raw image of the water droplets shadowgraph [Jiang *et al.* (2010)].

[1] The microscope resolution was not mentioned.

Another method of particle sizing was suggested in [Palero & Ikeda (2002)] using a dual Nd:YAG laser (400 mJ/pulse at 532 nm) and two CCD cameras (1008×1018 *pixels*, Kodak ES1.0) with 60 mm lenses for imaging. Droplets with different diameters were discriminated by detecting changes in scattered light intensity. This approach was explained as: *"for particles large compared with the wavelength of illumination, the intensity of the light scattered is proportional* to the droplet square diameter". It was suggested (by the authors) that droplets under 30 µm in diameter follow the airflow and droplets bigger than 50 µm penetrate due to their large momentum. The greyscale of images was divided accordingly into three layers representing three ranges of particle size: 1. less than 30 µm, 2. between 30 and 50 µm, and 3. for particles larger than 50 µm. The mechanism of categorising droplets according to their ability to penetrate seems to be inaccurate since a droplet penetration is a function of several parameters such as the discharge velocity of fluid (i.e. pressure) and the atomiser diameter. Particles of the same diameter can have different average velocities. If imaging was performed during a continuous course of fluid injection ignoring time delay after start of injection, particles captured when repeating the experiment would belong to different injection events, and thus more small particles are expected to be flowing slowly around the high speed main jet. The "multi-intensity layer" method used by [Palero and Ikeda (2002)] suggests that by modifying an image contrast different diameter clusters could be defined. Although some small particles with low light scattering profile are eliminated when increasing the intensity threshold, in most cases droplets have a gradient profile, and increasing the threshold will only decrease the detected particle diameter. This leads to a lack of accuracy from droplets appearing in several intensity layers but with different diameters.

Difference in image intensity can be used with PIV for velocity calculations of different phases. Seeding particles can be used for measuring the velocity of a flowing air current in a fuel mixture. Solid seeding particles usually produce higher levels of intensity than fluid droplets at the image plane. Alternatively, a 3CCD camera (3 colours) can be used for recording images of a multi-phase flow [Angarita-Jaimes *et al.* (2008)]. Different fluorescent tracers react differently to a laser sheet, and therefore fall into different colour channels at the 3CCD[1].

The light scattering images show the light diffraction profile of the droplets rather than the image of the droplets themselves. Therefore, resolving a droplet diameter cannot be measured directly from a scattering image, especially when dealing with a diameter range close to the laser beam wavelength. So, although large droplets reflect more light than small droplets do, images can only provide a general view of the fluid mass distribution within a spray pattern, but it cannot be directly used for an accurate calculation of droplet diameters at the microscopic range. Spray characterisation methodology is dependent on the type of flow whether it is dense or not. The flow studied in the current research is considered as a low density flow due to the low flow rate required in the engine system. Using adequately thin light-sheet it is possible to “see through” the flow and distinguish between individual droplets

[1] In Angarita-Jaimes et al. (2008), for example, UV-excitable fluorescent tracers (Bis-MSB) are used for the measurements of the gas phase velocity.

Chapter 5. Light Scattering by Small Fluid Droplets

This chapter presents an introduction to the light scattering by small fluid droplets. The scattering pattern of a monochromic light beam is dependent on several parameters including the source wavelength, the droplet refractive index and the droplet/particle diameter.

There are several drawbacks of the light diffraction method in particle sizing. The first is that Mie solution always assumes that the particles are perfectly spherical, which is not always true especially for relatively large droplets travelling at high velocity (i.e. high Weber numbers). The second drawback is the complexity of the scattering profile of droplets close in size to the wavelength. The light scattering methods need a careful calibration of the sensors using droplets with accurately determined diameter and refractive index. The multi-droplets scattering in sprays with wide diameter range makes the measurements even harder since only the average scattering of a continuous flow is possible in this case.

Because of the previous reasons, and due to the high cost of the commercial diffraction-based particle sizing devices, the light scattering method was not used for the purpose of droplet sizing. However, using the generated Mie curves in this chapter, it was possible to use the scattering technique to calculate the scattering efficiency of fluid droplets/particles with predefined diameters. These findings were later used to address problems related to the design of a jet-noise experimental platform, where fluid smokes

(droplets less than 0.3 microns in diameter) were used for the seeding of a jet (nozzle) flow. The question to be answered was how the relative angle between the view field of two cameras and the laser sheet can affect the correlation quality between images produced by two cameras. These results are important in stereoscopic PIV tests where the seeding density and light balance between the cameras are crucial. Also, Mie curves were used to compare between scattering profiles generated using different materials and particle/droplet diameters so that the PIV seeding process can be optimised for the current experimental rig design.

5.1. Background

When an electromagnetic (EM) wave encounters an obstacle, some of the electrons in the electronic cloud within the obstacle material oscillate at the same frequency of the incident wave. The obstacle in this case becomes a secondary source of (EM) waves. The light scattered out of a particle is a result of the interaction between the particle material and the light wave. Most of the scattered light is in the forward direction and has a frequency spectrum similar to that of the incident light [Hahn (2009)]. A particle acts as a scattering centre, and the diffracted light pattern can be measured and then mathematically analysed in order to determine the particle size [Ley (1999)].

Mie theory[1] (after Gustav Mie) is a general solution of the light diffusion problem for all particle sizes. It justifies why larger particles scatter an incident light at smaller angles than smaller particles, which has been long observed by researchers [Godefory & Adjouadi (2000)]. Mie scattering patterns produced by different particles are related to the optical

[1] Sometimes referred to as Mie-Lorenz Theory (MLT)

properties of the particles and the surrounding medium. In simplified studies the refractive index has not been taken into consideration, adopting the assumption that the scattered light is dependent only on the particle size. Due to the complexity of the mathematical expressions of the Mie solution, approximations can be carefully used in some special cases. For instance, in the Fraunhofer approximation, which has been used in previous sizing systems, particles are assumed to be opaque [Crowe, *et al*.(1998), Ch.9] and therefore, the optical properties of the particle material are not taken into consideration, implying that a certain volume of particles always scatter the same amount of light regardless of their diameters. Fraunhofer approximation uses Babinet principle of diffraction, which states that the diffraction patterns for both an opaque body and a pinhole of the same cross-section are identical. This approximation can be applied only when particles are much larger than the light wavelength[1] and have a high relative refractive index. Rayleigh scattering theory is another exceptional approximation of the Mie model. Rayleigh approximation offers a great deal of simplification in the mathematical model and surpasses Fraunhofer's by including the optical properties of particles. However, the Rayleigh approximation is only applicable for particles much smaller than the wavelength.

The scattering data and Mie graphs in this section are generated using Matlab code mainly based on [Mätzler (2001)], [Bohren & Huffman (1983)] and [van de Hulst (1981)]. Only the elastic light scattering is investigated in this study where energy transfer into particles is negligible. The Mie curves were used in the jet-noise tests to estimate the scattering efficiency of the fluid smoke seeding droplets, and compare it with the efficiencies of the conventional seeding (solid) particles.

[1] In ISO 13320-1 standard, it is suggested that the diameter should be larger than 50 µm without mentioning the wavelength.

5.2. Understanding Light Diffraction

The simplest form of light diffraction pattern could be the "single-slit diffraction" which can be obtained by Fraunhofer solution as:

$$I_\theta = I_0 Sinc^2\left(\frac{d\sin\theta}{\lambda}\right) \qquad (5\text{-}1)$$

Where (d) is the width of the slit, (θ) is the diffraction angle, (λ) is the wavelength, and (I_0) is the intensity of the incident wave. Fraunhofer diffraction has the same mathematical definition as Fourier transform[1]. Figures 5.1 and 5.2 show computer simulation of diffraction patterns produced by a circular and rectangular aperture respectively. An assumption is always made that the measured particles are perfectly spherical. Therefore, a particle could be thought of as a circular aperture with the same radius. Particles interact with light in four ways: diffraction, reflection, absorption, and refraction.

Let α be a "particle size parameter" defined as follows:

$$\alpha = \frac{2\pi r}{\lambda} = \frac{\pi d}{\lambda} = kr \qquad (5\text{-}2)$$

Where (r) is the particle radius, (d) is the diameter, (λ) is the light wavelength and (k) is the wave number.

[1] The "Sinc" function is applied in the single-slit case. For the circular aperture (Airy-disk) case, the first-order Bessel function is used. The first minimum in this case is at a radius equal to 1.22 λ R/2r. [Laufer (1996), Ch.7]

The light intensity of the scattered light is calculated as a function of the scattering angles (Φ, ϑ) where (Φ) is the vertical scattering angle and (ϑ) is the horizontal scattering angle, both with respect to the incident light wave (Figure 5.1). The light intensities in both directions can be written as:

$$I_{\phi} = I_0 \frac{1}{R^2} \sigma_v \qquad (5\text{-}3)$$

and:

$$I_{\theta} = I_0 \frac{1}{R^2} \sigma_h \qquad (5\text{-}4)$$

Where (R) is the distance between the particle and the outgoing wave,[1] and (I_0) the light intensity of the incident wave (W/m^2). (σ_v) and (σ_h) are called the "differential scattering cross sections". The scattering cross section represents the amount of energy carried by the incident wave falling on an area (σ), which is the same amount of energy scattered in all directions plus the energy absorbed by the particle (conservation of energy principle).

[1] (R) could be considered as the distance between the particle and the observer when R is big enough in comparison with the angle θ (where sinθ ≈ tanθ)

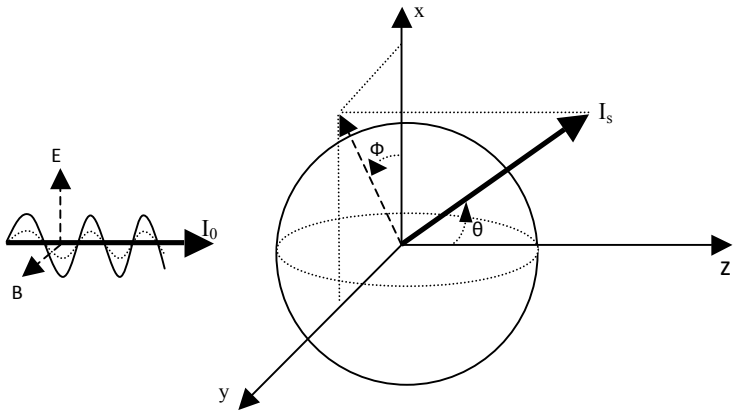

Figure 5. 1 Diffraction angles in 3D coordinates. I_s is the intensity of the scattered light and I_0 is the intensity of the unpolarised light beam.

When the incident light is unpolarised the scattering light intensity is given by:

$$I_s = I_0 \frac{1}{R^2} \sigma_s \qquad (5\text{-}5)$$

Where σ_s is the average of σ_h and σ_v.

5.2.1. Mie Theory

Mie theory provides a solution for Maxwell's wave equations of a plane electromagnetic wave scattered by a homogeneous sphere [Crowe, *et al*. (1998), Ch.9]. In a particle with a certain amount of transparency, the refracted light through the particle generates secondary scatters beside the primary edge scatters, so that the refractive index should be included into the diffraction equations in the case of liquid droplets [Jones (2003)]. Beside the refractive index, the wavelength and the angle of measurement should be known parameters when applying the theory on particle sizing.

The idea of particle sizing using static laser diffraction methods is that a particle scatters light at an angle related to its diameter. The Mie scattering pattern shows a dominant forward lobe for large particles, while small particles generate more isotropic scattering patterns and they show stronger scattering power at shorter wavelength[1]. The amplitude functions of a scattering pattern are calculated from infinite series as follows:

$$S_1(u) = \sum_{i=1}^{\infty} \frac{2i+1}{i(i+1)} [a_i \pi_i u + b_i \tau_i u] \quad (5\text{-}6)$$

$$S_2(u) = \sum_{i=1}^{\infty} \frac{2i+1}{i(i+1)} [a_i \tau_i u + b_i \pi_i u] \quad (5\text{-}7)$$

Where: $u = \cos(\theta)$ (5-8)

The angular functions (π_i) and (τ_i) are defined in terms of the Legendre polynomials [van de Hulst (1981), Ch9] as:

$$\pi_i(\theta) = \frac{P_n^{(1)}(u)}{\sin\theta} \quad (5\text{-}9)$$

$$\tau_i(\theta) = \frac{dP_n^{(1)}(u)}{d\theta} \quad (5\text{-}10)$$

The coefficients (a_i) and (b_i) are called the scattering coefficients (or Mie coefficients or reflection coefficient [Solimeno et al.(1986), ch5]) and they are defined by complex mathematical modules of spherical Bessel functions related to the refractive index (n) and the particle size parameter (α) as follows:

$$a_i = \frac{\psi_i(\alpha)\psi_i'(m\alpha) - m\psi_i(m\alpha)\psi_i'(\alpha)}{\xi_i(\alpha)\psi_i'(m\alpha) - m\psi_i(m\alpha)\xi_i'(\alpha)} \quad (5\text{-}11)$$

[1] … and this is why sky is mostly blue.

$$b_i = \frac{m\psi_i(\alpha)\psi_i'(m\alpha) - \psi_i(m\alpha)\psi_i'(\alpha)}{m\xi_i(\alpha)\psi_i'(m\alpha) - \psi_i(m\alpha)\xi_i'(\alpha)} \quad (5\text{-}12)$$

where (Ψ) and (ξ) are Ricatti-Bessel Functions related to spherical half-order Bessel function of the first kind $J_{n+0.5}(x)$ (more information in [van de Hulst (1981), Ch.8] ,[Ludlow (2008)]), and [Solimeno et al.(1986), Ch5]. The amplitude function (S) is usually a complex number directly connected to the scattered light intensity through the formula:

$$I_s(u) = I_0 \frac{S^2(u)}{k^2 R^2} \quad (5.13)$$

Noting that the overall amplitude function for unpolarised light is given as:

$$S^2(u) = \frac{|S_1(u)|^2 + |S_2(u)|^2}{2} \quad (5\text{-}14)$$

The scattering cross section previously defined in the equation (5-5) could now be derived from equation (5-13) when θ=0 (or u=1) and therefore, the expression of the scattering cross section in Mie theory is given by:

$$\sigma_s = \frac{\lambda^2}{4\pi^2} \sum_{i=0}^{\infty} (2i+1)(|a_i|^2 + |b_i|^2) \quad (5\text{-}15)$$

Noting that

$$\pi_i(0) = \tau_i(0) = \frac{1}{2} i(i+1) \quad (5\text{-}16)$$

Similarly, the extinction cross section could be written as:

$$\sigma_e = \frac{\lambda^2}{4\pi^2} \sum_{i=0}^{\infty} (2i+1) - [\mathrm{Re}(a_i + b_i)] \quad (5\text{-}17)$$

The light absorption, then, can be calculated by the difference between the two cross section values [van de Hulst (1981), Ch1; Wedd (2003)]. The absorption cross section is written as:

$$\sigma_a = \sigma_e - \sigma_s \tag{5-18}$$

Finally, the scattering efficiency (Q_s) is a dimensionless factor defined as a normalization of the calculated scattering cross section (σ_s) by the geometric cross section of a particle (πr^2) [Hahn (2009], thus:

$$Q_s = \frac{\sigma_s}{\pi r^2} \tag{5.19}$$

Mie theory therefore is valid in all particle sizes and has the advantage of considering the refractive index into the model, but it is still an approximation since particles are considered to have a smooth surface illuminated by a plane wave rather than an elliptical wave, which is not always true. The plane wave assumption is considered to be more acceptable when the laser sheet is much wider than the particle size [Guerrero, et al. (2000)]. For particles illuminated by a Gaussian beam, a modified theory called Generalized Lorenz-Mie theory (GLMT) is developed [Grehan, *et al.* (1992)], adding a new coefficient (g_i) to the amplitude series in formulas (5-6) and (5-7). The amplitude series in GMLT are written as follows:

$$S_1(u) = \sum_{i=1}^{\infty} \frac{2i+1}{i(i+1)} [a_i \pi_i u + b_i \tau_i u] g_i \tag{5-20}$$

$$S_2(u) = \sum_{i=1}^{\infty} \frac{2i+1}{i(i+1)} [a_i \tau_i u + b_i \pi_i u] g_i \tag{5-21}$$

The coefficient (g_i) is a complex expression integral containing spherical Bessel functions (ψ1) and Legendre polynomials (P_i^1). A much simpler approximation called the "localized approximation" [see Maheu, *et al.* (1987)] is derived as follows:

$$g_i = \exp\left\{-\left(\frac{(i+0.5)}{b_0}\right)^2\right\} \tag{5-22}$$

$$b_0 = 2\pi\left(\frac{R_w}{\lambda}\right) \tag{5.23}$$

Where b_0 is called beam waist parameter and R_w is the beam's waist radius (the beam waist effect on the diffraction pattern was investigated in [Ren et al. (1996)]).

5.2.2. Rayleigh Solution

Rayleigh scattering occurs when a particle is much smaller than the light wavelength. The particle can be as small as an individual molecule in this case. In Rayleigh approximation, the scattering coefficients (a_i) and (b_l) (formulas 5-11 – 5-12) with an (α) order less than five are considered while all the higher order coefficients are neglected. This seems acceptable as (α<<1). The only remaining coefficient in this approximation is:

$$b_1 = -j\frac{2}{3}\left(\frac{m^2-1}{m^2+2}\right)\alpha^3\left[1+\frac{3}{5}\left(\frac{m^2-2}{m^2+2}\right)\alpha^2\right] \tag{5-24}$$

By eliminating the fifth order side, the coefficient is reduced again into:

$$b_1 = -j\frac{2}{3}\left(\frac{m^2-1}{m^2+2}\right)\alpha^3 \tag{5-25}$$

Applying (b_1) value in (5-15) equation gives the differential scattering cross section, which can be divided into vertical and horizontal sections as follows:

$$\sigma_v = \frac{\lambda^2}{4\pi^2}\alpha^6\left(\frac{m^2-1}{m^2+2}\right) \tag{5-26}$$

And we have:

$$\sigma_h = \sigma_v \cos^2\theta \tag{5-27}$$

For unpolarised light source, the scattering cross section is given as:

$$\sigma_s = \frac{\sigma_v + \sigma_h}{2} \tag{5-28}$$

Therefore, form 5-26, 5-27 and 5-28 the scattering cross section is written as:

$$\sigma_s = \frac{\lambda^2}{8\pi^2}\alpha^6\left(\frac{m^2-1}{m^2+2}\right)^2\left(1+\cos^2\theta\right) \tag{5-29}$$

Changing α value from (5-2)

$$\sigma_s = \left(\frac{d}{2}\right)^6\left(\frac{2\pi}{\lambda}\right)^4\left(\frac{m^2-1}{m^2+2}\right)^2\left(\frac{1+\cos^2\theta}{2}\right) \tag{5-30}$$

The last formula is called the Rayleigh scattering solution.

5.3. Influential Factors in Light Diffraction Patterns

The assumption that all particles have a homogeneous spherical shape is made in the following discussion.

5.3.1. Particle/Droplet Size

The overall intensity of scattered light always increases as the particle size increases for the same wavelength. Particles can be divided into two main categories according to the earlier defined size parameter (α):

a. **Particles much larger than the light wavelength (α>>1):** the diffraction pattern in this case follows the Mie model, and the increment in light intensity is proportional to the particle diameter squared (d^2). The scattering pattern shows that light has a higher power at low angles (diffraction rings) and gradually fades out when moving into wider angles.

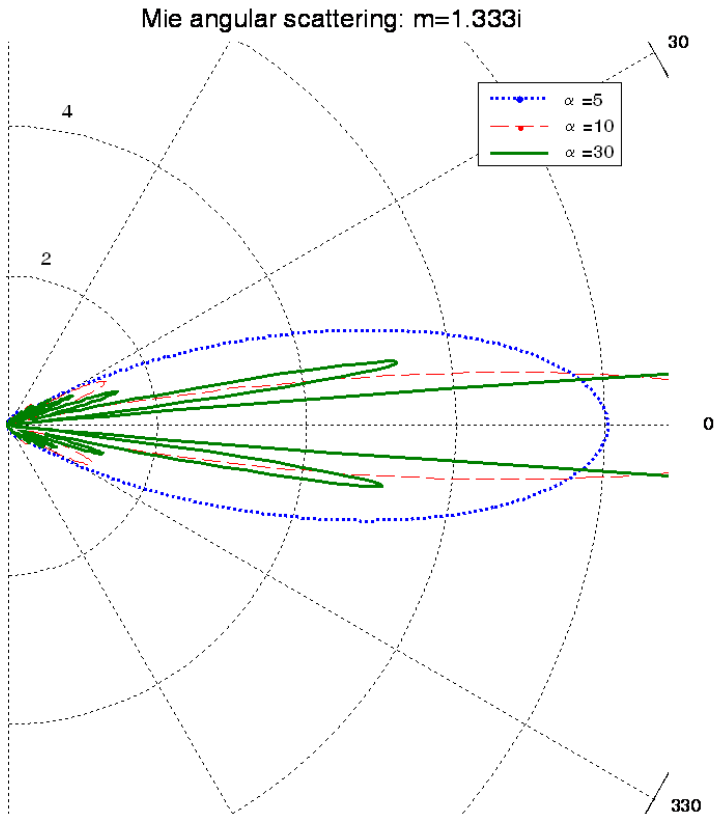

Figure 5.2 Light scattering angle for different values of (α=*k.r*) at refractive index m=1.333 (Water).

b. Particles much smaller than the light wavelength (α<<1): the diffraction pattern follows Rayleigh approximation in which the scattered light intensity decreases in proportional to (d^6) of the particle, and the light distribution is isotropic [Brewster (1991), ch.9]. From (5-5) and (5-30), the light intensity at different angles can be calculated as:

$$I(\theta) = I_0 \frac{1+\cos^2(\theta)}{2R^2}\left(\frac{2\pi}{\lambda}\right)^4\left(\frac{m^2-1}{m^2+2}\right)^2\left(\frac{d}{2}\right)^6 \qquad (5\text{-}31)$$

Where (I_0) is the incident light intensity, (θ) is the scattering angle, (R) is the particle distance from the observer, (m) is the refractive index (magnitude) of the particle material, and (d) is the diameter of the particle. The rapid fall in the scattered light intensity limits this methodology from providing accurate results for particles smaller than 100 nm in diameter. Figure 5.3 shows the relation between the scattering efficiency and the particle size parameter (α). Here is a numerical example derived from the last equation; the ratio of the scattered light to the incident light intensities at the zero degree for: R= 1 m, λ=532 nm (green laser), and m =1.333 (water at 20° C), is given as:

$$\frac{I(0)}{I_0} = 1.2863\times10^{25}\left(d\right)^6$$

This gives values equal to ($20.10X10^{-20}$) for (50 nm) particles and ($0.05X10^{-20}$) for (40 nm) particles.

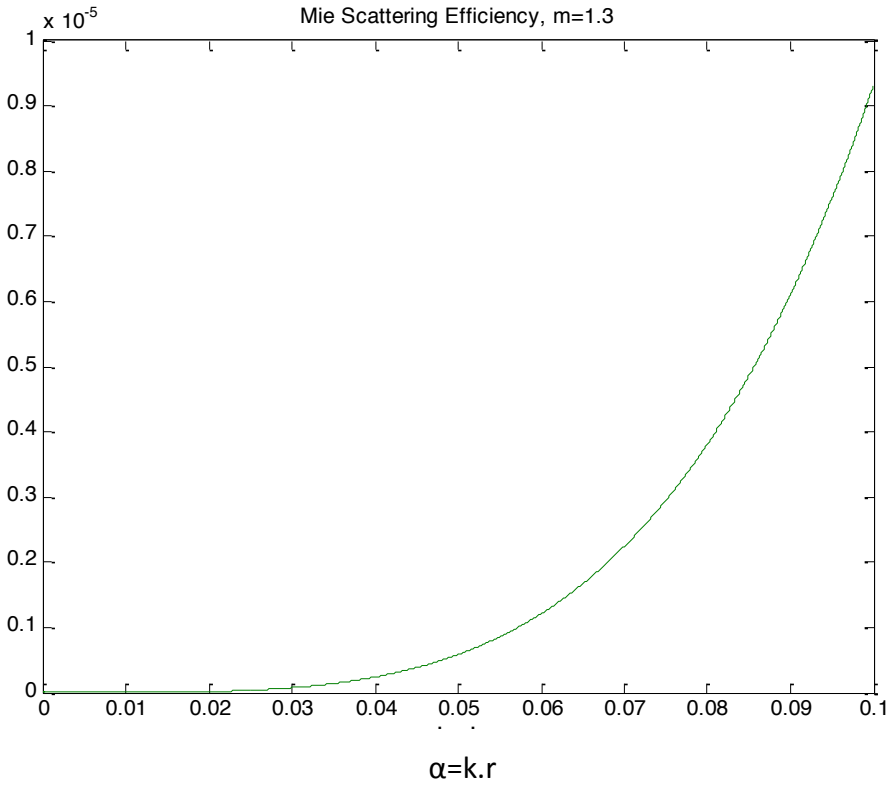

Figure 5.3 The outputs of the scattering efficiency function against small values of (α).

From the previous discussion, the rule which is used in light diffraction particle sizing instruments is: **Small particles scatter less light than bigger particles but with much wider angles.**

5.3.2. Angle of Observation

The particle size distribution of a group of particles could be estimated by measuring the light intensity at different angles. In practical sizing instruments, an array of photo detectors is used. The output current produced by a typical photo sensor is proportional to both the light intensity and the sensing area of the sensor. Designing a device that correlates a particle size only with the angle of observation requires all detectors to be producing the same fixed output current. The scattered light intensity is higher at low angles

(with respect to the incident light beam) and is gradually reduced at wider angles. So, smaller detectors can be used at the low angles and increasingly larger ones at the wider angles. This method provides a quantisation process on which particles are categorised into clusters depending on the scattering angle. Figure 5.4 represents the angular scattering profile for (α=10) and (α=100) where light intensity is more concentrated at the low angles for the larger particles. A close-up view into the diffraction lobes (Figure 5.5) shows that smaller particles scatter light at larger angles but with less number of lobes compared with those of smaller particles.

5.3.3. Particles Concentration and Volume

The measured light intensity at the detectors depends on the overall volume of the particles within the area of interest [Wedd (2003)]. The volume of a single spherical droplet is given by:

$$V = \frac{4}{3}\pi r^3 \qquad (5\text{-}24)$$

If we consider two particles having a relation between their radii given by: (r_1=n.r_2), then the relation between the two volumes is given by:

$$\frac{V_1}{V_2} = \left(\frac{r_1}{r_2}\right)^3 = n^3 \qquad (5\text{-}25)$$

A similar argument is applicable in the cross section area of the particles as follows:

$$\frac{A_1}{A_2} = \left(\frac{r_1}{r_2}\right)^2 = n^2 \qquad (5\text{-}26)$$

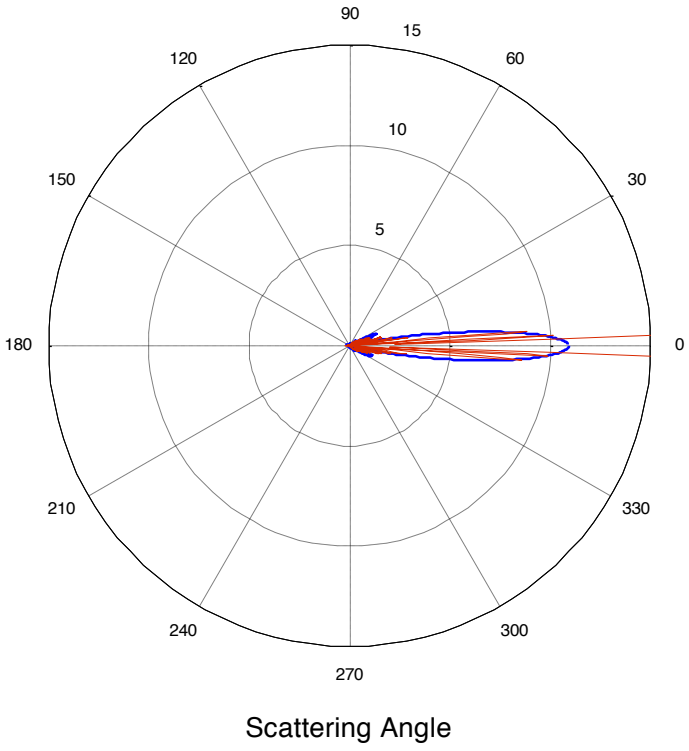

Figure 5.4 Angle of scattering for two diameters; α= 10 (blue) and α= 100 (red).

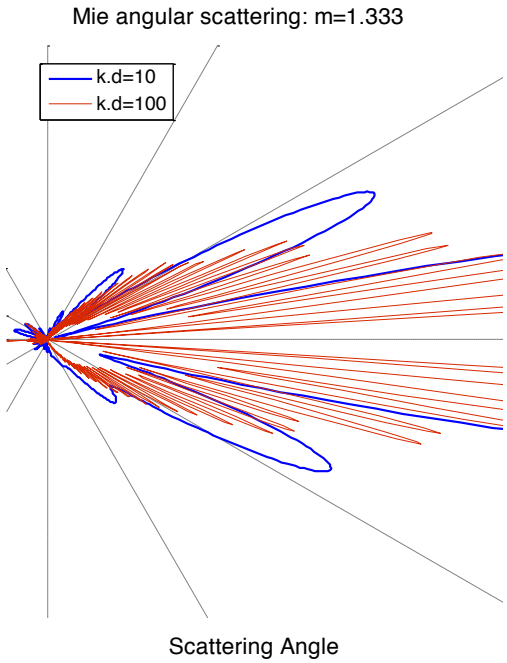

Figure 5.5 A close-up view to the diffraction lobes.

Therefore, one particle with a diameter of 100 μm has the same volume as a thousand of the 10 μm particles, but has a light scattering power only as a hundred of the 10 μm particles. The proportional relation between the light received by the detectors and (r^2) explains why practical laser diffraction systems usually calculate the volume of particles at each diameter cluster rather than the number of particles [see Wedd (2003)].

5.3.4. Refractive Index

The wavelength (λ) mentioned in the scattering expressions is a relative wavelength which depends on the refractive index of the surrounding medium (m_0) through the relation:

$$\lambda = \frac{\lambda_0}{m_0} \tag{5-27}$$

The refractive index is usually given as a complex number:

$$\tilde{m} = m + ik \tag{5-28}$$

The real part (m) is the index representing the phase speed, whilst the imaginary part (*k*) is called the "*extinction coefficient*" which represents the relative absorbency of the particle [Ley (1999)]. The smaller the imaginary part (*k*) of a material is, the more transparent it is. In many fluids, the extinction coefficient is very small (less than 10^{-4}) and can be ignored, so the extinction efficiency equals to the scattering efficiency in this case. The refractive index (*m*) of a material in Rayleigh scattering model is the magnitude of the complex index:

$$|\tilde{m}| = \sqrt{m^2 + k^2} \tag{5-29}$$

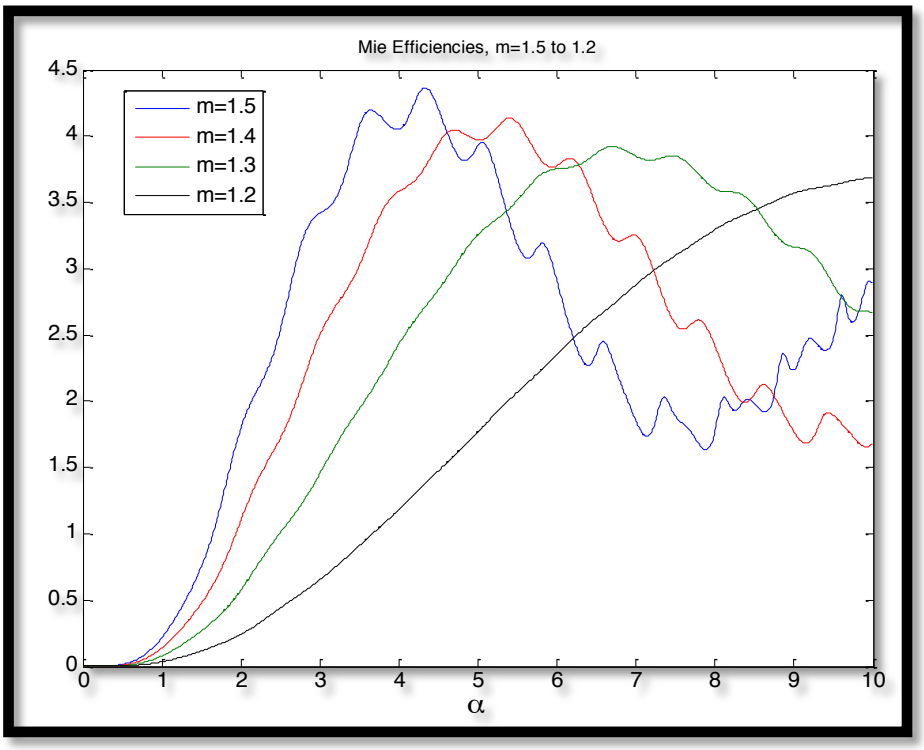

Figure 5.6 Scattering efficiencies generated for different values of refractive index. Size factor α=k.r.

Therefore, the relative refractive index between the particle material and the surrounding medium affects the scattering intensity[1]. The higher the refractive index of a particle the more light it scatters. The Mie scattering efficiency against (α) is generated for different refractive indices as illustrated in (Figure 5.6). The extinction coefficient (k) is only important in solid materials. It is shown in (Figure 5.7) that when (k) increases, the absorption increases, and therefore less light is scattered out by the particle material.

[1] Both the real part of the refractive index (m) and the imaginary part (k) are slightly dependent on the wavelength and the temperature too.

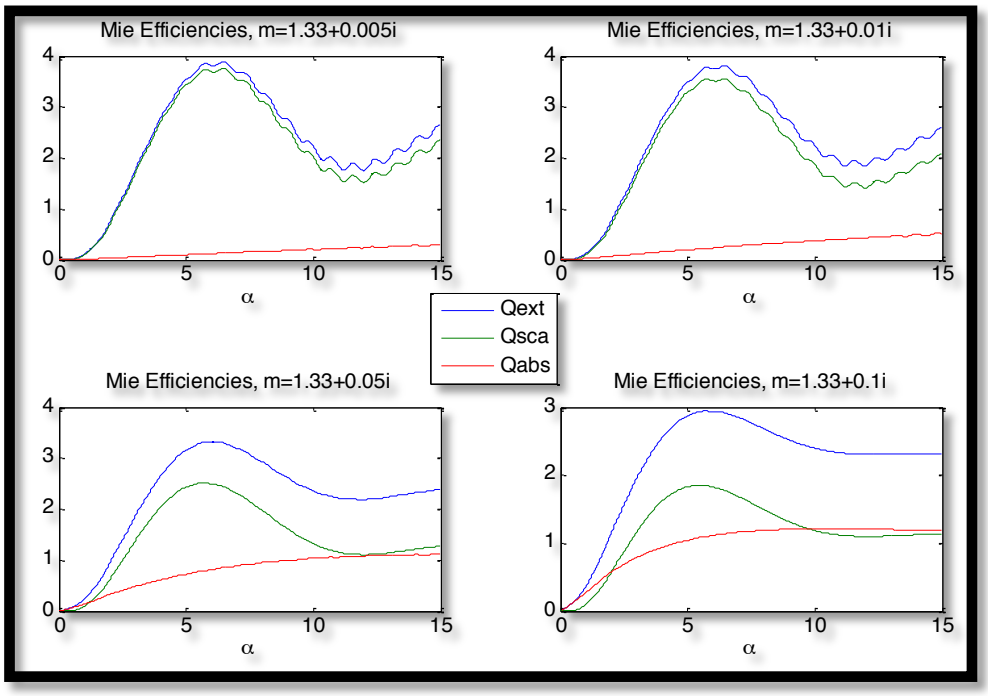

Figure 5.7 Absorption effect analysis by plotting Mie efficiencies for different extinction coefficients (k); Qext is the extinction coefficient (in blue) which equals to the scattering efficiency (in green) plus the absorption efficiency (in red). Large values of (k) are selected for analysis purpose as its effect become negligible at values less than 0.0001.

5.3.5. Material Colour Against Light Wavelength

The direct connection between the scattering efficiency and the light wavelength is clear in the mathematical model since the size factor (α) involves both the particle diameter (d) and the wavelength (λ) (equation 5-2). Therefore, the wavelength effect can be seen in (Figure 5.3) and (Figure 5.6), where the scattering efficiency improves as the wavelength decreases for the same particle size. However, this is not always true since the scattering efficiency starts fluctuating when the particle size becomes bigger relative to the wavelength as shown in (Figure 5.8). In other words, the relative relation between the particle size and the source wavelength rules the diffraction behaviour, and it could vary according to the size range. Moreover, the scattering efficiency at a specific angle and wavelength may vary according to the particle colour.

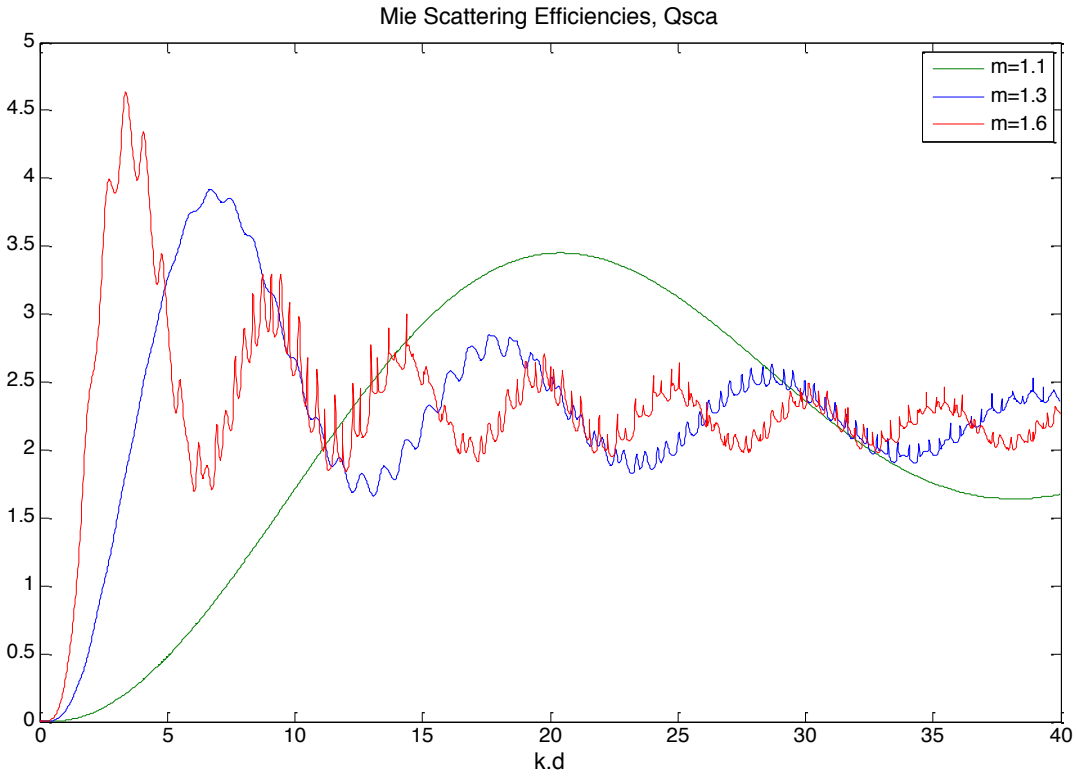

Figure 5.8 Scattering efficiencies for three different materials at wide range of (α=k.d); the wave number k=2π/λ.

The colour of the Titanium dioxide (TiO_2) particles is almost complete white; hence it scatters all the visible wavelengths around equally. What should be taken into account is the percentage of the complementary colour component in that object material with respect to the illumination light colour, which increases the absorption ability of the particles. The wavelength range 500-530 of the green laser, for example, is the complementary colour of the magenta (red-purple) colour. Another example is the soot particles which absorb most of the radiation, which makes the diffraction efficiency very low.

5.4. Related Experiments

In [Godefory & Adjouadi (2000)] microscopic particle sizing was attempted by simply calculating the distance between peaks and valleys (diffraction rings) in light scattering

patterns, using a 670 nm diode laser. It was noticed that the spacing between peaks is inversely proportional to the particle diameter.

$$k = \frac{1}{\overline{\Delta p} d_a} \qquad (5\text{-}30)$$

$\overline{\Delta p}$ is a manually calculated average spacing between the profile peaks, and (d_a) is the actual diameter of the particle. A number of calibration particles with defined diameters were used to calculate the constant (k) so that the diameter of any particle can be calculated by only calculating the average spacing $\overline{\Delta p}$. The reported method relies only on practical observations where the spacing between peaks $\overline{\Delta p}$ is considered constant. In this section, the method is theoretically investigated and evaluated.

Although it is true that the space between peaks increases as the particle diameter increases, it is incorrect to assume that this increment is linear as suggested in (5-30). It is clear from the Mie phase function that the spaces between diffraction maxima and minima are governed by the scattering angle, which follows equations (5-6 – 5-12). For a better clarification, the phase function graph of three different diameters is generated as shown in Figure 5.9.

Assume that the wave number (k) is 10 μm^{-1} for example, and then the diameter of the plotted particles is 5, 7, and 9 micrometers respectively. The spacing between fringes on the camera sensor is directly connected to the angle of observation by the equation:

$$\Delta p = R \tan(\theta) \qquad (5\text{-}31)$$

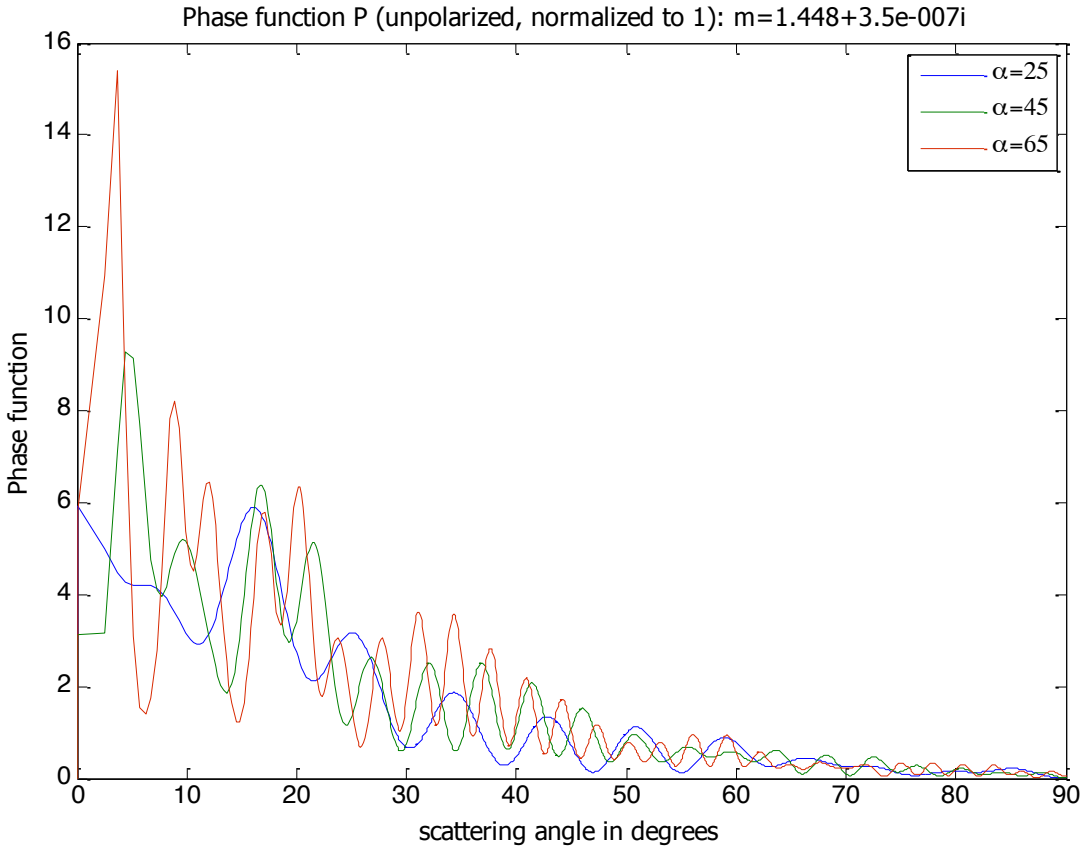

Figure 5.9 Phase function (from 0 to 90 degree) generated by 2000 sample for three values of α.

where (R) is the distance between the sensor and the particle. The last expression becomes more acceptable when R is much larger than the focal depth of the camera, so that a consideration that all particles are located at the same focal plane can be made.

The calibration step in this method finishes by the calculation of the mean value of the k^* constant generated at each known diameter.

$$\overline{k^*} = \frac{\sum_i \frac{1}{\tan(\overline{\Delta\theta}_i).d_i}}{i} \qquad (5\text{-}32)$$

where (i) is number of samples used in the calculation.

Using the example shown in (Figure 5.11) we found that the average angle spacing for each diameter is as follows:

Table 5.1: Changes in the diffraction fringes angle for different particle diameters.

Diameter (d) in micrometer	**Average change in angle between peaks** $\overline{\Delta\theta}$	$\tan(\overline{\Delta\theta})$	**Standard deviation**	$k^* = \frac{1}{\tan(\overline{\Delta\theta}).d}$
9	5.33	0.093	14.2 %	1.19
7	6.20	0.109	6.5 %	1.31
5	8.47*	0.149	7.1 %	1.34

The average of the three calculated k^* values in this example is equal to 1.28 with a 6% deviation from the mean value. Now, if this is an acceptable margin of error, then the diameter of a particle can be estimated by only the average spacing between peaks (or angles) by applying the formula.

$$d_c = \frac{1}{\tan(\overline{\Delta\theta})\overline{k}^*} \qquad (5.33)$$

where (d_c) is the calculated diameter.

This was theoretically tested (using Matlab) by generating the phase function of a 3 µm (in diameter) particle. The calculated $\tan(\overline{\Delta\theta}_3)$ was 0.256. Therefore, d_c =3.05 µm. The error in the last example was around 1.7 % which is comparable with the error (1.18 – 4.94 %) reported in [Godefory & Adjouadi (2000)]. However, this is not the only expected error as it is added to errors in the calculation of $\Delta\theta$ (or ΔP) generated by the imaging technique and image processing. Another drawback of this method is the difficulty in performing the

calibration step due to the need for calibration particles with accurately determined diameters of the same object material.

First proposed by [Adrian & Yao (1985)], the particle diameter *d* is theoretically calculated from the particle image on the image sensor (d_e) using the formula:

$$d = \frac{\sqrt{d_e^2 - d_s^2}}{M} \qquad (5\text{-}34)$$

Where *M* is the magnification of the lens and (d_s) is the diameter of the point response function of the diffraction intensity distribution calculated at the first minimum ring in the diffraction pattern of airy disc, and it can be obtained from the expression:

$$d_s = 2.44(M+1)\lambda f / D \qquad (5\text{-}35)$$

Where λ is the wavelength of the light source, *f* is the focal length of the lens, and *D* is the aperture diameter.

An investigation about particle position using particle diffraction pattern analysis was investigated by [Guerrero J A, *et al.* (2000)] using GLMT. It was tried through this approach to increase the accuracy in the particle position determination from the CCD sensor (distance from the sensor at Z-axis) in comparison with the Nelder-Mead optimization method which relies on the changes in the Gaussian profile as a particle travels through the light beam. Kihm and Chigier [Kihm & Chigier (1991)] have performed particle sizing of water sprays (of a airblast atomiser) using Malvern light diffraction instruments. They found that the most effective factor in decreasing a particle size is the air velocity.

Chapter6. Visualisation of the Heavy Fuel Spray Project; Instrumentation and Data Acquisition

6.1. Introduction

A digital imaging technique was developed for the visualisation and analysis of fuel sprays for the application of fuel injection in IC engines. This project was started in response to the need to provide a comprehensive evaluation of different fuel injection systems before using in a new small rotary (Wankel) engine design; the objective being to improve the combustion efficiency and engine performance. High-power lasers, high-resolution CCD cameras and a long-range microscope were employed to perform the experimental work. Characteristics of interest in this study are in both the macroscopic and the microscopic range. A global dispersion model of the fuel spray was generated for different pressures and frequencies. Spray formation and velocity analysis was conducted using different types of injectors. A micro-droplets sizing method was developed and examined for measuring non-spherical droplets in low-density sprays using high-resolution shallow DOF microscope.

6.2. Engine Specifications and Fuel Delivery System

Fuel injection systems were evaluated for the “Sonic 35” single rotor Wankel engine (Figure 6.1) developed by Cubewano Ltd., aiming to improve the output power and the fuel efficiency of this type of engines. The engine weighs less than 5 kg and produces around 8.5 hp (6.3 kW) of power at 9200 rpm. The main challenge in small rotary engines market is to produce a low vibration engine with a high power-to-weight ratio. The small physical dimensions of the current engine (see appendix 6.1) introduce new challenges in terms of the fast evaporation and the need to perform atomisation at low injection pressures. Other challenges in this design include the management of the injection cycle in the case of high rotational speed of around 15000 rpm, and the problem of the cold start of the engine. The injection mechanism in this case is an indirect injection into a manifold. This involves fuel mixture suction into the combustion chamber due to reduction in pressure produced by the rotor movement. The fuel injector is mounted on a throttle body (Figure 6.2) which leads to the intake manifold (approximately 25x70 mm^2). The original throttle body of the engine includes a small cavity between the nozzle exit and the intake manifold, preventing the visualisation of the first 20 mm of the spray jet (downstream of the nozzle). The analysis of the discharge spray velocity requires observation of the fluid jet at the nozzle exit at an early stage of the spray formation process. For this reason, a new throttle body with an open end has been designed and used during the tests. This modification facilitates the attachment of the injector body to the test rig and switching between injectors.

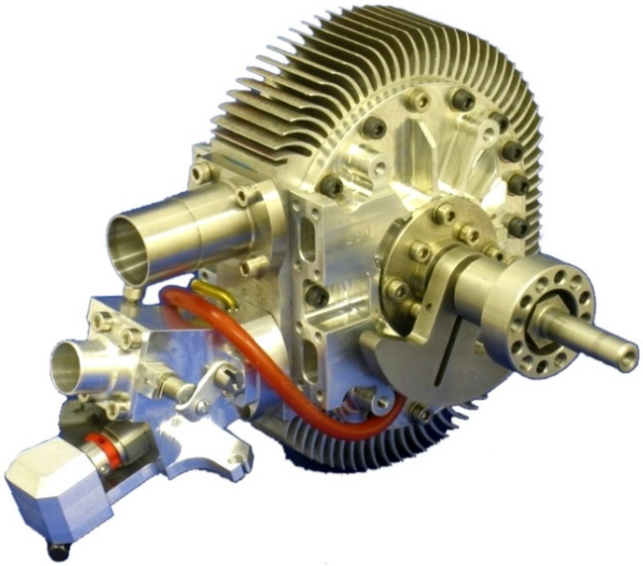

Figure 6.1 Cubewano Sonic 35 air cooled engine weighs around 4.8 kg (Sonic 35 Specifications)

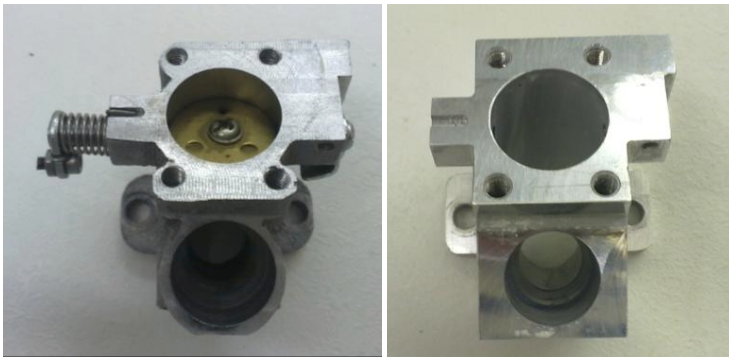

Figure 6.2 (Left) The throttle body used by the engine manufacturer; (Right) The modified throttle body used for the imaging of the fuel spray (designed in the University of Warwick)

In the case of direct imaging using a flashgun, the fuel injector was needed to be held by a tripod, so a new injector casing was designed (Figure 6.3), ensuring a full optical access to the nozzle end, and providing a high degree of isolation (connecting the inlet with the injector body after sealing by rubber rings) in order to avoid any fuel leakage due to the fluid pressure behind the injector inlet.

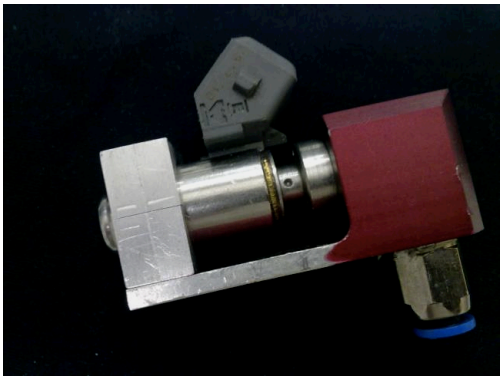

Figure 6.3 A fuel injector fitted into a new casing design for the direct imaging experiments.

A fuel delivery system delivered the fuel to the injector after raising the fuel pressure into the injector working pressure. The fuel delivery circuit consisted of a fuel tank, fuel pump, mechanical flow control, pressure relief valve, filter and pressure gauge connected together by fitting pipes. Figure 6.4 shows the main components used in the fuel delivery system.

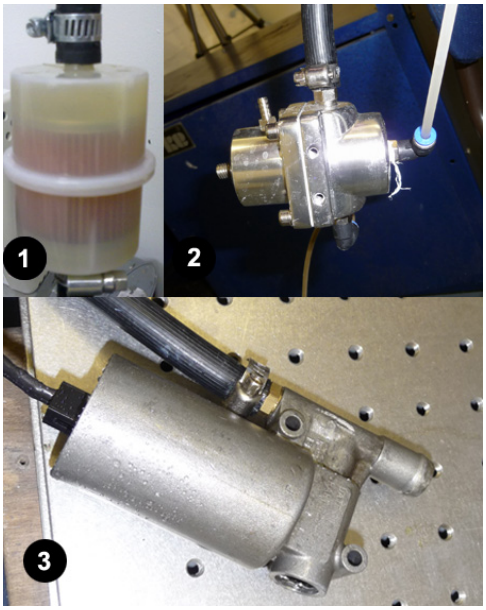

Figure 6.4 Components in the fuel delivery system; (1) fuel filter, (2) pressure relief valve, (3) 10 bar fuel pump.

The fuel pump was a single-port electric fuel pump (12V, 1A), which can generate up to 10 bar pressure. A non-return valve in the fuel pump prevents the fuel from flowing back into the fuel tank even when the pump is switched off. The pressure relief valve was set at a pressure range (1-10 Bar). The pressure relief valve was connected to the fuel reservoir through a return line. A 10-micron filter was fitted to the intake part of the system for removing particulate matter that could cause injector plugging.

6.2.1. Fuel Injectors

Two families of fuel injectors were tested during the experimental work in both the University of Warwick and Cubewano Ltd. The first injector was a conventional 12V electronic gasoline injector "IWP23 Pico injector" (Figure 6.5), that delivers 158 cc/min (static flow) at 3 bar pressure (see IWP023 Datasheets). This injector is designed for racing applications and typically needs around 9.6 Watts of power to operate, with a maximum pressure of 5 bar. It is also described by the manufacturer as a "fast pulse response" injector. The injector was examined in laboratory and seemed to operate well for injection frequency below 310 Hz, providing a pulse width as short as 1.6 ms. If such an injector was fitted in an engine that takes one pulse per revolution, it should theoretically provide a rotational velocity up to 18600 rpm. This family of injector is used in automobile engines and can produce either a single jet or multi jet sprays. The fluid atomisation in this injector is carried out using an actuating electromagnet which moves an internal injector valve, and then the injector dispenses the pressurized fuel during each pulse through a final nozzle 584 microns in diameter.

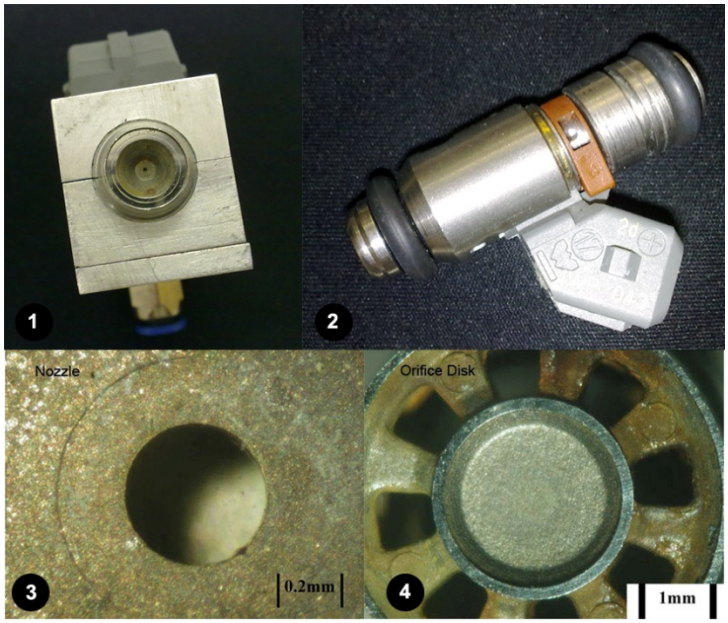

Figure 6.5 IPW023 gasoline injector, (1) front view shows a single nozzle injector in the casing (not original), (2) a side view of the fuel injector showing the electrical plug and the sealing rings, (3) a microscopic view of the end nozzle, (4) a microscopic view of the orifice disk.

Another type of injector was tested in response to the light-weight high-speed low flow-rate engine requirements. The new injector was a micro-dispensing system (Lee VHS M/2) developed by the 'Lee Company' mainly for applications that need micro-litre and nano-litre dispense volumes including medical (drug delivery) and ink jet applications. The objective of the test was to evaluate the injector performance and make the necessary arrangements to fit it into the rotary engine design. A maximum operation frequency of 3.3 kHz was measured in laboratory. The high injection frequency offers a better control of the flow rate of the fluid, and also allows operating at higher speeds (the engine speed is 15,000- 18,000 rpm). It weighs less than 8 g, compared with 35 g for the standard IWP gasoline injector. A good advantage of this injector is the possibility of replacing the end nozzle for the same injector body. The nozzle orifice diameter ranges from 255 µm down to 125 µm (Figure 6.7).

The “062 MINSTAC” atomiser was found to produce well atomised sprays with a 50° angle in the initial assessment.

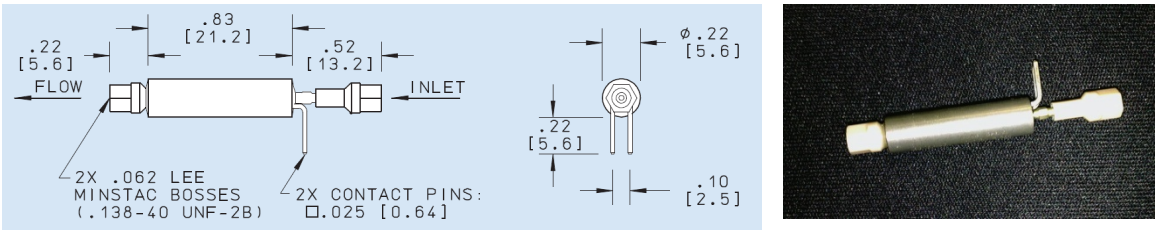

Figure 6.6 Lee VHS M/2 (very high speed) fluid injector

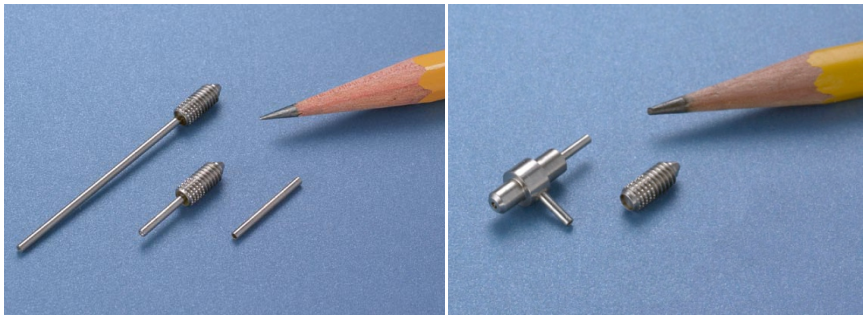

Figure 6.7 Lee nozzles; left: “Plain orifice” nozzles; right: 062 MINSTAC atomiser.

6.3. Jet- A1 (JP-8) Heavy Fuel Characteristics

The applied fuel in the current project was the Jet A-1 (JP8) kerosene-grade by request from the sponsor (Cubewano Ltd.). Kerosene is a thin clear liquid that is commonly used to power turbine engined aircrafts. In general, it has a higher flash point[1] than petrol, making it much safer. The disadvantage of the high flash point, however, is the difficulty in carrying out a cold start of the engine. For this reason, a heater matrix was introduced at the final orifice in order to improve the evaporation ability of the fuel (see Figure 3.2 and 3.3 for the evaporation rate of kerosene). The minimum flash point of the JP-8 is 38°C, the boiling

[1] The lowest temperature at which a fuel can form a volatile mixture with the air.

temperature is 165–265 °C [Hemighaus, *et al.* (2006); Kutz (2006)], and it starts freezing at (-47) °C. The dynamic viscosity of kerosene is 2.5 g/m.s, and its density is 775.0-840.0 kg/m^3 at room temperature [Exxonmobile report (2005)]. Because of the low injection pressure in the current work, fuel sprays were lower in density and slower in penetration than the sprays of the conventional diesel and gasoline systems, which have been reviewed in the literature review.

6.4. Direct Imaging System

6.4.1. Direct Imaging System Setup

Spray images were captured by a high-resolution CCD Nikon D200 SLR digital camera (10.2 megapixels) during the investigation of the global spray pattern, with a relatively long exposure time, using an electronic shutter system with a 125 µs top speed. The imaging period, however, was controlled by the illumination time of the flash light rather than the shutter speed in most cases. A standard Nikkor SB 800 flashgun was used for illumination, placed at 45-55° with the camera, and was remotely triggered by a wireless (Bluetooth) link.

The camera was equipped with a 55 mm (focal length) Nikkor lens[1] (maximum aperture of f/2.8) designed for the close-up photography. The focal length of a camera lens represents the minimum distance from an object that can remain in focus, and therefore it determines the angle of view. The lens with a higher focal length has a narrower angle of view.

The aperture of a lens is the window of light to the camera sensor. The size of the aperture is normally controlled by flaps which open and close in steps (lens stops). The ratio

[1] 35 mm, 50mm nikkor lenses have been occasionally used.

of the focal length to the aperture diameter is called the f-number. So, increasing the f-number practically means reducing the amount of light allowed to the sensor. This is used to control the image brightness so that it is not saturated by the flashlight. On the other hand, a very tight aperture leads to a lower sensitivity of the sensor. In both cases (of too much and too little light) image information is lost. Therefore, the aperture size should be selected to fit the dynamic range of the sensor, depending on the incident light intensity, the imaging angle, and the size of the object to be imaged. Also, when a lens is stopped down in aperture, more parts of the image will come in sharp focus, as a smaller aperture provides a deeper depth of field (DOF). When using a flood-lighting or a wide angle flash light, it is necessary to obtain a shallow (short) DOF in order to reduce the effect of defocused particles and be able to resolve individual particles, particularly in dense flows.

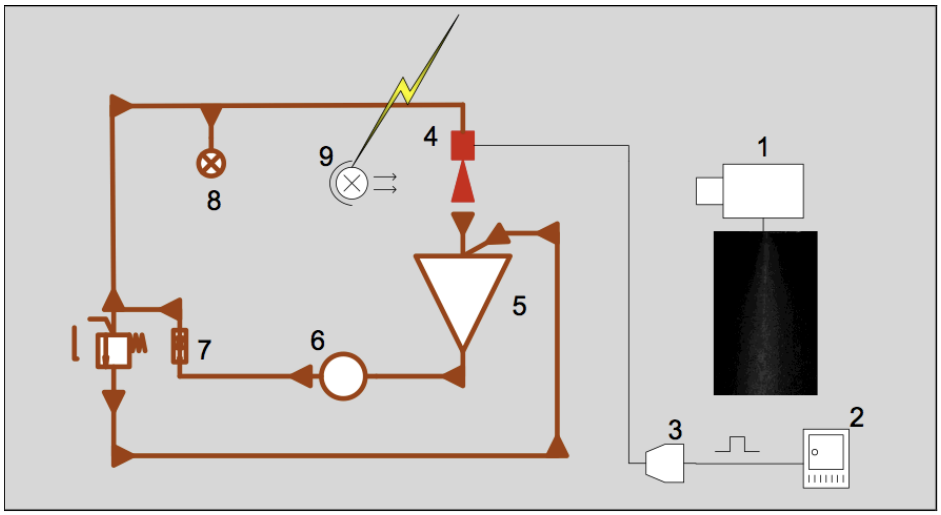

Figure 6.8. Direct imaging system setup and fuel delivery circuit. (1) SLR digital camera (2) programmable control unit (3) driving circuit (4) fuel injector (5) fuel container/collector (6) fuel pump (7) pressure relief valve (8) pressure gauge (9) wireless flash gun

6.4.2. Data Acquisition in the Direct Imaging Method

Fuel injectors were evaluated using deionised water and examined later using jet fuel at room temperature (20º). The experimenter acquired images manually at this stage.

The resolution of the acquired images is 2896 x 1944 pixels, and the camera exposure time is 0.62 second. The digital camera captures the image during the prolonged aperture when a flashgun is fired. The flash light duration determines the brightness of the spray images by adjusting the "flash power" (Figure 6.9). Measurements are repeated, for each test point for a better quantitative representation of the spray data.

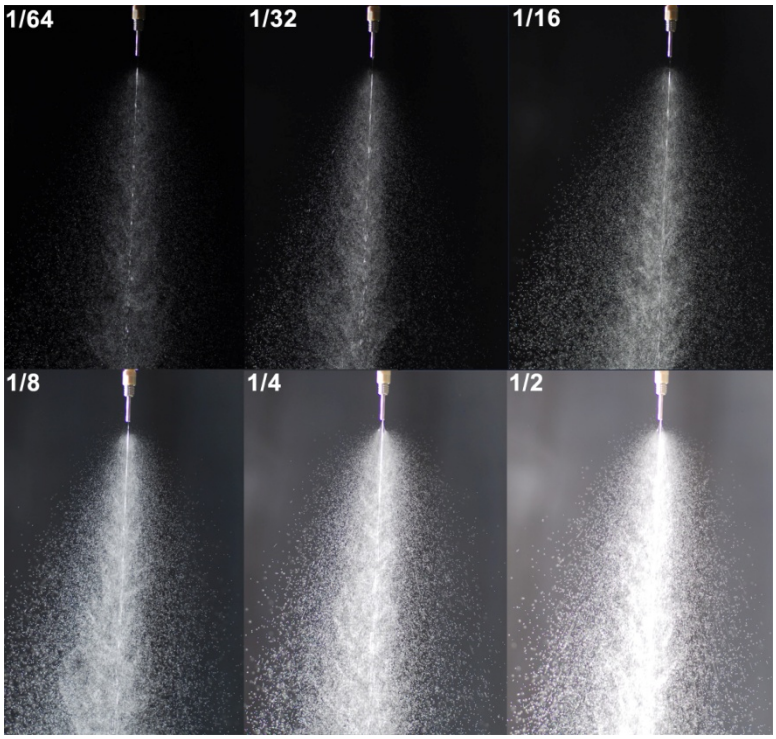

Figure 6.9 Unprocessed images taken by Nikon D200 SLR camera at different flash power settings for DI water sprays generated by LEE medical injector at pressure P=6 bar. Flash power 1/2 corresponds to a light pulse duration of 1/1100 sec, 1/4 to 1/2700 sec, 1/8 to 1/5900 sec, 1/16 to 1/10900 sec, 1/32 to 1/17800, and 1/64 to 1/32300 sec.

6.5. Laser Imaging System

6.5.1. Development of Spray Visualisation Experimental Rig

A laser imaging experimental rig was developed in the Optical Engineering Laboratory (OEL, University of Warwick) to be tested and evaluated and then moved to

Cubewano Ltd. test cell (Birmingham) in order to perform spray visualisation experiments on jet fuel. The visualisation system (Figure 6.10) consisted of:

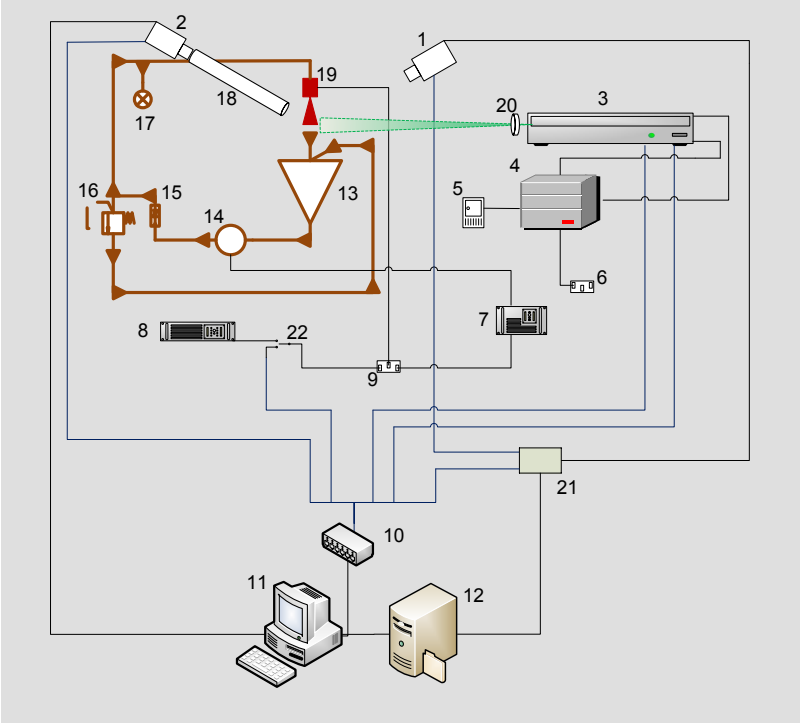

Figure 6.10 The laser imaging experimental for high speed spray jet [Zakaria *et al.* 2010]. (1) high resolution first CCD camera (2) second CCD camera (3) Nd:YAG laser head (4) Laser Power Supply (5) laser controller (6) 3-Amps AC main power (7) adjustable DC power supply (8) TTL signal generator (9) injector driver circuit (10) PC-Control Unit (11) Control PC (12) data storage RAID (13) fuel supply (14) fuel pump (15) flow control (16) Pressure relief valve (17) pressure gauge (18) K2 microscope (19) fuel Injector (20) laser sheet optics (21) PCO camera controller (22) trigger switch (23, 24) surveillance cameras (25) optical table (26) rail.

6.5.1.1. Camera System

Advanced camera system was employed in this project to meet a set of requirements including large sensor size, high sensitivity and low noise level. In addition, for droplet tracking and velocity calculation, a short interframe time[1] compared to the flow speed was essential. Two CCD cameras were used in this test as shown in Table 6.1.

[1] The inter-frame time is a dead time between the two images in the double shutter mode where no exposure can be done.

Table 6.1: The specifications of the cameras used in the laser imaging tests.

Camera	Resolution (pixel)	Frame-rate (Hz, Max)	Inter-frame time (ns)	Dynamic Range (bits)	1st frame minimum exposure (µs)
PCO Pixelfly	1360 x 1024	50	5000	12	5
PCO 2000	2048 x 2048	14.7	180	14	0.5

Figure 6.11 PCO camera systems 1. PCO2000, 2. PCO Pixelfly.

Both cameras can operate in the double shutter mode to perform PIV. The exposure time of the first frame can be determined by the computer software, while the exposure time of the second frame is the readout time for the first frame. The pixel actual size is 7.4 × 7.4 μm^2 (sensor size 15.6 x 15.3 mm^2) in PCO 2000.[1] The PCO cameras are externally triggered using a TTL signal (through an external power supply for PCO 2000 and a PCI card for PCO Pixelfly). The quantum efficiency for the CCD sensor is 55-60% at the green laser wavelength.

[1] 6.45µm x 6.45µm for PCO Pixelfly.

6.5.1.2. Laser

The illumination system was a green (λ= 532 nm) double pulse Q-switched Nd:YAG laser, provided by "Oxford Lasers". The maximum output power of this laser is 200 mJ (increased to 600 mJ in jet noise test) for a pulse width as short as 5 ns. The laser head involves two independently controlled lasers (dual cavity) to generate double-pulse beams that follow the same path to the only final shutter. A time delay between the trigger of the optical pump and the laser beam pulse was calculated, which is mainly the upper-state life-time of the lasing medium needed to reach the maximum population inversion. The measurements in the laboratory showed a 175 μs delay for the first laser and 156 μs for the second. Therefore, there was an inherited time difference of 19 μs between the generated double pulses. This difference, however, can be controlled by adjusting the settings of the pulse sequence of the Q-switch. The laser system can be locally and remotely controlled, and it can operate at a maximum repetition rate of 50 Hz.

6.5.1.3. Laser Sheet Optics

The experiments showed that a good quality laser sheet can be generated by combining two cylindrical lenses rotated in an angle relative to each other. A light sheet approximately 3 mm in width at the object plane was generated by two cylindrical convex lenses (f/100mm and f/50mm) as shown in Figure 6.12. The Gaussian pattern of the beam was reduced using a shutter in front of the sheet optics reducing the sheet width to approximately 2 mm.

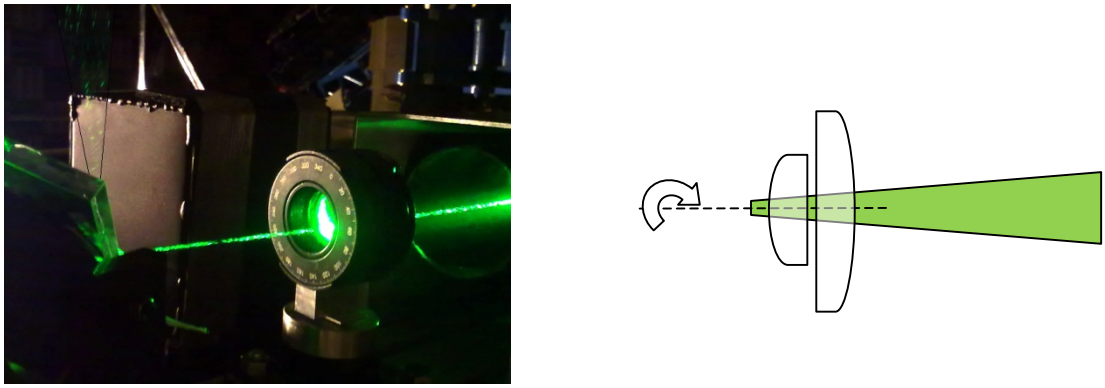

Figure 6.12 Light sheet formation by cylindrical lenses

The laser beam was directed by Nd:YAG dielectric mirrors (ThorLabs; NB1-K12) mounted on an adjustable base for accurate alignment. These mirrors have a high damage threshold (5 J/cm^2 for 10 ns Pulse) and a high level of reflectivity (between 99.8% and 99%)[1] at 532 nm wavelength (Appendix 6.2).

6.5.1.4. Control System

In practical IC engines, an engine control unit (ECU) is usually used for the management of the injection period and frequency as well as the ignition timing. New control systems were developed to meet the requirements of the different injectors, and to allow the analysis of their behaviour against the different operation parameters. The control system sends a pulse train to a driver circuit which powers up the injector valve. The control signal profile was monitored by a standard oscilloscope to accurately define the pulse timing and to observe the injector response to the control signal. The IWP (gasoline) injector was driven by a transistor switch connected to a high-power relay. A standard relay (DS2E-Panasonic) was used initially but eventually replaced by a high-speed relay (reed relay CRF05-1A) when high injection frequency was required. This decreased the operation time

[1] Depending on the angle of incidence.

of the relay from 5 ms in the first into 0.1 ms in the second, with a very short release time of 0.02 ms on the high-speed relay. The Lee valves were electrically driven by a spike and hold driver. A high voltage spike of 24-40V was required in the beginning of the injection cycle in order to actuate the valve and reduce the response time of the needle lifting under high pressure [Lee-VHS-M/2 datasheets]. The spike voltage lasts for a very short time (0.3 ms)[1] only, and then it is replaced by a 3.5-5V hold voltage during the rest of the injection period to avoid heating up the injector and damaging it by the high current. The control circuit converts the TTL signal into the required spike and hold profile (Figure 6.13). The control (pulse-train) signal was initially generated by a standard function generator for general tests. However, as a precise determination of the injection timing and duration was needed, a more accurate method was considered.

A microprocessor system (programmable hardware) was developed for producing the required driving TTL signals. The core of the system was an MSP430 (Texas Instruments) chip, which is a 16 bit ultra-low power, containing analogue to digital converters (12 and 16 bit), communication interfaces, operational amplifiers, and an LCD controller. The programmable system allows assigning different channels for triggering the injector, the cameras, and the lasers, and defining pulse timing accurately. Also, the integrated counters and the LCD drive allow the monitoring of the number of injection events for the accurate calculation of the flow rate. The temperature of the injector was monitored using a standard thermocouple connected to an ADC channel. The programme of the micro-controller unit (MCU) was written in micro-C language[2] (appendix 6.3). The advantage of this system is that once the operating software is uploaded, it becomes a standalone battery powered system.

[1] The spike time was made to be adjustable as a longer time is needed in the case of the high fluid pressure.
[2] C language for embedded systems for programming MSP430 using IAR development environment.

However, the accuracy of this system is restricted by the operation frequency of the processor (Max. 8 MHz).

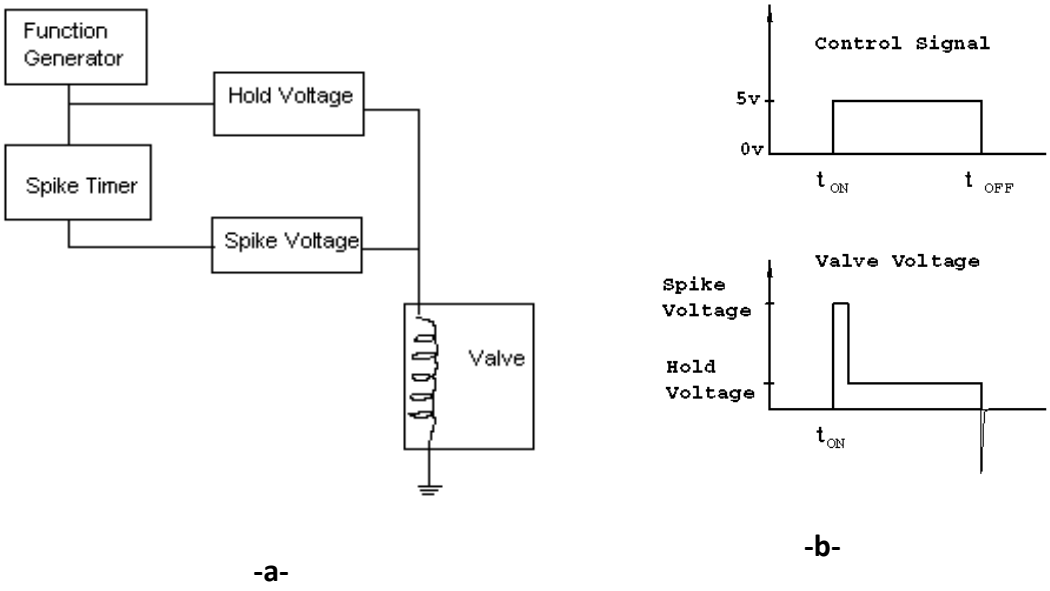

Figure 6.13 a. The hold and spike driver diagram, b. The control signal generated by the driver circuit [Lee-VHS-M/2 datasheets].

Another control system was used in this project; a USB PC-control hardware with a 16 TTL output, which was designed primarily to facilitate PIV systems. It provides a user-friendly PC interference (YAPP)[1] that allows defining a sequence of actions easily with an accuracy of 5 ns. The ability of defining variables and the flexibility of modifying the experimental conditions helped in speeding up the data acquisition process.

[1] Developed by Andrew Skeen, University of Warwick.

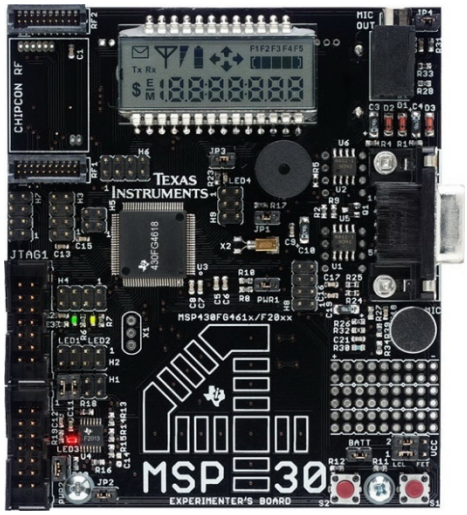

Figure 6.14 MSP430 development board developed by TI two processors (MSP430FG4618 and MSP430F2013) with an LCD display (TI website).

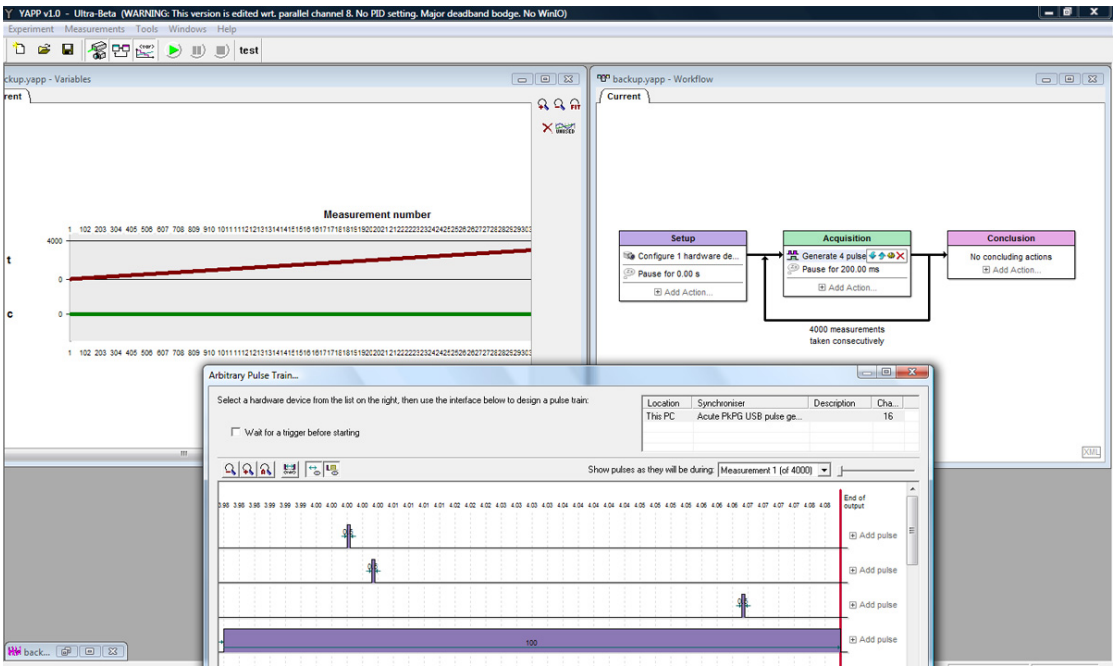

Figure 6.15 YAPP control software snapshot.

6.5.1.5. Long Distance Microscope

A specialised long distance microscope model K2/SC (Infinity) was employed for close-up imaging of fuel droplets. This microscope is designed for high-resolution imagery due to its compatibility with large image sensors up to (24 x 36 mm). It contains a focus ring

and an adjustable iris for the depth of field and brightness control. It also provides chromatic and spherical correction, producing a flat focus field. The microscope is attached to a close-up (CF) parfocal objective especially designed for this type of tests in order to improve the resolution of the microscope. The calibration of the assembly using a glass calibration target showed that the maximum available resolution of this assembly is 885 nm (with a standard deviation of 22.5 nm) for the closest working distance (WD=92 mm) from the focused object. The numeric aperture in this case (K2 data sheets) equals to NA= 0.207. The smallest radius which a microscope can resolve is calculated through the relation [Laufer (1996), Ch.7; Curry (1957), Ch.6]:

$$\delta = 1.22\frac{\lambda}{D_L} f = 0.61\frac{\lambda}{NA} \tag{4-7}$$

where D_L is the diameter of the entering lens and f is the focal length for the microscope. Therefore, for a given wavelength of an Nd:YAG laser λ=532 nm, the actual spatial resolution that allows distinguishing between particles is 1.568 μm only. The magnification factor in this case is 3.05 doubled by the magnification tube (2.5X). A protection cone is attached to the microscope front end to protect the lens from the surrounding droplets, which also reduces the reflection effect, and thus the optical noise. The shallow depth of focus (DOF) of the microscope allows producing sharp images at a specific focal plane, which is advantageous especially in the case of dense flows. The depth of focus reported by the K2 manufacturer is around 10 μm only (compared with DOF=225 μm reported by [Esmail *et al.*(2010)], and DPF=140-300 μm reported by [Kashdan *et al.* (2007)]).

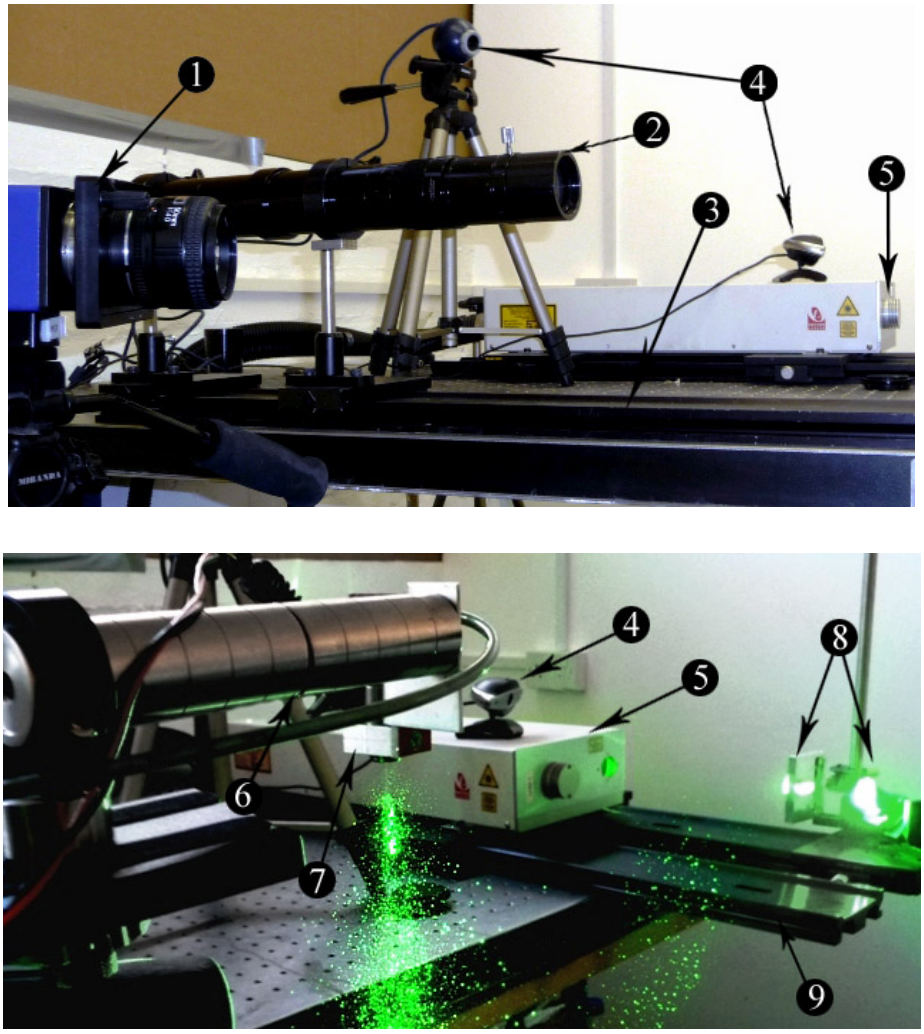

Figure 6.16. The laser sheet imaging system; 1. PCO2000 camera with a Scheimpflug adaptor, 2. K2 long range microscope, 3. Optical table, 4. Monitoring cameras, 5. Laser head, 6. Injector holder, 7. Injector, 8. Laser sheet optics, 9. Rails.

6.5.1.6. Computer System & Frame-Grabbing Software

A central computer was used for the experiment remote control and image recording. The computer was connected to the control hardware and the data line of the cameras. It is also connected to a data storage RAID to enable fast data storage. Images were recorded using CamWare V2.21 frame-grabbing software, which saves files in both TIFF and BMP formats, and also provides a control of the exposure and the brightness levels.

6.5.1.7. Other Instruments

A set of webcams was used for the observation of the rig from the control cell while running the experiment. Webcams are practical in performing laser alignment and laser sheet focusing, as it is not possible to see the laser beam behind the safety goggles. An independent signal generator is used when continuous injection pulse train is needed. The injector is powered by an independent DC power supply (0-40 V). The imaging instruments were mounted on an optical table with rails for the adjustment of the microscope and the laser sheet optics.

6.5.2. Data Acquisition

Light scattering images were acquired for the analysis of the macroscopic global spray characteristics, while the microscopic analysis was performed using backlight shadowgraphs. Although in literature shadowgraph techniques have been used in the global spray case too, spray shadowgraphs do not provide details about the density distribution within the spray image; instead, the shadowgraph generates a solid image of the spray pattern. A shadowgraph with a relatively deep depth of focus produces images that include the shadow of different layers at the same time, leading to a misrepresentation of the mass distribution of the spray droplets within the spray area. Also, solid spray images cannot be used for PIV when velocity data are required.

Double-frame images were produced by triggering the double lasers with a short time delay between them (10-50 μs). In order to obtain sequential images of the high speed jet using a low-repetition-rate laser, the instant of laser trigger (t_L) was shifted by a constantly increased delay (T_s) so that the lasers are fired at different instants during the

injection event. This is added to the injection delay (T_d) between the actual *Start of Injection* (SOI) and the triggering moment (t_{inj}), as described in the following formula:

$$t_L(i,j) = t_{inj} + T_d + (T_s \times i)$$

where the index (i) defines the time resolution of the imaging process, and (j) is the experiment repetition index of images groups captured under the same timing settings. The system was automated so that small time steps could be used. A time step as small as (T_s= 2 μs) was tested to provide spray progression data at high time resolution.

6.5.2.1. Imaging Angle and Scheimpflug Correction

The laser sheet must be positioned within the focal plane of the camera lens in the 2D imaging in order to obtain sharply focused images. Therefore, the image sensor plane is normally made parallel with the laser sheet plane, i.e. making a 90° angle between the focal plane and the lens normal axis, with a small tolerance depending on the focal depth of the lens and the thickness of the laser sheet.

The Mie scattering pattern of micro-droplets close to the wavelength shows that most of the light energy scatters at small angles (to the incident beam) at the forward lobe, and produce another smaller back-scattering lobe, so that 90° angle could be in many cases the minimum energy point at the scattering profile. Therefore, only large droplets can be resolved by the camera from this angle. For this reason the macroscopic imaging was performed at sharper angles (55°-60°), which makes the laser sheet and the camera sensor unparalleled. By doing that, it is not possible to bring the entire object plane into focus. A Scheimpflug system was used to address this problem. In Scheimpflug principle the object plane is in sharp focus when the image, the lens, and the object planes intersect along one

common line. Therefore, a Scheimpflug adaptor was fitted between the camera lens and image sensor for the adjustment of the lens angle.

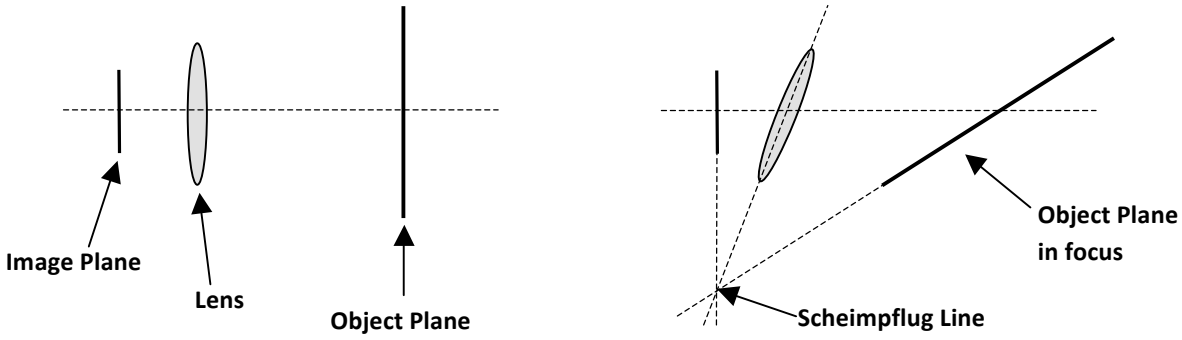

Figure 6.17. The principle of the Scheimpflug correction.

6.5.2.2. Calibration

The camera was focused on a target placed on the field of view (FOV). In the case of macroscopic characterisation, a calibration ruler with 0.5 mm divisions was used as a target for both focusing and estimation of the FOV area. The size of the image pixel is then calculated using Matlab (imtool library). The pixel size in Figure 6.18 for example was calculated by taking 20 measurements from different positions in the image, and it was 50 μm/pixel, with a 0.7 μm margin of error.

For the microscope calibration, a calibration plate containing calibration patterns with known dimensions is used. Figure 6.19 shows the "England finder" calibration (glass) plate with 1 mm^2 labelled squares that are also divided into sections for the accurate determination of the FOV. The best resolution obtained by the K2 microscope during our tests was 885 nm with a standard deviation of 22.5 nm (using 20 measurements).

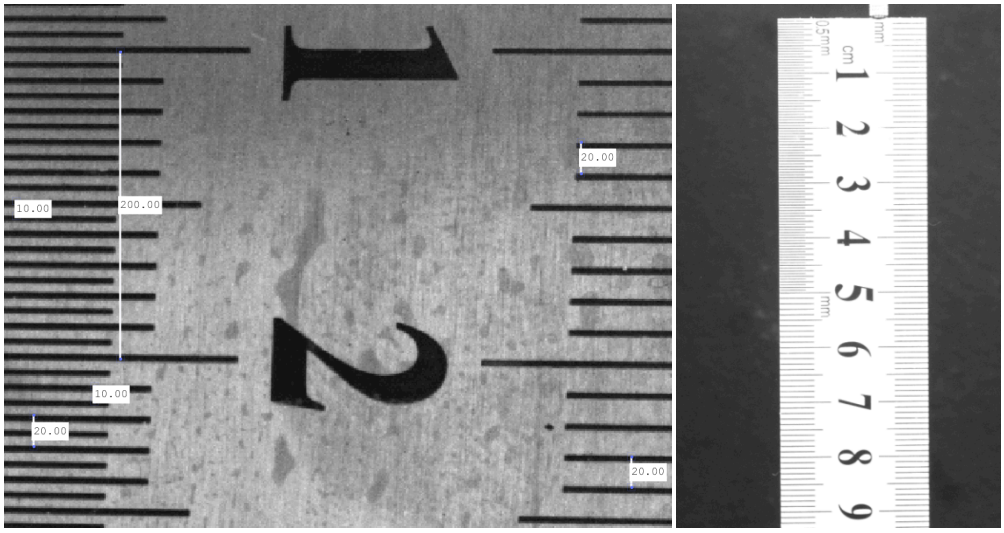

Figure 6.18 field of view measurements using a flat ruler in the focal plane

The depth of focus (DOF) of the microscope was measured by moving the calibration target back and forth by small steps in front of the microscope's lens, and then taking images until finding the middle of the focal depth, where the Gaussian effect on the calibration object is minimum, as shown in Figure 6.19. The focused part of a droplet in shadowgraphy is the dark area of the image, so when a droplet is located away from the focal plane, the grey level of the droplet changes starting from the edges making the shadow of the droplet brighter (more details about this point in [Lee & Kim (2004)]). Table 6.2 demonstrates changes in the width of a 25 µm calibration object as the calibration plate moves out of focus.

Table 6.2: The DOF calibration for the K2 microscope

Moving the subject out of focus (µm)	5	10	20	30
Average increment in width at 70% of the peak (µm)	1.4	2.2	3.6	8.8
Average Increment in width at 90% of the peak (µm)	0.5	1.2	2.1	-

Careful selection of the threshold can eliminate the out of focus particles. Figure 6.20 demonstrates the changes in the calibration plate image profile when it moves out of focus. As the sharpness of an image decreases, the shadow of the object becomes brighter, making it much difficult to distinguish between the object and the background. By applying a strict threshold (90%) of the profile peak, blurred drops more than 30 µm outside the DOF are automatically rejected, along with their diffraction effect. The short focal depth of the microscope helps in the distinction between the in-focus and the defocused particles, noting that this method can be only applied with a flat focal plane where the defocusing effect is uniform over the entire image frame. The maximum error using the 90% threshold was 2.1 µm in the case of the 25 µm object on the calibration plate. Therefore, the maximum expected error in the droplet diameter due to their Gaussian profile is around 8.4%.

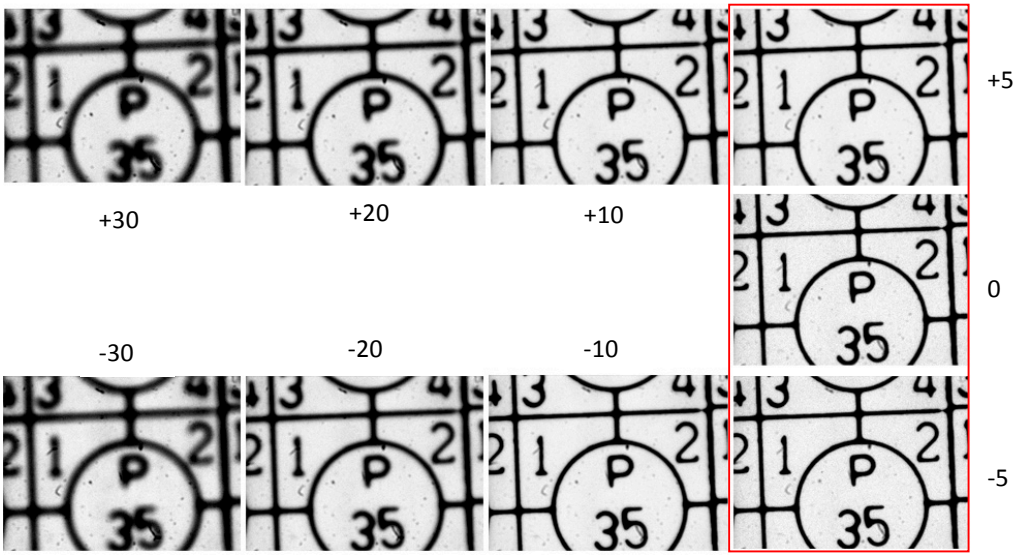

Figure 6.19: The calibration plate in the field of view of the microscope and the measurements of the focal depth (numbers in microns).

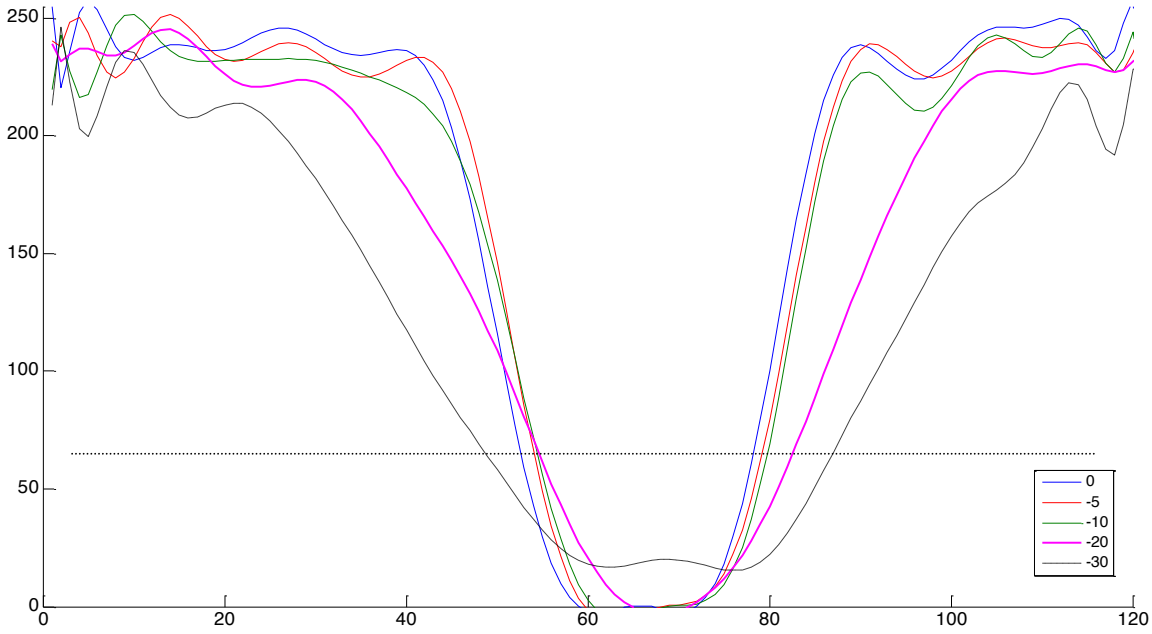

Figure 6.20 The Gaussian blur effect due to defocusing of the calibration plate (distances in microns; axes in pixels); graph is generated by Matlab code (Appendix 6.4).

6.5.2.3. Rig Modification for Micro-Shadowgraph

The micro-shadowgraph was carried out using the K2 microscope and the PCO camera. In order to generate a homogeneous backlight, a set of light diffusers was mounted in front of the microscope lens. The author chose to use a sequence of two diffusers, 5° and 10°, 5 cm apart from each other. This setup gave a uniform backlight along the entire image frame and removed the speckle noise, which allows resolving the micro-droplets with minimum image processing. Another dielectric mirror was needed in this case for the redirection of the laser beam toward the diffusers as shown in Figure 6.21.

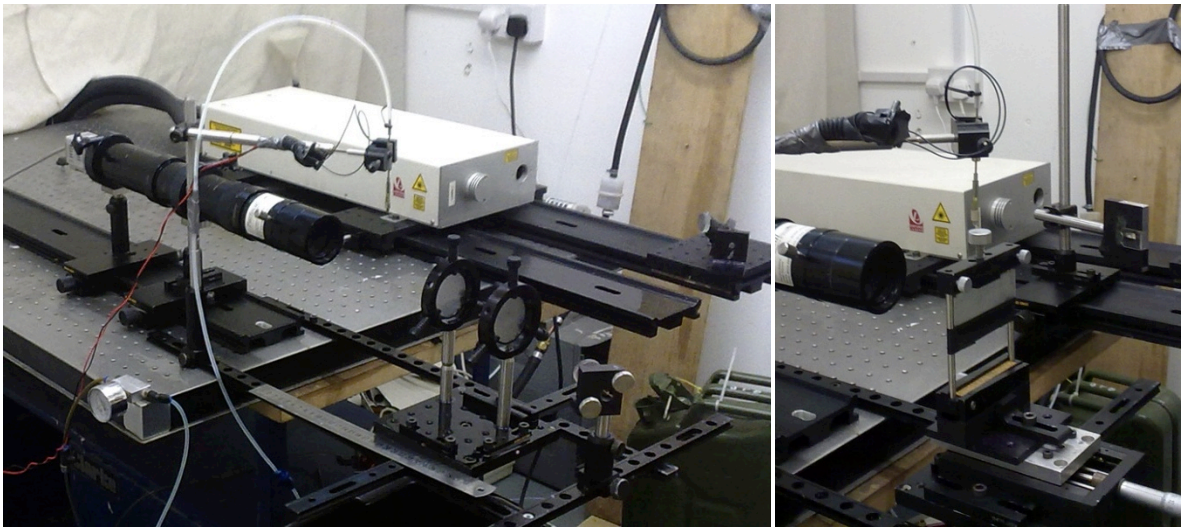

Figure 6.21: The microscopic shadowgraph set-up for imaging the kerosene droplet less than 100 microns in diameter. (Left) the K2 long range microscope with the PCO pixelfly camera fitted in and the light diffusers in front of it; (Right) the calibration plate in front of the microscope.

6.5.2.4. Flow Rate Measurements

The volumetric flow rate of the injectors was measured using a laboratory pipette directly connected to the nozzle exit. The measurements were repeated 10 times for each test point for more accuracy in the volume reading. A pulse train with a predetermined number of pulses was sent to the injector. The flow rate in this case is the measured volume of liquid divided by the time needed to produce that volume as follows:

$$Q_V = \frac{V}{(T_{on} + T_{off})n}$$

Where V is the fluid volume, T_{on} and T_{off} are the opening and closing periods of the valve respectively and n is the number of the injection events. The flow rate was measured for various frequency and duty-cycle values and at different levels of injection pressure.

6.5.2.5. Test Scheme

The following table records a list of the tests carried out for the spray data acquisition.

Table 6.3: A schedule of data acquisition sessions.

No	Test Purpose	Fluid	P (Bar)	f (KHz)	Instrumentation	Location	notes
1	Investigation of Lee injector with three nozzle sizes (127, 190, 250 µm diameter)	Milli-Q (water)	4.2-10	1.4 - 2.2	Nikon D200 + flash gun	Warwick OEL	Pump current ≈ 3.5 A 1 pixel = 1mm
2	Investigation of Lee injector with three nozzle sizes (127, 190, 250 µm diameter)	Milli-Q (water)	1.8-10.2	2.2	Nikon D200 + flash gun	Warwick OEL	8 image/ condition 1 pixel =0.8mm
3	Repeat the Lee injector test for close-up view	Milli-Q (water)	1- 10	1- 3.3	Nikon D200 + flash gun	Warwick OEL	1 pixel =63 µm Flash power= 1/2 - 1/64
4	Flow Rate measurement for Lee injector	Milli-Q (water)	10	1.4-2.8	MCU + volume measure	Warwick OEL	
5	Flow Rate measurement for Lee injector at different duty cycles	Milli-Q (water)	10	2.2	MCU + volume measure	Warwick OEL	Duty cycle: 12.5% - 87.5 %
6	Investigation of IWP023 gasoline injector	Milli-Q (water)	1- 5	0.1-0.31	Nikon D200 + flash gun	Warwick OEL	Driving circuit was developed 1 pixel= 95 µm
7	Evaluation of the laser imaging system for of IWP023 injector sprays.	Milli-Q (water)	1-5	0.1-0.31	PCO pixelfly + Nd:YAG laser+ MCU	Warwick OEL	Light scattering images

8	Evaluation of the laser system using double-pulse mode (droplet tracking).	Milli-Q (water)	3	0.2	PCO pixelfly + Nd:YAG laser+ MCU	Warwick OEL	Matlab correlation software is used.
9	Evaluation of the microscopic imaging system of IWP023 injector sprays.	Milli-Q (water)	5	0.2	PCO pixelfly + Nd:YAG laser+ K2 microscope + MCU	Warwick OEL	Double images are acquired with 25 µs delay.1 pixel = 5.5-3.95 µm
10	Testing the new MCU software for better time accuracy.	Milli-Q (water) + JP8	5	0.2	PCO pixelfly + Nd:YAG laser+ K2 microscope + MSP430 MCU	Warwick OEL	Double images are acquired with 10- 4 µs delay. 1 pixel = 5.5- 3.95 µm
11	Testing the PC-control box along with the YAPP software as control environment for the entire system	Milli-Q (water) + JP8	5	0.2	PCO pixelfly + Nd:YAG laser+ K2 microscope + PC control Unit	Warwick OEL	Time response for the lasers was calculated
12	Macroscopic data Acquisition of IWP023 injector sprays using high res camera.	JP8	1-5	0.15-0.4	PCO 2000 + 55mm lens+ Nd:YAG laser+ PC control Unit	Cubewano	Double images are acquired with 30 µs separation.
13	Macroscopic data Acquisition of IWP023 injector with heater matrix fitted on.	JP8	1-5	0.15-0.4	PCO 2000 + 55mm lens Nd:YAG laser+	Cubewano	
14	Investigation of the spray development process during the injection event.	JP8	1-5	0.15-0.25	PCO 2000 + 55mm lens+ Nd:YAG laser+	Cubewano	Images at specific instants after start of injection
15	Investigation of the droplet size for IWP injector family.	JP8	1-5	0.15-0.25	PCO 2000 + K2 microscope+ Nd:YAG laser+	Cubewano	

16	Testing multi-orifice IWP injectors (spray development & droplet size)	JP8	1-6	0.25	PCO 2000 + 55mm lens+ PCO pixelfly camera+ K2+ Nd:YAG laser	Cubewano	Temporal resolution for spray progress = 50 µs
17	Microscopic characterisation using micro-shadowgraph for IWP sprays	JP8	1-6	0.25	PCO2000+ Nd:YAG laser+ K2	Cubewano	Microscope resolution ≈ 1.1 µm/pixel
18	Visualisation of the spray pattern and droplet scattering, using the Lee injector with new atomiser (nozzle) design	JP8	1-5	0.25	PCO 2000 + 55mm lens+ PCO pixelfly camera+ K2+ Nd:YAG laser	Cubewano	Long exposure time was used for spray pattern
19	Microscopic characterisation using micro-shadowgraph for the Lee atomiser	JP8	1-5	0.25	PCO pixelfly camera+ K2+ Nd:YAG laser	Cubewano	Microscope resolution ≈ 0.9 µm/pixel

6.6. Image Processing

The majority of the image-processing tasks were carried out using Matlab programming language. In addition, LaVision DaVis software was used for PIV analysis. In the spray pattern investigation, images were loaded to the program,[1] and then a processing window within the image was defined in order to reduce the processing time by removing the unimportant parts of the image. The mean image was then calculated at each test point.

[1] The size of the images needed to be read in Matlab at the same time was too big creating an internal memory problem in the software, so that images were loaded in groups and then erased from the memory once moving to the next test condition.

The contrast was enhanced by applying a 2D median band-pass filter so that the peripheral particles became sharper, which helped in the calculation of the spray cone-angle. From the high-contrasted image, the binary (black-and-white) image was generated by applying a manually defined threshold. Then, the gaps between spray elements were filled up using a filling up function, which takes a filling-up decision at each pixel according to the status of the neighbouring pixels.

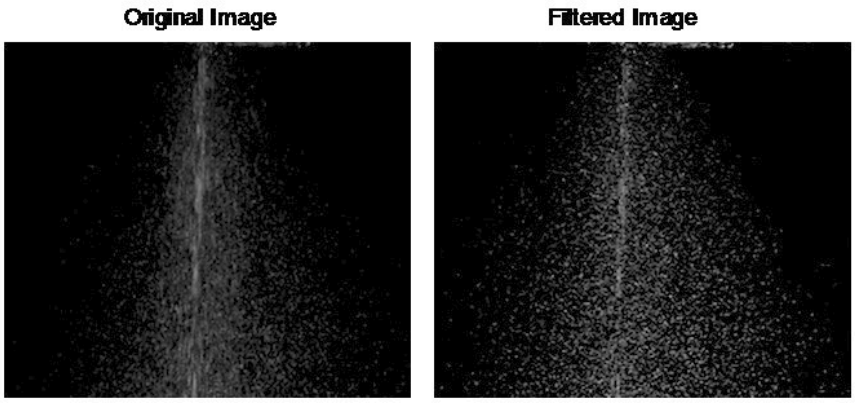

Figure 6.22: High contrast binary image is generated by applying median band-pass filter and then a 4.7% threshold.

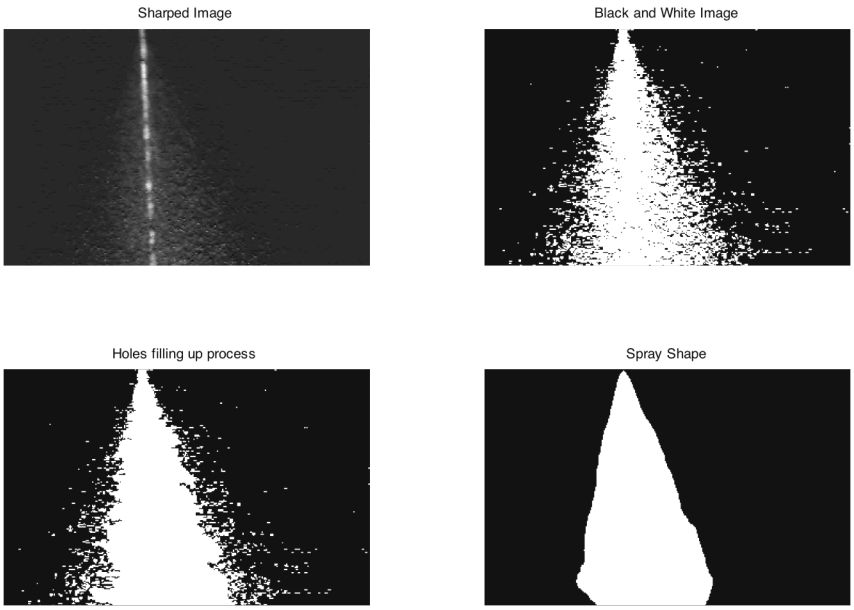

Figure 6.23 Stages of image processing for the extraction of the spray pattern. Another example of a gasoline injector less density spray in appendix 6.5.

An edge detection procedure was performed afterwards, which eliminates isolated droplets and tracks the counters of the spray pattern. A median filter is finally applied for smoothing out the hard edges. This process is repeated for different test conditions.

6.6.1. Discrete Cosine Transform (DCT) in Spray Analysis

2D discrete cosine transform (2D- DCT) was applied on the spray pattern images for a numerical representation of the spray sheet area. The DCT has wide applications in image and video compression. The DC coefficient of the transformed image contains the "image energy" and corresponds to the overall light intensity received by the camera sensor [Tjahyadi, *et al.* (2004)]. The DC coefficient is associated with the average brightness of the entire image matrix, while the rest of the AC coefficients depend on the deviations from that average [Seibt (2006)]. The DC coefficient was used to compare between the droplet density distributions of different sprays.

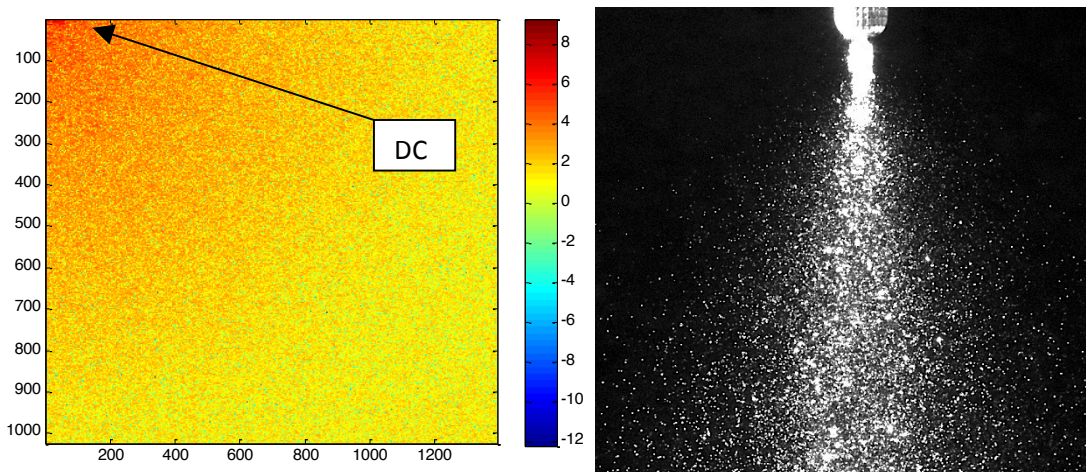

Figure 6.24: 2D-DCT transformation for a fuel spray image (colour bar is in logarithmic scale), the injector here is the Lee medical dispenser provided by the 062 MINSTAC atomiser.

The DCT is used as a low-pass filter by setting the AC coefficients with high amplitude into zero, leaving only information that have high deviation from the average image. This is

useful in reducing the power of the bright areas in the image, thus making the peripheral droplets sharper. It was also found that the right sittings of the “cut-frequency”/ threshold can generate an image containing only the on-focus droplets (see Appendix 6.6).

6.6.2. Principal Component Analysis in Spray Disintegration Detection

Principal Component Analysis (PCA) is a multivariate statistical technique that extracts the most important data amongst a massive amount of data. Images are data arrays where each point represents a grey grade value, and PCA can reduce the dimensionality of the data set into a smaller number of independent variables. PCA has been used recently in data face recognition and data compression applications due to its ability to remove the redundancy in the data.

PCA was used in the current project as an indicator for the similarity between images taken under the same conditions by calculating the covariance matrix. The greatest variance by the data comes on the first principal component (first coefficient), whereas the low-order components contain the low frequency features of the data. The images data were reshaped from the original 2D form into vectors (rows) where the columns, in this case, represent the repetition of the experiment. In PCA, images should be centred by subtracting the mean image from each of them.

The idea was that the images of the well-atomised fluid would have less similarity between them, and therefore less correlation, while the fluid jet may show far less differences during the first few microseconds after injection before disintegration. Similarly, nozzles that produce sprays with a poorly atomised central jet would have a high correlation factor. The principal components, therefore, can be used as an indicator for the atomisation quality in the time scale during the injection cycle.

6.6.3. Shadowgraph images processing

The field of view of the microscope was approximately (1.231 mm x 0.906 mm), providing a maximum resolution of 885 nm per pixel, which is considerably higher compared to the published work in the fluid microscopic shadowgraphs (16.5 microns per pixel in [Jiang et al.(2010)], 7.1 in [Esmail et al. (2010)], and 5.6 in [Berthoumieu et al.(1999)]). The minimum number of pixels considered to resolve a single droplet was 4 pixels (around 3.45 μm). Only droplets smaller than 100 μm were included into the diameter distribution calculations due to the small number of larger droplets detected by the microscope. The background image was subtracted from each data image to eliminate the effect of the light profile in the background and any permanent mark on the microscope. The particle sizing routine was then called for each image, which locates the connected objects in the image and label them. The inputs of the particle sizing routine were the image array and its resolution. The outputs were the diameter array, number of detected droplets, the mean and median diameters, and the standard deviation. A “fill up” function was then used to cover up the gaps sometimes created because of the light beam partly penetrates through the transparent drops. The area of each connected object was calculated, and then the corresponding diameter was derived, meaning that the results show the diameter of the closest sphere to the detected shape of the droplet (Equivalent Spherical Diameter (ESD) method). This routine was repeated for all images at each test position, and the results were accumulated in the diameter array. The overall arithmetic mean and Sauter mean diameters are then calculated, and the diameter probability distribution is presented using distribution histograms.

6.6.4. PIV analysis

Double images were processed to produce velocity vector field of the spray, using particle image velocimetry (PIV) via LAVision Davis 8 platform by applying cross-correlation function on image pairs. The pre-processing procedure included energy correction and intensity normalisation (Figure 6.25).

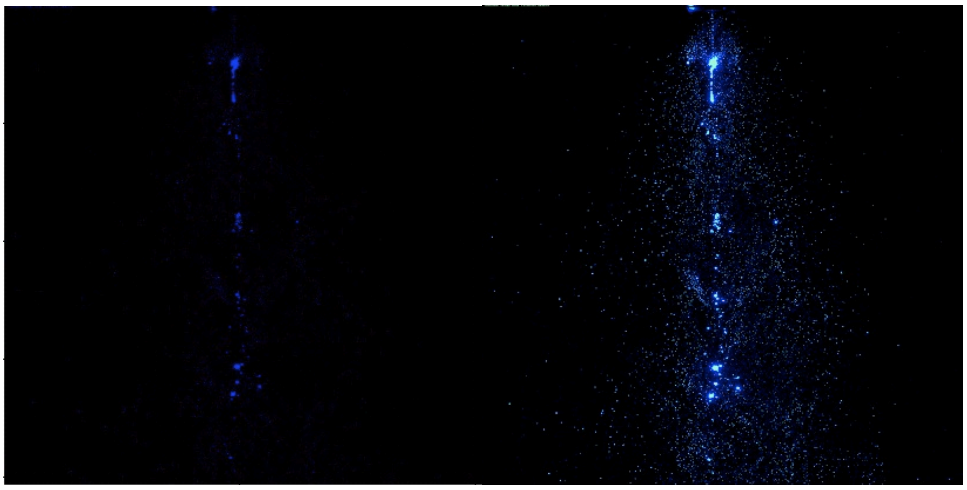

-a- **-b-**

Figure 6.25 PIV pre-processing; (a) original image (b) energy corrected normalised image.

Two stages of image multi-pass (2D) cross-correlation were used, in which the interrogation window of the second stage was smaller than that of the first one. The widow size is dependent on the spray density, and therefore on the image resolution. Bigger windows were used in the microscopic images (resolution less than 8 microns per pixel) than in the macroscopic images (resolution more than 30 microns per pixel). The displacement in a certain window between two images was represented by the maximum correlation which provides the length and direction of the displacement vector.

Chapter7. Results and Discussion

This chapter demonstrates the main findings of the current research. The first part shows results related to the fuel spray analysis in both macroscopic and microscopic ranges. The spray pattern and cone-angle are derived from the global spray images using image-processing techniques (see tests no.10, 11, 12, 13, 16 and 18 in Table 6.3). The spray development process in the temporal domain is investigated using images acquired by synchronising the imaging system with the fuel injector (see tests no.14-16 in Table 6.3). The PCA technique is suggested as an indicator for a spray degree of disintegration (atomisation quality) at different moments after the start of injection. Shadowgraphs are used in section 7.5 for calculating the droplet size (probability) distribution (see tests no.15-19 in Table 6.3). PIV analysis of the fuel spray for both the global view and the microscopic range is presented using the double-exposure data (see tests no.12, 13, 16, 18, and 19 in Table 6.3).

The second part of this chapter (section 7.8) demonstrates the results of applying the Mie scattering theory on sub-micron fluid droplets (see chapter 5) generated by a smoke generator. Oil smoke is used for seeding a jet flow in a stereoscopic PIV system. The results show the effect of the relative angle between the camera line-of-sight and the laser-sheet on the scattering efficiency, and therefore on the brightness balance between the cameras. The correlation quality between images produced by two cameras is evaluated for different seeding particles.

7.1. Introduction

Optical diagnostics were developed to evaluate fuel injectors prior to application in a rotary engine design. The objective was to investigate the global characteristics of fuel sprays (tip-penetration, development-velocity, overall area, and density distribution). Droplet size distribution was carried out to assess the efficiency of the atomisation process in producing small droplets (less than 5 microns). Two injector families were evaluated: (1) the IWP standard gasoline injector (a single-hole and a four-hole), and (2) the Lee injector (Section 6.2.1).

Two types of spray visualisation have been applied, as presented in the previous chapter: (1) a direct visualisation of the whole spray surface using a conventional camera and flash-gun (section 6.4), and (2) a laser based sheet interrogation (section 6.5) which 'cuts a slice' through the spray profile. Both techniques have benefited from the low-density nature of the spray. In particular, the laser light-sheet method showed a little evidence of multiple particle light scattering.

The direct imaging approach was used for the initial assessment of the fuel injection systems. The spray cone-angle was directly measured from the spray images. At low pressure using a long exposure (typically 50 - 60 μs), the injection spray cycle was visualised as a series of fluid segments (Figure 7.1). This showed the atomisation process over a number of cycles in one frame. As the pressure increased, the images showed that the atomisation started earlier during the injection cycle, and the spray size became larger than the lower pressure case.

The direct imaging method provided a general view of the spray pattern and the effect of the operation parameters on that pattern. However, when precise results in the temporal domain were required, the laser-sheet method was applied.

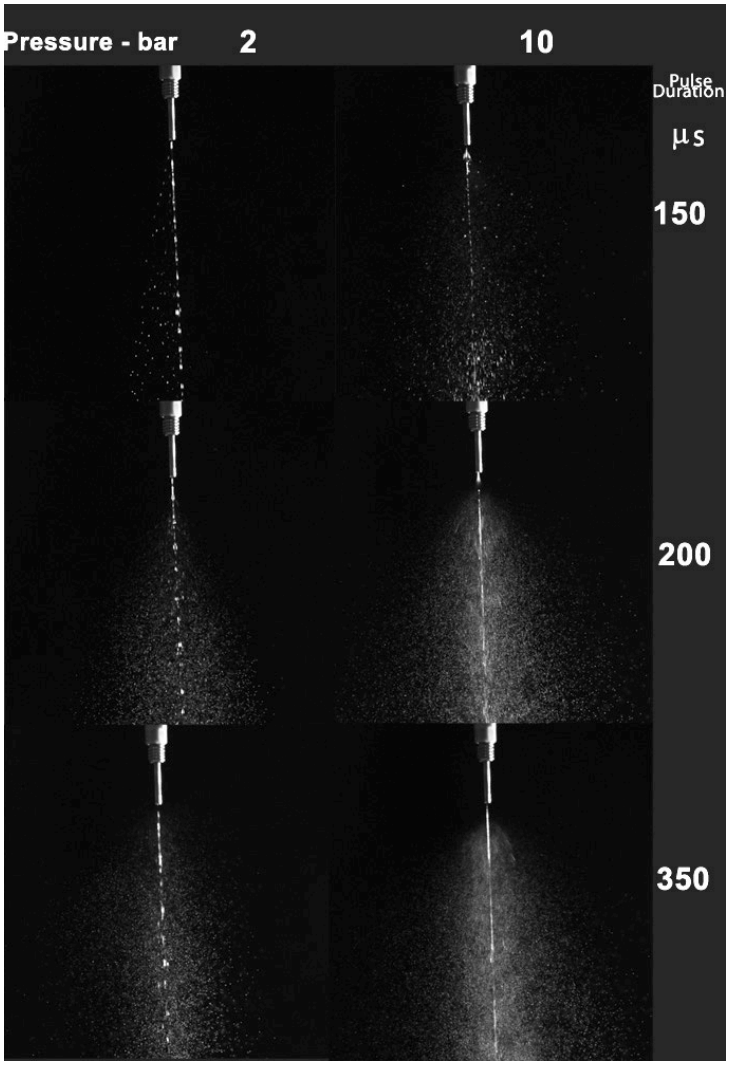

Figure 7.1: Raw Images for sprays generated using the Lee injector (D_0 = 125 µm, long nozzle; L_0= 8.8 mm) using direct imaging method for several injection pulse-width and pressure values. Flash light pulse duration = 56.2 µs.

The laser sheet method confirmed the results found using the global spray characteristics, such as spray-sheet area and cone-angle with the following differences:

1. The accuracy of the laser method was higher due to the larger number of samples obtained using an automatic trigger system. A mean spray distribution pattern could be made over several exposures. Typically this number was 4 to 8 images for the direct imaging approach, compared to 200 - 500 images in the laser sheet case.

2. The laser sheet focuses on a short depth of field (1-3 mm), which reduces the effect of the defocused droplets.

3. The optical instantaneous power of the laser is higher than the standard flash-gun. As a result, smaller droplets can be resolved, especially in the case of the microscopic imaging.

4. The direct imaging is a simpler approach to apply, but it provides less quantitative information of the spray development process.

5. PIV is only possible using the short laser pulses in the double-pulse mode.

6. Mie scattering analysis is only possible using the laser beam, due to its monochromaticity and well-defined scattering directionality.

The direct imaging method, therefore, provides an initial qualitative understanding of the fuel. But for the purpose of quantitative measurement, the laser-sheet method is a superior approach. The following findings are the result of the experiments performed on the fuel injection systems using the laser-sheet method. The results of applying the light-scattering theory on sub-micron seeding particles are presented in section 7.6.

7.2. Spray Pattern

7.2.1. Mean Image and Spray Pattern Model

A spray pattern shows how fluid droplets distribute in a given space. It shows the size, density and uniformity of a spray.

The mean-image of the overall spray view was produced by overlapping a number of instantaneous images together (500 images per test condition). The mean-image represents the likelihood of having a droplet at any point within the field of view. Figure 7.2 shows fuel sprays generated by two different IWP gasoline injectors (D_0=584 microns). The first was a single-hole nozzle, and the second was a four-hole nozzle. The colour-coded image shows the brightness level of the pixels, and therefore the optical energy received by the image sensor. It was found that the fluid density of the first atomiser (Figure 7.2- A) is very high in the central jet, decreasing gradually towards the peripheries. In the second nozzle (Figure 7.2- B), however, the central jet has almost vanished, and the droplets distributed over a larger area than in the first nozzle. This suggests that the multiple-hole nozzle produces sprays with a more uniform density distribution than the single-hole nozzle. An assumption can be made that the lower light intensity levels in the peripheries are generated droplets small compared with the central jet. In order to confirm this initial reading of the mean-image, a further investigation into the spray development process with time domain was made.

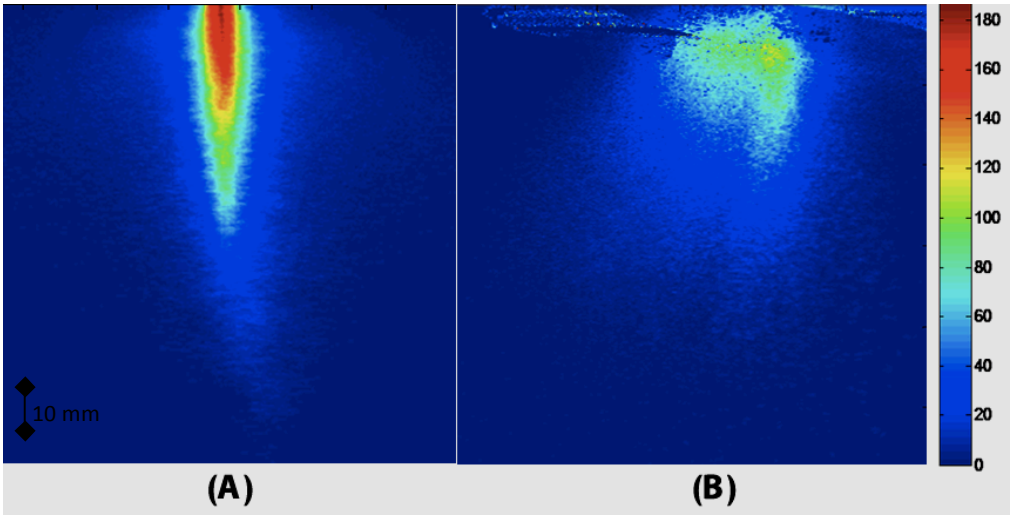

Figure 7.2. Spray intensity map using image overlapping (mean-image); the test fluid is Jet-A fuel at 5 bar pressure and injection period of 2 ms. (A) single-hole gasoline IWP injector; (B) four-hole IWP gasoline injector.

7.2.2. Spray-Sheet Area and Image Energy

Two numerical factors were used for comparing different spray patterns. The first was the geometric 2D-area. This was calculated by applying a threshold on the mean-image, to produce a binary image. The spray area is the summation of all the binary pixels, multiplied by the actual pixel size. Figure 7.3 shows a kerosene spray area against the differential pressure, generated by processing 500 images per condition.

This geometric area factor provides an indication of the spray size, without information about the droplet distribution in space. Accordingly, sprays with different densities may have the same detected area.

The second factor was the overall energy of the mean-image. This factor is the average of all pixels in one image, represented by the DC coefficient of the discrete cosine transform. It provides an indication of the total surface-area of all the fluid droplets.

Both factors can be used to characterise the spray. The geometric area is dependent on the spray dispersion angle and it represents the area of space within which the spray is likely to spread. However, it does not provide any particle density information. The image energy factor, on the other hand, is associated with the light scattering intensity, which can be considered proportional to the droplet diameter squared (d^2) in the Mie region (d>> 160 nm in the case of 532 nm laser). Therefore, the second factor (the image energy) provides a better representation of the overall surface-area-to-volume ratio, since it is associated with the spray droplet density (image energy ~ $\sum n_i.d^2_i$).

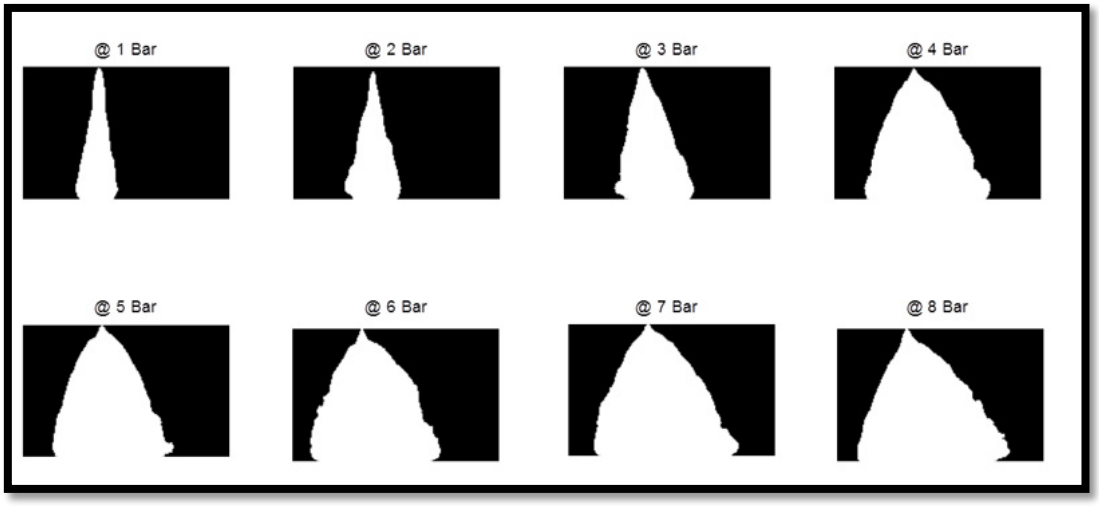

Figure 7.3 Processed images of kerosene sprays generated by the Lee injector, using long nozzle (L= 8.8 mm, D= 125 µm), showing the pressure effect on the spray pattern.

Figure 7.4 shows the pressure response of a standard gasoline injector "IWP023" using the spray geometric area and the image energy. Both factors steadily increased as the injection pressure increased. The effect of the pressure was lower when it exceeded 4 bar. The comparison between the two factors (see Figure 7.4) shows that the pressure effect is higher on the spray area than on the image energy. This is because the spray area calculation procedure treats all pixels equally by binarising them, while pixels have different

energy profile in the image energy case (depending on the droplet diameter). This example shows that increasing the injection pressure has a larger impact on the spray size than on the surface-area-to-volume ratio.

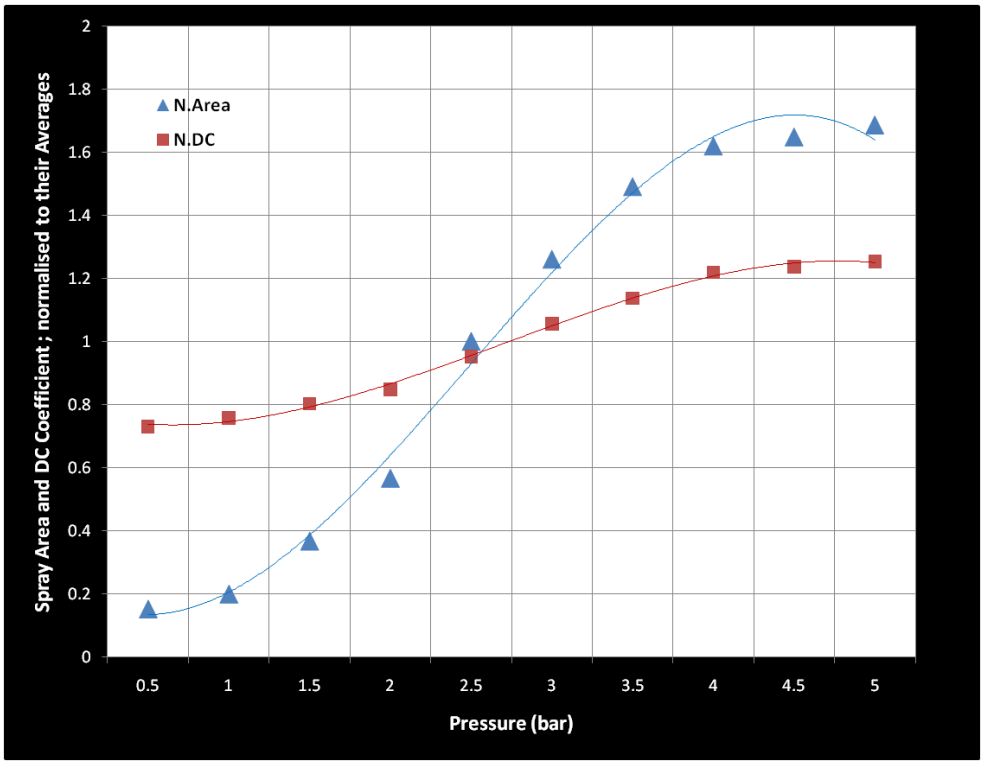

Figure 7.4 Normalised spray sheet area and DC coefficient against the differential pressure for the IWP023 gasoline injector at 280 Hz.

7.2.3. Spray Pattern Detection Using Prolonged Exposure

Using the laser-sheet method, it was possible to capture instantaneous images during the injection cycle. This temporal information was advantageous for the analysis of the spray development process. However, for the general pattern view of a spray, the short pulse-width of the laser requires a large number of samples in order to accumulate a statistically acceptable result.

It was found that the data size and processing time can be considerably reduced by using a long exposure time (0.5-1 sec). This was carried out by including a predetermined number of injection events into a single photo frame. Figure 7.5 shows two raw images taken for a fuel spray produced by a multi-orifice injector (IWP, 4 holes). The first image was captured using 0.6 sec exposure time at an injection frequency of 250 Hz. The second image shows a single injection event taken 3.2 ms after the start of injection.

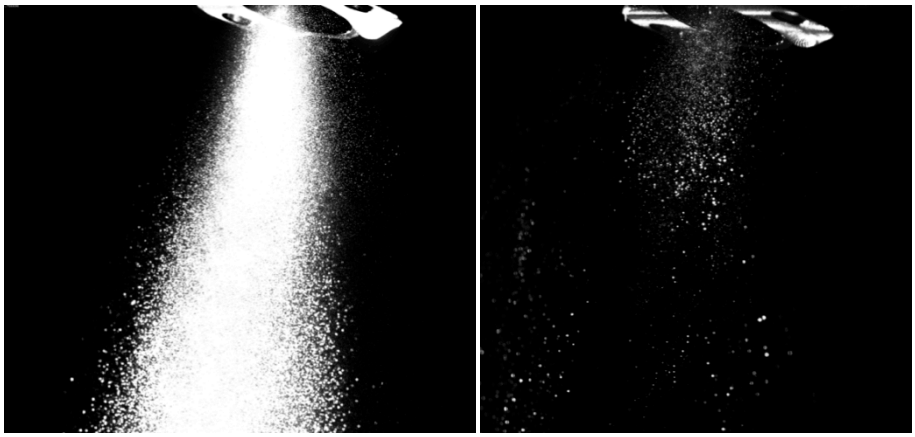

(a) **(b)**

Figure. 7.5. Raw images of the kerosene spray produced by a multi-hole (4) EFI at fuel pressure equals 5 bar; (a) long- exposure method for shape detection exp=0.6 sec, $f_{(laser)}$=20 Hz, and (b) instant imaging of the same spray at the moment 3.2 ms ASOI using a single pulse (5 ns).

7.2.4. Spray Cone-Angle Calculation

The calculation of a spray cone-angle was based on the "near-field angle" and "far-field angle" definitions (chapter 2), at distances equal to $60D_0$ and $100D_0$ from the nozzle tip, respectively (D_0 is the nozzle diameter). Figure 7.6 shows a sample of the angle calculation process using Matlab.

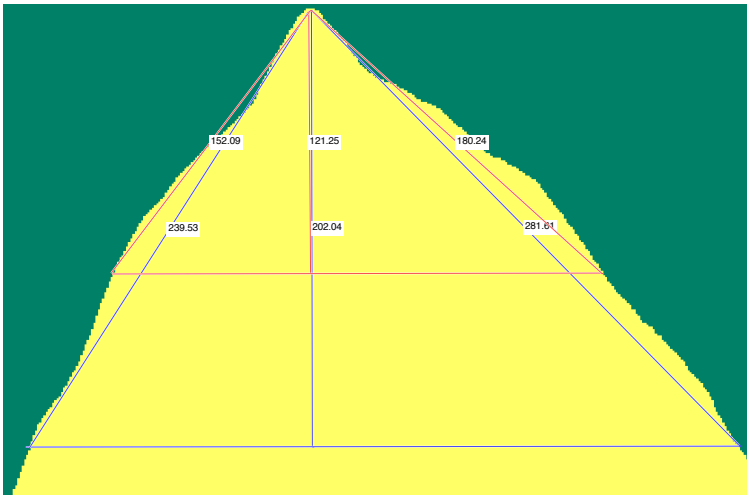

Figure 7.6 Calculation of a spray near-field angle and far-field angle; D_0= 125 µm (the Lee injector).

7.2.4.1. Spray Angle Against Differential Pressure

The injection pressure was considered to have the main effect on the spray angle in the initial analysis. By increasing the pressure the fluid discharge velocity increases. However, there is a limit where increasing the pressure has no further effect on the spray angle. Moreover, increasing the injection pressure higher than that limit for some injectors can reduce the spray cone-angle. This can be explained by the connection between the fluid pressure and the injection frequency.

The process of the fuel injection involves a pulsed discharge of the fluid, rather than a free (static) flow. As a result, the higher the injection pressure, the higher the load on the internal needle of the injector, which slows the (frequency) response of the electromagnetic mechanism of the injector. For this reason, the spray profile calculation has taken account both of the fluid pressure and injection frequency.

Figures 7.7 and 7.8 present the angle calculation results for both the medical (Lee) and the gasoline (IWP) injectors, respectively (noting that the maximum operation pressure

for the first injector is 10 bar against 5 bar for the second). The results reveal that the most effective pressure region in increasing the cone-angle was between 2-4 bar. The near-field angle was generally larger than the far field angle for both nozzles, the fact which agrees with the results reported in the fuel injection literature.

The Lee injector produced wider angles than the IPW023 injector for the same pressure levels, mainly because of the difference in the nozzle diameter (see Appendix 7.1 for the Lee 062 MINSTAC atomiser angle calculation).

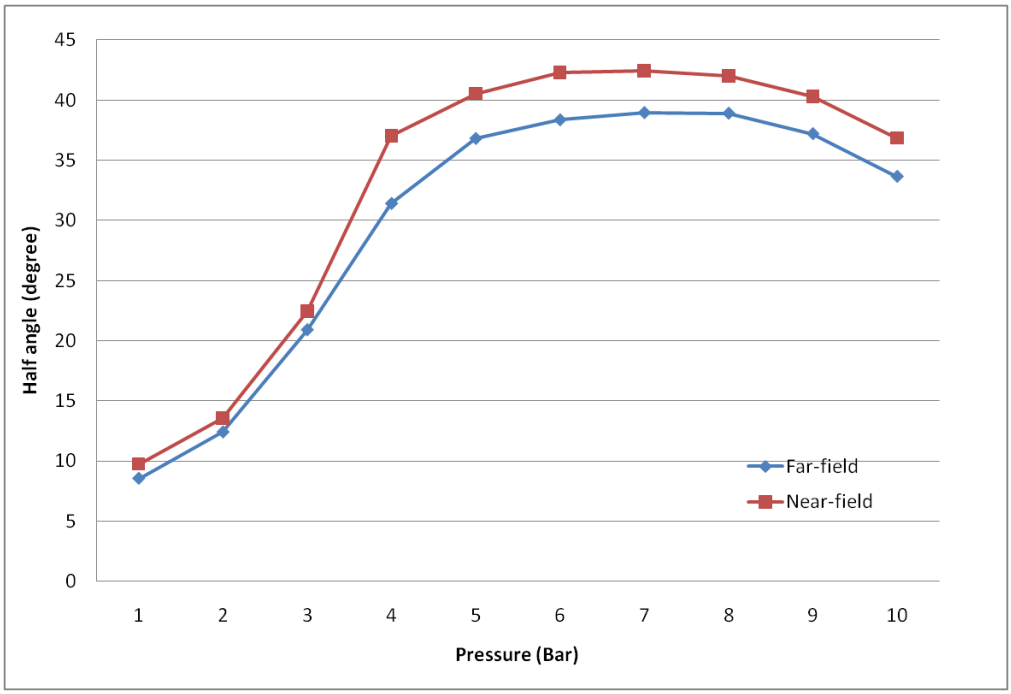

Figure 7.7 Spray (half) angle against differential pressure; Injector Lee medical injector (Jet-A spray); f= 2 kHz, D_0= 125 µm (plain orifice nozzle).

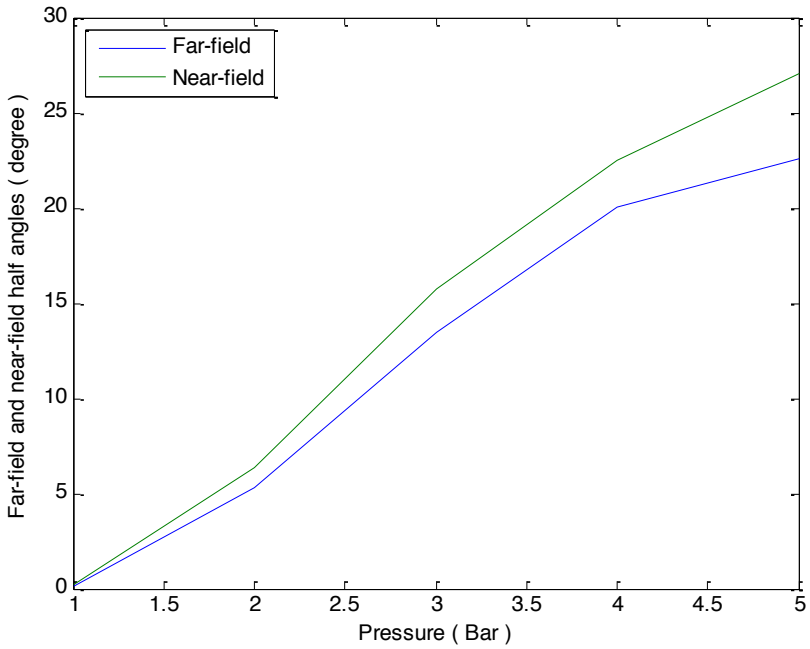

Figure 7.8 Spray (half) angle against differential pressure; Injector IPW023 gasoline injector (Jet-A spray); D_0= 584 µm, measured at 280 Hz injection frequency.

7.2.5. Spray Profile of the Lee Injector Using the MINSTAC Atomiser

The end-nozzle of the Lee injector was modified (by the manufacturer) to improve the fluid atomisation quality. The original Lee nozzle was a metallic plain orifice. The relatively high length to diameter ratio of these nozzles (L/D ≈ 70 - 390) negatively affected the atomisation quality, especially at low pressure levels. The new "062 MINSTAC" atomiser had a low length to diameter ratio (L/D ≈ 25, see Figure 6.7).

Using the new nozzle (Figure 7.9), it was possible to distinguish between the primary and secondary atomisation areas in the spray image. The spray profile had the shape of a hollow-cone next to the nozzle exit, with 11-13 disruption waves on the surface. The spray sheet started disintegrating approximately 5 mm downstream of the nozzle exit.

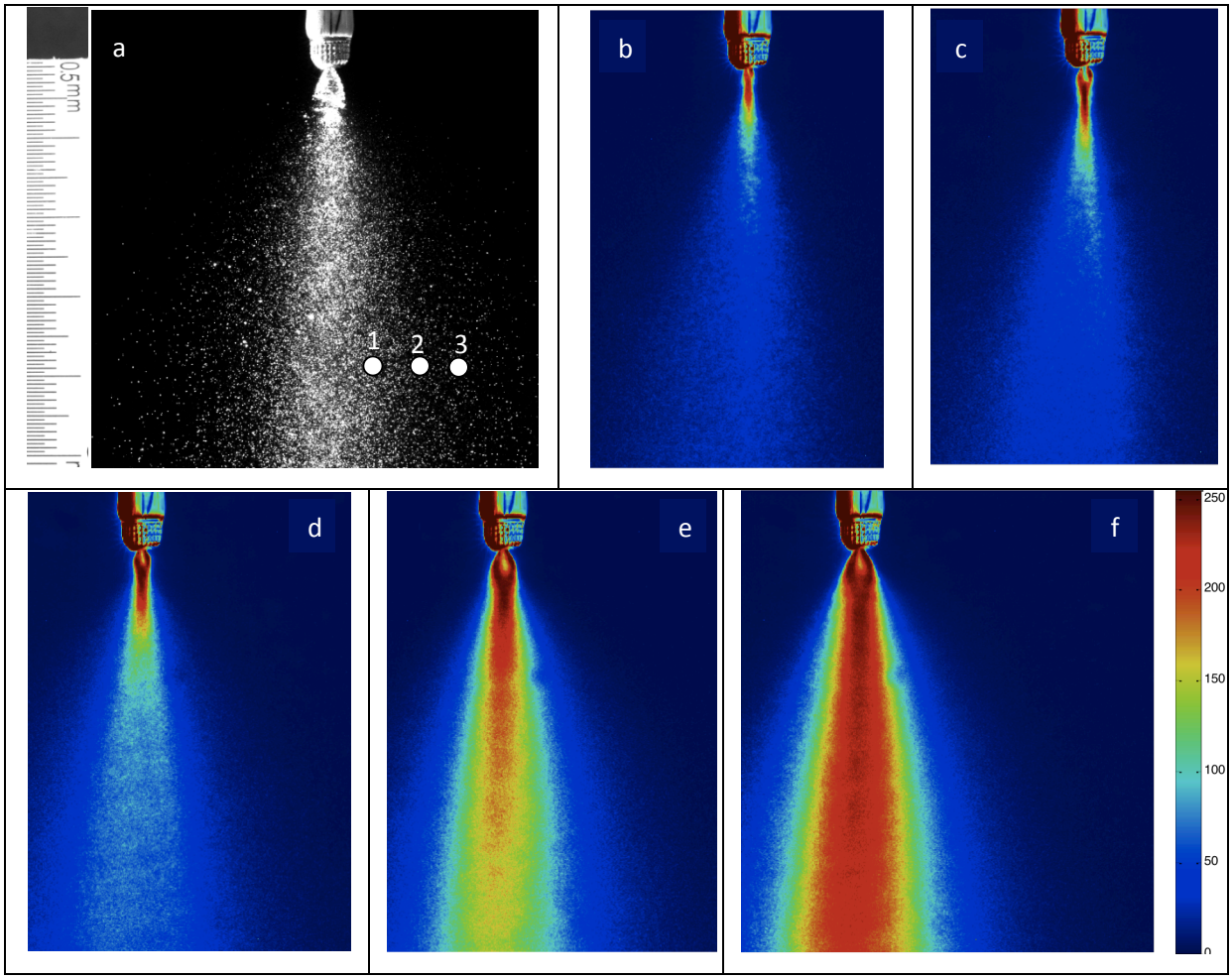

Figure 7.9 The pressure effect on the sprays produced by the Lee injector with the MINSTAC atomiser fitted in; a. The raw image sample of the spray using a prolonged exposure (laser sheet imaging, see Appendix 7.2 for a higher resolution) showing the three points where the particle measurements were carried out, b. spray density map at 1 bar pressure, c. 2 bar pressure, d. 3 bar pressure, e. 4 bar pressure, f. 5 bar pressure.

The connection between the injection pressure and frequency was investigated as shown in Figure 7.10. The differential pressure ranges between 1 and 10 bar, and the pulse duration ranges between 250 and 500 µs (50% duty cycle). The graph shows that the size of the spray stopped increasing when the fluid pressure exceeded 8 bar for all frequencies. The size of the spray then started to decrease due to the load applied on the valve needle inside the injector. Therefore, applying a high pressure decreases the injector ability to respond to the electromagnetic field in its coil, until it stops completely at a "cut-off" pressure.

For the same pressure level, increasing the injection frequency had a positive effect on increasing the spray surface size. This was explained by the improvement in the atomisation quality as a result of the high speed movement of the injector's valve. In addition, an instant drop in the pressure occurs during the long injection period, which is faster than the reaction of the fuel pump in maintaining a constant pressure.

Similarly, when the injection exceeds a critical top frequency, the response of the electromagnetic mechanism gradually declines until the valve fails to open due to the saturation of the current-coil. A frequency-band was determined for the optimum operation of the injectors. It is worth mentioning here that, for some injectors, a very low frequency could heat up the injector and cause permanent damage.

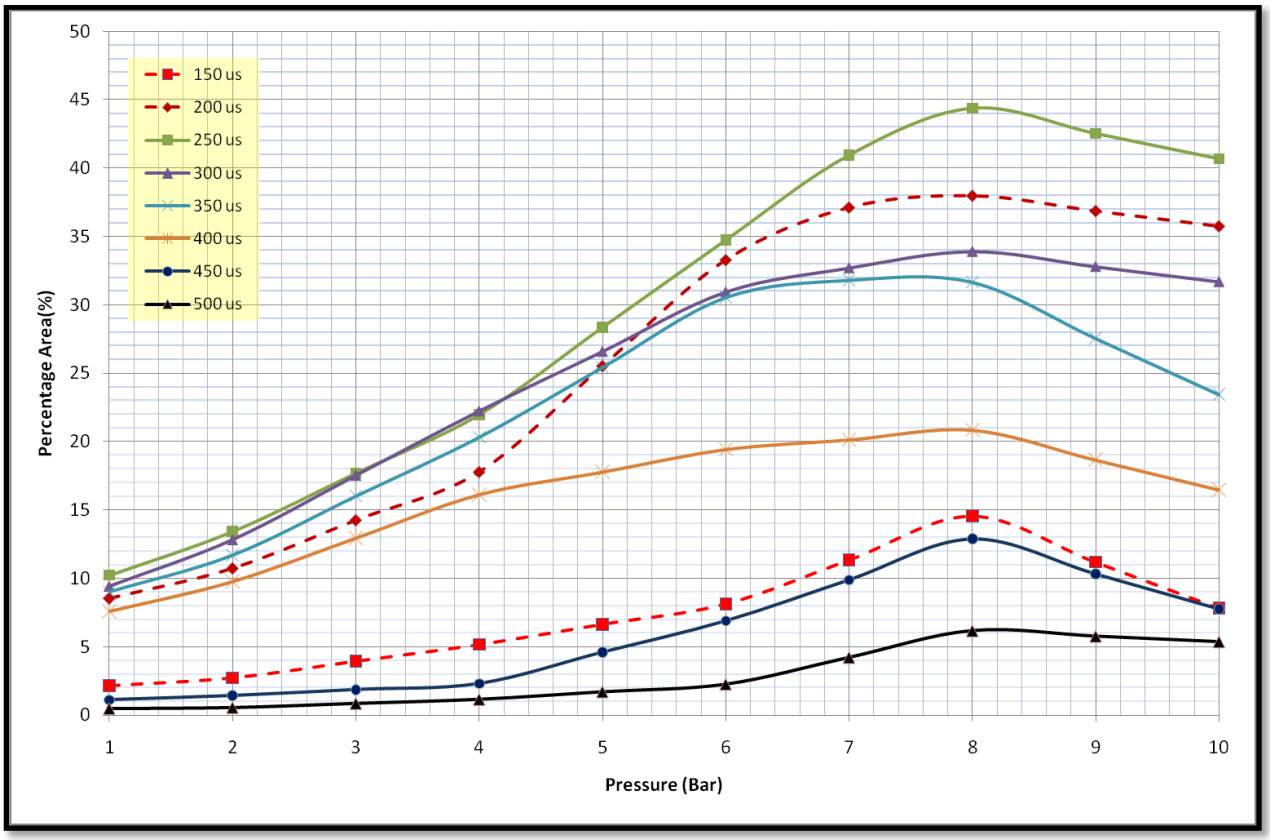

Figure 7.10: Percentage area (the ratio of the spray area to the overall size of the determined window) against the differential pressure for different injection pulse durations.

7.3. Spray Development Process

7.3.1. Spray Tip penetration and Velocity

The spray development process during the injection cycle was investigated using the laser sheet imaging method. The tip velocity of a spray against time was measured using double-exposure frames with a time interval of 5-50 microseconds. The fuel injector was synchronised with the laser sheet and the camera, using the control system (shown in section 6.5.1.4).

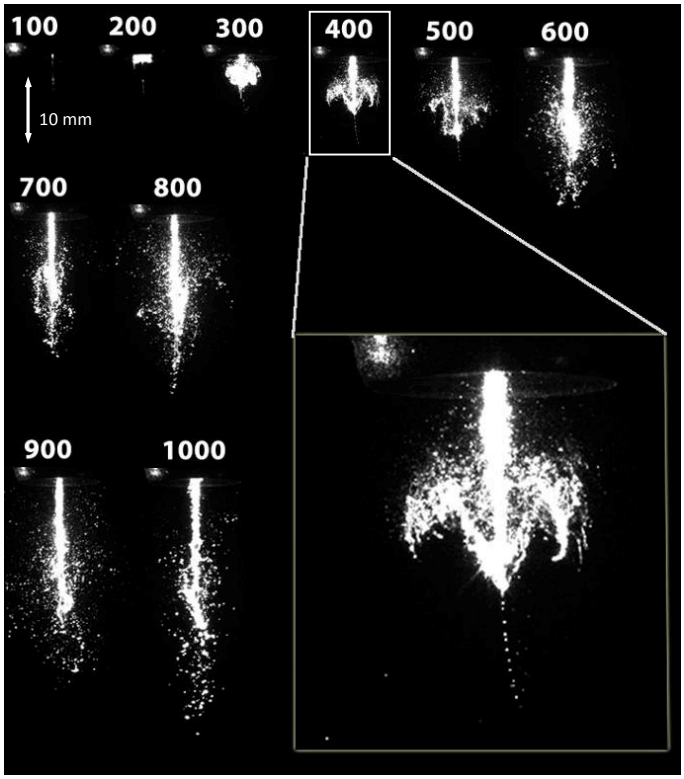

Figure 7.11 Visualization of a fuel jet development during the first millisecond. Particles breakup region is located as well. Time is presented in microseconds. Low injection pressure of 3 bars. Injection pulse-width T_{inj} = 2 *ms*. Atomizer is a single nozzle with a diameter of 584 *μm.*

The images sequence of a single-hole nozzle (IWP023) injector spray (Figure 7.11) showed that the atomisation process started on the jet surface 400 μs after the start of

injection (ASOI). The atomisation in this type of injectors at low pressures (less than 3 bar) was relatively poor. Thus the central jet travelled much faster than the atomised parts in the peripheries. During an injection period of 2 ms, the spray penetrated around 50 mm (vertically downstream of the nozzle) for a 5 bar injection pressure, as shown in figure 7.12. This is compared with a 90 mm tip penetration calculated in [Hwang *et al*. (2003)], using the same injection pulse-width, but much higher differential pressure of 350 bar and around half of our nozzle's diameter.

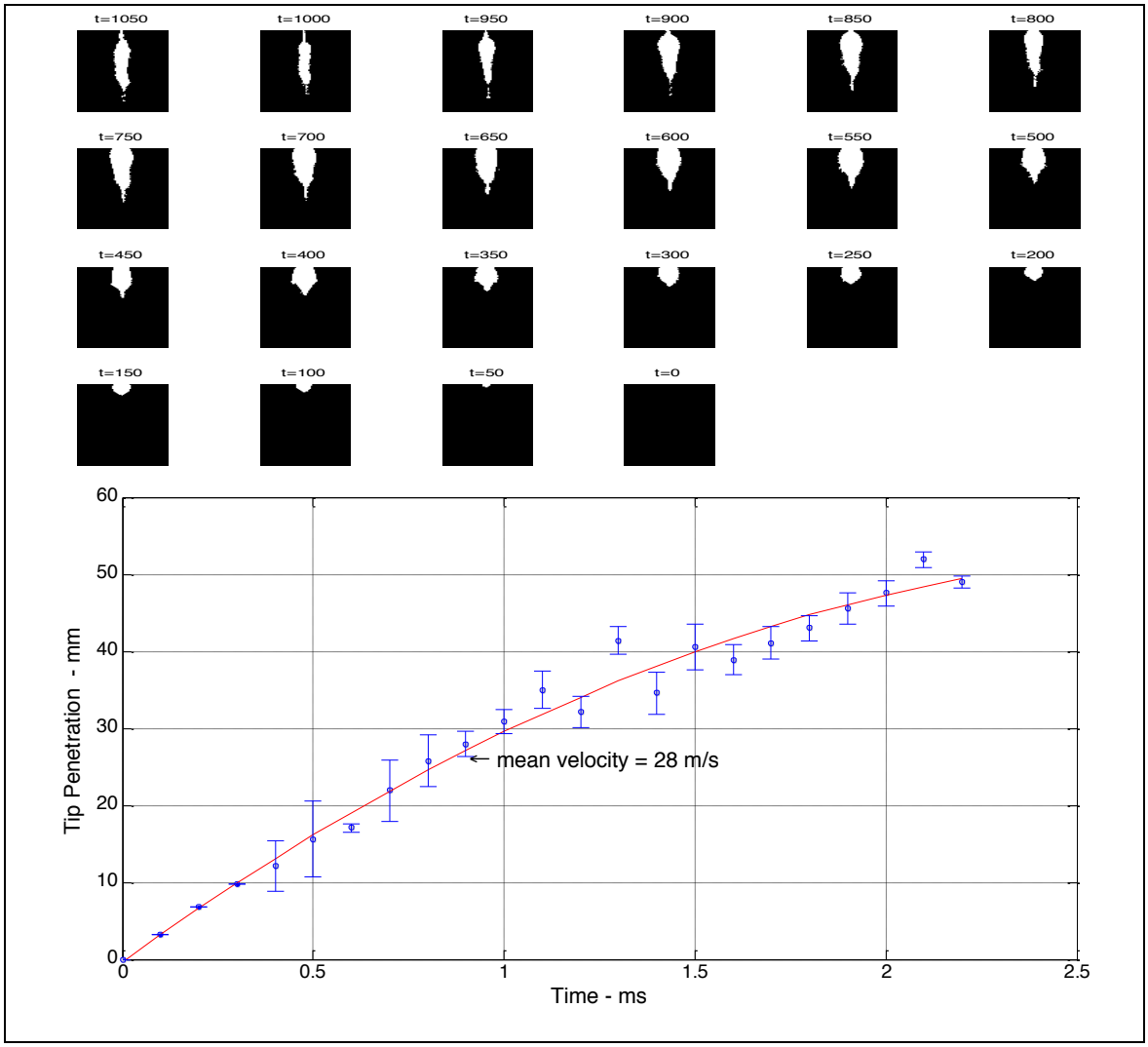

Figure 7.12 The spray development processed images and the tip penetration against time graph (with a second-order polynomial fit) estimating the mean velocity. Injection pulse = 2ms , P= 5 bar using single-hole gasoline injector (D= 584 µm).

An average spray velocity of 28 ms^{-1} was estimated in the single-hole nozzle, compared with a 20 ms^{-1} using the multi-orifice nozzle (4-holes) for the same gasoline injector family (See Appendix 7.3).

The fluid **discharge velocity** is directly proportional to the square root of the differential pressure (formula 2-1). However, increasing the pressure is associated with an increase in the cone-angle and a decrease in the average droplets diameter, which negatively affects the **tip velocity** of the atomised jet.

Figure 7.13 presents the effect of the differential pressure on the tip penetration in the time domain. The penetration graph turned from an exponential-like model, for pressures less than 4 bar, into a logarithmic-like model, for pressures above 4 bar. This can be explained by the changes on the aerodynamic resistance of the surrounding air and frictional losses. The tip penetration at the low pressures (poor atomisation) was mainly driven by the large droplets under the effect of their weight. In the case of high pressure, the spray contains smaller droplets travelling at higher velocity, so the tip acceleration decreased (by the drag force) during the injection cycle.

Other factors, such as the nozzle diameter and the fluid properties, play a role in the determination of the spray tip velocity. Narrower nozzles produced sprays with smaller droplets and wider angles, and thus slower vertical penetration. The kerosene spray was found to penetrate approximately 4% faster than the water spray during the first millisecond of a 2 ms injection cycle for the same nozzle (D_0=125 microns) and the same injection pressure (Appendix 7.4). This is because fluid sprays with lower viscosities normally penetrate faster. However, the PIV comparison between the two liquids shows that the kerosene has higher velocity components upstream (close to nozzle exit), but lower velocity

components downstream. The explanation was that the atomisation is better for the kerosene than water due to its lower surface tension[1]. As a result the kerosene droplets diffused over a wider angle, and the central jet disintegrated earlier during the injection cycle (Appendix 7.9).

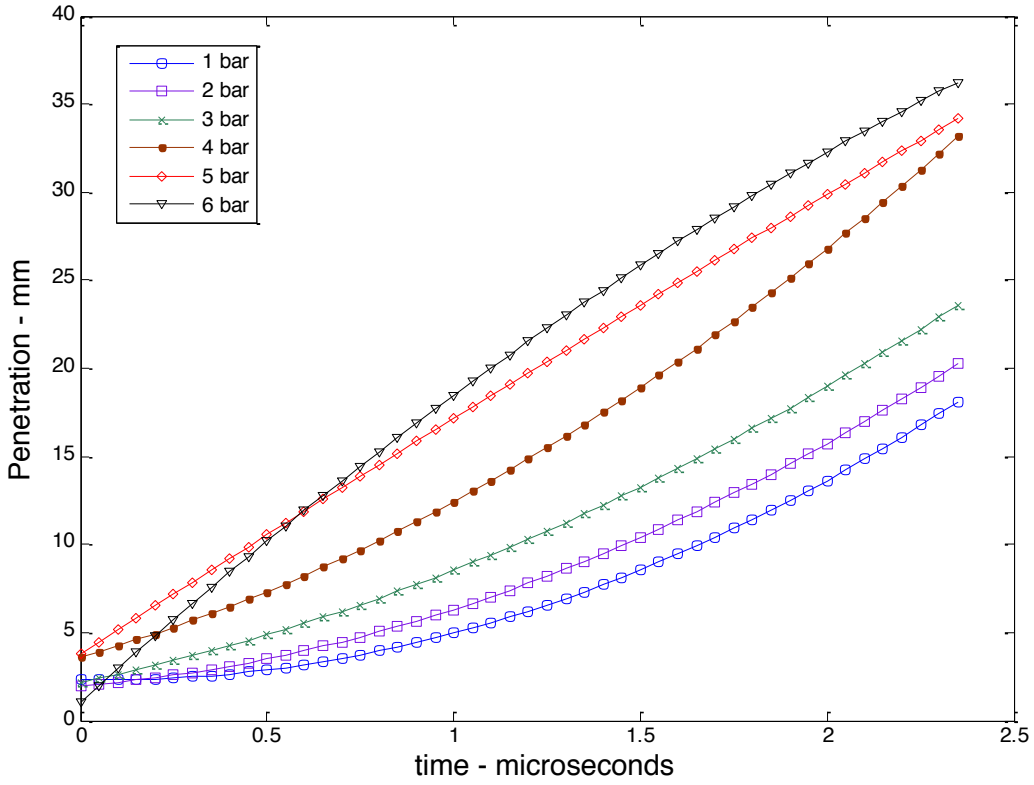

Figure 7.13 Spray jet penetration against time during the first 2.5 ms ASOI of the Lee injector. Spray penetrates faster at high pressure values.

7.3.2. Spray Formation Map

The tip penetration is an important characteristic in the fuel spray analysis, but it does not provide a comprehensive representation of the spray development process during the injection period. Therefore, a spray formation map was produced to illustrate the changes in the spray sheet area against time in the real dimensions.

[1] surface tension effect is more noticeable at low injection pressures[Lefebvre (1989)]

The map (Figure 7.14) suggests that the fluid jet was mainly integrated in one bulk during the first 0.5 ms (ASOI). This was followed by a fast fragmentation of the fluid until approximately 1.5 ms (ASOI); this period can be considered as the "primary atomisation" stage. Afterwards, the spray size increased slowly and the fluid density decreased gradually during the secondary atomisation stage. The tip penetration was faster during the primary atomisation than during the secondary atomisation due to the higher momentum of the fluid jet before the atomisation.

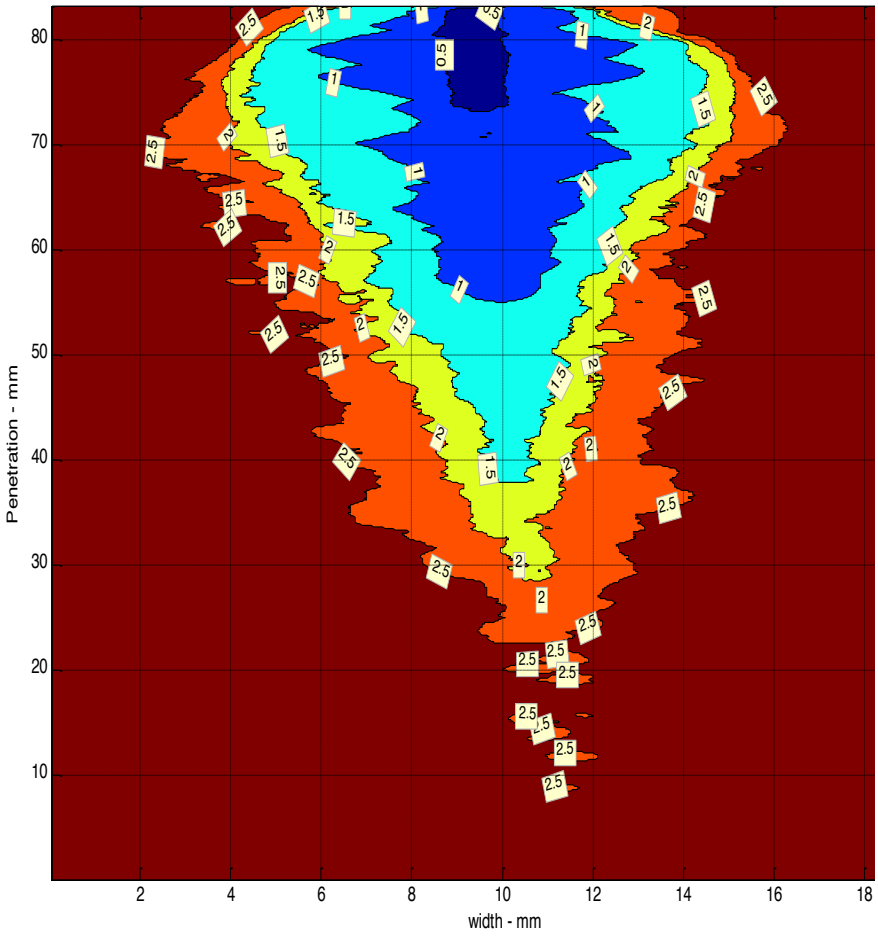

Figure 7.14 Kerosene spray formation map for the contours of the single-hole gasoline inject IPW023 at 5 bar differential pressure; dimensions are in millimetres; numbers inside the graph represents time in milliseconds (ASOI). Injection pulse-width T_{inj} = 2 ms. The density map of the same injector was shown in Figure 7.2(A); for the multi-hole injector (Figure 7.2 B) and the Lee atomiser samples see Appendix (7.5).

This map presents an individual injection event of a 2 ms injection-pulse. When several pulses were included in the formation map, low weight droplets by the previous injection events added new elements to the spray pattern. This increased the width of the spray jet downstream of the nozzle exit. The velocity difference between the central jet and the surrounding low-weight droplets gives the spray its cone-like shape (similar to the one captured by the long exposure photography). Appendix 7.5 shows the formation map of a spray jet during the first 5 ms (ASOI), including 2 injection cycles (2ms each with 1 ms resting time between them).

The spray-sheet area against pressure was previously measured using a number of pulses independently from the time (section 7.2.2). Here, the mean value of the spray sheet area was calculated in terms of the time (ASOI) and injection pressure (Figure 7.15). The spray size always increased as the time (ASOI) and pressure increased, unless it exceeds the cut-off maximum pressure.

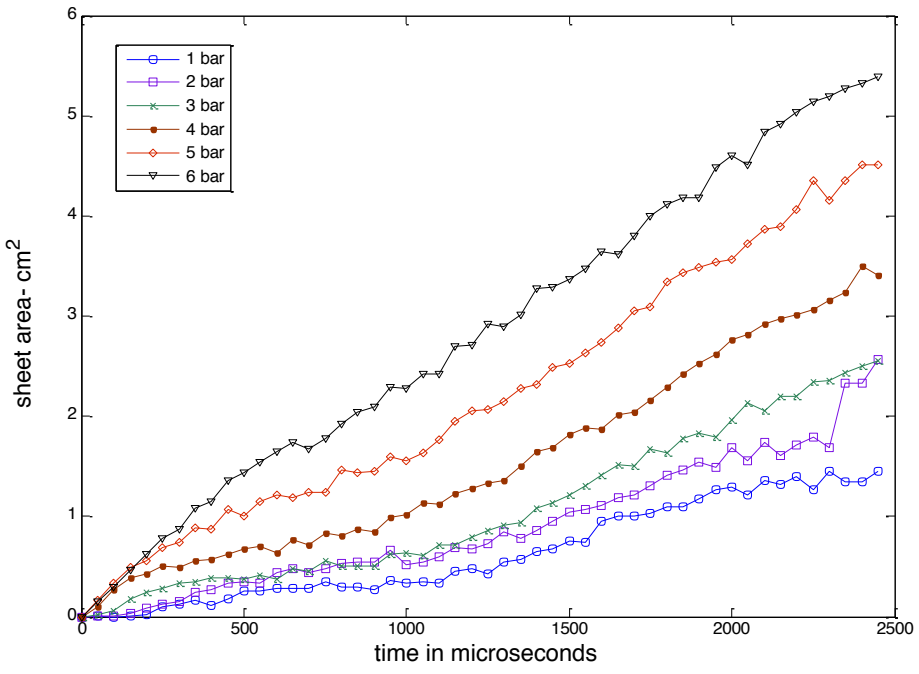

Figure 7.15 Kerosene spray sheet area against time ASOI for pressure range (1- 6) bar.

7.3.3. PCA Indicator for Fluid Disintegration

The principal component analysis (PCA) method was applied to produce a numerical indication of the fluid disintegration process. This method investigates the similarity in spray images taken for the same time delay settings (ASOI) using several injection events. The degree of disintegration of fuel sprays in the time domain is important for the optimum injection-ignition timing. The PCA indicator, therefore, can provide an indication of the atomisation quality for different nozzles and under different operation conditions.

The first PCA component in this case reveals the level of similarity between images, and the higher order components increase as the variation between the images increases. Well-atomised fluid images have less similarity in pattern than poorly atomised fluids. Figure 7.16 shows the component score for the first five components of the PCA for t=0.4 ms and t=0.6 ms (ASOI). The first component in this case declined from 84% at 0.4 ms to 73% at 0.6 ms, and reached 58% when the central jet started disappearing after 1.6 ms (ASOI). By the end of the injection pulse, the variance between the images became larger, so the high order components became more dominant.

A global overview of the fluid break-up stages was obtained by plotting the first PCA component against time (Figure 7.17). During the first millisecond of the injection pulse, the similarity in the spray pattern steadily declined due to the primary atomisation and the disintegration of droplets from the jet surface. The correlation factor reached 60% by the end of the first millisecond.

The declining speed of the correlation factor reflects the efficiency of the atomisation process. Figure 7.18 shows the break-up rate of a fuel spray during the first 400 microseconds of injection, using a temporal resolution of 50 μs.

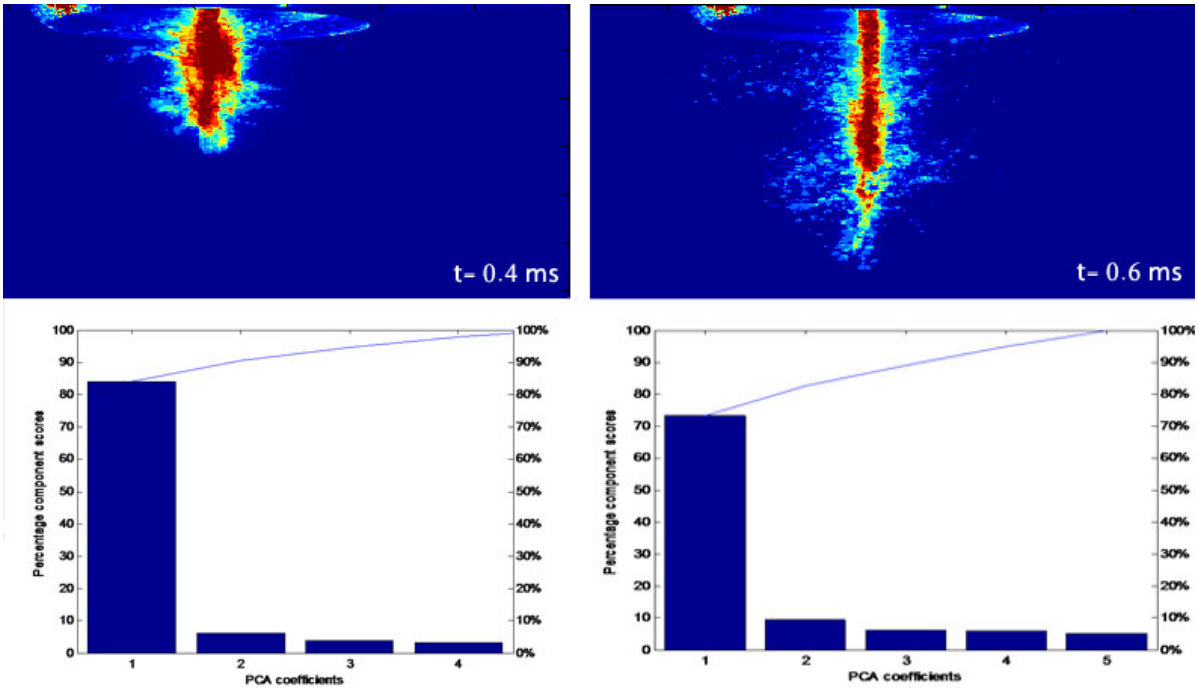

Figure 7.16 PCA scores for the first 5 components at 0.4 and 0.6 millisecond (ASOI), 5 bar pressure, T_{inj} = 2ms, D_0= 584 µm.

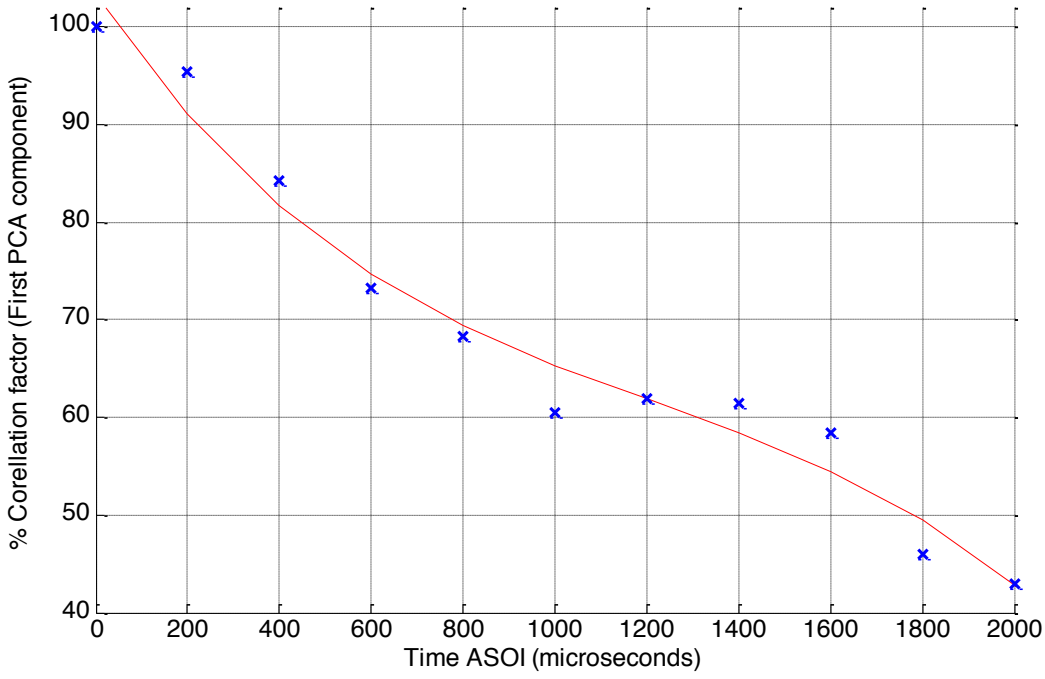

Figure 7.17 The first PCA component against time after the start of injection; fluid pressure= 5 bar, T_{inj} = 2ms, time step = 200 µs.

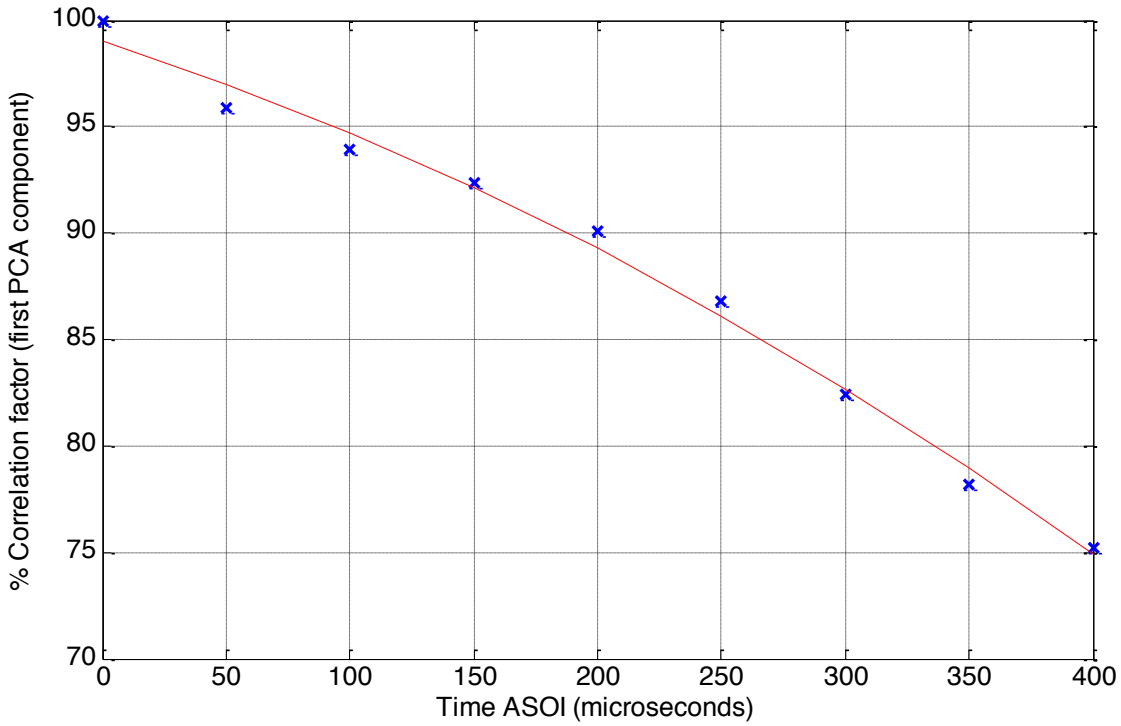

Figure 7.18 The first PCA component against time during the first 400 µs after the start of injection; fluid pressure= 5 bar, T_{inj} = 2, time step = 50 µs.

7.3.4. Spray Breaking up on a Solid Surface

The spray pattern of the conventional gasoline injector IWP023 showed a poor atomisation rate in the central jet due to its relatively wide orifice (D_0= 584 µm) and low operation pressure. The fuel delivery rate measurements showed that nearly 40% of the fluid was found in the centre of the spray jet in less than 20° of the spray cone. The suggested solution for improving the fluid atomisation in this case was by introducing a metallic sharp surface (1.5 mm 90° edge hoax key) in front of the nozzle exit.

The surface was mounted approximately 2 cm downstream of the nozzle exit, so that the high density (central) components of the spray hits it approximately 900 microseconds after the start of injection at 5 bar pressure. This allowed breaking up the central jet with a minimum interference with the wide angle droplets produced by the primary atomisation.

The density distribution map suggested that a better atomisation was produced by the sharp surface at the late stages of the injection cycle. This can be seen by the increase in the spray surface area and the wider distribution of the fluid for the same injected volume of fluid. The PIV analysis showed that introducing a solid surface has created droplets with higher velocity in the different directions than in the original case, the fact which increases the disturbance of the flow downstream of that surface (see Appendix 7.8).

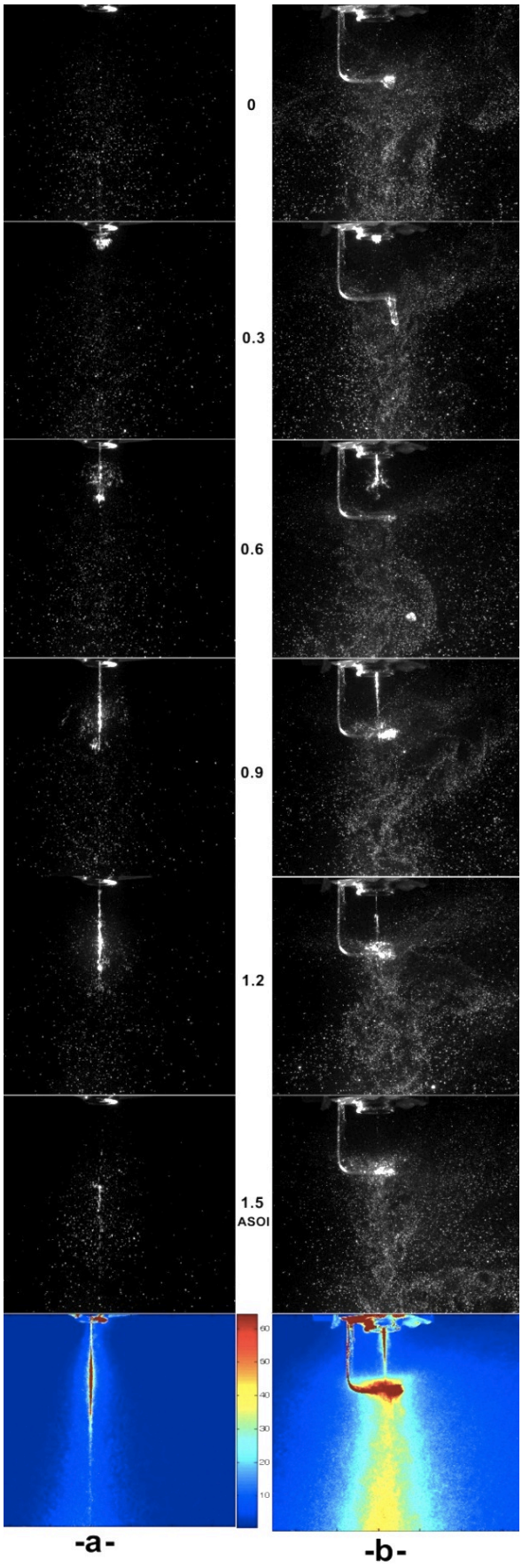

Figure 7.19 Spray breakup process on a sharp surface (time is in milliseconds after start of injection), and the colour-coded mean images; (a) without the surface, (b) with the surface.

7.4. Flow Rate Calculations

The volumetric flow-rate was calculated against the injection frequency (pulse-width), duty cycle (on/off ratio) and fluid pressure. The initial results on the Lee injector, using a plain orifice nozzle (D_0= 125 µm, L= 8.8 mm) at 5 bar pressure, showed that changing the frequency has a little effect on the flow rate. If an injector has a stable response throughout the frequency range of the experiment, then in theory the amount of discharged fluid using a certain number of pulses should not change whether it is injected rapidly (high frequency) or slowly (low frequency). In practice, the flow rate was noticed to decrease for frequencies higher than 1.8 kHz, as shown in Figure 7.20.

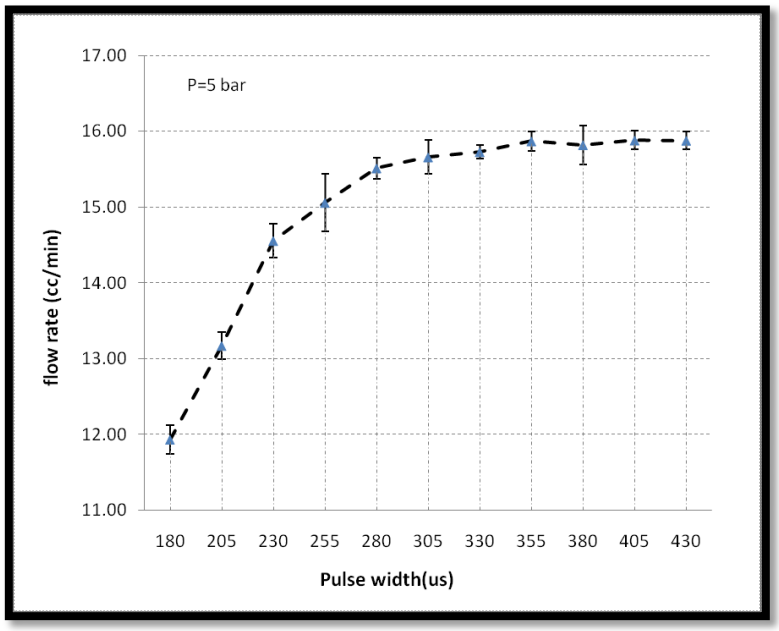

Figure 7.20 The flow rate of the Lee medical dispensing setup for 5 bar differential pressure. Each point represents 50000 injection events at the corresponding pulse width (duty cycle 50%).

The engine was operated using various duty cycle settings. The duty cycle was usually adjusted between 50% (2 ms open and 2 ms closed) and 25% (1 ms open and 3 ms closed) for 15000 rpm rotational speed. The relation between the flow rate and the duty

cycle appeared to be nearly linear, as shown in Figure 7.21. A similar effect was found for the duty cycle on the Lee atomiser flow rate (Appendix 7.6). The calculations also showed that the flow rate was proportional to the operation pressure. Table 7.1 shows a comparison between the conventional gasoline injector (IWP23 Pico injector) and the Lee atomiser (both for JP8 fuel):

Table 7.1 Flow rate comparison between the conventional gasoline injector IWP023 and the Lee medical injector with the new MINSTAC atomiser.

	Q (cc/min) at 3 bar	Formula (Linear approximation)[1]	D_0 (µm)	f (Hz)
IWP023	66.43	Q(cc/min)= 4.35 (ΔP) + 38.39	584	240 (50%)
Lee + MINSTAC	19.50	Q(cc/min)= = 4.8(ΔP) + 6.6	125	500 (50%)

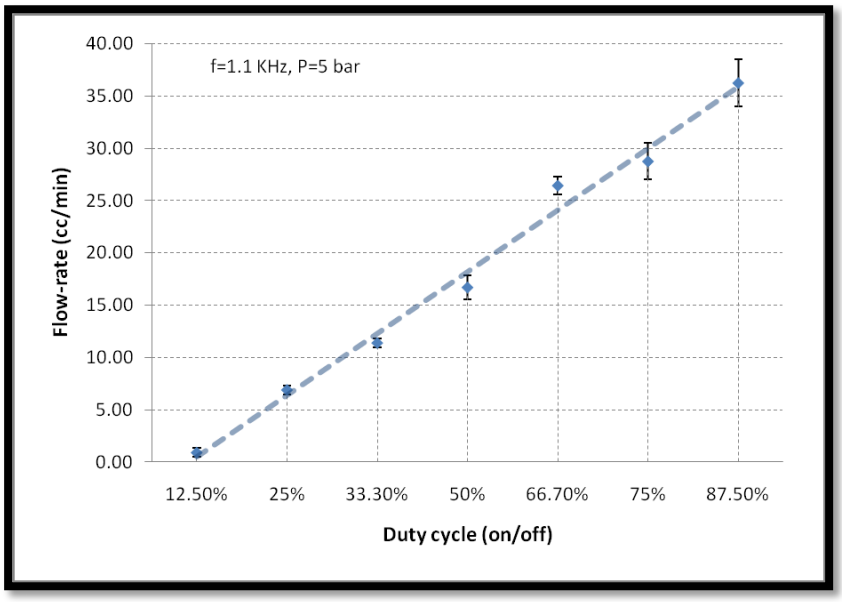

Figure 7.21 The flow rate of the Lee medical dispensing setup for 5 bar differential pressure against the duty cycle ratio.

A static flow rate of 158 cc/min at 3 bar is reported in the IWP023 injector

[1] For the gasoline IWP023, the approximation: Q (cc/min) = 37.15 $(\Delta P)^{0.3266}$ was better than the linear one.

manufacturer datasheets, against 66.43 cc/min calculated in laboratory using pulsed injection at 240 Hz (50%) for the same pressure level. The comparison between one minute of a static flow and two minutes of a pulsed flow (50% duty-cycle) showed that the flow rate of the injector was 16.5% higher in the case of the static flow (with 2% standard deviation). The flow-rate of the IWP gasoline injector was roughly four times higher than the Lee atomiser; the nozzle diameter of the latter is approximately 4.5 times smaller.

The comparison between Figure 7.22 and Figure 7.23 leads to the conclusion that the conventional gasoline injector always provides a higher flow rate through its valve than the Lee injector for the whole pressure range (the Lee valve can operates at higher frequencies), even though the Lee injector generates wider angles and larger sheet areas. This can be only explained by the fact that **the Lee micro-injector is a better atomiser, producing sprays with larger surface areas than the conventional injector that uses less amount of fuel.**

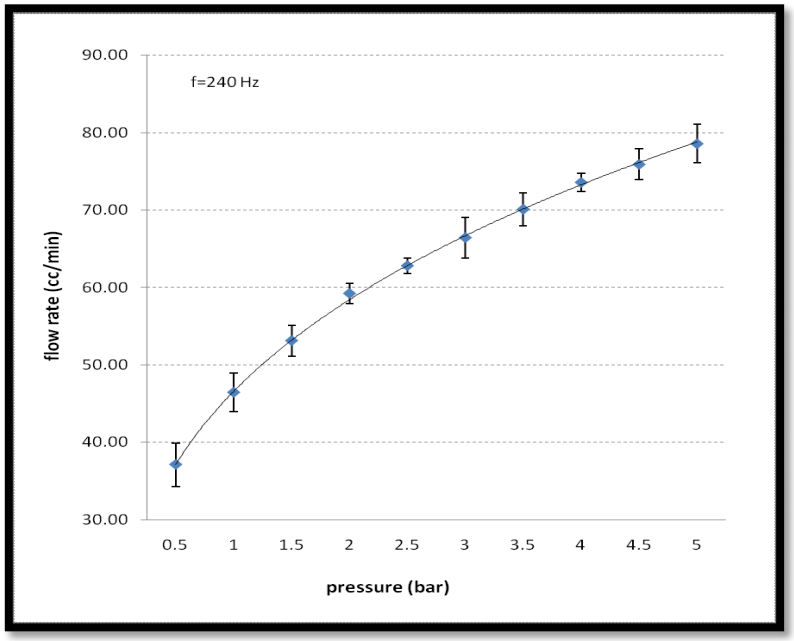

Figure 7.22 The flow rate against pressure for IWP023 conventional gasoline injector at 240 Hz injection frequency.

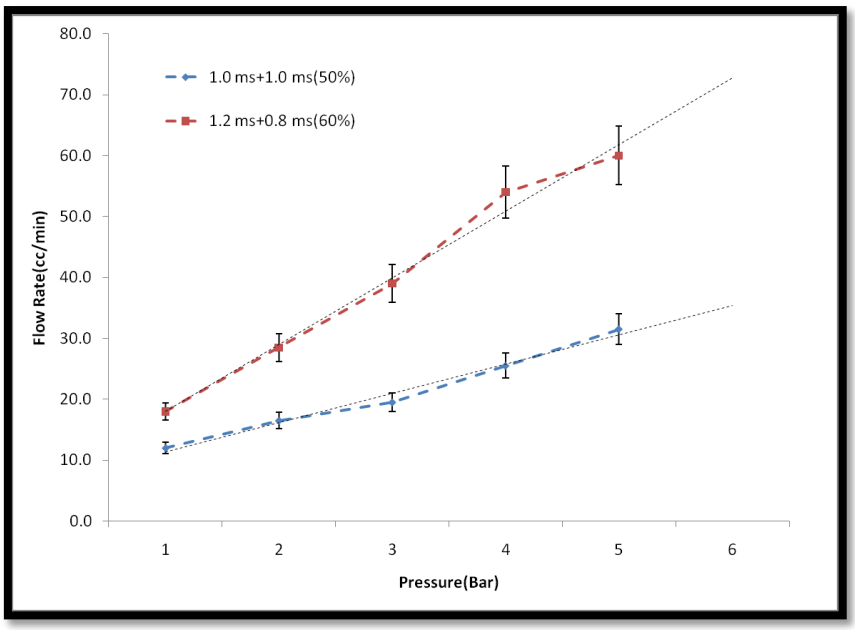

Figure 7.23 The flow rate against pressure for the Lee medical injector provided with the MINSTAC atomiser (D_0=125 µm at 500 Hz injection frequency). The effect of the change in the duty cycle from 50% to 60% is presented.

7.5. Droplet Size Distribution

Microscopic shadowgraphs were used for obtaining the droplet size distribution by performing a direct droplet count and classification within a small field of view (chapter 6). It was possible to obtain highly contrasted images for resolving fluid droplets by generating a homogeneous back-illumination. Figure 7.24 shows (part of) two raw shadowgraph images taken for different nozzles. The total number of detected droplets per test condition (500 images) was 20,000 to 62,000 droplets, depending on the pressure and point of observation. The number of droplets per frame increases as the injection pressure increases.

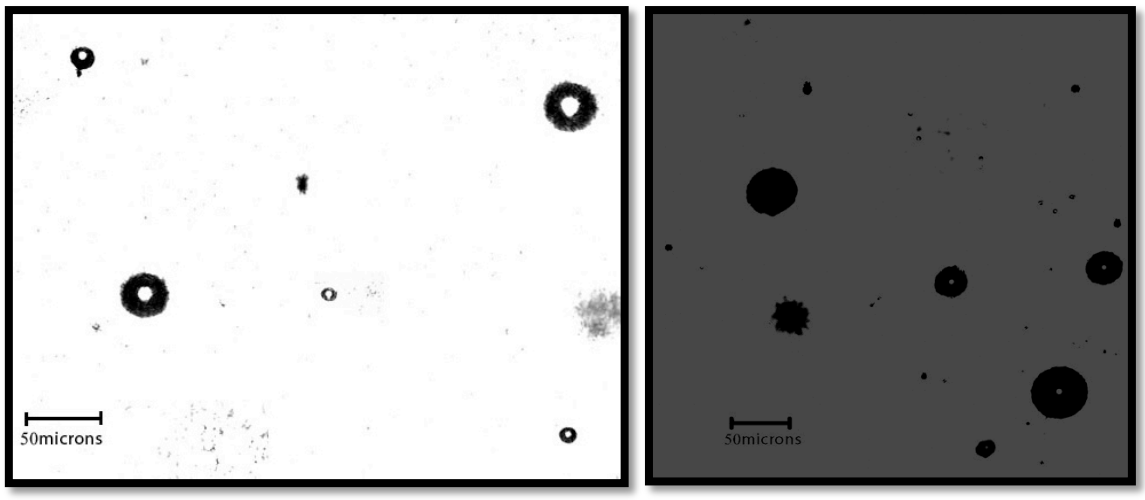

-a- -b-

Figure 7.24 Part of raw microscopic shadowgraph images showing kerosene droplets in air for (a) the IWP023 gasoline injector, and (b) the Lee atomiser.

Droplet size measurements were conducted on three positions, as previously presented in Figure 7.9. The size of the interrogation area at each position was (1.231 mm x 0.906 mm), located 4 cm downstream of the nozzle tip. The first area was approximately 1 cm away from the jet axis, with 30 mm separation between the three points.

7.5.1. Arithmetic Mean-Diameter (AMD)

The Arithmetic Mean-Diameter (AMD) was calculated for each interrogation area, and for an injection pressure ranges between 1 to 5 bar. As illustrated in Figure 7.25, the AMD decreased as the pressure increased, and it was lower in the peripheries than close to the centre of the jet. Using a 5 bar injection pressure, the AMD was 8.6 microns close to the jet axis, and 6.6 microns at the furthest position from the axis.

Increasing the injection pressure is associated with changes in the spray density distribution as previously presented in (section 7.2). When the central jet velocity increases by the high pressure levels, some large droplets drifted away from the jet axis to wider

angles. This could explain the minor changes in the AMD in some cases, and the fluctuation in the (1.3 cm) position in Figure 7.25. However, droplets were always smaller at the wide angles than at the central jet.

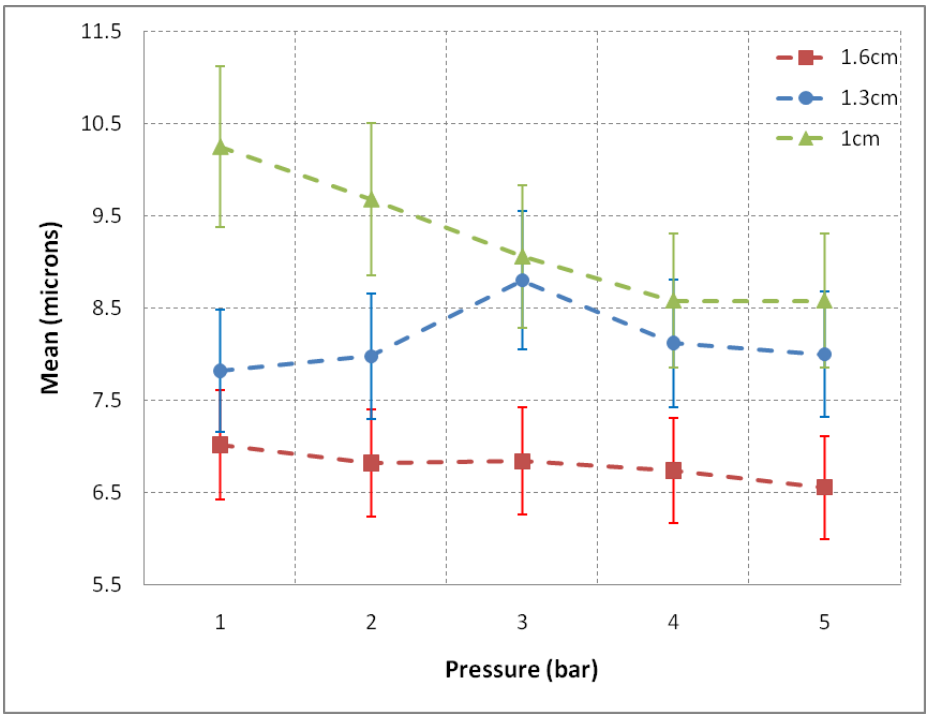

Figure 7.25 Arithmetic mean diameter (AMD) of the Lee injector spray at the points 1, 1.3, 1.6 cm away from the central jet (4 cm downstream the nozzle tip; see Figure 7.9).

7.5.2. Sauter Mean-Diameter (SMD)

The Sauter Mean-Diameter (SMD or D_{32}) represents the volume to surface ratio (see section 2.4.1.1). The SMD gives an extra weight for large droplets than in the AMD. Figure 7.26 shows the SMD calculations of the Lee atomiser. The SMD decreased as the injection pressure increased for the points further than 1.3 cm away from the jet axis, while it showed an opposite behaviour when measured closer to the jet axis.

By matching between the diameter results and the spray density map under different pressure values for the same spray (Figure 7.9), it was clear that the high density area was

growing away from the jet axis at the high pressure levels. Therefore, the particle distribution close to the jet axis was influenced by the large droplets scattered to wider angles. The SMD at 5 bar ranges between 18.2 and 32.2 µm, as presented in Figure 7.26.

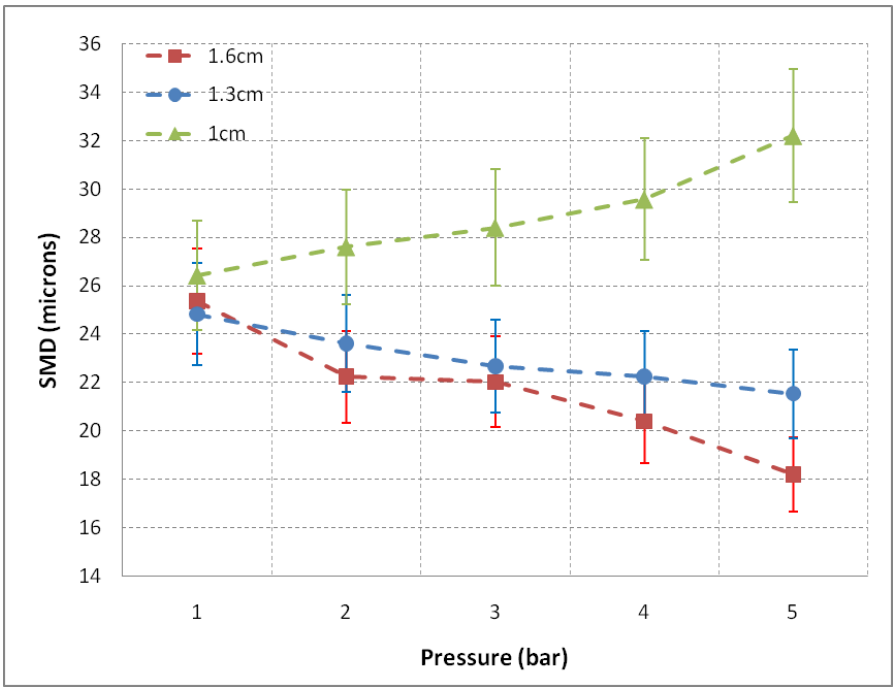

Figure 7.26 Sauter mean diameter (SMD) of the Lee injector spray at the points 1, 1.3, 1.6 cm away from the central jet (4 cm downstream the nozzle tip).

7.5.3. Probability Distribution

Figure 7.27 shows the droplet size probability distribution of the Lee injector at 3 bar, using the average of the three interrogation areas. Around 68% of the droplets were concentrated at the small droplets domain between 3.5 to 7 microns.

The percentage distribution against pressure is presented in Figure 7.28. The MMD ($D_{0.5}$) was approximately 5.5 µm in the 3 bar case, compared with 4.6 µm in the 5 bar case. The diameter of 90% of the detected droplets ($D_{0.9}$) was less than 16 µm at 3 bar and 10 µm at 5 bar.

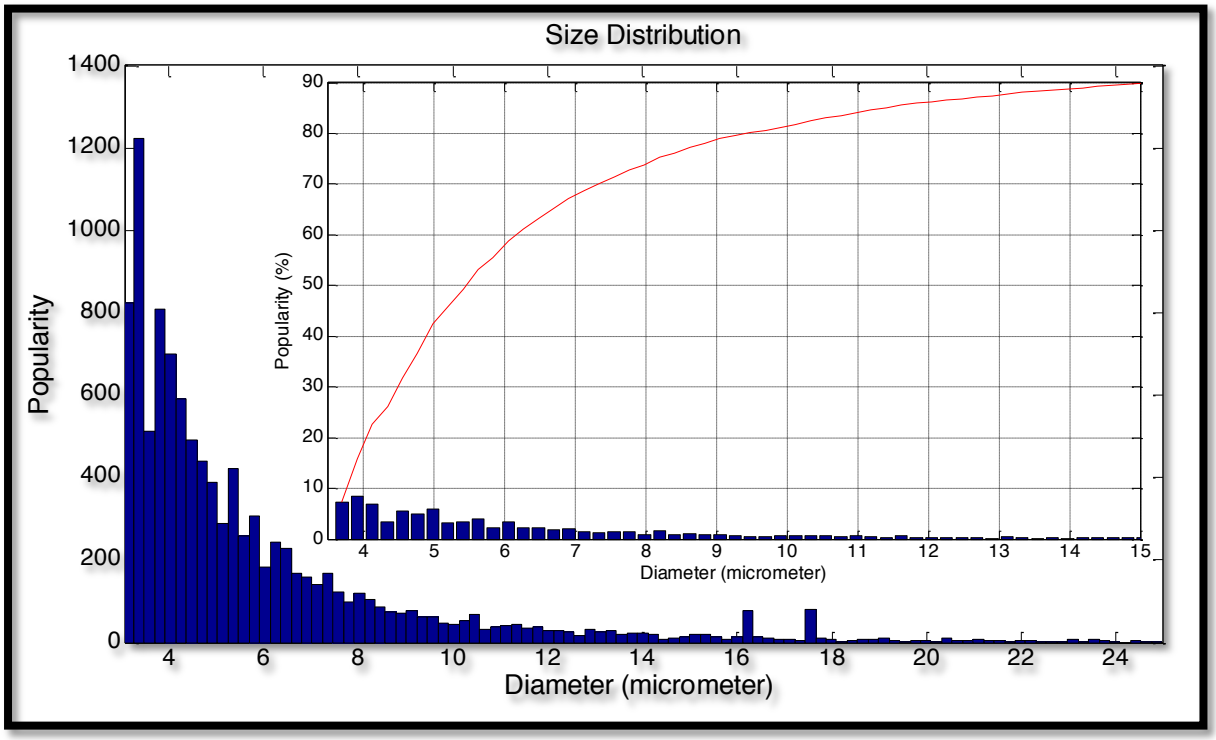

Figure 7.27 Droplet size (probability) distribution of the Lee injector at 3 bar pressure. Only diameters less than 100 microns are taken into consideration. The graph inside shows the percentage distribution.

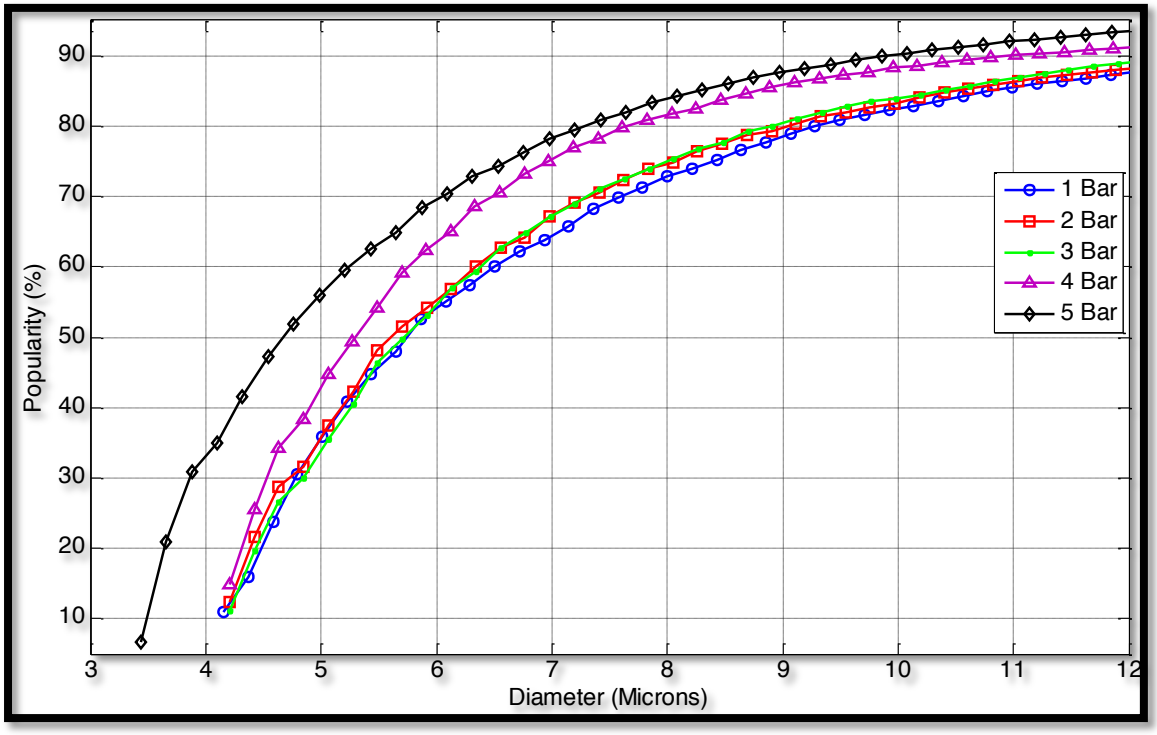

Figure 7.28 Percentage distribution of the Lee injector sprays at different pressure values.

A comparison between the droplet distributions of the different injectors was carried out. Unfortunately, the resolution power of the microscope at the time of testing the standard gasoline injectors (single-hole IPW023 and four-hole IPW043, D0= 584 µm) was 5.5 µm/pixel only. The reason was that the close-up objective (CF4 for K2 microscope; see Section 6.5.1.5) was not available during the tests on the standard injector, which later improved the resolving ability of the microscope to 0.855 µm/pixel for the Lee atomiser. The smallest size can be detected in the case of standard injector was 22 µm (four pixels per particle). Therefore, the comparison was only possible within the common range (22-100 µm) between the two injectors.

Table 7.2 shows that a four-orifice nozzle (IPW043) produced smaller droplets than a single-hole nozzle (IPW023) of the same injector family under the same operation conditions. The Lee atomiser produced droplets 17%-25% smaller in SMD than the standard injector.

Table 7.2 Droplet diameter information for three selected injectors at 5 bar pressure 4 cm downstream of the nozzle tip (1.6 cm away from the central jet).

Injector Model (n, D)	$D_{0.5}$ (µm)	$D_{0.7}$ (µm)	AMD (µm)	SMD (µm)
IWP023 (1h, 584 µm)	44	52	45.39	52.07
IWP043 (4h, 584 µm)	38	44	41.48	47.01
Lee (1h, 125 µm)	31	40	31.29	38.92

The probability distribution of the three injectors is illustrated in (Figure 7.29). It shows that the peak probability of the Lee atomiser is always at the smallest possible size end of the graph. The distribution profile of the IWP injector had its peak at 34-38 µm diameter

size. This suggests that the Lee injector has a higher probability of producing droplets less than 22 microns in diameter.

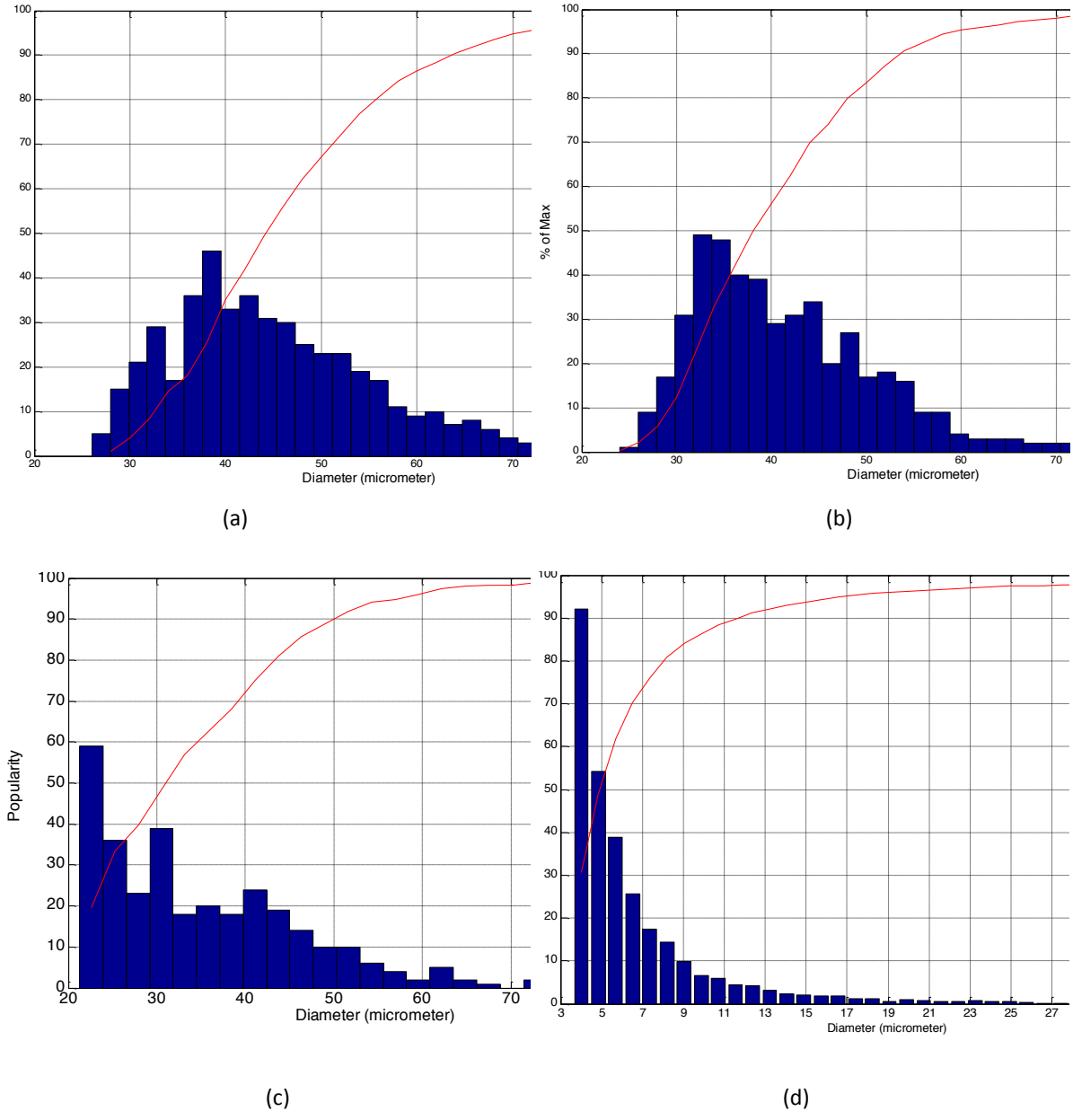

Figure 7.29 JP8 particle size histograms for (a) IPW023 gasoline single-hole injector, (b) IWP043 gasoline four-holes injector, and (c) The Lee injector, all for 5 bar pressure and diameter range (22-100 µm). In (d) the Lee droplet distribution at 5 bar using the high resolution settings (3.5 - 100 µm).

7.5.4. The Effect of the Heating Matrix on the Droplet Size

A heating matrix was developed to aid the cold start of the engine. The matrix was mounted on the throttle body of the injector in front of the nozzle (approximately 1 cm downstream the orifice, see Figure 5.14). The heater was switched on for 30-45 seconds at the beginning of the engine operation (depending on the ambient temperature). It was required to examine the effect of the matrix on the atomisation quality after switching the heater off.

An instant observation of the fuel spray after passing the matrix (Figure 7.30-b) shows that large fuel drops (200- 500 µm) were dripping off the heater surface. This can be explained by fluid droplets condensing on the matrix fins and producing larger droplets. The sharp surface of the matrix also caused the scattering of some other droplets to wider angles than usual.

(a) **(b)** **(c)**

Figure 7.30 The influence of the heating matrix on the spray profile using IPW043 multi-hole injector at 3 bar pressure; (a) heating matrix, (b) fuel spray with the heater, (c) fuel spray without the heater.

An analysis of the droplet size distribution (Figure 7.31) showed that introducing the heater matrix slightly increased the probability of producing smaller droplets in the range (22-45 microns). The matrix produced larger droplets for the rest of the diameter range (45-

100). For example, $D_{0.3}$ (30% of the droplets) was 32 microns without the matrix, compared with 28 microns with the matrix. $D_{0.9}$ was 52 microns in the first case and less than 60 microns in the second. However, the SMD was significantly increased from 78 (without the matrix) to 93 with the matrix. This is due to the lower surface to volume ratio produced by the large droplets.

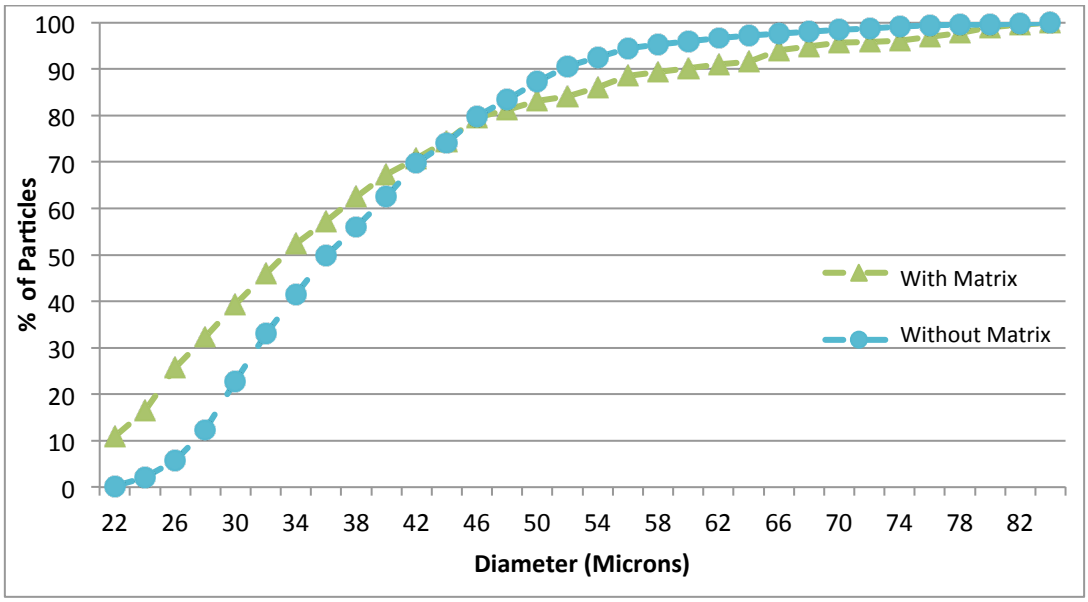

Figure 7.31 The influence of the heating matrix on the spray droplet size distribution using IPW043 four-hole injector at 3 bar pressure.

7.6. PIV and Droplet Tracking

7.6.1. PIV for Spray Development Analysis

The droplet velocity distribution was produced using a cross-correlation based PIV technique (see sections 4.2.5.2 and 6.6.4). Using double-exposure images with a short time interval (10-30 µs) provided a comprehensive view of the flow velocity, under different operation conditions.

The IWP gasoline injector produced sprays with high velocity components close to the jet axis (Figure 7.32). The velocity gradually reduced due to the secondary atomisation during the injection cycle, producing smaller droplets with lower velocities. The changes in velocity between the beginning and the end of the injection incident can be seen by including two successive injection pulses to the velocity vector map (Figure 7.32). The distance between the two high-velocity spots of two successive pulses increased as the injection pressure increased. This agrees with the previously presented results associated with the average tip-penetration (section 7.3.1). In addition, the high velocity components in the low-pressure case remained concentrated on the spray tip area, while it was more distributed over the spray area in the high-pressure case. This indicates that the instability of the fluid is much higher in the high-pressure case.

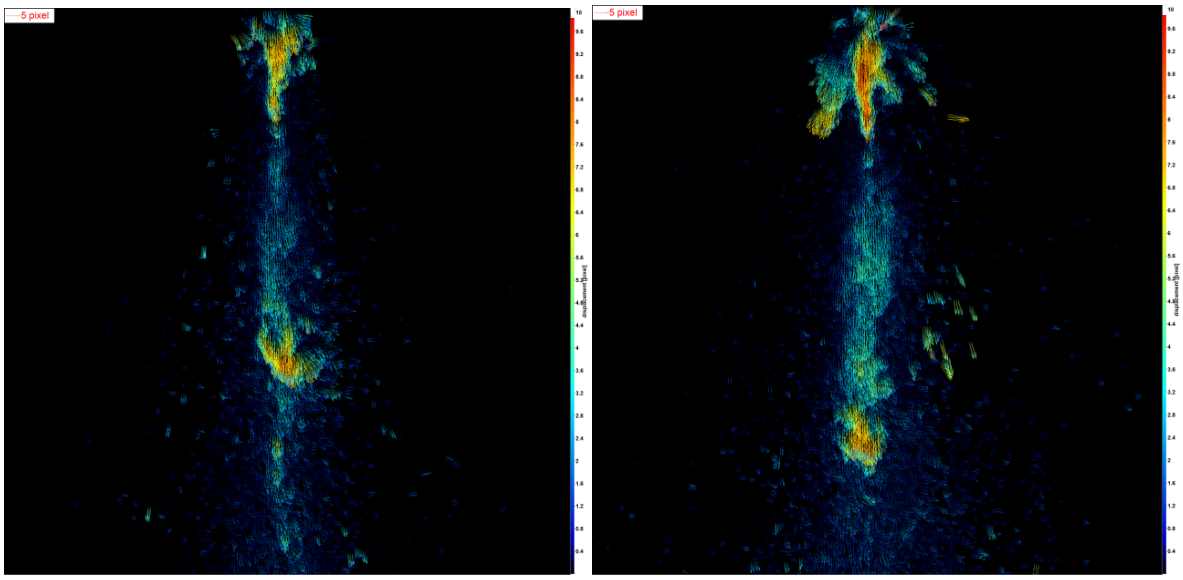

-a- **-b-**

Figure 7.32 Kerosene spray vector field at (a) 2 bar and (b) 3 bar injection pressure, with operation frequency of 250 Hz (2ms pulse-width, 50% duty-cycle) using single-orifice IWP injector. Separation between double pulses=15 µs, resolution=52 µm/pixel (1 pixel displacement = 3.47 m/s). Images taken 1.6 ms ASOI (1.6+2 ms for the downstream pulse).

The velocity of the central jet ranged between 24 and 28 ms^{-1} at 1.6 ms ASOI and 2 bar pressure. The velocity at the same position was 26-32 ms^{-1} at 3 bar pressure. Lower velocity components were distributed at the peripheries, with a higher overall velocity in the 3 bar case than in the 2 bar.

Figure 7.33 shows sprays generated by the same injector using 5 bar pressure. Double-frames were produced using 15 µs delay, and 400 µs between test points (500 double-frame images per point). The high velocity components penetrated downwards of the nozzle exit during the injection cycle. The velocity and density of these components were reduced due to the secondary atomisation and air resistance. In the 5 bar pressure, high-velocity components (up to 34.7 m/s) were distributed in a larger area than in the lower pressure (2-3 bar) case.

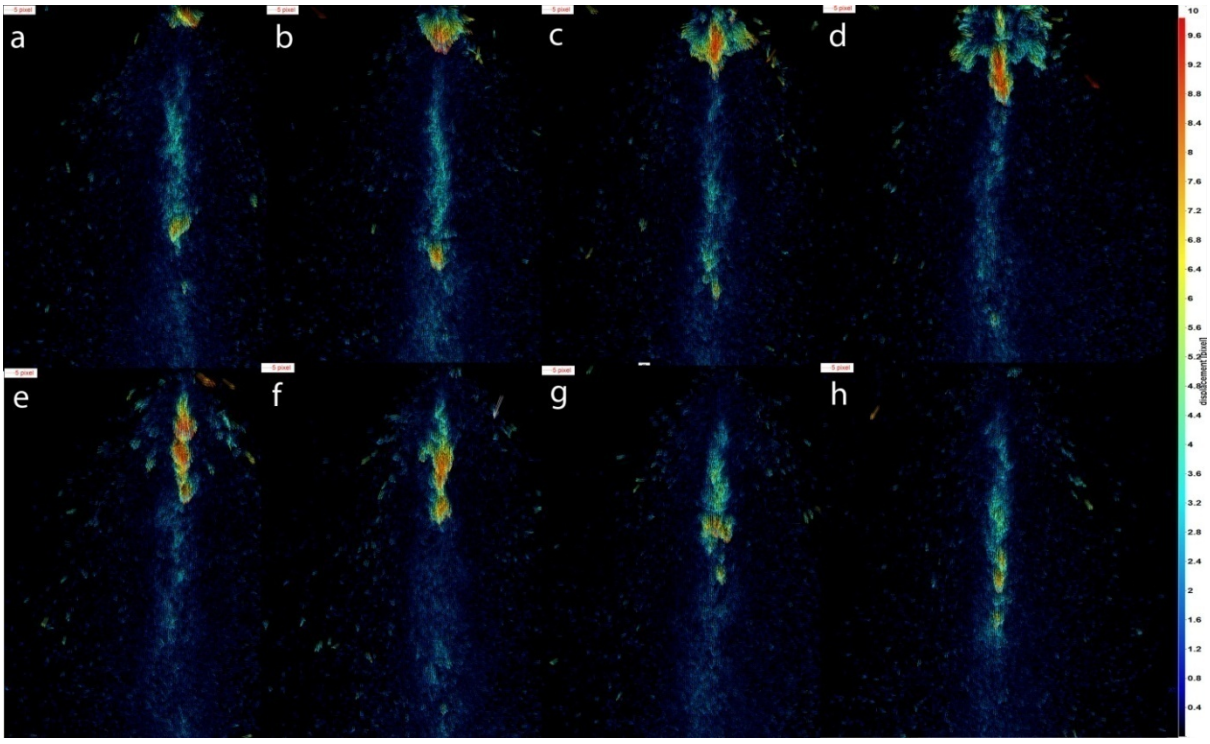

Figure 7.33 Kerosene sprays at 5 bar injection pressure and 250 Hz frequency (2ms pulse-width) using single-orifice IWP injector. Separation between double pulses=15 µs, resolution=52 µm/pixel (1 pixel displacement = 3.47 m/s). Images taken 400 µs apart (a: at 0.4 ms, h: at 3.2 ms).

The comparison between Figure 7.33-d and Figure 7.32 shows the pressure effect on the velocity distribution (all at 1.6 ms ASOI). As the injection pressure increases, higher velocity droplets are disintegrated from the central jet surface and scattered to wider angles. By the end of the injection burst (Figure 7.33-e), satellite droplets start losing energy and stay behind the spray tip (as if the central jet is gradually evaporating). The velocity vectors after 3.2 ms of the start of injection are mostly within the (10-18 m/s) range at the centre, and less than 8 m/s at the spray sides.

The velocity distribution of a four-hole nozzle was different from that of a single-hole nozzle. The high velocity vectors of the four-orifice injector were not concentrated at the middle during the early stages of the injection cycle (Figure 7.34). Instead, velocity vectors within the intermediate velocity range (20-31 m/s) were distributed in a wide area of the spray (apparent clearly between 300 and 700 µs ASOI), and gradually moving towards the spray sides. This can explain the lower average tip-velocity of the multi-orifice sprays than the single-hole sprays for the same injector family, as previously presented.

Two high velocity lobes (34-48 m/s) can be seen in the spray sides between 700 µs and 1000 µs ASOI, along with low velocity elements in the leading tip and the close to the nozzle. The high velocity components eventually advanced towards the spray peripheries, leaving the low velocity small droplets behind them at the top and the middle of the spray (Figure 7.35). By the end of the injection pulse, the high velocity components at the sides eventually break up into lower-velocity segments. The fluid disturbance of this type of injector is noticed to be higher than that of the single-hole injector.

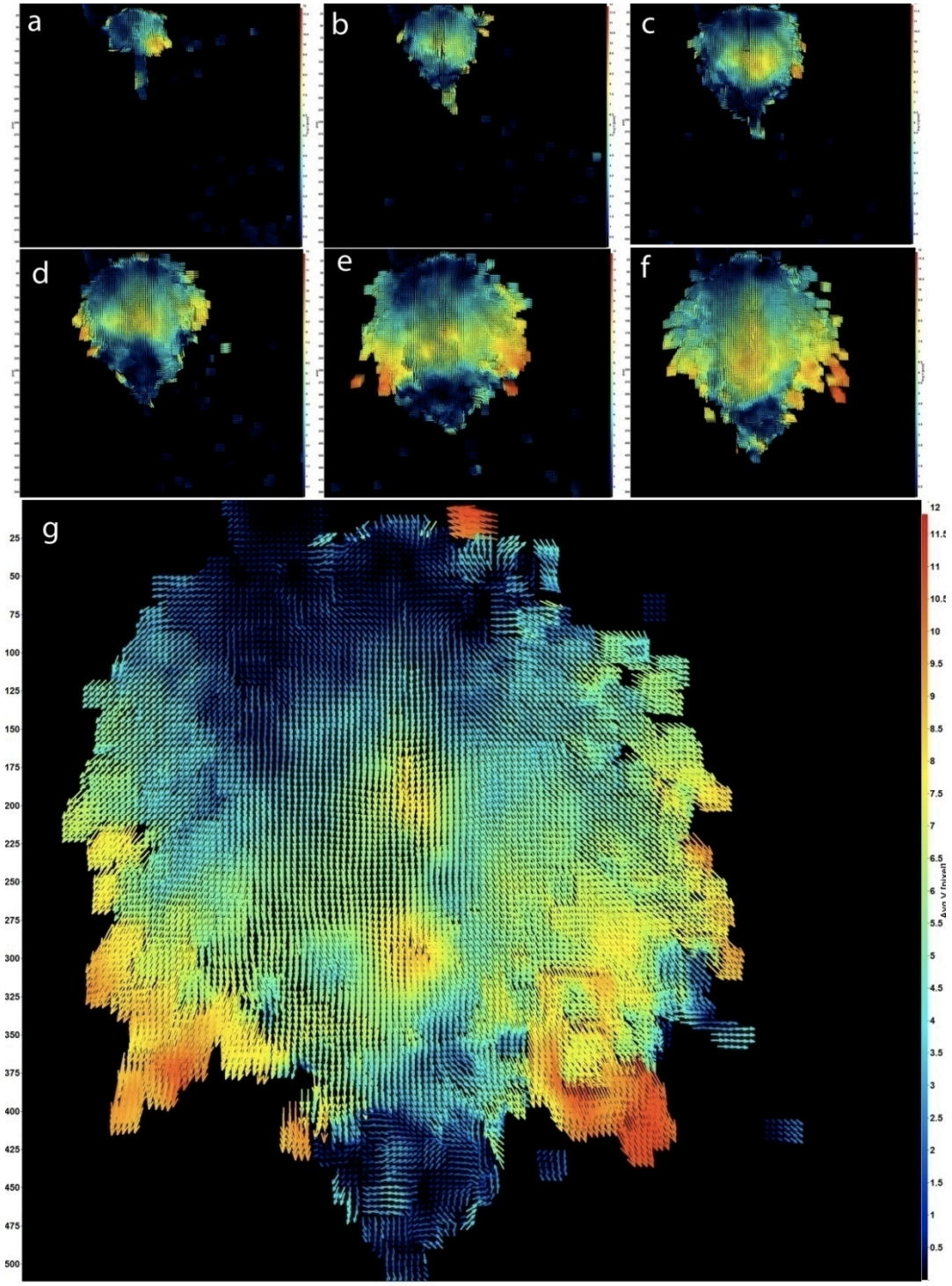

Figure 7.34 PIV (mean velocity) of the early atomization stage of kerosene at 5 bar pressure using four-orifice nozzle. Pulse width=2 ms; separation between double pulses=15 µs; resolution=52 µm/pixel (1 pixel displacement = 3.47 m/s); images are taken 100 µs apart (a- at 100 µs, g- at 700 µs).

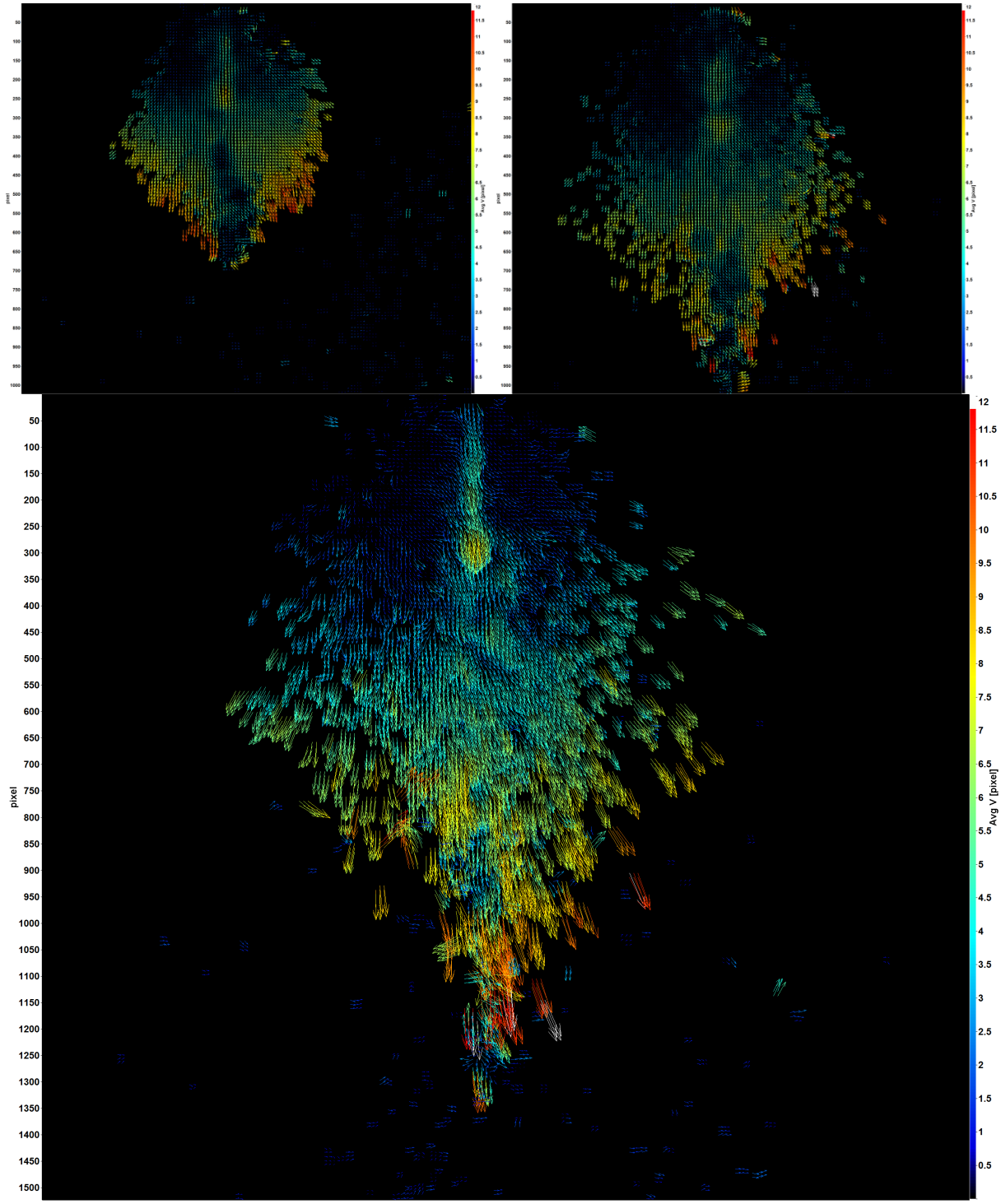

Figure 7.35 PIV of kerosene spray at 5 bar pressure (mean velocity) using four-orifice nozzle. Pulse width=2ms, Separation between double pulses=15 µs, resolution=52 µm/pixel (1 pixel displacement = 3.47 m/s); at 1 ms (top left), 1.5 ms (top right), and 2ms (bottom) ASOI.

7.6.2. Primary Atomisation

Figure 7.36 shows the early breakup process of the kerosene jet after 600 µs of the start of injection, using a single-orifice IWP gasoline injector at 5 bar. The fluid fragmentation occurred mainly on the surface of the central jet at this stage. Small fluid ligaments scattered away from the jet axis in wide angles. A similar pattern was observed by repeating the imaging test using the same time delay. The correlation between spray images in this case (600 µs ASOI) was 84% (for more samples, see Appendix 7.7). Vector field produced by applying PIV at that moment shows that the jet velocity is approximately 38-40 m/s for the fluid tip, reduced to 22-28 m/s for the side segments disintegrated from the parent jet. Smaller droplets scattered on the peripheries have relatively low velocities (less than 10 m/s).

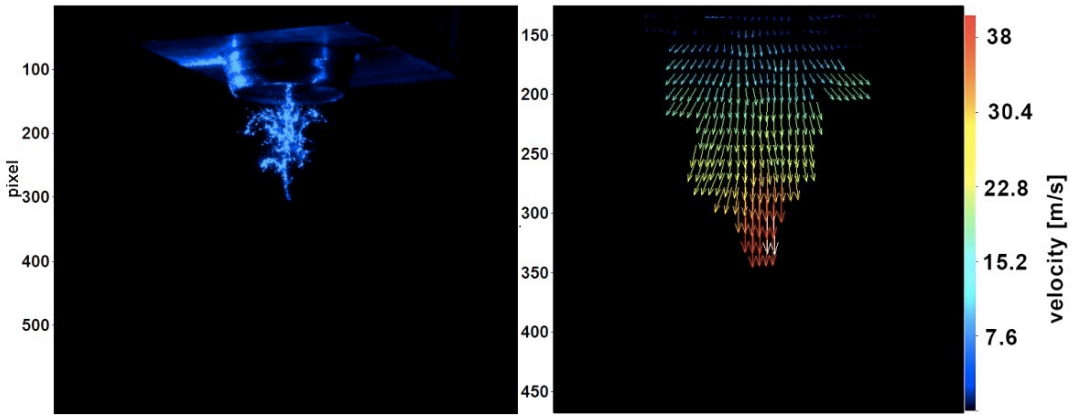

Figure 7.36 PIV of primary breakup 600 microsecond ASOI using single-orifice IWP gasoline injector and JP8 kerosene fuel; resolution: (1pixel=58 microns); time delay between double frames = 15 microseconds.

7.6.3. Microscopic Droplets Tracking

Particle tracking method was applied in order to calculate the velocity distribution of the micro-droplets. Figure 7.37 shows the velocity vector field of a four-orifice IWP injector spray at 5 bar injection pressure (4 cm downstream of the nozzle, 1.5 cm off axis). The vector velocity represents the average of 500 injection pulses (2 ms pulse-width) taken 2 ms ASOI, using 30 µs time delay between the double-frames. The purpose of this analysis is to investigate the velocity of the microscopic droplets (less than 100 microns). The droplet velocity can be then associated with the droplet size. The velocity in this case is calculated for individual droplets, rather than for the speckle patterns in the overall spray.

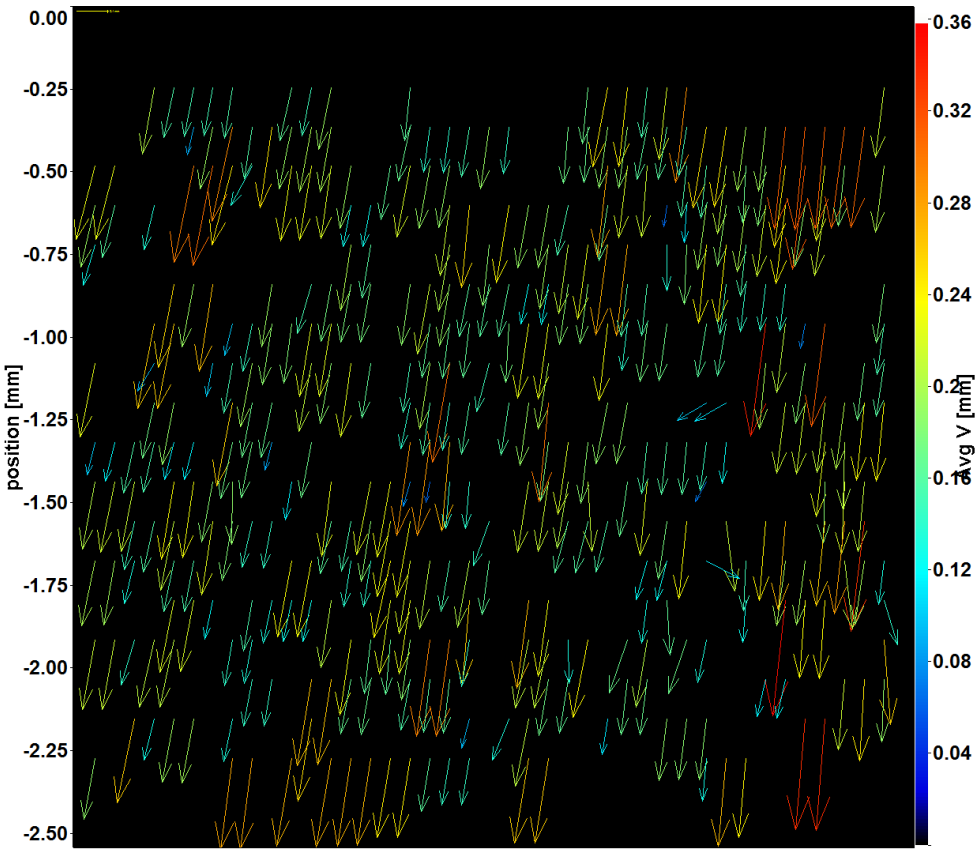

Figure 7.37 Average PTV of the fuel micro-droplets (resolution= 1.24 microns/ pixel, 500 images). The injection frequency equals 250 Hz using four-orifice gasoline injector. The delay between frames=30 µs. P=5 bar. Images are taken 2 ms ASOI.

The droplet density is very low in the case of high resolution microscopic imaging. The low particle density negatively affects the image correlation accuracy. Therefore, the calculation of an image peak correlation needs to be performed using larger interrogation windows than in the global spray. Using a resolution of 1.24 microns per pixel, two stages of image-correlation were applied. The first correlation pass used a 128x128 pixels interrogation window, and the second pass used 64x65 pixels window. This is compared with a maximum of 32 x 32 pixels window size for the global spray analysis. As illustrated in Figure 7.37, the top velocity detected in this case was 12 ms^{-1}, while the velocity of the vast majority of the droplets was lower than 8 ms^{-1}.

A lower spatial resolution of (5.5 microns/pixel) was tested in order to obtain a higher particle density. This provided a wider field of view (11.26 X 11.26 mm^2) for a more comprehensive representation of the droplet movement (Figure 7.38). The correlation interrogation windows in this case were 64X64 pixels for the first pass, reduced to 16X16 pixels in the second pass. The microscopic PIV confirmed that a four-orifice injector (Figure 7.38 a, b) produces particles generally moving slower than those produced by a single-orifice injector (Figure 7.38 c ,d) for the same conditions. The vector field of the four-orifice injector spray shows less velocity changes when moving away from the jet axis than in the single-orifice injector. This is similar to what the global velocity distribution showed in Figures 7.33 and 7.36. The multi-hole injector sprays were also more disturbed than the single-hole sprays.

The velocity probability distribution against pressure (Figure 7.39) suggests that the majority of the velocity vectors are concentrated in the low velocity region (less than 1 m/s RMS). This becomes more apparent in the higher-pressure case.

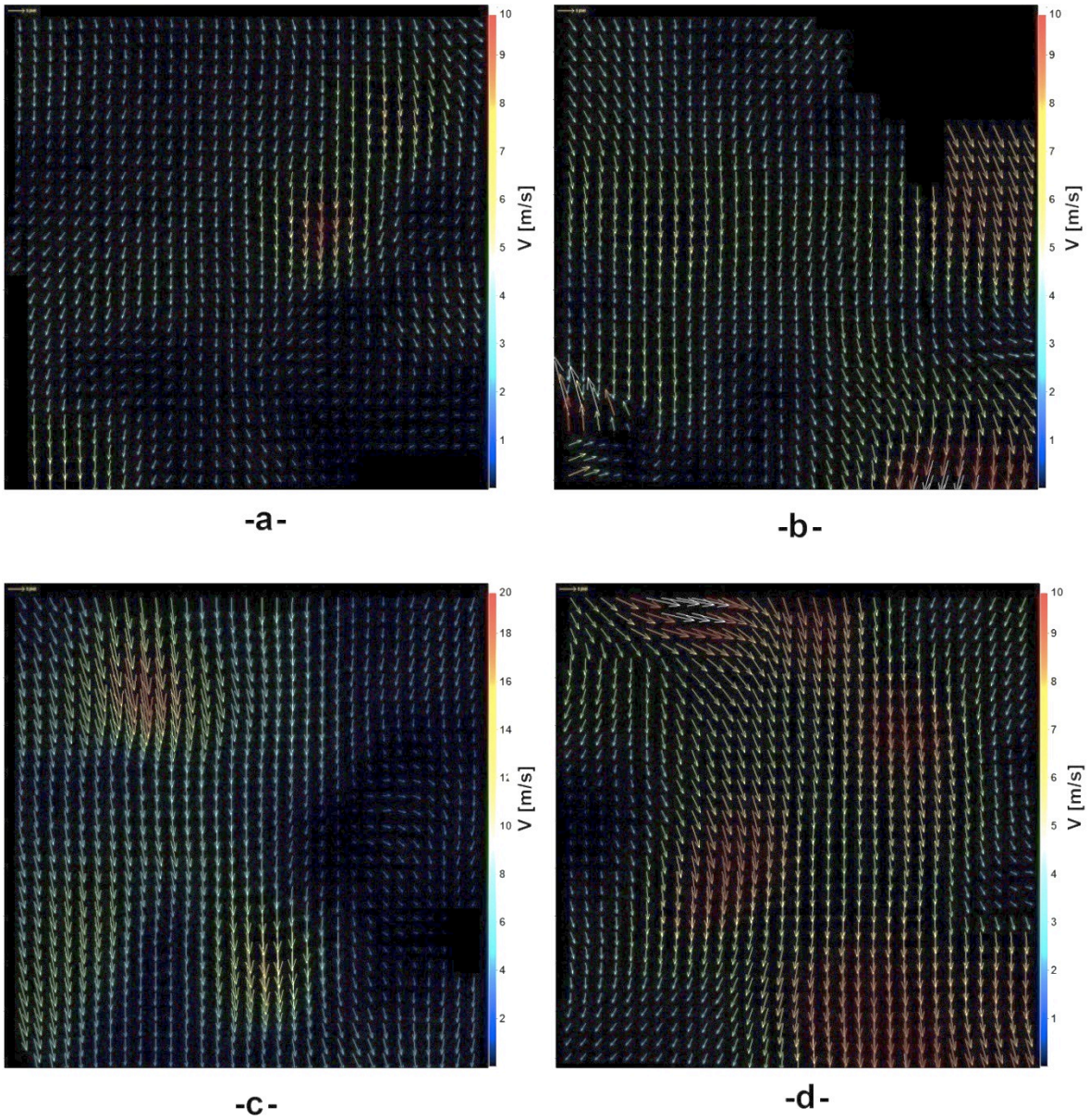

Figure 7.38 Microscopic PIV for IWP gasoline injector at 3bar pressure (resolution=5.5 microns/pixel). a- four-orifice 1 cm off axis, b: four-orifice 1.5 cm off axis, c: single-orifice 1 cm off axis, d: single-orifice 1.5 cm off axis.

7.7. Spray Characterisation Discussion

1. Two methods were used for the visualisation of the global fuel sprays; the direct imaging using a standard flash-gun, and the laser-sheet imaging using a pulsed Nd:YAG laser. Both techniques have benefited from the low density nature of the spray. In particular the laser light sheet shows little evidence of multiple particle light scattering. The direct imaging provides a qualitative indication of how the spray jet develops using multiple injection cycles in a single image frame. The laser-sheet is superior in the investigation of the spray development process and in the micro-droplet sizing techniques. This is due to the high-power instantaneous pulses of the laser. The laser is also used in the light-scattering analysis due to its monochromaticity.

2. A fluid spray density distribution can be produced by overlapping a large number of the global spray images. The mean-image shows the distribution of the atomized droplets depending on the light intensity levels. The density distribution depends on the scattered light at the angle of observation, and therefore, it provides an indicator of the droplet size distribution. This was confirmed by the droplet diameter measurement. The PIV results also showed that the flow velocity at the lower density regions is lower than the high density regions.

3. The comparison between the single-hole nozzle and the four-hole nozzle showed different density and velocity distribution. The multi-hole nozzle produced larger and more disturbed sprays. The tip penetration of the multi-hole nozzle was slower, and its SMD was lower.

4. The 2D-geometric area of a spray produces a “solid” binary image of the spray. This is comparable to the shadowgraph of the global spray (discussed in the literature review). The geometric area is a good indicator of the spray size (angle and penetration), but it is not sensitive to the changes in the density distribution or the flow-rate. Small droplets scatter at wide angles and contribute more to the spray area than to the actual injected volume of fluid.

The image energy provides an indication of the surface-area-to-volume ratio, and it is sensitive to the changes in the spray density.

5. A spray characteristics (size, penetration, angle, flow rate, etc...) are affected by the frequency response of the fuel injector. The frequency response of an injector is dependent on the applied pressure, and on the electromagnetic mechanism of the injector. A fuel injector should be evaluated against the operation frequency and pressure (Figure 7.10) in order to optimise the fuel injection process.

The Lee injector was considered as a good solution for the JP8 fuel injection problem in Cubewano Sonic small engine because of its low flow-rate and high frequency. Multiple injection pulses per engine revolution can be used, which provides a better control of the fuel delivery rate.

The Lee injector produced its maximum possible spray size at a frequency of 2 kHz. The flow rate in this case was 15 cc/min (Figure 7.20) at 5 bar. The droplet mean-diameter was smaller for the Lee injector than for the ordinary gasoline injector.

6. The tip penetration can be calculated in the time domain by synchronising the fuel injector with the laser-sheet and the camera. The tip penetration presents (mostly) the

central jet velocity. For a single orifice gasoline injector (D_0=584 µm, P=5 bar), the tip-velocity decreased from 40 ms^{-1} at 0.2 ms (ASOI) to 21 ms^{-1} at 2.5 ms (ASOI). This is corresponding to a decrease in the flow's Weber number from 40 to 11.5 respectively. The critical Weber number (see chapter 2) for a droplet breakup is around We=10 for the hydrocarbon fuels.

The tip penetration is an important characteristic in fuel spray analysis, but it does not provide a comprehensive representation of the spray development process during the injection period. Therefore, a spray development map was produced, as shown in Figure 7.14.

7. Principal Component Analysis (PCA) method was applied to investigate the similarity in spray patterns in the time domain. The principal component provided an indication of a spray's degree of disintegration throughout the injection cycle. A low correlation factor between images is corresponded to a high disturbance of the spray.

8. Introducing a metallic surface in front of the nozzle exit caused a further disintegration of the fluid. This was the case when the central jet was diffused by a singular blade. However, introducing a heating matrix (Figure 7.30-a) produced very large droplets, and thus it reduced the SMD of the spray.

9. Microscopic shadowgraph imaging method was applied to provide a statistical overview of the particle size distribution (as small as 4 microns) of low-density sprays. The Lee injector produced smaller droplets than the ordinary injector (see the probability distribution in Figure 7.29). This could justify why the Lee medical injector has around four

times less flow rate than the IWP injector, although it produces sprays much wider than the latter (see the cone-angle calculations, Figures 7.7 and 7.8).

10. Shadowgraphy and light scattering provide complementary methods for particle velocity calculation at the microscopic range. Shadowgraphs are preferable for the higher density sprays where there is a lower possibility of overlapping between particles. The diffraction patterns in the light-scattering method can be used to track droplets smaller than the resolution limit of the microscope (sub-micron droplets).

11. The PIV analysis shows that when the injection pressure increases the spray elements are discharged at a higher velocity rate. However, by the end of the injection cycle, the overall velocity of a spray is lower in the high-pressure case (5 bar) than in the low-pressure case (3 bar). This can be explained by the higher degree of atomisation during the jet development produced by the higher injection pressure. The higher discharge velocity is associated with a high Weber number, which leads to a higher atomisation rate. This causes a disintegration of the central jet and a rapid decrease in its velocity. In contrast, low pressures cause less segmentation in the central jet, and therefore a large number of big size elements maintain a relatively high velocity until late stages of the cycle (as the Weber number is not high enough for a further splitting-up).

These results, therefore, explain the small differences in the tip-penetration against pressure (Figure 7.13), compared with the more significant differences in the spray area (Figure 7.15).

7.8. Light Scattering of Seeding Particles in Stereoscopic PIV Systems

7.8.1. 3C-PIV for Jet Noise Test Experimental Rig

The emphasis of the modern aircraft engineering is to develop safer, cleaner and quieter engines. Although computer based modelling and simulation significantly contributes in this type of research, but in many cases there is no alternative for physical testing. The project of the jet noise measurement was carried out by the University of Warwick in the Noise Test Facility (NTF) at QinetiQ, Farnborough, UK, which is one of the world's largest anechoic (echo-free) chambers, with a maximum length of 27 m, a width of 26 m and a height of 14 m. This allows noise measurements to be made at large distances, which is essential for improving the accuracy in noise measurements. QinetiQ facilities provide the ability to perform the tests on the models of the largest aero-engines at 10% linear scale. Three airstreams were used for testing the nozzle including the flight stream, the bypass and the core. Figure 7.39 shows the experimental rig with the possible positions of the two (3C) cameras, showing the corresponding angle between the camera-target line of sight and the laser sheet plane.

7.8.2. PIV Seeding Particles

In Particle Image Velocimetry applications, it is very important to determine the suitable material and the concentration of the seeding particles. Seeding is usually performed using ultra-low-weight microscopic particles (powder) or droplets (smoke). The problem of low light levels at the image sensor is common in this type of experiment, although high power lasers are normally used. An Nd:YAG laser (532 nm) with around 600

mJ output power was used in our experiments. Imaging was performed using three CCD PCO2000 cameras.

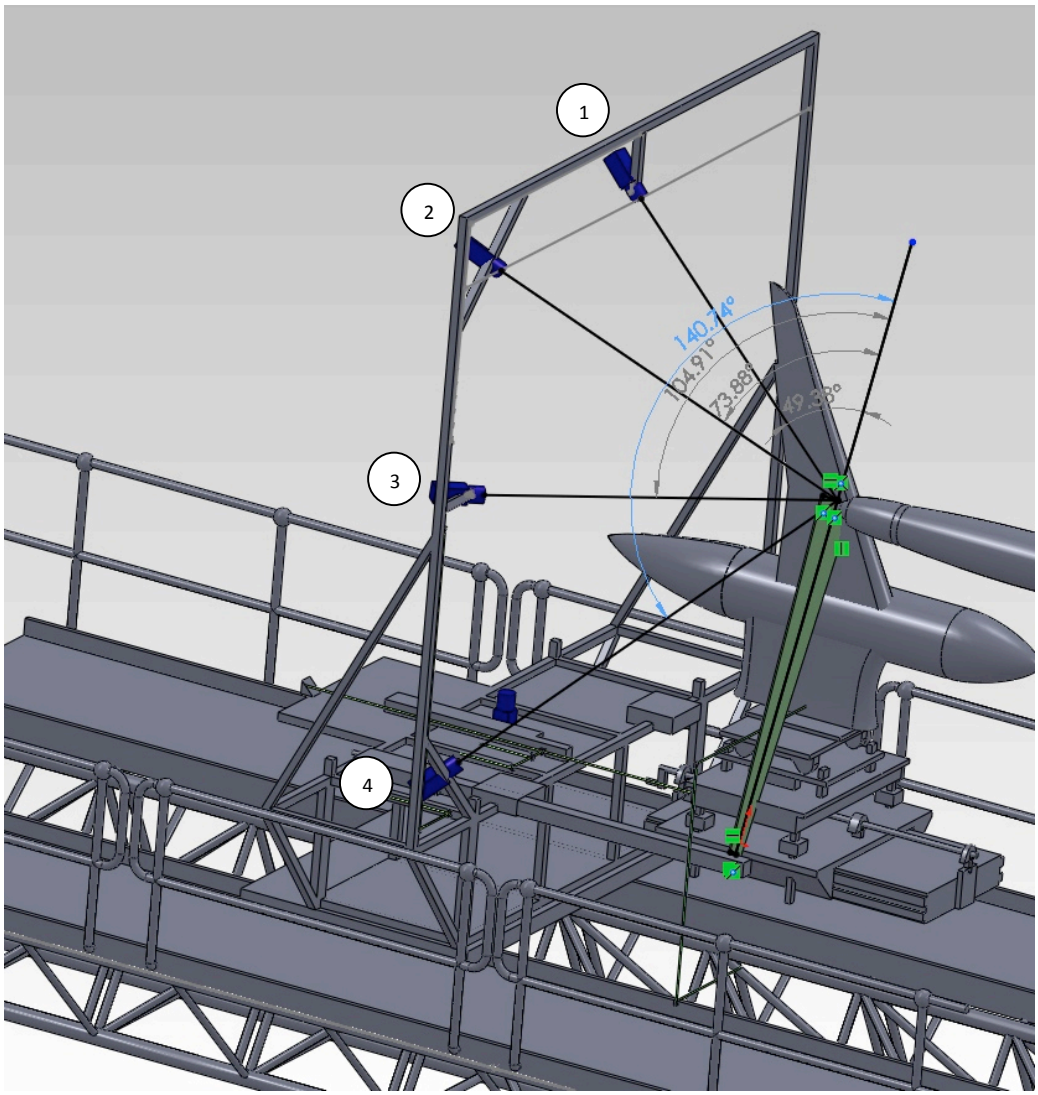

Figure 7.39 Warwick stereoscopic-PIV Experimental Rig.

The distance between the CCD and the seeding particles is important to the light intensity amplitude at the collection optics. Instruments in practical large-scale industrial flow tests are needed to be placed at a sufficiently long distance in order to avoid the

interference with the flow [Timmerman et al. (2009)]. This problem becomes more obvious in the case of stereoscopic 3C-PIV since imaging from different angles is required.

The determination of the relative angle between each camera and the laser sheet is crucial for obtaining adequate information about the jet flow. It is not only that the low light levels reduce the ability of resolving the structure of the flow elements, but also the unbalanced brightness between the cameras leads to poor correlation between the results, and therefore difficulties in performing a 3C-PIV (see appendix 7.11 for the difference in light intensity between the two cameras when using the top-bottom configuration).

7.8.3. Light Scattering of the Seeding Particles (Mie Curves)

The two main requirements for the seeding particles are to satisfactory follow the measured flow and to scatter enough light to be captured by the camera sensor. The smaller the particles, the quicker they respond to the flow motion; a good representation of the high velocity flow requires the seeding size to be of the order of tenths of a micrometre. Typically, seeding size below 0.45 µm would follow turbulent oscillations of 10 kHz with 99% amplitude accuracy [Melling (1997) in Timmerman et al. (2009)]. The seeding particles should also withstand the high temperature especially in the core and the bypass flow. Titanium dioxide TiO_2 (refractive index 2.6-2.7) with 3-5 microns mean diameter is a popular choice for PIV experiments in both gas and liquid media due to its low price and high scattering efficiency (see Figure 7.40). However, Aluminium oxide (refractive index around 1.77, melting point 2054°C), conglomerates less than the titanium dioxide making it a preferred choice in applications involved dense seeding in air (see Appendix 7.12 for the aluminium oxide scattering profile for particles range (0.2-1) micron).

In laser speckle velocimetry, in which the camera tracks the changes in the speckle pattern, a large concentration of seeding particulates is needed in the field of view, compared to the particle tracking velocimetry which uses lower seeding density [Skeen (2006), Adrian & Westerweel (2011), ch.1]. The speckle patterns can be produced by the oil smoke seeding method, which can create high density seeding with ultra-light particles.

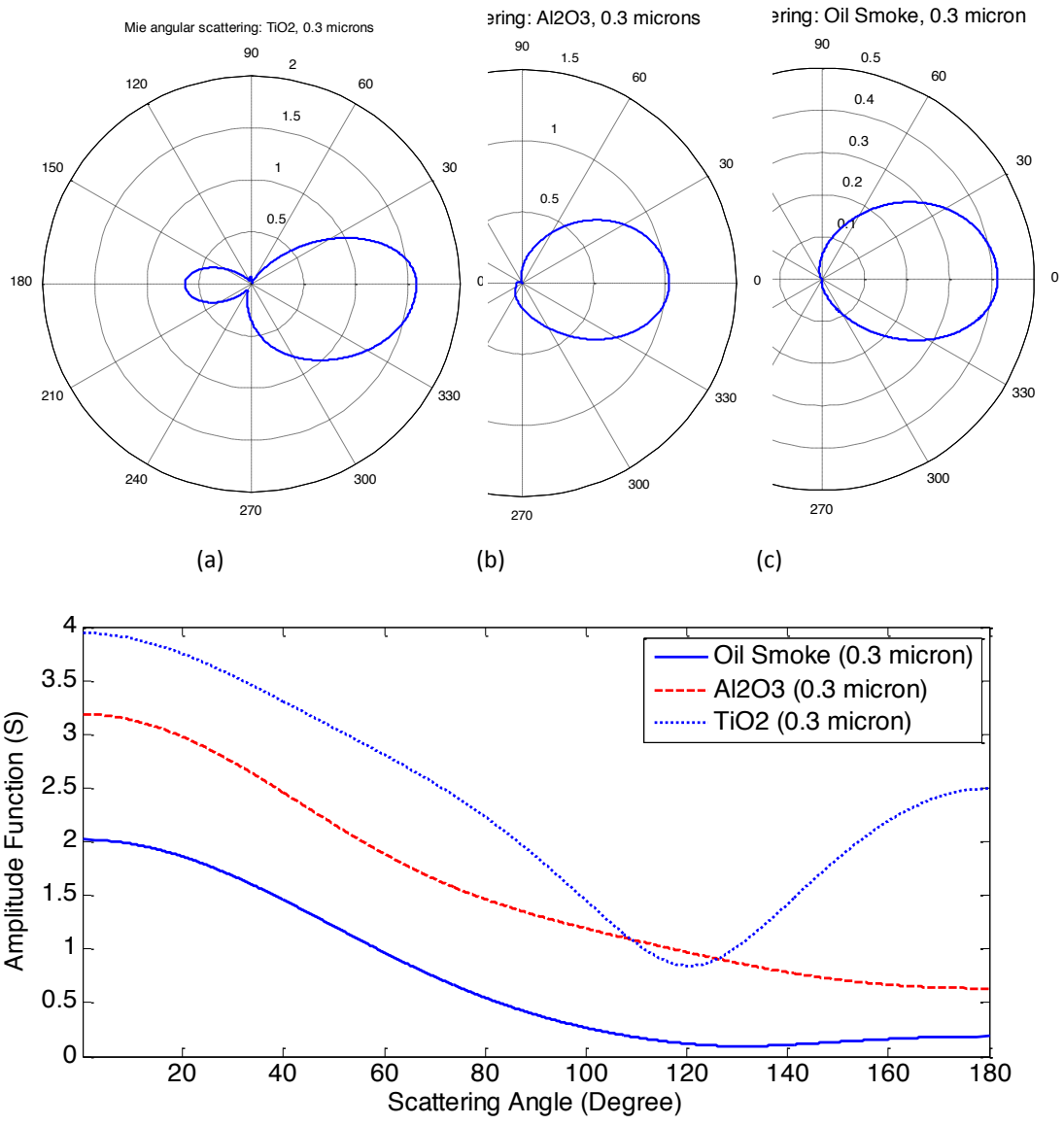

Figure 7.40 The scattering profile of three different seeding materials for particle size 0.3 microns in diameter; (a) Titanium dioxide TiO_2, (b) Aluminium oxide (Al_2O_3), and (c) Oil smoke (refractive index m=1.47).

In the current jet noise test, aluminium oxide was used for seeding the core and the bypass of the flow, delivered by separated controllable seeders, providing a homogeneous seeding. The flight stream, on the other hand, was seeded using an oil vapour generator (Concept Vi-Count Compact aerosol generator), which produces 0.2–0.3 μm droplets of white oil, vaporized using nitrogen. The emphasis will be on the oil smoke particles since no difficulties were found in resolving the Aluminium oxide particles due to their relatively high scattering efficiency. The low brightness of the images was clearly problematic in the fluid smoke case.

7.8.4. Evaluation of the Camera View Angle for Oil Smoke Seeding

A laser scattering experiment was carried out in the PIV Lab (University of Warwick) for the evaluation of the camera view-angle effect on the image brightness due to the variations on the light scattering angles before conducting the jet noise test, in a trail to imitate the conditions of the actual noise test in the noise test facilities (NTF) using similar instruments. The camera was free to move along a vertical beam, covering a range of angles from 45° to 140°. A smoke was generated using Shell Ondina EL Oil, producing particles 0.28 μm in mean diameter (maximum of 2 μm). Images were taken at 30 vertical positions (90 images each), and then processed to compute the overall energy of the mean image at each test point. The camera settings (exposure, aperture, dynamic range) were kept constant during this experiment. Figure 5.41 shows a diagram of the experiment setup.

The experimental results in Figure 5.43 present the global scattering calculations against the scattering angles, noting that the scattering angles are calculated between the forward laser beam and the camera line of sight. A degree of uncertainty in the

experimental results should be considered due to the difficulty in producing a regular smoke seeding, beside the effect of the reflections in the background.

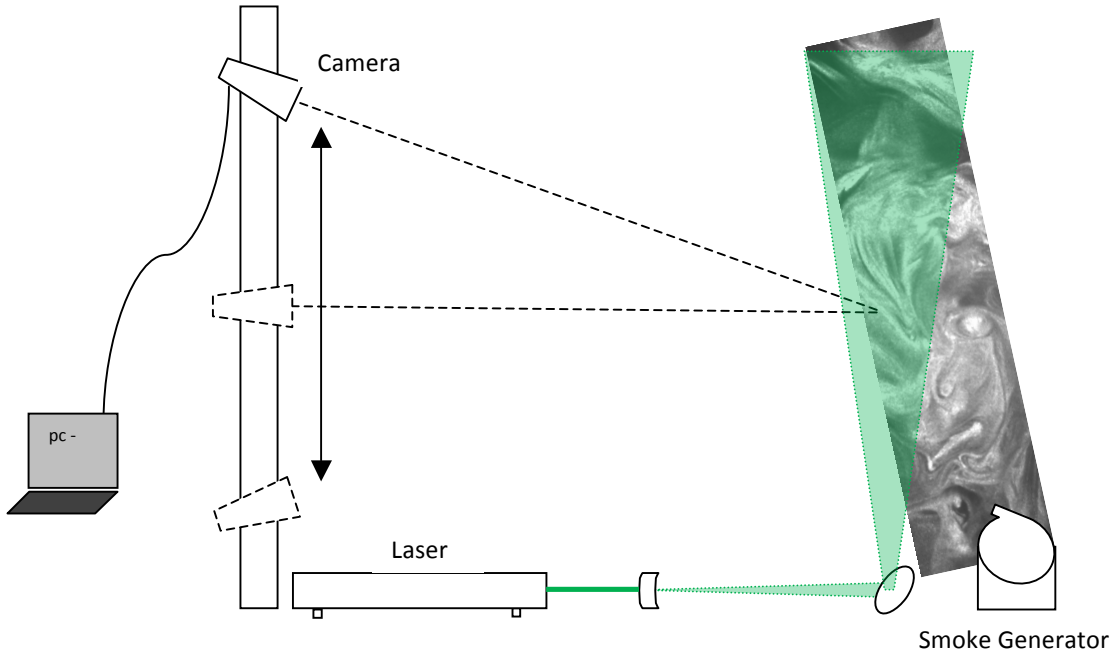

Figure 5.41 The light scattering experiment setup diagram.

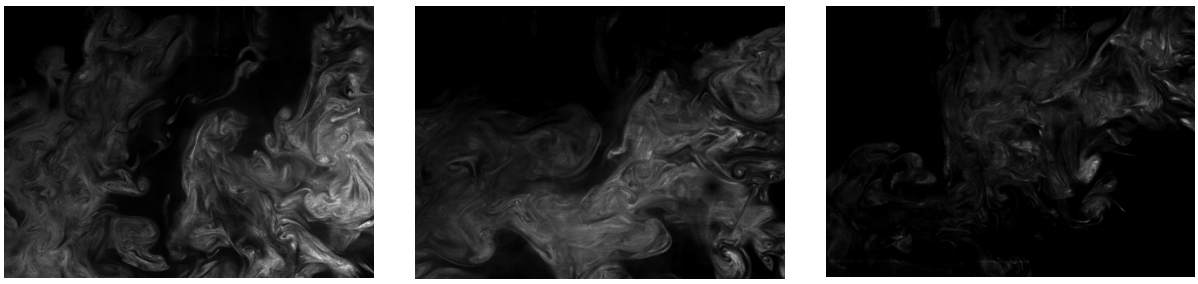

60° 85° 110°

Figure 5.42 Three samples of the smoke images at three different angles.

The scattering map of the oil smoke is a combination of a wide range of particle sizes; therefore, taking only the mean diameter into consideration could lead to a certain degree of uncertainty in the results, knowing that larger particles contribute much more than smaller ones in the overall intensity of the received optical energy. The theoretical

results obtained by Mie solution are shown in Figure 5.44 for a range of diameters between 0.25 and 1.00 micron. The average graph of these different values is calculated for each angle and illustrated in Figure 5.44(b).

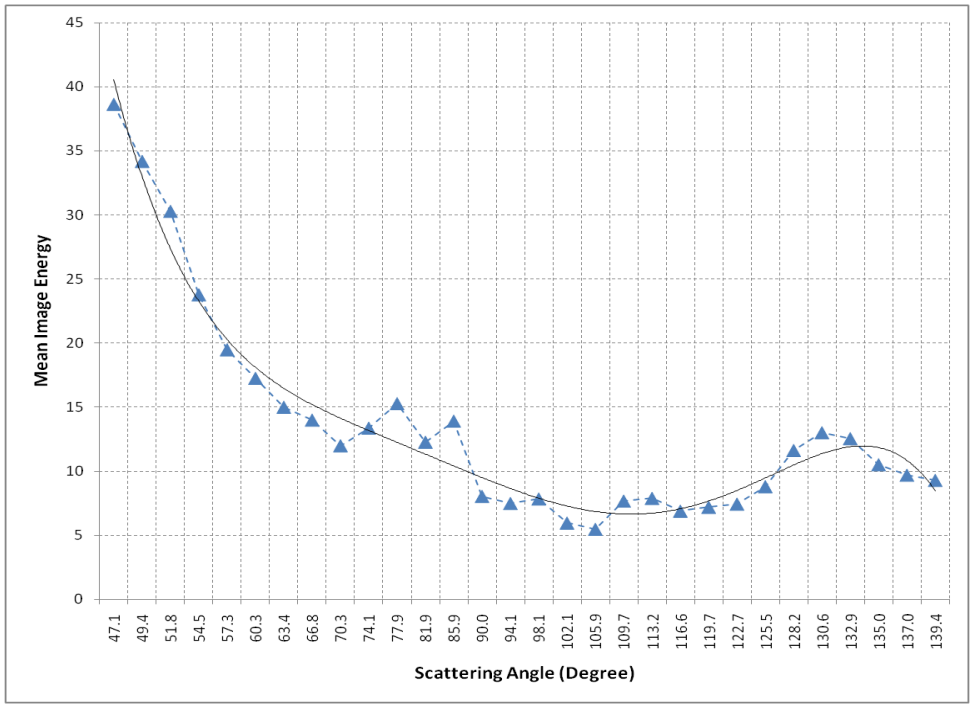

Figure 5. 43 The experimental result of the image average brightness against the scattering angle. The trend-line is the polynomial fit of the 5th order.

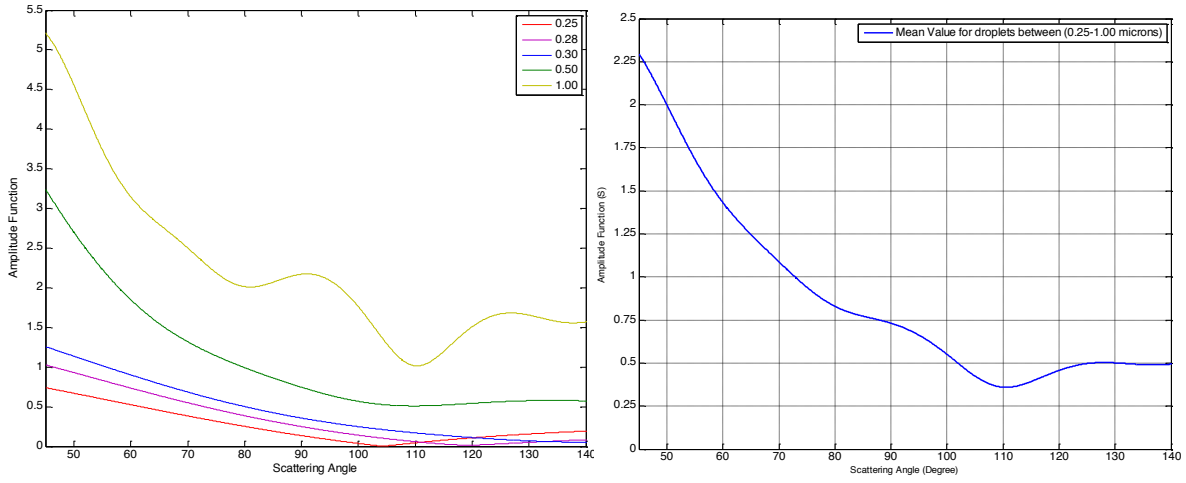

(a) (b)

Figure 5. 44 The theoretical calculation of the Mie scattering profile for the smoking oil (diameters in microns, angles in degrees), and (b) the mean value (theoretical) of the light scattered by the smoke particles ranging from 0.25 to 1 micron in diameter.

The following table presents a comparison between the four possible positions of the cameras on the rig design (as shown in Figure 7.39):

Table 7.3: The effect of the scattering angle on the global light intensity received by a CCD camera.

Camera Position (Figure 5.20)	Scattering Angle (degrees)	Image Mean Energy (Empirical) / scaled to the maximum		Amplitude Function (Theoretical)/ scaled to the maximum	
1	48	39	100%	2.05	100%
2	74	13.5	34.6%	0.85	41.4%
3	105	7	17.9%	0.35	17.1%
4	140	9.5	24.4%	0.5	24.4%

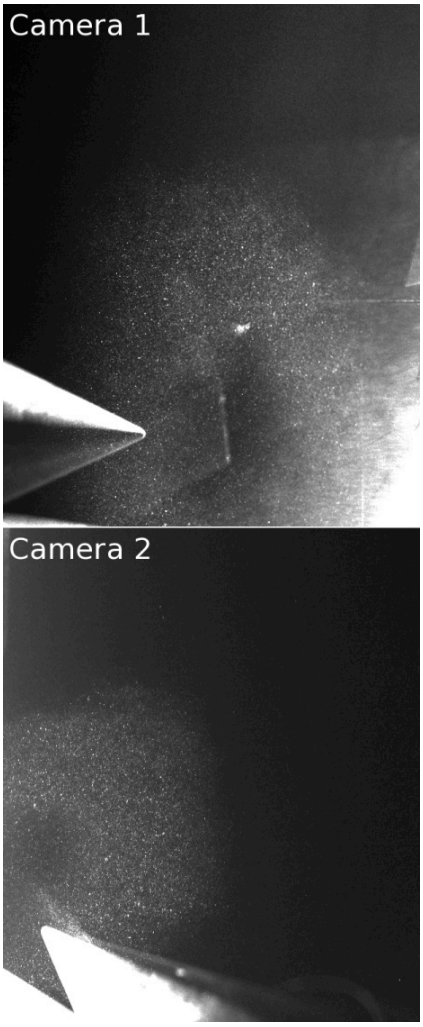

The suggested solution in this case was to use positions 2 and 3 for the stereo cameras, so that the light energy received by the top camera is as twice as the bottom camera. Therefore the aperture of the bottom camera should be stepped down one step in order to balance between the two images. Figure 5.45 shows a sample image during the noise test as a result of adopting the previous recommendation. While the larger particles are clearly visible in both views and the two images can produce a good correlation, the speckle pattern of the oil is still more visible in the top camera.

Figure 5.45 Image sample from the jet noise test using positions (2) and (3) ; Cam 1 at the top left of the rig; Cam 2 at the bottom left of the rig.

7.8.5. Correlation Quality of Seeding Particles

The aerodynamic testing provided a unique testing evaluation of the light scattering performance between two different submicron particle distributions of the same size. The Aluminum oxide particles created much brighter scattered images and could be viewed as individual particles. Whereas, the oil particles had a different, much less intense, Mie scatter profile and could not be viewed individually, only as the laser light sheet generated speckle pattern surface. However, a strong velocity correlation was obtained from both types of distribution. This posed several questions pertinent to understanding how a global measurement could be made of a submicron particle distribution, specifically for particles below the optical resolution limit of the microscope as described in the previous chapter. The first aspect of the investigation was to validate that both the speckle and particle correlations had comparable accuracy and resolution. The second aspect to use the particle size, interrogation wavelength and Mie scattering dependence to calculate particle size was beyond the scope of this thesis. However, a discussion of the implications of the combined approach has been made in the 'Further Work' chapter.

The vector field of a multiphase flow is produced in PIV using the normalised cross-correlation function between two interrogation windows. The seeding material plays an important role in determining the correlation quality according to the optical properties of the particles, as explained earlier in this chapter. In this section, an analysis of the image correlation quality is presented using the jet flow data, including two types of seeding particles. Aluminium Oxide was used for seeding the jet core, while oil smoke was used for the flight stream (Figure 5.46). Since the diffraction pattern of the two materials is different even for the same size particles, it was important to investigate how this can change the

correlation results (velocity calculations) especially when different sizes of interrogation windows are used.

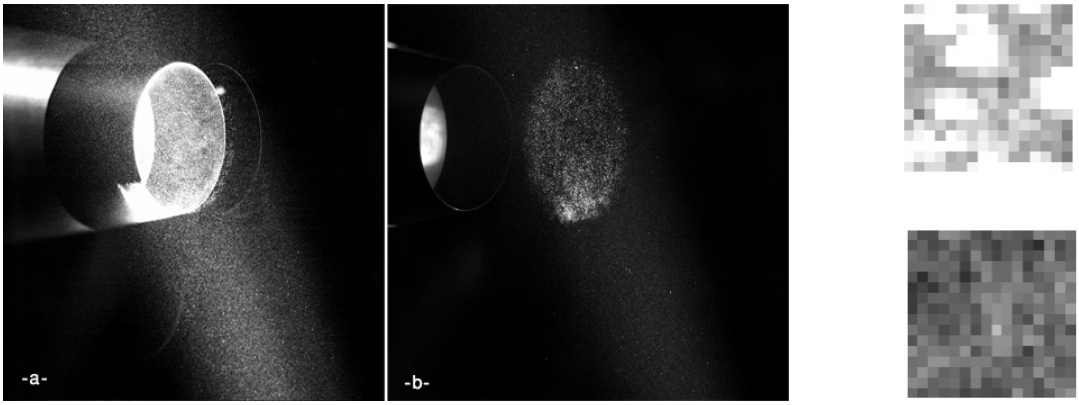

Figure 5.46 Jet flow laser-sheet imaging using aluminium oxide seeding particles for the core and oil smoke for the flight-stream, at (a) 0D and (b) 1D downstream of the nozzle. Top: a close up view of the aluminium particles; down: a close up view of the oil smoke, both using 16 X 16 interrogation window.

Aluminium oxide particles have rather complex patterns producing an equally complex speckle pattern at the light scattering image. The oil droplets, on the other hand, can be considered as perfect spheres because of the low Weber number at this diameter range (approximately 0.3 microns). Therefore, the scattering pattern of the oil droplets is more uniform and repetitive than in the solid particles. In the oil smoke case the speckle pattern is determined by how the droplets are positioned in the interrogation window (differences in concentration) and by the minor differences in droplet size, while the non-uniformity of the solid particles leads to a wide variety of scattering patterns, improving the ability of the correlation function to track the individual droplet displacement between the successive frames. Figures 5.47 and 5.48 show the results of applying the normalised cross-correlation function on the core and the flight stream respectively. A relatively large interrogation window of 46X46 pixels was selected to be correlated with a 256X256 window, while both windows share the same centre point. The two images represent the

case of high quality correlation, where the peak correlation point is well defined and contrasted from the rest of the correlation elements.

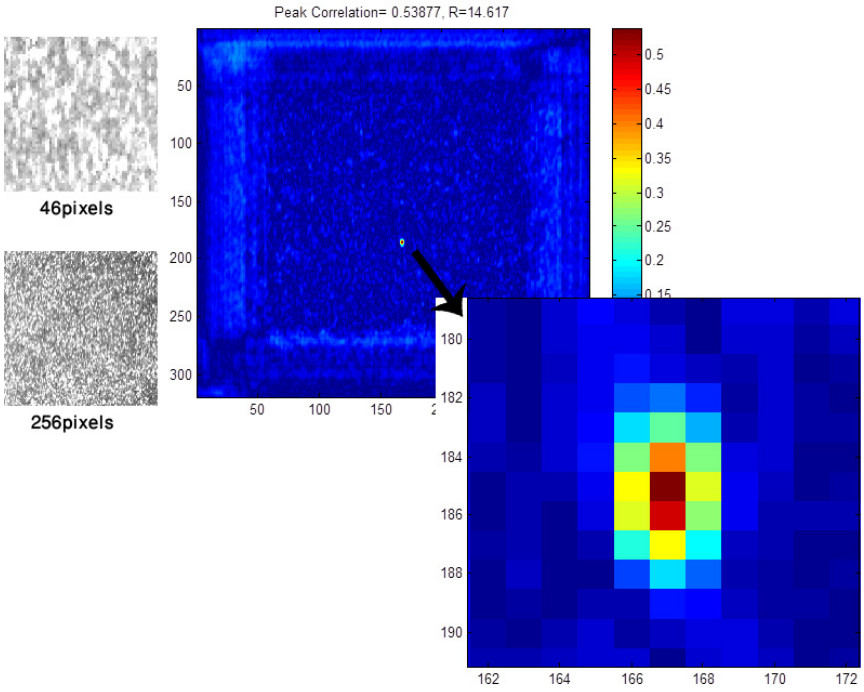

Figure 5.47 Cross-correlation result using 46X46 pixels interrogation window and aluminium oxide particles for seeding.

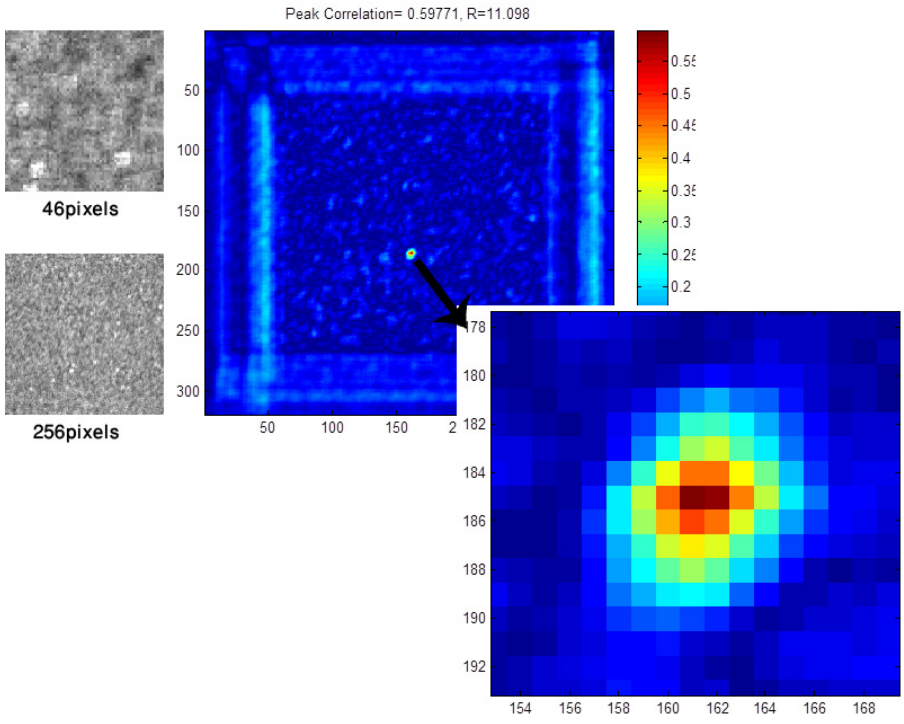

Figure 5.48 Cross-correlation result using 46X46 pixels interrogation window and oil smoke for seeding.

Although both positions provided a good quality correlation, the aluminium oxide particles provided a much precise determination of the peak-correlation position than the oil smoke, which could be seen in the sharpness difference between the two (color-coded) correlation images. The value of the peak correlation can often reflects the efficiency of the system in detecting similar patterns between frames. However, when the size of the interrogation window is reduced, the contrast between the peak correlation and the rest of the correlation image decreases and the possibility of obtaining more than one peak correlation arises, leading to misleading results in the displacement calculations. For this reason, a new factor was defined for the correlation quality. The error factor (or R-factor) represents the ratio between the peak correlation point and the mean correlation image (the average of all correlation items). The possibility of detecting a wrong correlation increases when the correlation image contains correlation items close in value to the peak correlation (hot spots), therefore the exponential function was used in the mean image calculation instead of the linear average in order to give extra weight to the correlation items very close to the peak correlation. The error factor was therefore given by the formula:

$$R = \frac{P_{corr}}{\ln\left(\frac{\sum e^{x}}{(t+k-1)^{2}}\right)} \qquad (7\text{-}1)$$

Where P_{corr} is the peak correlation item, x is the correlation item value (correlation image pixels), t and k are the sizes of the two interrogation windows.

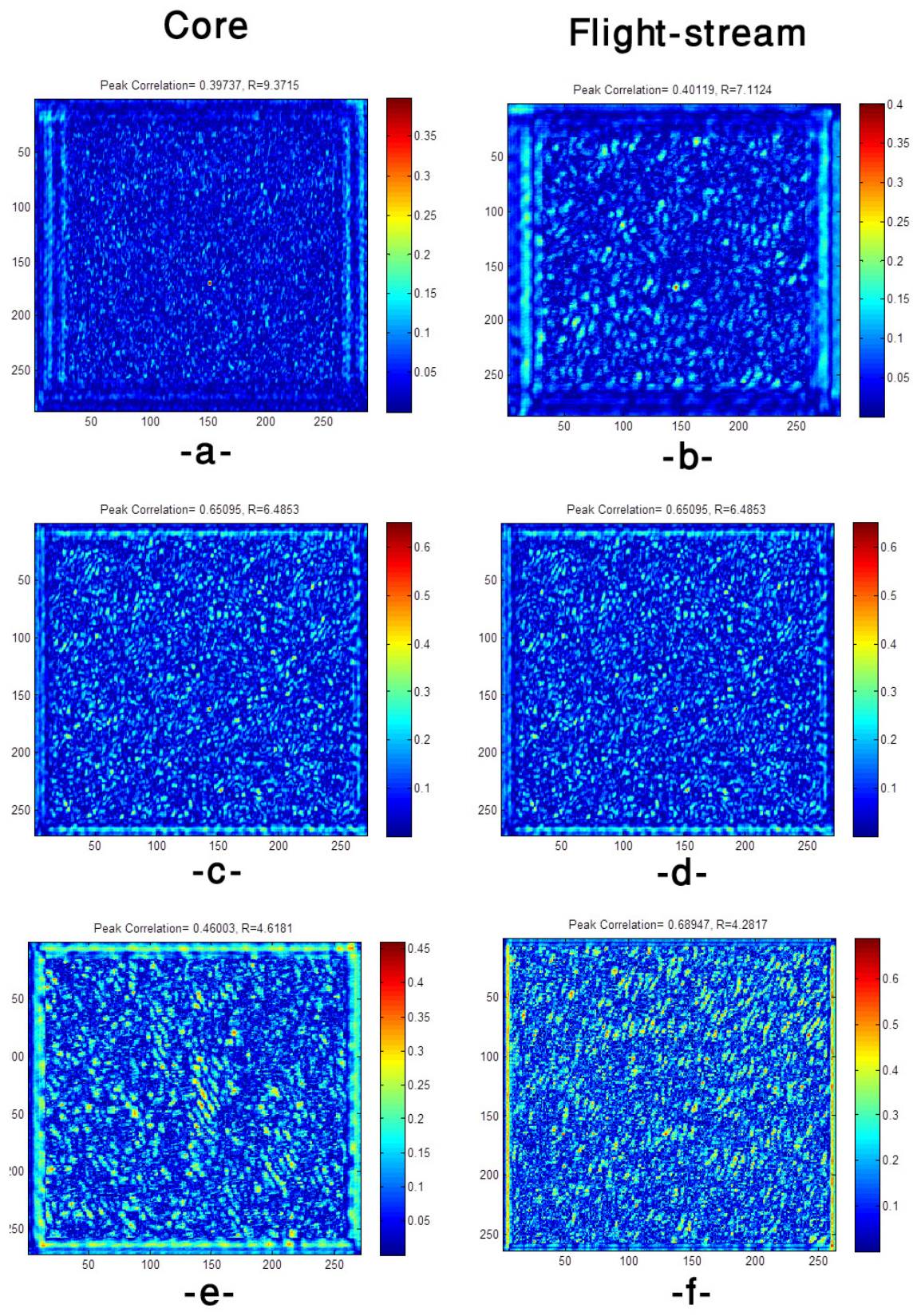

Figure 5.49 Correlation maps for different correlation window size; a: core (32X32), b: flight-stream (32X32), c: core (16X16), d: flight-stream (16X16), e: core (8X8), f: flight-stream (8X8).

Figure 5.49 shows samples of the cross-correlation images for different interrogation window size. Table 7.4 presents the peak correlation, R-factor and standard deviation calculations for different window size and for both aluminium oxide particles and oil droplets, calculated by the average of 25 samples at each test point.

Table 7.4 Image cross-correlation calculations for the aluminium oxide particles (core) and oil smoke (flight-stream); showing the peak correlation value, error factor and standard deviation

Window Size	Peak_corr	R_factor	std
256X64 core	0.56	12.11	0.0074
256X64 flight	0.52	11.6	0.0066
256X32 core	0.58	9.66	0.0074
256X32 flight	0.51	7.76	0.008
256X16 core	0.58	6.19	0.0105
256X16 flight	0.56	5.13	0.0122
256X8 core	0.74	4.11	0.0177
256X8 flight	0.65	3.98	0.0141

In conclusion; the two types of correlation approach are both valid. In the case of the Aluminium oxide, where the particles are highly reflective there is a strong correlation. The accuracy of the correlation and the certainty of finding a matching correlation pair between successive integration frames increases as the interrogation frame size decreases to value of 8x8 pixels. Whereas, in the speckle case, the Mie scattered light intensity pattern is formed by the complex phase front addition of several oil particles with the light sheet. This provides a 'more' unique Gaussian scatter distribution. The cross-correlation function formed has a wider and 'more' gradient profile. However as the interrogation window is

reduced to value close to the width of the Gaussian peak, (in this case a 16x16 pixel window) the uniqueness of the profile is reduces and the quality of the correlation falls.

A secondary factor is the two dimensional shape of the correlation profiles. The particle correlation is seen to carry an optical astigmatic distortion, due to the scheimpflug stereo configuration used. This does incur an error in the velocity correlation; whereas the speckle correlation shows less evidence of the distortion.

Thus for a spray distribution which falls below a conventional visualisation of the particles field, a Mie scattered speckle approach is a valid measurement method of calculating position and velocity. The secondary aspect, particle size determination has been described in the 'Further Work' chapter but not experimentally investigated.

Chapter8. Conclusion and Further Work

8.1. Conclusion

8.1.1. Development of Spray Visualisation System

In this thesis, a design and construction of a fluid spray visualisation system (Figure 6.10) was presented for the investigation of fuel injection solutions for small rotary engines. The visualisation system performed laser sheet imaging and backlight shadowgraphy on high speed sprays using class-4 Nd:YAG pulsed laser and high-resolution CCD cameras for the data acquisition of the kerosene (JP8) fuel using different atomisers at low injection pressure levels (1-10 bar). A programmable electronic control system was developed in order to produce the required control signals for synchronising the laser sheet with the cameras and fuel injectors. The overall spray visualisation was used to extract the spray pattern, tip penetration and cone-angle. Successive images were captured using short time delay (5-50 microseconds) for the investigation of the velocity distribution of the spray droplets. The fluid discharge velocity was accurately calculated and compared against the group velocity of the atomised fluid and connected with the mean droplet diameter (Figure 2.4).

8.1.2. Droplet Size Measurement Using Microscopic Shadowgraphs

A long-range microscope with a flat focal plane and shallow depth of focus was employed for the microscopic imaging of the fuel droplets at 3.5-100 microns diameter range. Using careful calibration and high contrast backlight (diffused lighting) method, the imaging limit of the microscope was found to be 885 nm per pixel, which is comparable with

current research. Laser diffraction methods are unable to provide an accurate size measurement of non-spherical droplets. The sphericity assumption is only acceptable for very small and slow droplets located sufficiently downstream the primary break-up region of a spray where the Weber number is extremely small. The external forces in this case are not sufficient to cause any change in the droplet shape. Using imaging based diffraction techniques, small droplets were much more difficult to detect by their scattering pattern than large droplets due to the significant change on the light intensity level for small diameter changes (see Figures 5.4 and 5.5). Therefore, light scattering measurements of droplets at the Rayleigh range (k.r <1) require sensitive optical sensors that cover a wide dynamic range of optical intensity. Shadowgraph imaging method was found to be an effective method for particle size analysis of non-spherical micro-droplets. The images obtained were used to calculate the droplet size distribution, the SMD and the AMD of the fuel spray at particular points of the spray area. The effect of the injection pressure on the droplet size was also investigated (Figures 7.25 and 7.28). It was found that when discharged at higher pressure levels, fluids are more likely to produce smaller droplets at an early stage of the injection period. In this case, droplets with a low Weber number (less than 10) are generated, travelling at low velocity and increasing the cone-angle. At lower pressure levels, a central jet with relatively large droplets (higher than 100 microns in diameter) was formed, causing a late disintegration of the jet, and consequently larger mean diameter. It was also found that evaluated electrical fuel injectors produce smaller droplets when operated at higher frequency for the same pressure level.

8.1.3. **Novel Injection System**

A new injection solution using a micro-dispensing system (Lee, medical system) was introduced in order to meet the light-weight, high-speed, low flow rate engine requirements, producing an effective fuel atomisation at low fluid pressure levels (3-5 bar) for the cold start of the engine. The frequency response of the fuel injectors and its influence on the spray characteristics was reviewed in the case for an injection frequency in the range 0.25 – 3.3 kHz. Increasing the injection frequency was found to increase the global surface area of the spray. However, increasing the injection frequency up to a critical top frequency had a negative effect on the response of the electromagnetic mechanism of the injector. This was found to reduce the spray global area and the fluid delivery rate.

The Lee micro dispenser was found to provide sprays wider in angle and higher in the global area than in the conventional injector, using approximately 10 times higher injection frequency. The high injection frequency offers more freedom in the control of the flow rate using multiple injections per revolution, hence allowing operation at higher engine speed.

The effect of introducing solid surfaces in front of the spray flow, such as sharp edges and heater matrixes, was also investigated. It was found that a singular sharp edge downstream of the nozzle exit, at a distance far enough not to disturb the primary break-up, can improve the atomisation of the central jet and increases its surface area. The heater matrix, switched off soon after the engine started, had a negative impact on fuel atomisation. Droplets were found to condense on the fins surface producing a larger drop distribution (Figure 5.14).

8.1.4. **Velocity Distribution Using PIV**

Particle image velocimetry (PIV) analysis was conducted on different sprays for tracking the velocity changes on the spray components during the injection incident. It was noticed that the discharge velocity increases when the injection pressure is increased. The central jet velocity after atomisation (approximately 2 ms ASOI) was found to be lower in the high pressure case than in the low pressure case. This is due to the higher friction losses on the small droplets produced by the high pressure.

The start of fluid disintegration could be observed around 400 microsecond ASOI where fluid ligaments at the jet surface (Figure 7.34 for 600 μs ASOI). The fluid disintegration was found to start by forming small elements of Vorticity, pushing the small droplets back toward the nozzle exit. The higher the Weber number is at the moment of fluid discharge, the slower the velocity components of the spray by the end of the injection cycle.

As the injection pressure was increased, higher velocity droplets started disintegrating from the jet surface, spreading to wide angles (15-20°) by the end of the injection cycle. The velocity of the new droplets dropped rapidly to less than 8 m/s at the spray peripheries. The high discharge velocity (high Weber number) causes a rapid atomisation at an early stage of the injection incident, while large droplets are formed in the central jet due to the poor atomisation at low pressure levels.

Different injectors were found to have different velocity distribution. The four-orifice gasoline injector for example generated a disruption area in the central part of its spray (Figure 7.35). Droplet tracking at the microscopic range was also investigated, using high resolution imaging (1.24 - 5.5 microns per pixel), and the results were compared with the mean droplet diameter data (Figure 7.38).

8.1.5. **Light Scattering of Seeding Particles**

The light scattering (Mie) theory was reviewed and applied for determining the camera view angle in the optical diagnostics of fluid droplets. The theory was used to address a number of seeding related problems in a stereoscopic PIV system using oil smoke seeders (AMD=0.3 microns). Laser diffraction experiments were carried out and the results were compared with the theoretical analysis. A very good agreement was found between them, which was validated by further experimental work on the jet engine noise test conducted in QinetiQ NTF.

Laser scattering of large droplets (more than 100 microns in diameter) was investigated in (section 5.5). It was noticed from the images taken at (90°) angle that the "edge" and "surface wave" phenomena became more dominant than the light corona generated by the light diffraction effect for this type of droplets.

The correlation quality of the normalised cross-correlation function in PIV systems was investigated using the jet flow data. Different correlation patterns were detected for different seeding materials due to the differences in shape and optical properties. Although smaller correlation interrogation windows lead to a higher resolution velocity vector field, decreasing the window can result in the reduction of the correlation quality. This was found to be the case because part of the Gaussian speckle pattern is lost in the small window. Therefore, more than one correlation point could be found within the image frame due to the lack of uniqueness of the scattering patterns. In this case, the particle displacement using the peak correlation point could lead to misleading results. An error factor (R) was defined instead, where the "degree of correlation" was dependent on the contrast of the peak correlation point against the rest of the correlation image.

In general, solid particles were found to correlate better than fluid droplets for the same seeding concentration. The reason is the complex speckle pattern of the solid seeding particles.

8.1.6. **Image Processing**

Using image processing, statistical information regarding spray patterns was acquired. This mainly involved image threshold and edge detection techniques. The spray formation process, especially during early atomisation stages, was investigated and discussed against injection pressure and frequency. The tip penetration of the spray was calculated against different time delay settings.

Several factors were defined for the comparison between the characteristics of the different sprays including: the spray sheet 2D area, the mean image energy map (light scattering), and the PCA indicator in the spray degree of disintegration.

Using the first PCA component, it was possible to detect the similarity in the spray images at any instant during the injection cycle. The PCA indicator enabled tracking the fluid disintegration process at an early stage of the injection incident. Images with low PCA first-coefficient have more random elements (instability) and therefore a better atomisation quality.

Colour-coded dispersion maps of a spray can be generated using the mean-image of a number of unsaturated samples under the same conditions. The overall image energy using laser scattering method represents the spray surface area since the light intensity is proportional to the droplet diameter squared in the Mie diffraction region.

The comparison between the group velocity calculation and the velocity distribution calculation (via PIV) showed that both methods can accurately estimate the tip penetration of a spray. However, the group velocity calculation using image threshold is more related to the high velocity components in the central jet. This is because the small droplets have lower diffraction efficiency than large droplets and they may be eliminated by the threshold. The PIV analysis provided more detailed information about velocity changes and it is independent of the light intensity since no threshold is needed. The PIV results showed the overall velocity distribution of the flow.

8.1.7. Flow Rate Calculation and Evaporation Rate Estimation

The flow rate of the fuel injectors was measured against the injection pressure (Figure 7.22), frequency (Figure 7.20) and duty cycle ratio (Figure 7.21). The new atomiser (Lee) was found to be a superior atomiser to the conventional gasoline injector, but with 3.5 times lower flow rate at the same pressure levels. This was found advantageous in the current engine design. The low flow rate and the high operating frequency of the injector can improve the freedom of the fuel delivery process by including several injection pulses per revolution. The high control of the pulse width can be used in developing adaptive injection systems, where changes in the engine operating parameters (such as speed, load and temperature) are followed by instantaneous change in the fuel delivery rate.

A theoretical study concerning the evaporation rate of the kerosene was presented using the available resources in literature. The droplet lifetime graph was generated and discussed in light of the current rotary engine requirements (Figure 3.3).

8.2. Further Work

The Lee injector is planned to be fitted into the current engine design in the near future. The fuel efficiency of the engine can be then calculated in order to evaluate the possible gain by using the new injection strategy. An optical window could be then designed for an inside engine flow analysis which would show the mechanism of fuel-air mixing inside the combustion chamber and the effect of the rotor motion. Other types of fuel could be tested, providing that the rotary engine is more suitable for alternative fuels with lower octane number than a conventional piston engine.

An experimental study of the evaporation rate on individual kerosene droplets could be performed using high-speed video camera in order to confirm the results reported in literature. The effect of temperature on the atomisation process could be further investigated. A CFD simulation of the sprays generated by the current nozzles can be produced and compared with the experimental results reported in this research (Appendix 8.1). A new nozzle design can be then introduced to optimise the flow-rate and spray area for the engine design. However, fluid sprays simulations are not sufficient in calculating the velocity distribution of the droplets or the flow rate of the fluid, but it can be useful in investigating the effect of the fluid and ambient pressure on the overall spray pattern.

In the microscopic shadowgraphy, the number of rejected droplets can be reduced by applying diameter correction for the out-of-focus particles using a Gaussian fit or by the calibration using the point spread function (similar to that in [Fdida & Blaisot (2010)]. The sampling mechanism could be automated for covering the entire spray dispersion area in the particle size distribution analysis. Imaging based analysis of droplet diameter using the Mie diffraction pattern could be further investigated using the available data, starting with

calibration using individual droplets with defined diameter (see [Ren *et al.* (1996)] for a simulation results about diffraction at 90 degree using water droplets). The problem with the scattering pattern image is that the spatial position of the droplet is not determined by the diffraction pattern. One solution could be by using a stereoscopic imaging to provide a 3D image of the particle.

The limit of the imaging based system in the current research was 3.5 microns particles, which was satisfactory to the project objectives. The resolution of the microscopic imaging system is dependent on the numeric aperture and the wavelength of the illumination source (equation 4-7). The Mie theory can be further applied in order to measure droplets at the sub-micron range where measurements using microscopic shadowgraphy are not possible. Sub-micron droplet and particle measurements are of importance to PIV seeding and fuel evaporation applications. This could be performed by studying the diffraction pattern of individual fluid droplets. This may be possible by the optical coherence tomography (OCT) using the partial coherence of the light source to accurately determine the position of a particle with a few micrometres resolution. The particle size can be then estimated by comparing the intensity ratio of the scattered light with the corresponding Mie curve.

Another method for sub-micron particle sizing is by using a wide-spectrum light source (halogen lamp for example) then measuring the spectrum variation of the scattered light [see Xu (2007)]. The scattering efficiency of a particle/droplet is dependent on the wavelength, view angle, refractive index, and diameter. Therefore, by measuring the scattered light intensity at a certain view angle, using a number of the wavelengths or a wide-spectrum light source, it is possible to estimate a particle diameter from the Mie curve of the same wavelength band. This method is known in the particle sizing literature [Xu

(2007), Cai & Wang (1992), Dellago & Horvath (1993)] as light extinction method (LEM). This method has been used to estimate the average droplet size and concentration over a small area of a particle system. This method allows estimating a droplet diameter (0.1 – 5 microns) by calculating the ratio of the Mie extinction efficiencies (Figure 5.9) of two or more wavelengths. The effect of the wavelength variation on the scattering efficiency was previously reviewed in section 5.3.5 (see Figure 5.10).

The light scattering experiment in section 5.6 was carried out using a monochromic illumination source (532 nm), but for several angles. Because of the good agreement between the experimental results and the Mie curve for the oil droplets (0.3 microns), it could be possible to estimate the mean droplet size using the Mie curves at different view angles (Figure 5.11).

Similarly, for the jet flow data, it could be possible to estimate the mean diameter of the seeding particles using different view angles and different seeding materials (different refractive indices). Images were taken using three cameras looking at three different angles, containing aluminium oxide particles and oil smoke in the same image frame. Therefore, by comparing the intensity levels, the particle diameter can be located on the Mie scattering curve for the selected angles and refractive indices. Avoiding the sensor saturation with high intensity elements is essential in this case, in order to follow the intensity variations in the image.

A commercial three camera system has been developed by LaVision, which uses cross-correlation to determine tomographically the position of particulates within a defined light sheet. Currently, this is for a positional accuracy of 50 µm but could be extended using the K2 imaging lens (similar to the one used in this thesis) to a positional accuracy of the order

of 10µm. Finally it has yet to be determined if the diffraction light scattering speckle measurements described in this thesis could be extended to identify the actual scattering body.

To summarise, this section described how to create a global visualisation which simultaneously identifies particle size, position, velocity and cloud density. By combining a multi-camera Mie intensity ratio mapping it should be possible to identify a sub-micron particle distribution. This is of value, for example, for measuring jet spray evaporation rates and for combustion particulates which are typically in the range 0.1 to 0.5µm.

List of References

Abraham J., Wey M.J., and Bracco F.V. (1988), "Pressure Non-Uniformity and Mixing Characteristics in Stratified-Charge Rotary Engine Combustion", SAE technical paper, no.880624, in the International Congress and Exposition, Detroit, Michigan

Adrian R. J. and Westerweel J. (2011), "Particle Image Velocimetry", Cambridge University Press

Adrian R. J. and Yao C. S. (1985), "Pulsed laser technique application to liquid and gaseous flows and the scattering power of seed materials", Applied Optics, Vol. 24, No. 1, pp.44-52

Akhmanov S.A. and Nikitin S.Yu (1997), "Physical Optics", Oxford University Press

Anderson W., et al. (1996), "Understanding the thermodynamics of direct injection spark ignition (DISI) combustion systems: an analytical and experimental investigation", SAE Technical paper, 962018

Annamalai K. and Puri I.K. (2007), "Combustion Science and Engineering", CRC series in Computational Mechanics and Applied Analysis, Taylor & Francis

Ansdale R.F. (1968), "The Wankel RC Engine; Design and Performance", Iliffe Books Ltd., London

Armaroli N. and Balzani V. (2011), "Energy for a Sustainable World: From the Oil Age to a Sun-Powered Future", Wiley-VCH

Arregle J., Pastor V. and Ruiz S. (1999), "The Influence of Injection Parameters on Diesel Spray Characterization". SAE1999-01-0200

Babajimopoulos A., Lavoie G.A. and Assanis D.N. (2003), "Modeling HCCI Combustion with High Levels of Residual Gas Fraction – A Comparison of Two VVA Strategies", SAE paper no. SAE 2003-01-3220.

Bae C.; Yu J.; Kang J.; Kong J.; and Lee KO. (2002), “Effect of nozzle geometry on the common-rail diesel spray”. SAE Paper No. 2002-01-1625.

Bejan A. and Kraus A. D (2003), “Heat Transfer Handbook”, John Wiley & Sons, pp.1359-1400

Benjamin C. (2005), “The Modern Revolution in Physics”, 3rd ed, Light & Matter, USA

Berthier J. (2008), “Microdrops and Digital Microfluids”, William Andrew Inc, USA

Berthoumieu P, Carentz H, Villedieu P (1999), “Contribution to droplet breakup analysis”, International Journal of Heat and Fluid Flow, 20, pp.492-498

Bohren C.F. and D.R. Huffman (1983), “Absorption and Scattering of Light by Small Particles”, John Wiley, New York, NY.

Brennen C.E. (2005), “Fundamentals of Multiphase Flows”, Cambridge University Press

Brewster M.Q (1991), “Thermal radiative transfer and properties”, John Wiley & Sons.

Cai X.S and Wang N.N (1992), “Determination of particle size distribution using the light extinction method”, Advanced Power Technology, Vol.3, No.3, pp. 153-161

Chang W.S.C. (2005), “Principles of Lasers and Optics”, Cambridge University Press, UK

Chathcart G. *et al*.(2005), “The Application of Air-Assist Direct Injection for Spark-ignited Heavy Fuel 2-Stroke and 4-Stroke”, SAE, 32-0065

Chin J.S. and Lefebvre A.H. (1931), “Steady-State Evaporation Characteristics of Hydrocarbon Fuel”, Vol. 23, No. 4, pp.360-364

Choi S. and Oh Y. (2011), “A study on spray characteristics of non-esterified biodiesel fuel”, ScienceAsia 37: pp.174–177

Combustion & Flow Diagnostics (Part A&B).Vol. 2002-01-0747. Presented at SAE 2002 World Congress & Exhibition, SAE, Detroit, MI, USA.

Comeau D., LaTourette K., and Pate J. (2007), “The effect of Weber number and spread factor of a water droplet impinging on a super-hydrophobic substrate”, Program in

Applied Mathematics, University of Arizona Tucson, AZ USA 85721, available online: *math.arizona.edu/~dcomeau/research/CLPpaper.pdf*

Cookson *et al.* (1987), "Investigation of the Chemical Basis of Kerosene (Jet Fuel) Specification Proper ties", Energy & Fuels , 1, pp. 438-447

Crowe C.T. ; Sommerfeld M; and Tsuji Y (1998), "Multiphase Flows with Droplets and Particles", CRC Press, USA

Crua C. (2002), "Combustion Processes in a Diesel Engine", PhD thesis, University of Brighton, UK

Curry C. (1957), "Wave Optics; Interference and Diffraction ", Edward Arnold Ltd., London

Dagaut P. and Cathonnet M. (2006), "The ignition, oxidation, and combustion of kerosene: A review of experimental and kinetic modeling", Progress in Energy and Combustion Science, Vol. 32, Issue 1, pp. 48-92

Dechoz J and Rozé C (2004), "Surface tension measurement of fuels and alkanes at high pressure under different atmospheres", Applied Surface Science, vol. 229, Issues 1-4, 15, pp. 175-182

Dellago C. And Horvath H. (1993), "On the accuracy of the size distribution accuracy of the size distribution information obtained from light extinction and scattering measurements- I. Basic considerations and Models", J. Aerosol Sci., Vol. 24, No. 2, pp. 129-141

Dormanb R. G. *et al.* (1951), "The Atomization of Liquid in a Flat Spray", Br. J. Appl. Phys., vol.3, pp.189-192

Drain L.E. (1980), "The Laser Doppler Technique", John Wiley & Sons Ltd., UK

Esmail M, Kawahara N, Tomita E, and Sumida M (2010), "Direct microscopic image and measurement of the atomization process of a port fuel injector", Measurement Science and Technology (IOP), 21 (2010) 075403 (11pp)

Faiz A, Weaver C.S, Walsh M.P (1996), "Air pollution from motor vehicles: standards and technologies for controlling emissions", The World Bank, Washington, USA

Fdida N. and Blaisot J. (2010), “Drop size distribution measured by imaging: determination of the measurement volume by the calibration of the point spread function”, IOP, Meas. Sci. Technol. 21 (15pp)

Ferguson C.R. and Kirkpatrick A.T (2001), “Internal Combustion Engines”, 2nd Ed., John Wiley & Sons, USA.

Fleming J.W. *et al.* (2001), “ Water Mist Monitoring in Large-Scale Fire Suppression Research: Fundamental Issue”, Halon Options Technical Working Conference, pp. 397-406

Ganesan V. (1996), “Internal Combustion Engines”, McGraw-Hill, USA

Garrett T K (1991), “Automotive Fuels and Fuel Systems; Gasoline”, volume.1, Pentech press, London.

Garrett T K (1994), “Automotive Fuels And Fuel Systems; Diesel”, volume.2, Pentech press, London.

Ghassemi H.; Baek S. W.; and Khan Q. S. (2006), “Experimental Study On Evaporation Of Kerosene Droplets AT Elevated Pressures And Temperatures”, Combust. Sci. and Tech. (Taylor & Francis), Vol. 178,pp. 1669–1684.

Gilles T. (2004), “Automotive service: inspection, maintenance, repair”, 2nd Ed., Thomson Delmar Learning, USA

Glassman I, and Yetter R.A. (2008), “Combustion”, 4th ed., Elsevier, 2008

Glassman I, edited by Dryer F. L. and Sawyer R. F. (1997), “Physical and chemical aspects of combustion: a tribute to Irvin Glassman”, Gordon and Breach

Godefory C. And Adjouadi M.(2000), “Particle sizing in a flow environment using light scattering patterns”, Wiley InterSience, Particle and particle systems characterization, Vol. 17 Issue 2, pp. 47 – 55

Gordon D. G. (1959), “Mechanism and Speed of Breakup of Drops”, J. of Appl. Phys. v.30, no. 11, pp. 1759-1761.

Graeme J. (1996), “Photodiode Amplifiers; Op Amp Solutions”, McGraw-Hill, USA

Grehan G, Gouesbet G, and Guilloteau F, “Comparison of the diffraction theory and the generalized Lorenz-Mie theory for a sphere arbitrarily located into a laser beam”, Optics Communications, Vol. 90, Issues 1-3, pp.1-6, 1992

Guerrero et al. (2000), “Particle positioning from CCD images:experiments and comparison with the generalized Lorenz–Mie theory”, Meas. Sci. Technol. 11 , pp. 568–575.

Guerrero J A, et al. “Particle positioning from CCD images: experiments and comparison with the general Lorenz-Mie theory”, Measurement Science and Technology, Vol. 11, No. 5, pp. 568-575, 2000

Guildenbecher et al.(2011), “Droplet Deformation and Breakup”, in Ashgriz (Ed.), “Handbook of Atomization and Sprays; Theory and Applications”, Springer

Guildenbecher, et al.(2011), “Droplet Deformation and Breakup”, in Ashgriz (Ed.), “Handbook of Atomization and Sprays; Theory and Applications”, Springer

Gupta S. C. (2005), “Optoelectronic Devices and Systems”, Prentice-Hall of India Pvt.Ltd

Hahn D.W., “Light scattering theory”, University of Florida, 2009, available online: http://plaza.ufl.edu/dwhahn/Rayleigh%20and%20Mie%20Light%20Scattering.pdf

Harstad K. and Bellan J. (2004), “Modeling evaporation of Jet A, JP-7, and RP-1 drops at 1 to 15 bars”, Elsevier, Combustion and Flame, Vol.137, Issues 1-2, pp. 163-177

Hasegawa Y. and Yamaguchi K. (1993), “An experimental Investigation on Air-Fuel Mixture Formation Inside a Low-Pressure Direct Injection Stratified Charge Rotary Engine”, SAE technical paper, no.930678, International Congress and Exposition, Detroit, Michigan, 1993

Hemighaus G, *et al.* (2006), “Aviation Fuels Technical Review”, Chevron Corporation

Hewitt A J. *et al.* (1997), “The Importance of Droplet Size in Agricultural Spraying”, Atomization & Sprays, vol. 7 (3), pp. 235 – 244

Hoffman J A. *et al.* (1997), "Comparison between air-assisted and single fluid pressure atomizers for direct injection SI Engines via spatial and temporal mass flux measurements", SAE, 970630

Holst G. C. (1998), "CCD Arrays Cameras and Displays", JCD publishing and SPIE Optical Engineering Press, Washington USA

Hwang J. S., Ha J. S. and No S. Y.(2003), " Spray Characteristics of DME in Conditions of Common Rail Injection System (II)", International Journal of Automotive Technology, Vol. 4, No. 3, pp. 119−124

IWP023 Datasheet, available online http://www.compsystems.com.au/

Iyer V., Abraham J. (1997), "Penetration and Dispersion of Transient Gas Jets and Sprays", Combustion Science and Technology", 130: 1, pp. 315 - 334

J. Choi; S. Lee, H. Shin; and C. Bae, "Fuel-Spray characteristics of high pressure gasoline injection in flowing fields", JSME Int J Ser B, Vol. 43, No. 4, p. 576-581, Japan 2000

Jiang Y., et al. (2010), "Measuring particle size distribution using LED-illumination", International Journal of Multiphase Flow 36 (2010) pp. 193–201

Jones R. M. (2003), "Particle size analysis by laser diffraction", ISO 13320 standard report, Malvern Instruments Ltd, UK, 2003.

Julian T. Kashdan, John S. Shrimpton, Adam Whybrew (2007), "A digital image analysis technique for quantitative characterisation of high-speed sprays, Optics and Lasers in Engineering", Vol. 45, Issue 1, pp. 106-115

Kagawa R., Okazaki S., Somyo N., and Akagi Y. (1993), "A Study of a Direct-Injection Stratified-Charge Rotary Engine for Motor Vehicle Application", SAE technical paper, no.930677, International Congress and Exposition, Detroit, Michigan

Kamo R.; Yamada T.Y.; and Hamada Y. (1987), "Starting Low Compression Ratio Rotary Wankel Diesel Engine", SAE technical paper, no.870449, International Congress and Exposition, Detroit, Michigan

Karimi K.; *et al.* (2006), “Developments in Diesel Spray Characterisation and Modelling”, THIESEL 2006 Conference on Thermo- and Fluid Dynamic Processes in Diesel Engines.

Kay P.J. (2006), “Characterising Thermofluid Spray Dynamics For Energy-Efficient Automotive Engines”, PhD thesis, the University of Wales, Cardiff

Kennaird D.; Crua C.; Lacoste J.; Heikal M.R.; Gold M.R. and Jackson N. (2002), “In-cylinder penetration and break-up of diesel sprays using a common-rail injection system” In: SAE spring fuels and lubricants meeting and exhibition, SAE paper 2002-01-1626

Kihm K.D. and Chigier N. (1991), “Effect of Shock Waves on Liquid Atomization of a Two-Dimensional Airblast Atomizer”, Atomization and Sprays, vol.1, issue.1, pp.113-136

Klein-Douwel R.J.H., et al. (2007), “Macroscopic diesel fuel spray shadowgraphy using high speed digital imaging in a high pressure cell”, Fuel (Elsevier), Vol. 86, Issues 12-13, pp. 122-132

Kleinstreuer C (2003), “Two-Phase Flow; Theory and Applications”, Taylor & Francis, USA

Koechner W. (2006), “Solid-state laser engineering”, Springer, USA.

Krier H. and Wronkiewicz J.A. (1972), “Combustion of Single Drops of Fuel”, Combustion and Flame Vol.18, pp.159-166

Kumar K., Sung C.J. (2010), “An experimental study of the autoignition characteristics of conventional jet fuel/oxidizer mixtures: Jet-A and JP-8” , Combustion and Flame, Volume 157, Issue 4, April 2010, Pages 676-685

Kutz, M (2006), “Mechanical Engineers' Handbook - Energy and Power”, 3rd Ed., John Wiley & Sons, pp.573-613

Laufer G. (1996), “Introduction to Optics and Lasers in Engineering”, Cambridge University Press

Laven P. (2010), “Separating diffraction from scattering: the million-dollar challenge” Journal of Nanophotonics, Vol. 4, 041593

Lawes. M (2007), “Diffusion flames, droplet evaporation and droplet combustion”, online book: http://www.scribd.com/doc/34293208/Droplet-Combustion

Lee C.H., Lee K.H., and Lim K.B. (2010), “Effects of injection parameters on the spray characteristics of swirl and slit injectors using the Mie-scattering method”, International Journal of Automotive Technology, Vol. 11, No. 3, pp. 435−440 (2010)

Lee C.S.; Chon M.S.; and Park Y.C. (2001), “Spray Structure of High Pressure Gasoline Injector in a Gasoline Direct Injection Engine”, International Journal of Automotive Technology, Vol. 2, No. 4, pp. 165-170

Lee K.; et al.(1999), “The development of planar imaging technique for spray characterization”, IEEE Lasers and Electro-Optics, 1999. CLEO/Pacific Rim '99., vol.2, pp. 163 – 164

Lee S.Y. and Kim Y.D. (2004), “Sizing of Spray Particles Using Image Processing Technique”, KSME International Journal, Vol. 18 No. 6, pp. 879 -894

Lefebvre A.H. (1989), “Atomization and Sprays”, Hemisphere Publishing, USA 1989

Ley I (1999), “Particle size analysis- Evaluation laser diffraction systems”, ISO 13320-1 standard report, UK.

Lin S.P. (2003), “Breakup of Liquid Sheets and Jets”, Cambridge University Press, UK

Louthan L. (1993), “Development of a Lightweight Heavy Fuel Rotary Engine”, SAE technical paper, no.930682, International Congress and Exposition, Detroit, Michigan, 1993

Lu P. L., et al (1978), “Relation of chemical and physical processes in two-phase detonations”, Acta Astronautica, UK, Vol. 6, pp. 815-826

Ludlow I K, “Application of Riccati-Bessel functions in light scattering”, 11th Electromagnetic and Light Scattering Conference, pp.57-60, UK. Available online: https://uhra.herts.ac.uk/dspace/bitstream/2299/4077/1/903686.pdf

Maheu B, Gréhan G, and Gouesbet G, “Generalized Lorenz-Mie theory: first exact values and comparisons with the localized approximation”, Applied Optics Vol. 26, No. 1, pp.23-25, USA 1987

Makartchouk Andrei (2002), “Diesel Engine Engineering; Thermodynamics, Dynamics, Design, and Control”, Marcel Dekker, USA

Malacara D. and Thompson B.J. (2001), “Handbook of Optical Engineering”, Marcel Dekker, New York USA

Malot H and Blaisot J (2000), “Droplet Size Distribution and Sphericity Measurements of Low-Density Sprays Through Image Analysis”, Part. Part. Syst. Charact. 17 (2000), pp. 146-158

Mätzler C.(2002), “MATLAB Functions for Mie Scattering and Absorption”, Research Report, Institute of Applied Physics, University of Bern

Mätzler, C.(2002), “Drop-size distributions and Mie computations for rain .” IAP research report.

McGraw-Hill Encyclopedia of Science and Technology, Online version, available at : http://www.accessscience.com/

Melling A (1997), “Tracer particles and seeding for particle image Velocimetry”; Meas. Sci. Technol. 8 1406–16

Merrington, A. C., and Richardson, E. G. (1947), “The Break-Up of Liquid Jets”, Proc. Phys. Soc. Vol. 59, No. 33, pp. 1-13, London

Milonni P. W., Eberly J. H. (2009), “Laser Physics”, John Wiley & Sons.

Morgan R., Wray J., Kennaird D.A., Crua C. and Heikal M. (2002), “The Influence of Injector Parameters on the Formation and Break-Up of a Diesel Spray”, SAE 2001 Transactions Journal of Engines, 110 (3). pp. 389-399.

Muroki T., Kono S., Nagao A. (1986), “Mazda Rotary Engine Technology; Combustion Characteristics”, 21st IECEC, Vol.1, pp.361-366, San Diego, California

Naber J. and Siebers D.L. (1996), “Effects of Gas Density and Vaporization on Penetration and Dispersion of Diesel Sprays”. SAE960034

Nair S (2006), “Acoustic Characterization Of Flame Blowout Phenomenon", PhD thesis, Georgia Institute of Technology

Nakamura J. (2006), “Image Sensors and Signal Processing for Digital Still Cameras”, CRC Taylor & Francis, USA

Nasr G.G.; Yule A.J.; and Bendig L. (2002). “Industrial Sprays and Atomization; Design, Analysis and Applications”, Springer-Verlag London, UK, 2002

Nigmatulin R.I. (1991), “Dynamics of Multiphase Media”, Vol.1, translated from Russian edition, Hemisphere Publishing.

NOAA (National Oceanic and Atmospheric Administration), USA, Database of Hazardous Materials, available online at: http://cameochemicals.noaa.gov

Ochoterena R., Lif A., Nyden M., Andersson S., and Denbratt I. (2010), “Optical studies of spray development and combustion of water-in-diesel emulsion and microemulsion fuels”, Fuel (Elsevier), Vol. 89, Issue. 1, pp. 122-132

Okuda T.; Tomine K.; and Sugawara H. (2009), “Direct Photographic Method for Measuring Droplet Size Distribution in Fog”, SOLA, Vol. 5, pp.13-16

Okui N. et al. (2009), “Ignition and Combustion of Rotary Engine; Effect of spark-plug arrangement on flame propagation”, Review of Automotive Engineering, JSAE 20094643, vol.30, pp.379-385, 2009

Oppenheim A.K. (2004), “Combustion in Piston Engines; Technology, Evolution, Diagnoses and Control”, Springer, Germany

Osuga M et al. (2004), “New Direct Fuel Injection Engine Control Systems for Meeting Future Fuel Economy Requirements and Emission Standards”, Hitachi Review, Vol. 53, No. 4, pp.193-199

Pai M.G., Bermejo-Moreno I., Desjardins O., and Pitsch H. (2009), “Role of Weber number in primary breakup of turbulent liquid jets in crossflow”, Center for Turbulence Research Annual Research Briefs 2009, pp. 145-158

Palero V. R. and Ikeda Y. (2002), "Droplet-size-classified stereoscopic PIV for spray characterization", IOP, Meas. Sci. Technol., Vol. 13 , pp. 1050–1057

Pandey S. and Kushari A. (2008), "A Controllable Twin- Fluid Internally Mixed Swirl Atomizer", Recent Patents on Mechanical Engineering, vol.1, pp.45-50

Park S.W.; Kim S.; and Lee C.S. (2006), "Breakup and atomization characteristics of mono-dispersed diesel droplets in a cross- flow air stream", International Journal of Multiphase Flow (Elsevier) Vol.32 (2006) pp.807–822.

PCO 2000 datasheet, available online http://www.pco.de/sensitive-cameras/pco2000/

PCO pixelfly datasheet, available online http://www.pco.de/sensitive-cameras/pixelfly-qe/

Pfafflin J. R.; Ziegler E. N.; and Lynch J. M. (2008), "The dictionary of environmental science and engineering", 2nd ed., Routledge, UK (available at Taylor & Francis e-library)

Pilch M. and Erdman C.A. (1987), "Use of Breakup Time Data and Velocity History Data to Predict the Maximum Size of Stable Fragments for Acceleration-Induced Breakup of a Liquid Drop," Int. J. Multiphase Flow, 13, No. 6, pp. 741-757.

Poulton M.L. (1994), "Alternative Engines for Road Vehicles", WIT press, UK

Prasad R. And Bella V.R. (2010), "A Review on Diesel Soot Emission, its Effect and Control", Bulletin of Chemical Reaction Engineering & Catalysis, 5 (2), 2010

Ren K.F et al. (1996), "On the Measurements of Particles by Imaging Methods: Theoretical and Experimental Aspects", Part. Part. Syst. Charact. 13 (1996) 156-164

Robert Bosch GmbH (2005), "Ottomotor Management", 3.Auflage, Vieweg Verlag.

Robert Bosch GmbH (2006), "Gasoline-Engine Management", 3rd Ed, John Wiley

Rüdiger Paschotta (2011 online update), "Encyclopaedia of Laser Physics and Technology", RP Photonics Consulting GmbH, available online: http://www.rp-photonics.com

Satcunanathan S. (1971), "Ignition Delay of Individual Liquid Fuel Droplets", Ind. Eng. Chem. Process Des. Dev., 1971, 10 (3), pp 297–304

Schwaller A. E. (2005), “Total Automotive Technology”, 4th Ed., Thomson Delmar Learning, USA

Seibt P (2006), Algorithmic Information Theory: Mathematics of Digital Information Processing, Springer, Chapter 5

Seneschal J., Ducottet C., Schon J. P., Champoussin J. C., and Gucher P. (2003),“Automatic system for visualization and characterization of high pressure diesel sprays”, Proceedings of PSFVIP-4, Chamonix, France, 2003.

Senft J. R. (2007), “Mechanical Efficiency of Heat Engines”, Cambridge University Press, USA.

Sennaroglu A. (2007), “Solid-State Lasers and Applications”, CRC Press 2007, available online: http://www.crcnetbase.com/doi/book/10.1201/9781420005295

Shao J. and Yan Y. (2006), “Digital Imaging Based Measurement of Diesel Spray Characteristics”, IEEE Instrumentation and Measurement Tech. Conf. Proceedings. IEEE pp. 8-11.

Shao J. and Yan Y. (2009), “Digital Imaging Based Measurement of Diesel Spray Characteristics”, IEEE Transactions on Instrumentation and Measurement, vol. 57, no. 9, pp. 2067- 2073

Shinjo J. And Umemura A. (2010), “Simulation of liquid jet primary breakup: Dynamics of ligament and droplet formation”, International Journal of Multiphase Flow 36 (2010) pp. 513–532

Skeen A.(2006), “The Development of High-Speed PIV Techniques and Their Application to Jet Noise Measurement”, PhD thesis, School of Engineering, University of Warwick, UK

Solimeno S., Crosignani B., and Porto P.D. (1986), “Guiding, Diffraction, and Confinement of Optical Radiation”, Academic Press

Sonic 35 Specifications; available online: http://www.cubewano.com/media/1219/a4_sonic35_ac.pdf

Spicher U., Weimar H.J. (1997), “Direkteinspritzung bei Ottomotoren”, Tagung: Direkteinspritzung im Ottomotor, Haus der Technik, Essen, Marz.

Stamate M., Vascan I., Lazar, G. Lazar I., Caraman I., Caraman M. (2005), "OPTICAL AND SURFACE PROPERTIES TiO2 THIN FILMS DEPOSITED BY DC MAGNETRON SPUTTERING METHOD", Journal of Optoelectronics and Advanced Materials Vol. 7, No. 2, p. 771 – 774

Strong C, Erickson C, and Shukla D (2004), "Evaluation of Biodiesel Fuel: Literature Review", Western Transportation Institute, available online: http://www.mdt.mt.gov/research/docs/research_proj/biodiesel/final_report.pdf

Taatjes C.A, Hansen N., Osborn D.L., Kohse-Höinghaus K., Cool T.A. and Westmoreland P.R. (2008). "Imaging combustion chemistry via multiplexed synchrotron-photoionization mass spectrometry" Phys. Chem. Chem. Phys., 10, pp.20-34

Tayali N.E and Bates C.J. (1990), "Particle sizing techniques in multiphase flows: A review", Flow Meas. Instrum., Vol. 1, pp.77-105

Timmerman B H, Skeen A J, Bryanston-Cross P J, Graves M J (2009); "Large-scale time-resolved digital particle image velocimetry (TR-DPIV) for measurement of high subsonic hot coaxial jet exhaust of a gas turbine engine"; Meas. Sci. Technol, 20 , 074002 (15pp)

Tjahyadi R, Liu W, Venkatesh S (2004), "Application of the DCT Energy Histogram for Face Recognition", Proceedings of the 2nd ICITA conference , pp. 305-310

Towers D. P. and Towers C. E. (2001), "Cyclic Variability Measurement in I.C. Engine In-Cylinder Flows using High Speed PIV", 4th International Symposium on Particle Image Velocimetry, Göttingen, Germany, Paper no.155

Towers D. P. and Towers C. E. (2004), "Cyclic variability measurements of in-cylinder engine flows using high-speed particle image velocimetry", Meas. Sci. Technol., vol.15, pp.1917–1925

Turns S.R. (2000), "An Introduction to Combustion; Concepts and Applications", 2nd ed. McGraw-Hill

van Basshuysen R. (2009), "Gasoline Engine with Direct Injection",1st edition (English), Vieweg+Teubner, Wiesbaden Germany.

van de Hulst H. C., “Light scattering by small particles”, Dover, New York, 1981

van den Boom H.L.G.J. (2000), “Laser Diagnostics in Diesel Engines”, PhD thesis, Radboud University Nijmegen, Netherlands

Watanawanyoo P.; Chaitep S.; and Hirahara H. (2009), “Development of an Air Assisted Fuel Atomizer (Liquid Siphon Type) for a Continuous Combustor”, Applied Sciences, vol. 6 (3): pp. 380-386

Wedd M. W. (2003), “Determination of particle size distribution using laser diffraction”, Part. Techn, 2003, no. 032Q-Wedd (2003): 5-10, available online: http://www.erpt.org/032q/wedd-02.pdf

William T.Silfvast, “Laser Fundamentals”, 2nd ed., Cambridge University Press, UK 2004

Wilson J.S. (2005), “Sensor Technology Handbook”, Elsevier, USA, Ch.14 by Kenny.T, Standford University.

Wilson T., Bryanston-Cross P., and Chana K. (2002) "High bandwidth heat transfer and optical measurements in an instrumented spark ignition internal combustion engine" in

Wu Z.; Zhu Z.; and Huang Z.(2006), “An experimental study on the spray structure of oxygenated fuel using laser-based visualization and particle image velocimetry”, Fuel 85 (2006) pp.1458–1464

Xu F (2007), “Shaped Beam Scattering by a Spheroid and Online Wet Steam Measurement by Using Spectral Light Extinction Method”, PhD thesis, Rouen University

Zakaria R, Bryanston-Cross P, Addy S (2010), “Optical Diagnostics in High-Speed Fuel Spray; Methodology and Analysis”, Photonics (ICP), 2010 International Conference on Digital Object Identifier, pp. 1 – 6

Zhao H (editor, 2007), “HCCI and CAI engines for the automotive industry”, Woodhead Publishing Ltd., Cambridge, England, 2007

Web:

http://www.bp.com/sectiongenericarticle.do?categoryId=16003555&contentId=7020878

http://www.fueleconomy.gov/feg/atv.shtml

http://www.labautopedia.org/mw/index.php/Non-Contact_Liquid_Handling:_Basics_and_Technologies

http://www.natural-gas.com.au/about/references.html (Energy contents of different fuels)

http://www.retsch-technology.com/dltmp/www/96739-5e9c989806fc/034_Laser_Diffraction_Technique_en.pdf

http://www.handprint.com/HP/WCL/color1.html

http://www.philiplaven.com/p20.html

http://www.iapmw.unibe.ch/teaching/vorlesungen/radiative_transfer/skript/Lecture2009_9.pdf

http://www.ifp.uni-stuttgart.de/publications/phowo01/Blanc.pdf

http://www.fsienergy.com/H20INOIL.htm

http://www.princeton.edu/~fldryer/nasa.dir/backgrnd.htm

http://www.mazda.com/mazdaspirit/rotary (Mazda Motor)

http://omlc.ogi.edu/cgi-bin/mie_angles.cgi?diameter=2.0&lambda_vac=0.532&n_medium=1.0&nr_sphere=1.4&ni_sphere=0&n_angles=100&density=0.01

Appendices

Appendix 2.1 : Weber Number Graph

```
% Weber number against velocity and diameter
close all;clear all
roh=1.204; % air density (kg/m3)
st=0.027; % surface tension (kerosene, +-0.002)
UL=[1:0.05:50]; % Liquid Velocity m/s
D=[1:0.5:500]; % Diameter (microns)


for i=1:size(UL,2);
for j=1:size(D,2);
We(i,j)=(roh*(UL(i)^2)*D(j))/(1000000*st);% Weber number
end
end

mesh(D,UL,We)
xlabel 'Diameter (micron)'
ylabel 'Velocity (m/s)'
zlabel 'Weber number'
colorbar
```

Appendix 2.2 : Static Drop Formation

```
function [] =StaticDrop(d1,d2,step,roh,st,g,c)


d=[d1:step:d2]./1000000; %nozzle diameter micrometer
D=((6*st.*d)/(g*roh)).^(1/3); %Droplet diameter micrometer
plot(d.*1000,D.*1000,c); grid on % mm
xlabel('Nozzle diameter (mm)')
ylabel('Droplet diameter (mm)')
x=d./D;
[v,h]=find(x>1,1,'first'); %D=d
if h~=0
    hold on; line([0 h/1000],[h/1000 h/1000],'LineStyle','-.','color',c)
else
end
```

Appendix 3.1 : Efficiency of a perfect engine for different air/fuel ratios.

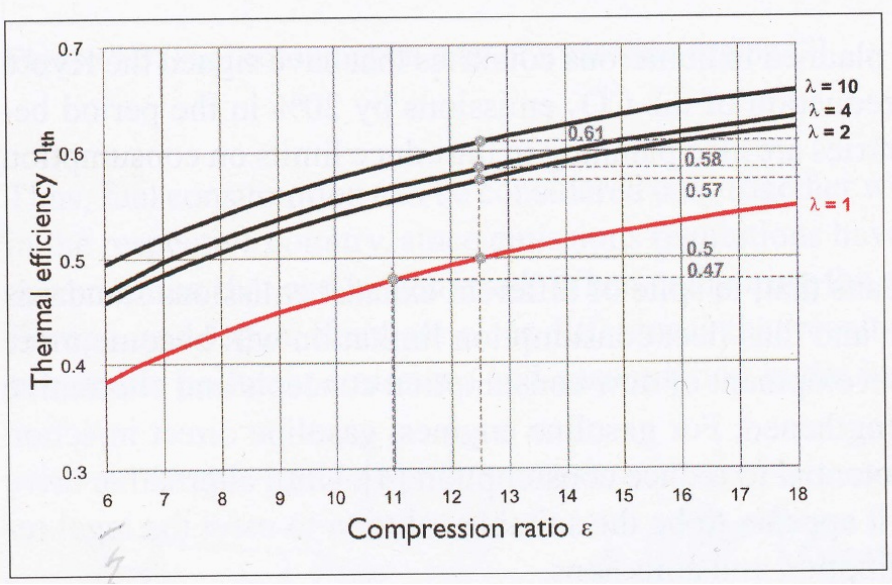

[Spicher et al. (1997), in Van Basshuysen (2009), p.187]

Note: In gasoline direct injection (GDI) engines, a jacket of non-combustible gases is used to reduce the heat transfer to the chamber walls [Robert Bosch GmbH (2006)].

Appendix 3.2: Plotting the evaporation rate of kerosene (Matlab code).

```
% Rami Zakaria, University of Warwick Sep. 2010
% this function calculate the end diameter of a kerosene drop % output,
(D)final diameter in mm
%inputs, (D0) initial diameter in mm
% rate, evaporation rate in mm2/s
% t, heating time in ms.
function [D,t0] =evap_rate(D0,rate,x,t)
D0s=D0.^2;
Ds=D0s-rate*(t/1000);
D=sqrt(Ds);
t0=x*D0s*1000;


% Calling the evaporation rate function


t=0:0.02:2;
figure;
[D,t0]=evap_rate(0.010,1.88,0.4,t);plot(t+t0,D*1000);hold on
[D,t0]=evap_rate(0.015,1.88,0.4,t); plot(t+t0,D*1000);
[D,t0]=evap_rate(0.020,1.88,0.4,t); plot(t+t0,D*1000);
[D,t0]=evap_rate(0.025,1.88,0.4,t); plot(t+t0,D*1000);
```

```
[D,t0]=evap_rate(0.030,1.88,0.4,t); plot(t+t0,D*1000);
[D,t0]=evap_rate(0.035,1.88,0.4,t); plot(t+t0,D*1000);
[D,t0]=evap_rate(0.040,1.88,0.4,t); plot(t+t0,D*1000);

[D,t0]=evap_rate(0.010,0.92,0.5,t);plot(t+t0,D*1000, 'r');
[D,t0]=evap_rate(0.015,0.92,0.5,t); plot(t+t0,D*1000, 'r');
[D,t0]=evap_rate(0.020,0.92,0.5,t); plot(t+t0,D*1000, 'r');
[D,t0]=evap_rate(0.025,0.92,0.5,t); plot(t+t0,D*1000, 'r');
[D,t0]=evap_rate(0.030,0.92,0.5,t); plot(t+t0,D*1000, 'r');
[D,t0]=evap_rate(0.035,0.92,0.5,t); plot(t+t0,D*1000, 'r');
[D,t0]=evap_rate(0.040,0.92,0.5,t); plot(t+t0,D*1000, 'r');

[D,t0]=evap_rate(0.010,0.42,0.9,t);plot(t+t0,D*1000, 'g');
[D,t0]=evap_rate(0.015,0.42,0.9,t); plot(t+t0,D*1000, 'g');
[D,t0]=evap_rate(0.020,0.42,0.9,t); plot(t+t0,D*1000, 'g');
[D,t0]=evap_rate(0.025,0.42,0.9,t); plot(t+t0,D*1000, 'g');
[D,t0]=evap_rate(0.030,0.42,0.9,t); plot(t+t0,D*1000, 'g');
```

Appendix 3.3: Dependency of evaporation rate on ambient pressure.

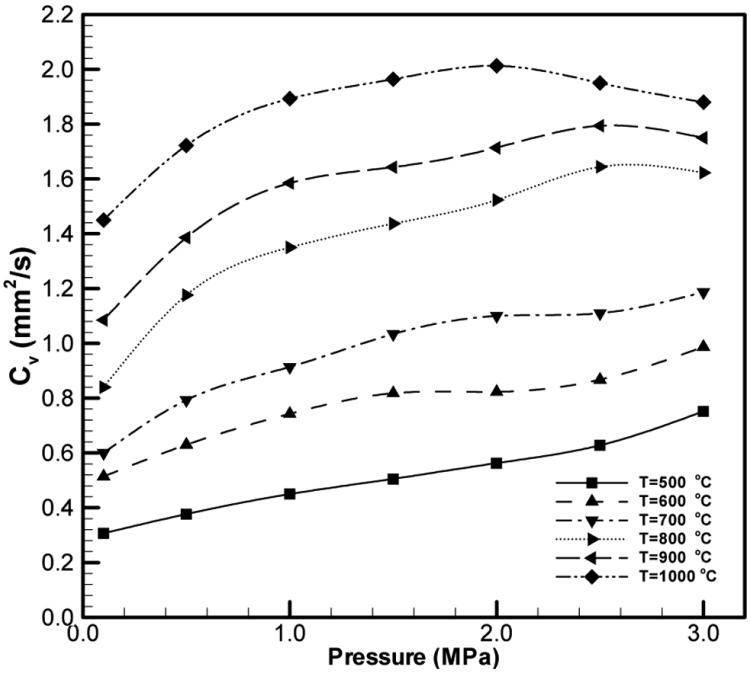

[Ghassemi et al (2006)]

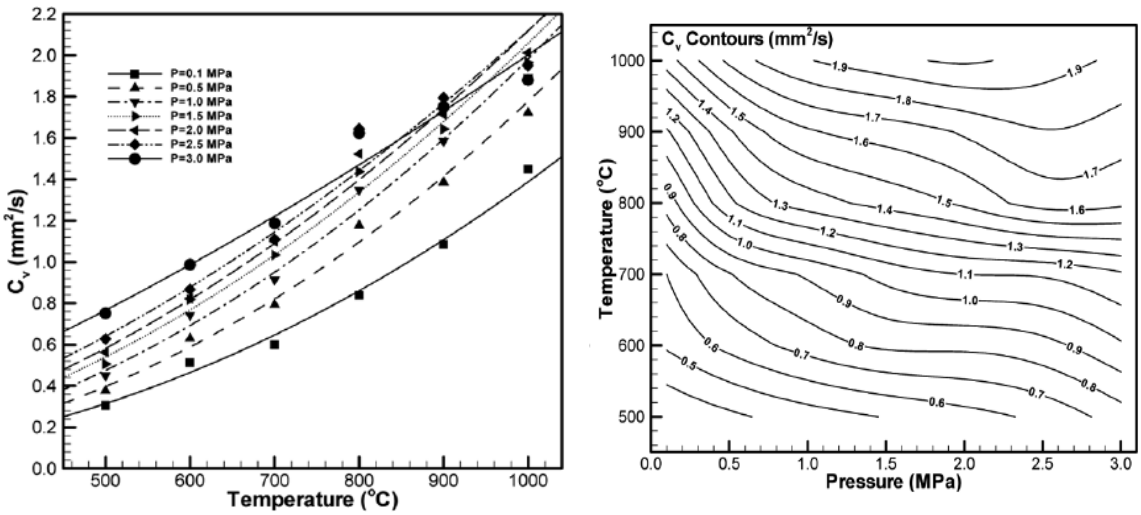

[Ghassemi et al (2006)]

Appendix 3.4: Influence of droplet size and air temperature on droplet lifetime.

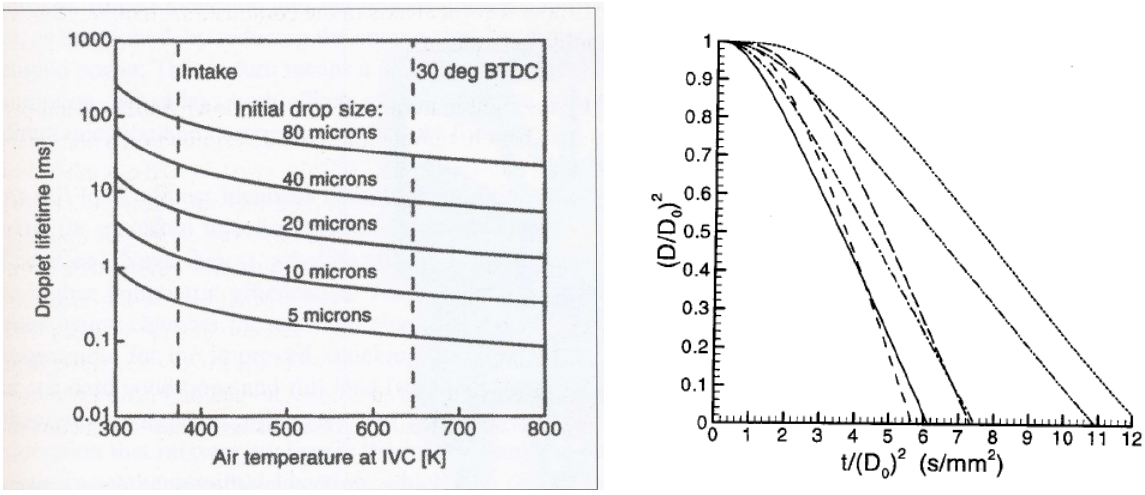

-a- -b-

-a- [Anderson et al (1996), in Van Basshuysen (2009), P.39] for temperature influence on droplet lifetime (Gasoline). –b- Kerosene evaporation rate [Harstad & Bellan (2004)].

Appendix 4.1: Kerosene drops breaking up

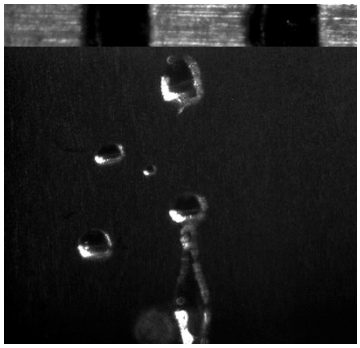

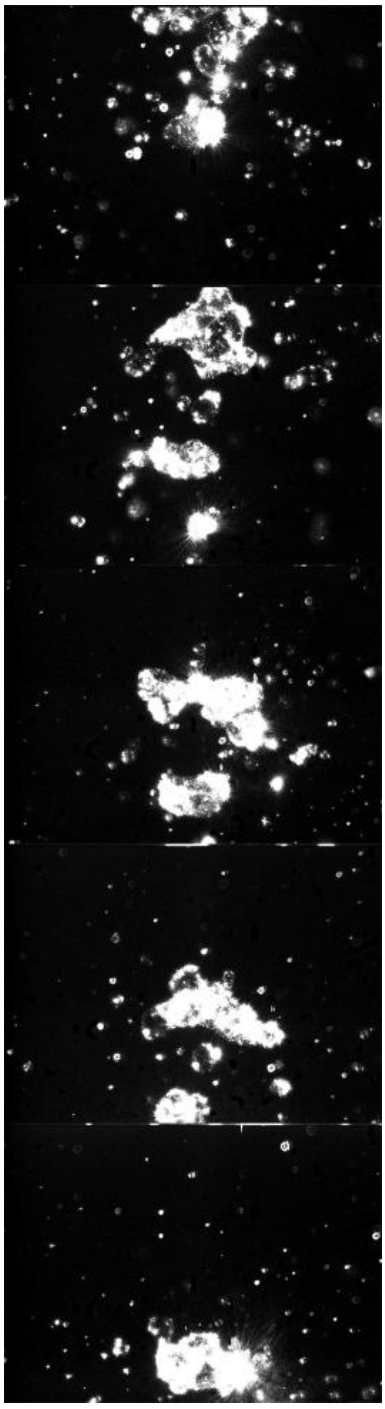

Appendix 4.2: Double pulsed image samples.

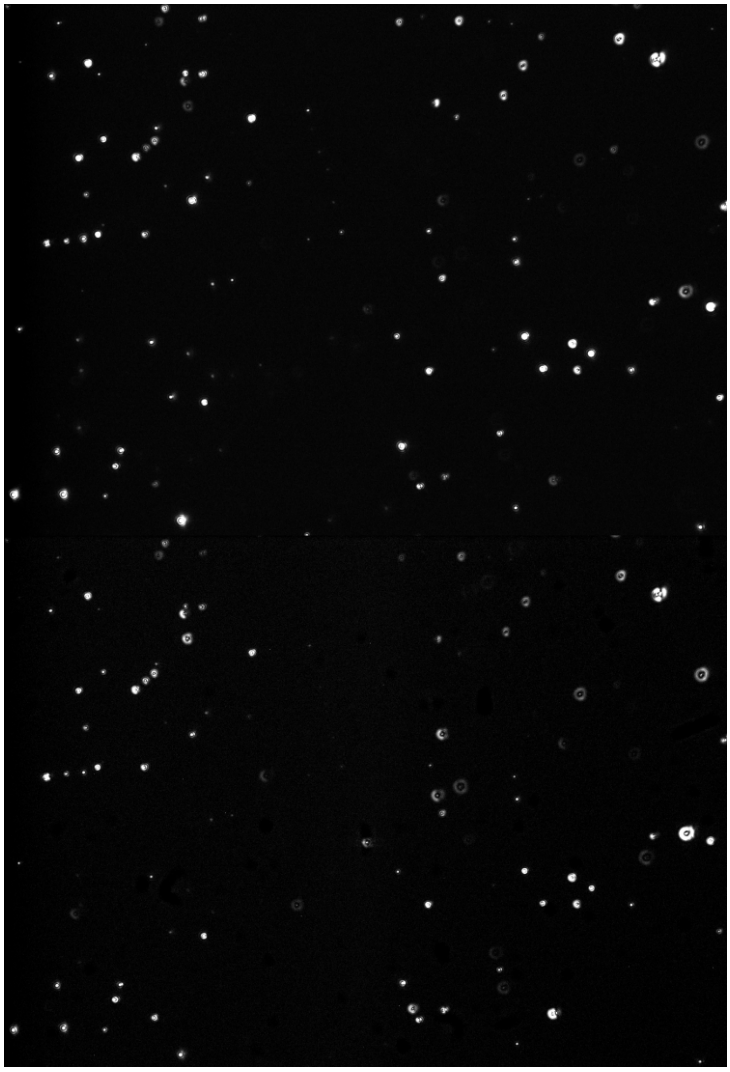

Double-frame double-pulse

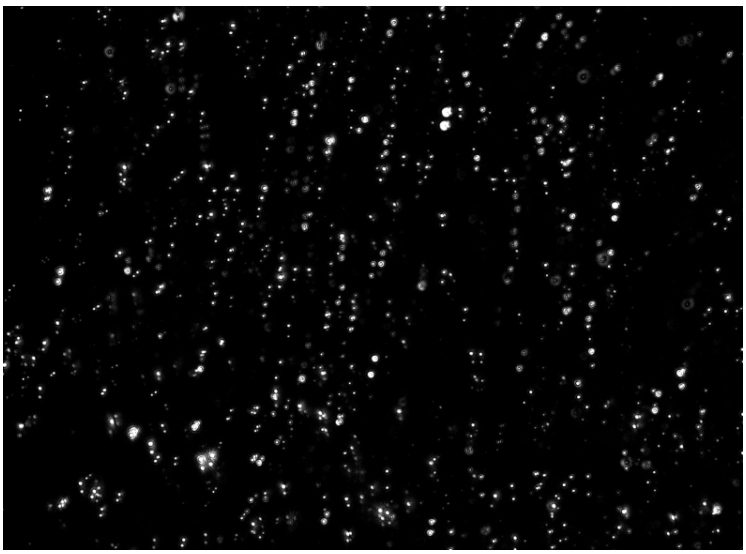

Single-frame double pulse (exposure overlapping)

Appendix 5.1: Evaluation of the Laser Diffraction-base Particle Sizing Systems

Laser diffraction methods in particle size measurements have been used since late 1970's [Ley (1999)]. Results obtain by these methods could directly have a particular margin of error due to the spherical droplet assumption. There are three main factors internationally recognised in the evaluation of this type of system [Ley (1999)], which are:

a. Accuracy in optical alignment.

b. Repeatability in instruments and samples: In ISO 13320-1 (1999) standard, it was suggested that the variation for particles greater than 10 microns in diameter should not exceed 3% at the median size (D_{50}) and 5% at the side distributions (D_{10}) and (D_{90}). These values can be doubled for particles less than 10 microns in diameter.

c. Resolution of the system or the ability to differentiate between different particle sizes: The position of the light sensors and the spacing between them is essential in determining the system sensitivity (see figure 5.7).

In the non-imaging techniques, it is possible to build up a system with a different range of sensitivity for each photo-detector, allowing the coverage of the huge difference in the scattered light intensity between the small and the large angles of observation. This flexibility in the "gain-control" is not available in the camera system, where both the physical control of the aperture or the software –based enhancement of the intensity histogram has an equal effect to all sensors. In the other hand, the camera system has the advantage of the high-resolution.

The intensity pattern of the laser beam normally have a Gaussian profile, thus the scattered light depends on the relative position of the particle within the light beam. So, beam dimensions should be dependent on the particle size. This problem is less important in the well focused systems where the focal depth is less than the width of the light beam. Attempts to produce more uniform laser beams ("top-hat") have been conducted in order to overcome the problem of intensity irregular distribution [Crowe, *et al.* (1998)].

Appendix 6.1 Cubewano Wankel engine design

[Cubewano Website: http://www.cubewano.com]

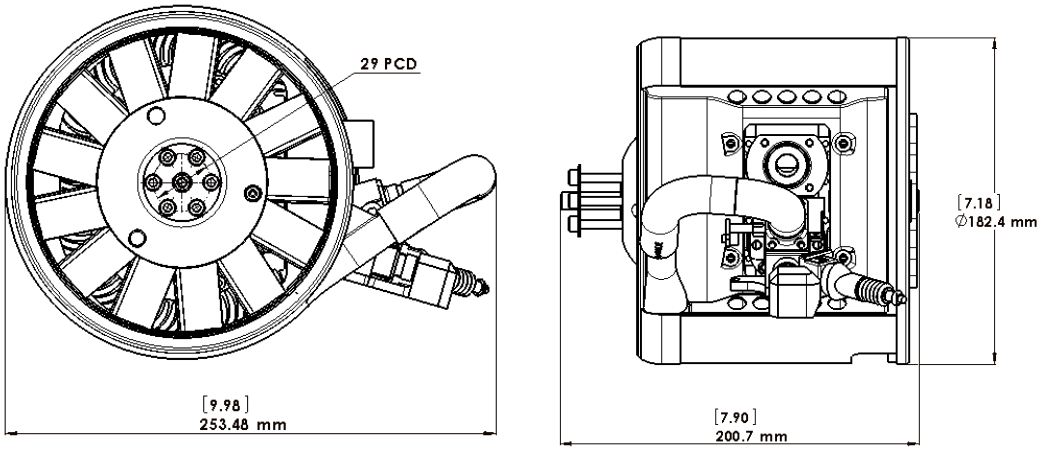

Appendix 6.2: ThorLabs; NB1-K12 dielectric mirror reflectivity curve

[NB1-K12 datasheet]

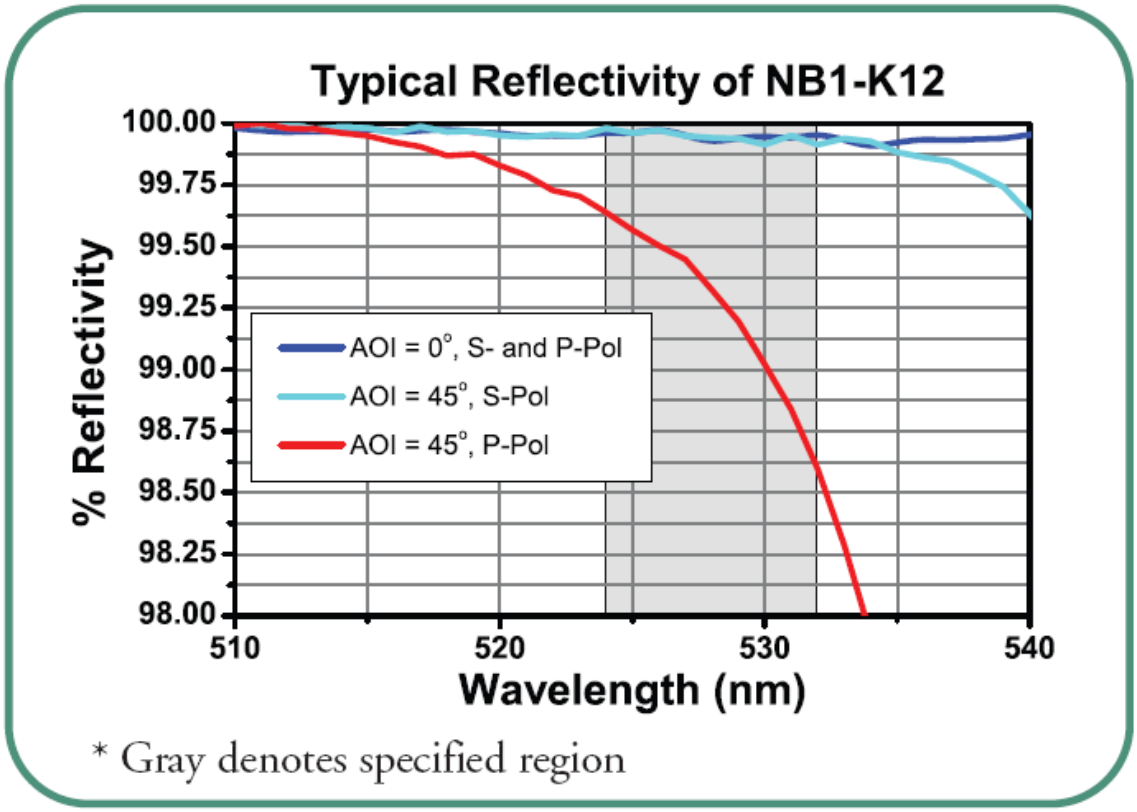

Appendix 6.3 : Microcontroller operation software written by micro-C embedded language

Programmable Hardware, MSP430:
Control.c:

```
#include <msp430xG46x.h>
#include<rami.h>

void main(void)

{
STOP_WD //WDTCTL=WDTPW+WDTHOLD;
FLL_CTL0|=XCAP14PF;
P2DIR=BIT1+BIT2;
P1IES=BIT0;
P1IE=BIT0;
_EINT();
while(1);
}

# pragma vector=PORT1_VECTOR
 __interrupt void P1ISR(void)


 {
   unsigned volatile int i;
   unsigned volatile int j;
  // for(i=1000; i>0;i--);
   P1IFG&=~BIT0; // reset the flag
   if((P1IN&0x01)==0)
   P2OUT^=BIT1;
   j=0;
   while (j!=10000)
   {


      //P2OUT|=BIT2;

      P2OUT^=BIT3;
      wait_u(50); // control the duty cycle (on)
      P2OUT=0;
      Wait_u(25); //off

      j++;
   }
   wait_u(1000);
   P2OUT=0;
   P1IFG&=~BIT0; // reset the flag
   wait_u(1000); // optional

}
```

Programmable Hardware, MSP430:
Synch.c:

```
#include <msp430xG46x.h>
#include<rami.h>
void main(void)
{
LCD_Init() ;
LCD_CLR;

STOP_WD //WDTCTL=WDTPW+WDTHOLD;
FLL_CTL0|=XCAP14PF;
SCFQCTL=SCFQ_4M ;
P2DIR=BIT3+BIT4+BIT5+BIT6;
P6DIR=FULL_BYTE ;

P1IES=BIT0;
P1IE=BIT0;
_EINT();
while(1);
}

# pragma vector=PORT1_VECTOR
 __interrupt void P1ISR(void)


 {

   unsigned volatile int i;
   unsigned volatile int j;
   unsigned volatile int Times;
   unsigned volatile int T1,T1_micro,T2,T3,T_between;

   Times=100000; //Number of Sycles

   T1=1;// on sycle
   T2=40000;// off sycle
   T3=0;
   T_between=12;//

   # define Laser1_Trig P6OUT^=BIT0; wait_n(T1);P6OUT^=BIT0; // Trigger Laser channel 1
   # define Laser2_Trig P6OUT^=BIT2; wait_n(T1);P6OUT^=BIT2; //  Trigger Laser channel 2
   # define Camera_Trig P6OUT^=BIT3; wait_n(T1);P6OUT^=BIT3;; // Trigger Camera (ISA)

   T1_micro=T1*8.7;

   LCDM3=0x68;
   LCDM4=digit[T1_micro/1000];
   LCDM5=digit[2];
```

```
  // for(i=1000; i>0;i--);
   P1IFG&=~BIT0; // reset the flag
   if((P1IN&0x01)==0)
   P6OUT=0;
   j=0;
   while (j!=Times)
   {

     Camera_Trig;
      Laser2_Trig;
      wait_n(T_between);
      Laser1_Trig;
      wait_u(T2);// off

      j++;
   }
   wait_u(1000);
   P6OUT=0;
   P1IFG&=~BIT0;
   wait_u(1000);
}
```

measure the temp and send it to PC through RS232

```
//USCI+Temp + LCD

#include <msp430xG46x.h>
#include <rami.h>
#include <in430.h>

volatile unsigned int i;
volatile unsigned int ADCresult;
volatile unsigned long int DegC,DegF;
unsigned int c1,c2,f1,f2;
void  INITIALISE_IO(void);       // Define pin functions - Set-up i/o

void main(void)
{
STOP_WD;
LCD_Init() ;
LCD_CLR;

ADC12_ON;//ADC12bit_set it on_with ref 2.5V
ADC12_SH(7,12);// sample and hold 0_7
ADC12_CH(10,1);//ADC12MCTL0=INCH_10+SREF_1;
//channel 10 of the internal sensor
ADC12_ST;//ADC12CTL1=SHP; //set_sampling_timer
ADC12_EN(0,360); //MEM0 and 3600 sycle pending
```

```
UCA0CTL0 |= UCMODE0;
UCA0CTL1 |= UCSWRST;

UCA0CTL1 &= ~UCSYNC;           //
 UCA0STAT=0x00;//
 UCA0STAT &= ~UCLISTEN;         //
 UCA0STAT &= ~UCSPB;            //
 UCA0STAT &= ~UCPAR;            //
 UCA0STAT &= ~UCPEN;

 UCA0CTL1 |= (UCSSEL0 + UCSSEL1); // Transmit Control Register.

                    // Use SMCLK
                    // Defines which clock source is used for baud-rate generation:
                    // SSEL1, SSEL0 0 External clock, UCLKI
                    //         0 1 for ACLK
                    //         1 0 or
                    //         1 1 for SMCLK
 UCA0BR0 = 0x6D;             // 9600 Baud with 1048576 Hz Osc.
 UCA0BR1 = 0x00;             //
 UCA0MCTL = 0x04;            //
 ME2 |= UTXE1;
 UCA0CTL1 &= ~UCSWRST;          // Latch module configuration.
 IE2 |= UCA0TXIE;

 INITIALISE_IO();          // Set-up i/o ports

 _EINT();                // Enable interrupts
 //_NOP();          // For debugging - break point

__enable_interrupt();

while(1)
{
ADC12_START; //ADC12 Start Conversion
LPM0;//__bis_SR_register(LPM0_bits);
DegC=((((long)ADCresult-1615)*704)/4095);
DegF=((DegC*9/5)+32);

c1=DegC/10;
c2=DegC-(c1*10);
f1=DegF/10;
f2=DegF-(f1*10);
// print on LCD
LCDM3=0x68;
LCDM4=digit[c2];
LCDM5=digit[c1];
LCDM7=0x71;
LCDM8=digit[f2];
LCDM9=digit[f1];
```

```
wait(70);

  IE2 |= UCA0TXIE;
 _EINT();
 __enable_interrupt();
}
}

#pragma vector=ADC12_VECTOR
__interrupt void ADC12ISR(void)
{
ADC12_GET;
LPM0_EXIT;//__bic_SR_register_on_exit(LPM0_bits);
}

#pragma vector=USCIAB0TX_VECTOR
__interrupt void USCIA0TX_ISR(void)

{
  unsigned int d= 50;
  UCA0TXBUF =0x61;
  IE2=0; wait_u(d);
  IE2 |= UCA0TXIE;
  UCA0TXBUF =c1+48;
  IE2=0; wait_u(d);
  IE2 |= UCA0TXIE;
  UCA0TXBUF =c2+48;
  IE2=0; wait_u(d);
  IE2 |= UCA0TXIE;
  UCA0TXBUF =0x43;
  IE2=0; wait_u(d);
  IE2 |= UCA0TXIE;
  UCA0TXBUF =f1+48;
  IE2=0; wait_u(d);
  IE2 |= UCA0TXIE;
  UCA0TXBUF =f2+48;
  IE2=0; wait_u(d);
  IE2 |= UCA0TXIE;
  UCA0TXBUF =0x46;
  IE2=0; wait_u(d); // IE2=0 is important to stop the interrupt

}
//*******************************************************************************

// UART0 RX ISR - Not used in this example

#pragma vector=USCIAB0RX_VECTOR
__interrupt void USCIA0RX_ISR(void)

{
```

```
 _NOP();
}
//*************************************************************************

void  INITIALISE_IO(void)       // Set-up i/o
   {
// PORT-3                       // UART and spare i/o lines
  P2SEL = 0x30;                  // P2[4..5] UART0 function
  P2DIR = 0xDF;                  // All P2.x outputs except P2.5=UART0_RX
  P2OUT = 0x00;                   // All P2.x reset
   }
```

Heading file

```
//rami.h

unsigned int i_count;
unsigned int j_count;

void wait(unsigned int SLOWDOWN_COUNT)
{
  for(i_count = 0; i_count < 1000; i_count++){for(j_count = 0; j_count < SLOWDOWN_COUNT;
j_count++);};
}

void wait_m(unsigned int SLOWDOWN_COUNT)
{
  for(i_count = 0; i_count < 100; i_count++){for(j_count = 0; j_count < SLOWDOWN_COUNT;
j_count++);};
}
void wait_u(unsigned int SLOWDOWN_COUNT)
{
  for(i_count = 0; i_count < 10; i_count++){for(j_count = 0; j_count < SLOWDOWN_COUNT;
j_count++);};
}

#define STOP_WD WDTCTL = WDTPW + WDTHOLD; // stop watchdog
//#define wait_cycle for(i = 0; i < 100; i++);

#define FULL_WORD (0xFFFF);
#define FULL_BYTE (0x00FF);

void BITINT_P1(unsigned int bitx, unsigned int edgex) //bit interrupt
{
void i_main(void);
{
  P1IES=edgex;
  P1IE=bitx;
  _EINT();
}
}
```

```
void DIS_BITINT_P1(unsigned int bitx) // disable bit interrupt
{wait_m(1);
  P1IFG&=~bitx;}

//*************************************************************************

//ADC12

//#define ADC12_ON            ADC12CTL0=ADC12ON;
#define ADC12_ON_REF15       ADC12CTL0=ADC12ON+REFON;
#define ADC12_ON            ADC12CTL0=ADC12ON+REFON+REF2_5V;
#define ADC12_ST            ADC12CTL1=SHP;

void ADC12_SH(int S,int H) // Set sample time
{
  int SH=S*100+H;
switch (SH)
 {
 case (0):
   ADC12CTL0 |=SHT0_0;
   break;
 case (1):
   ADC12CTL0 |=SHT0_1;
   break;
 case (2):
   ADC12CTL0 |=SHT0_2;
   break;
 case (3):
   ADC12CTL0 |=SHT0_3;
   break;
 case (4):
   ADC12CTL0 |=SHT0_4;
   break;
 case (5):
   ADC12CTL0 |=SHT0_5;
   break;
 case (6):
   ADC12CTL0 |=SHT0_6;
   break;
 case (7):
   ADC12CTL0 |=SHT0_7;
 case (8):
   ADC12CTL0 |=SHT0_8;
   break;
 case (9):
   ADC12CTL0 |=SHT0_9;
   break;
 case (10):
   ADC12CTL0 |=SHT0_10;
   break;
```

```
case (11):
  ADC12CTL0 |=SHT0_11;
  break;
case (12):
  ADC12CTL0 |=SHT0_12;
  break;
case (13):
  ADC12CTL0 |=SHT0_13;
  break;
case (14):
  ADC12CTL0 |=SHT0_14;
  break;
case (15):
  ADC12CTL0 |=SHT0_15;
  break;
// next case
case (100):
  ADC12CTL0 |=SHT1_0;
  break;
case (101):
  ADC12CTL0 |=SHT1_1;
  break;
case (102):
  ADC12CTL0 |=SHT1_2;
  break;
case (103):
  ADC12CTL0 |=SHT1_3;
  break;
case (104):
  ADC12CTL0 |=SHT1_4;
  break;
case (105):
  ADC12CTL0 |=SHT1_5;
  break;
case (106):
  ADC12CTL0 |=SHT1_6;
  break;
case (107):
  ADC12CTL0 |=SHT1_7;
  break;
case (108):
  ADC12CTL0 |=SHT1_8;
  break;
case (109):
  ADC12CTL0 |=SHT1_9;
  break;
case (110):
  ADC12CTL0 |=SHT1_10;
  break;
case (111):
  ADC12CTL0 |=SHT1_11;
```

```
  break;
 case (112):
  ADC12CTL0 |=SHT1_12;
  break;
 case (113):
  ADC12CTL0 |=SHT1_13;
  break;
 case (114):
  ADC12CTL0 |=SHT1_14;
  break;
 case (115):
  ADC12CTL0 |=SHT1_15;
  break;
 default:
   ADC12CTL0 |=SHT0_7;
 }
}
//*********************************************************************
void ADC12_CH(unsigned int CH,unsigned int ref_mode)
{
ADC12MCTL0=CH+ref_mode*0x10u;
}
//*********************************************************************
void ADC12_EN(unsigned int MEM,unsigned int Time)
{
 ADC12IE=(MEM+1);
 wait_u(Time);
 ADC12CTL0 |=ENC;
}

#define ADC12_START   ADC12CTL0 |=ADC12SC;//ADC12 Start Conversion
#define ADC12_GET     ADCresult=ADC12MEM0;//read ADC from memory

//*********************************************************************
// LCD

#define COM1 BIT2 // P5.2 LCD common driver outputs
#define COM2 BIT3 // P5.3 in port 5
#define COM3 BIT4 // P5.4

#define Seg3 BIT6 // P10.6
#define Seg2 BIT7 // P10.7

/*
** Setup LCD
*/
void LCD_Init(void)
{

#if defined( __MSP430_HAS_LCD_A__ ) /* LCD_A Module is available */
P5SEL |= COM1|COM2|COM3; // COM's are on P5
```

```
P10SEL &= ~(Seg2|Seg3);

LCDACTL = LCDFREQ_96 | // Divide by 96
LCD4MUX | // 4-mux / no blinking
LCDON; // LCD_A module on

// use S0 -> S31, 4 mux to the 120 segments we actually can use S2-S31
// these are LCD seg outouts
LCDAPCTL0 = 1*LCDS0 | // (0x01) LCD Segment 0 to 3 Enable: seg driver
1*LCDS4 |
// (0x02) LCD Segment 4 to 7 Enable: seg driver
1*LCDS8 |
// (0x04) LCD Segment 8 to 11 Enable: seg driver
1*LCDS12 |
// (0x08) LCD Segment 12 to 15 Enable: seg driver
1*LCDS16 |
// (0x10) LCD Segment 16 to 19 Enable: seg driver
1*LCDS20 |
// (0x20) LCD Segment 20 to 23 Enable: seg driver
1*LCDS24 |
// (0x40) LCD Segment 24 to 27 Enable: seg driver
1*LCDS28;
// (0x80) LCD Segment 28 to 31 Enable: seg driver

// // // or just enable all
//LCDAPCTL0 =0xFF;

// these are I/O
LCDAPCTL1 = 0*LCDS32 | // (0x01) LCD Segment 32 to 35 Enable: I/O
0*LCDS36;
// (0x02) LCD Segment 36 to 39 Enable: I/O

/*
** Segments S0 through S3 are disabled when the LCD charge pump feature
** is enabled (LCDCPEN = 1) and cannot be used together
** with the LCD charge pump. In addition, when using segments S0 through S3
** with an external LCD voltage supply, VLCD <= AVCC.
**
** S2 & S3 don't work with LCDCPEN set ???!!!???
*/
LCDAVCTL0 = 0*LCD2B | // (0x01) Selects 1/2 bias. 0 => 1/3 bias
VLCDREF_0 |
// (0x0x) Selects internal reference voltage for charge pump
0*LCDCPEN |
// (0x08) LCD Voltage Charge Pump Enable. Charge pump enabled
0*VLCDEXT |
// (0x10) Select external source for VLCD - generated internally
0*LCDREXT |
// (0x20) LCD mid voltages => V2 - V4 are generated internally
0*LCDR03EXT;
// (0x40) LCD voltage => V5 is AVCC.
```

```
#else
// old LCD controller
// use S0 -> S31, 4 mux to the 120 segments we actually can use
S2-S31
P5SEL = 0xFF;
// P5 is all LCD display
LCDCTL = LCDSG0_5|LCD4MUX|LCDON; // S2-S31 are LCD drivers
#endif

#if BL_CONTRAST_CONTROL
LCD_SetContrast(p.FactoryParams.LCD_Contrast); // restore contrast DAC
#endif
}
//*****************************************************************************

unsigned int DISPLAY(int num)
{
  unsigned int res;
switch (num)
 {
 case (0):
   res=0x5F;
   break;
 case (1):
   res=0x06;
   break;
 case (2):
  res=0x6B;
   break;
 case (3):
  res=0x2F;
   break;
case (4):
  res=0x36;
   break;
case (5):
  res=0x3D;
   break;
case (6):
  res=0x7D;
break;
case (7):
  res=0x07;
   break;
case (8):
  res=0x7F;
   break;
case (9):
  res=0x3F;
   break;
```

```
  default:
  res=0xFF;
 }
return res;
}
//*****************************************************************

#define LCD_CLR
LCDM1=LCDM2=LCDM3=LCDM4=LCDM5=LCDM6=LCDM7=LCDM8=LCDM9=LCDM10=LCDM11=LCDM
12=LCDM13=LCDM14=LCDM15=LCDM16=LCDM17=LCDM18=LCDM19=LCDM20=0x00;
#define LCD_TEST
LCDM1=LCDM2=LCDM3=LCDM4=LCDM5=LCDM6=LCDM7=LCDM8=LCDM9=LCDM10=LCDM11=LCDM
12=LCDM13=LCDM14=LCDM15=LCDM16=LCDM17=LCDM18=LCDM19=LCDM20=0xFF;

char digit[10]={0x5F,0x06,0x6B,0x2F,0x36,0x3D,0x7D,0x07,0x7F,0x3F};
```

Appendix 6.4 Matlab code for drawing the greyscale fit of the calibration object

```
clear all;clc
i=imread('G:\calibration_images\calibration\2470.bmp');

x1=680;
x2=800;
y=310;

c=i(y,x1:x2);

hold on
%plot (c,'y')

xx=polyfit(1:121,double(c),20);
ss=polyval(xx,1:121);
plot(ss)
```

Appendix 6.5: gasoline injector image processing stages

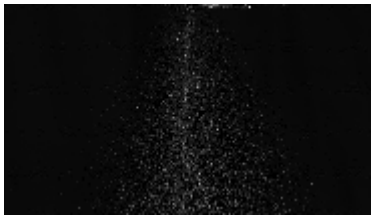
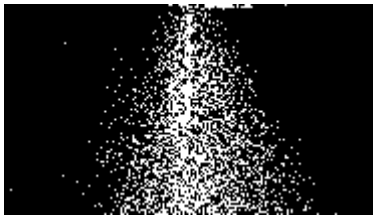
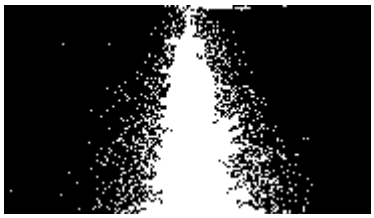


```
%% Process.m
%% Rami Zakaria, University of Warwick
%% Macroscopic analysis of sprays

clear all; close all; clc
number_of_frames=5;
pixel_size= 55.6; %um ... this is calculated manually.
D=250; % um ... nozzle diameter
Pressure=1:5;
Time=[180 205 225 260 285 310 340 360];

%load images
I=load_images (number_of_frames+1);

figure, imshow(I(:,:,3)); %show samples

%% mean value

mimage=mean(I,3);
figure; imagesc(mimage),colorbar

%% cut windows if necessary

% figure(4); pic = I(:,:,1);
% [y1,x1,c1] = impixel(pic);    % right click once to select point
% [y2,x2,c2] = impixel(pic);    % right click once to select point
% close figure 4
%figure(4); pic = I(:,:,2);

%% or select a window manually
 clear cuts
 x1=1;x2=1024;
 y1=1;y2=1350;
```

```
x_window= x1:x2;
y_window= y1:y2;

[L,W,n]=size(I);
for i=1:n
    cuts(:,:,i)=I(x_window,y_window,i);
end

figure, imshow(cuts(:,:,1));
mcuts=mean(cuts,3);
figure, imagesc(mcuts),colorbar


%% Intensity enhancement

clear enh_cuts;

for i=1:n
    enh_cuts(:,:,i) = adapthisteq(cuts(:,:,i));
end

    figure, subplot(1,2,1),imshow(cuts(:,:,5)), title('Original Image');
     subplot(1,2,2),imshow(enh_cuts(:,:,5)), title('Filtered Image');

%% 2D-DCT
for i=1:number_of_frames;
d(:,:,i)=dct2(cuts(:,:,i));
DC(i)=d(1,1,i);
end

figure; plot(Pressure,DC)
%_____________________________________________
%% Edge Detection

bw_thr=mean(std(std(single(enh_cuts))),3)/(90); % black and white threshold
fill_conn=4; % number of neighbour pixels to be filled up
filt_index=25; % filter index (?)


figure;
for i=1:number_of_frames;
    x=enh_cuts(:,:,i);
     %x_bw_f=imfill(im2bw(wiener2(x,[filt_index
filt_index]),bw_thr),fill_conn,'holes'); % black and white
     x_bw_f(:,:,i)=imfill(im2bw(medfilt2(x,[filt_index
filt_index]),bw_thr),fill_conn,'holes'); % black and white

    subplot(2,3,i);imshow(x_bw_f(:,:,i));
    area(i)=sum(sum(x_bw_f(:,:,i),2));
end

subplot(2,3,1);title('@ 1 Bar')
subplot(2,3,2);title('@ 2 Bar')
subplot(2,3,3);title('@ 3 Bar')
subplot(2,3,4);title('@ 4 Bar')
subplot(2,3,5);title('@ 5 Bar')
```

```
res=size(cuts,1)*size(cuts,2);
P_mass=(area/res)*100; % percentage mass
sheet_area=area*(pixel_size^2)/(10^8);
figure; plot(Pressure,sheet_area)
ylabel('Sheet area - cm^2');
xlabel('Pressure- Bar')

%% Automatic angle calculation

[wL,wW]=size(mcuts);

FF= round(100*D/pixel_size); % far field length
NF= round(60*D/pixel_size); % near field length

angle_F=zeros(number_of_frames,1);
angle_N=zeros(number_of_frames,1);


for frame_n = 1:number_of_frames


i=1; %% y position where the first non-zero pixel is detected %
j=1; %% the position of the first zero on X axis
    while x_bw_f(i,j,frame_n)==0
    j=j+1;
        if j==round(0.6*(wW)); %% stop at this position
        j=1;i=i+1;
        end
    end

mid_x= sum(x_bw_f(i,:,frame_n),2)/2; %find the middle of the shape at this
point
y1=i;
x1=j+mid_x;


j=1;
    while x_bw_f(y1+FF,j,frame_n)==0
    j=j+1;
    if j==wW;
        j=x1-1; % No angle case
        break;
    end

    end

x2=j;

angle_F(frame_n)=atand((x1-x2)/FF);


j=1;
    while x_bw_f(y1+NF,j,frame_n)==0
    j=j+1;
     if j==wW;
        j=x1-1; % No angle case
        break;
```

```
    end
    end

x3=j;

angle_N(frame_n)=atand((x1-x3)/NF);

end

figure; plot(Pressure,angle_F,Pressure, angle_N);
ylabel('Far-field and near-field half angles ( degree )');
xlabel('Pressure ( Bar )') ;
legend('Far-field','Near-field',2);
```

```
%% Process_Synch.m
%% Process
clear all; close all; clc
number_of_frames=22;

time=[number_of_frames*50:-50:50];

%load images
I=load_images3(number_of_frames+1);

figure, imshow(I(:,:,1)); %show samples


%% mean value

mimage=mean(I,3);
figure; imagesc(mimage),colorbar


 figure(4); pic = I(:,:,2); %% cut windows

 x1=45;x2=1404;
 y1=799;y2=1200;

close figure 4

x_window= x1:x2;
y_window= y1:y2;

[L,W,n]=size(I);
for i=1:n
    cuts(:,:,i)=I(x_window,y_window,i);
end

figure, imshow(cuts(:,:,1));
mcuts=mean(cuts,3);
figure, imagesc(mcuts),colorbar


%h = fspecial('sobel');
```

```
h=[1      2       1
   0      1      0
   -1     -2      -1];


figure; freqz2(h)
for i=1:n
    s_cuts(:,:,i) = imfilter(cuts(:,:,i),h);
end

    figure, subplot(1,2,1),imshow(cuts(:,:,3)), title('Original Image');
     subplot(1,2,2),imshow(s_cuts(:,:,3)), title('Filtered Image');

%_____________________________________________
%% Edge Detection

bw_thr=0.02; % black and white threshold
fill_conn=4; % number of neighbour pixels to be filled up
filt_index=20; % filter index (?)


figure;
for i=1:number_of_frames;
    x=cuts(:,:,i);
    x_bw=im2bw(x,bw_thr); % black and white
    x_bw_filled=imfill(x_bw,fill_conn,'holes'); % filling up
    x_bw_filled_filtered(:,:,i)=medfilt2(x_bw_filled,[filt_index
filt_index]);
    subplot(4,6,i);imshow(x_bw_filled_filtered(:,:,i)); title(['t=',
num2str(number_of_frames*50-i*50)])
    mass(i)=sum(sum(x_bw_filled_filtered(:,:,i),2));
end



res=size(cuts,1)*size(cuts,2);
P_mass=(mass/res)*100 % percentage mass
%figure; plot(Pressure,P_mass)
figure; plot(time,P_mass)
ylabel('Percentage Mass- %')
xlabel('time in microseconds')


%% Penetration calculation
 pixel_size= 50; %um ... this is calculated manually.

[wL,wW]=size(mcuts);

clear penet;
for frame_n = 1:number_of_frames


i=1; %% y position where the first non-zero pixel is detected % the number
22 here just to avoid the adge of the injector (photography error)
j=1; %% the position of the first zero on X axis
    while x_bw_filled_filtered(i,j,frame_n)==0
    j=j+1;
```

```
        if j==round(0.6*(wW)); %% stop at this position
        j=1;i=i+1;
        end
        if i==100;
            i=1;
            break;
        end
    end

mid_x= sum(x_bw_filled_filtered(i,:,frame_n),2)/2; %find the middle of the
shape at this point
y1=i;
x1=round(j+mid_x);


j=y1+1; % starting from the beginning of the jet and search for its end
    while x_bw_filled_filtered(j,x1,frame_n)~=0
    j=j+1;
    if j==wL;
        j=y1-1; % No angle case
        break;
    end

    end

y2=j-1;


penet(frame_n)=y2-y1;


end

figure;plot (time,penet*pixel_size/1000);
ylabel('Penetration - mm')
xlabel('time - microseconds')


%% contour extracting

SImage=sum(x_bw_filled_filtered,3); % sum of all BW images gives the
position of the spray at each time step

SImage_time=(number_of_frames*50-SImage*50)/1000; % each pixel value
represnts the time slot in ms
yaxis=[wL:-1:1]*pixel_size/1000; %invert  y axis, axis in mm
xaxis=[1:wW]*pixel_size/1000;
figure;
[C,h] = contourf(xaxis,yaxis,SImage_time);grid on;
text_handle = clabel(C,h);
set(text_handle,'BackgroundColor',[1 1 .8],'fontsize',8,'Edgecolor',[.7 .7
.7])


ylabel('Penetration - mm')
xlabel('width - mm')
```

```
%%load images
function [pics]= load_images(n)

filterspec='*.bmp';
dialogtitle='Set Directory:';
[filename, pathname] = uigetfile(filterspec, dialogtitle);
[filenames,amount,ext] = ReadImDir(pathname);

count=0;

for i=1:n-1
    count=count+1;
    pics(:,:,count) = (imread([pathname,filesep,char(filenames(i))]));
end

%%
```

```
function [filenames,amount,ext] = ReadImDir(directory,ext)

    knownExtensions = {'bmp'};
    if nargin == 1 | isempty(ext)
        for i = 1:length(knownExtensions)
            direc = dir([directory,filesep,'*.',knownExtensions{i}]);
            if ~isempty(direc), ext = knownExtensions{i};
                break
            end
        end
    end
    direc = dir([directory,filesep,'*.',ext]); filenames={};
    [filenames{1:length(direc),1}] = deal(direc.name);
    filenames = sortrows(filenames);
    amount = length(filenames)/2; % amount of pairs
```

```
function [cuts]=cut_window(number_of_frames,times,x1,x2,y1,y2)

for round=1:times
clear I;
start=1+number_of_frames*(round-1);
I=images_load(start,number_of_frames+start);

x_window= x1:x2;
y_window= y1:y2;

[L,W,n]=size(I);
for i=1:n
    cuts(:,:,i)=I(x_window,y_window,i);
end

figure, imshow(cuts(:,:,1));
mcuts=mean(cuts,3);
[cL,cW]=size(mcuts);
figure, imagesc(mcuts),colorbar
```

```
save (['cuts' ,char(round+48)],'cuts')
save (['mcuts' ,char(round+48)],'mcuts')
end


for i=1:times
load  (['cuts',char(i+48)]);
c(:,:,:,i)=cuts;
end

cuts=reshape(c,cL,cW,number_of_frames*times);
```

Appendix 6.6: Image compression using DCT for reducing redundancy in the image matrix

```
close all; clear all;clc
i1=imread('G:\PhD_28July\Snapshots\Img6546.JPG');
i1=rgb2gray(i1);
d=dct2(i1);
DC=d(1,1);

d1=d;
d1(abs(d1)> 50000) = 0;
i2=idct2(d1);
subplot(2,2,1),imshow(i2,[0 255])


d2=d;
d2(abs(d2)> 10000) = 0;
i2=idct2(d2);
subplot(2,2,2),imshow(i2,[0 255])


d3=d;
d3(abs(d3)> 2000) = 0;
i2=idct2(d3);
subplot(2,2,3),imshow(i2,[0 255])

d4=d;
d4(abs(d4)>500) = 0;
i2=idct2(d4);
subplot(2,2,4),imshow(i2,[0 255])
```

$$DC = \frac{\sum x}{\sqrt{M}.\sqrt{N}}$$

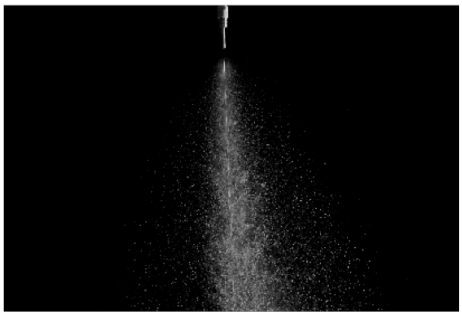
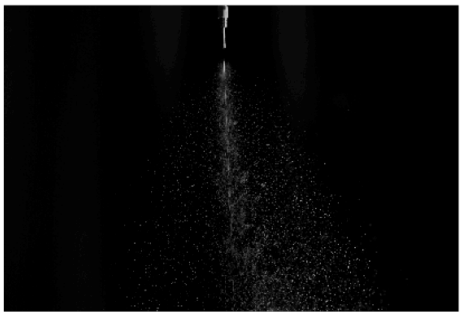

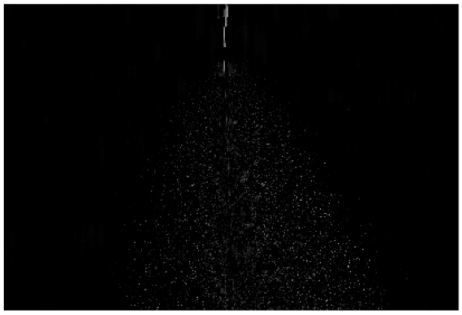

Appendix 6.7 jet fuel ignition delay time JP8

[Kumar & Sung (2010)]

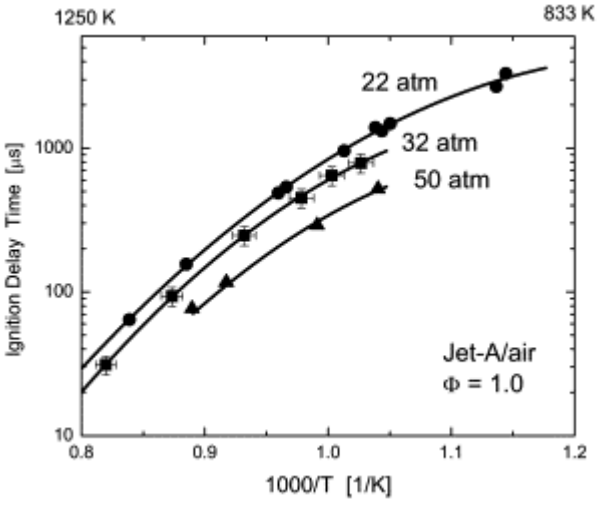

Appendix 7.1: Spray angle for Lee injector and atomiser at 280 Hz

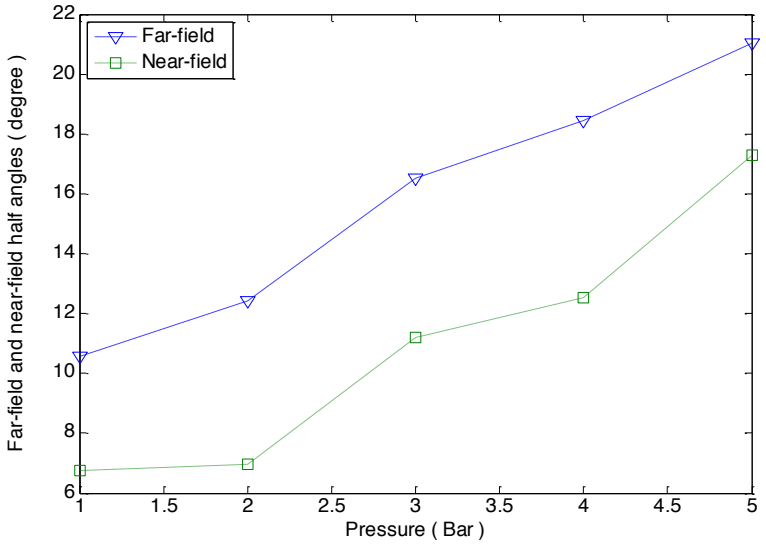

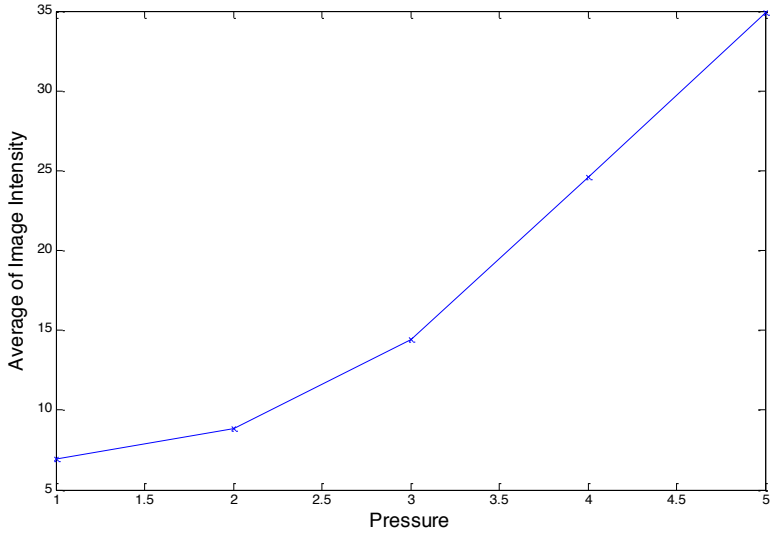

@ 1 Bar

@ 2 Bar

@ 3 Bar

@ 4 Bar

@ 5 Bar

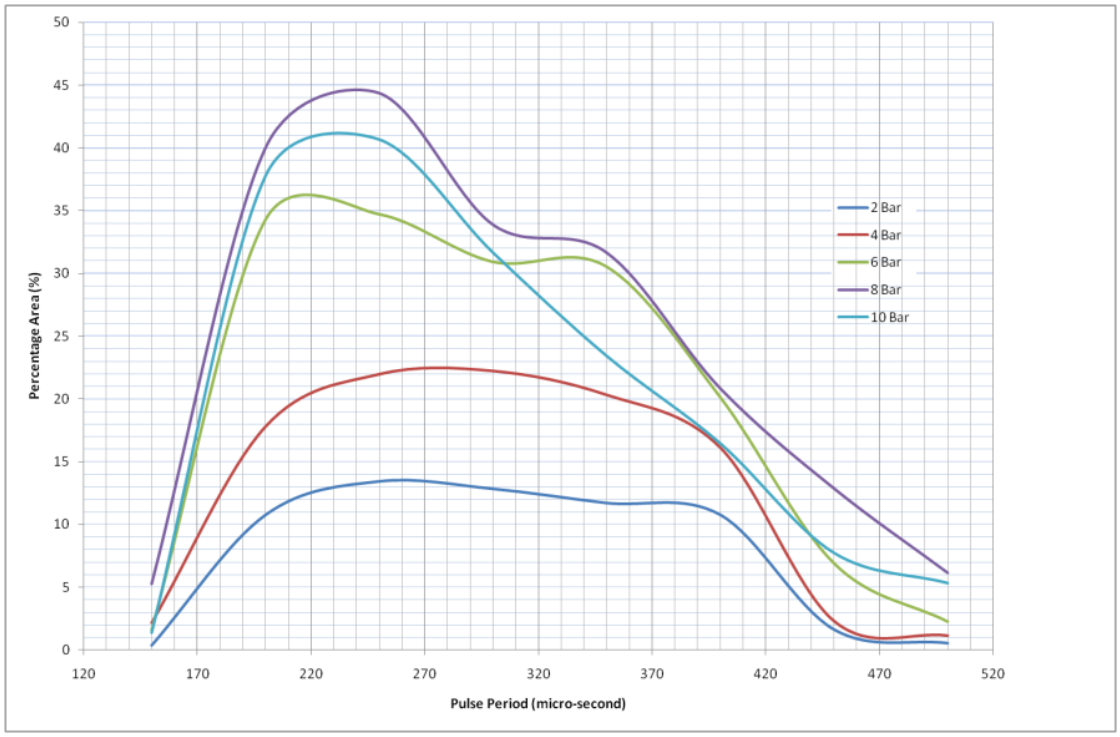

Appendix 7.2: Lee atomiser close-up view of the primary atomisation region

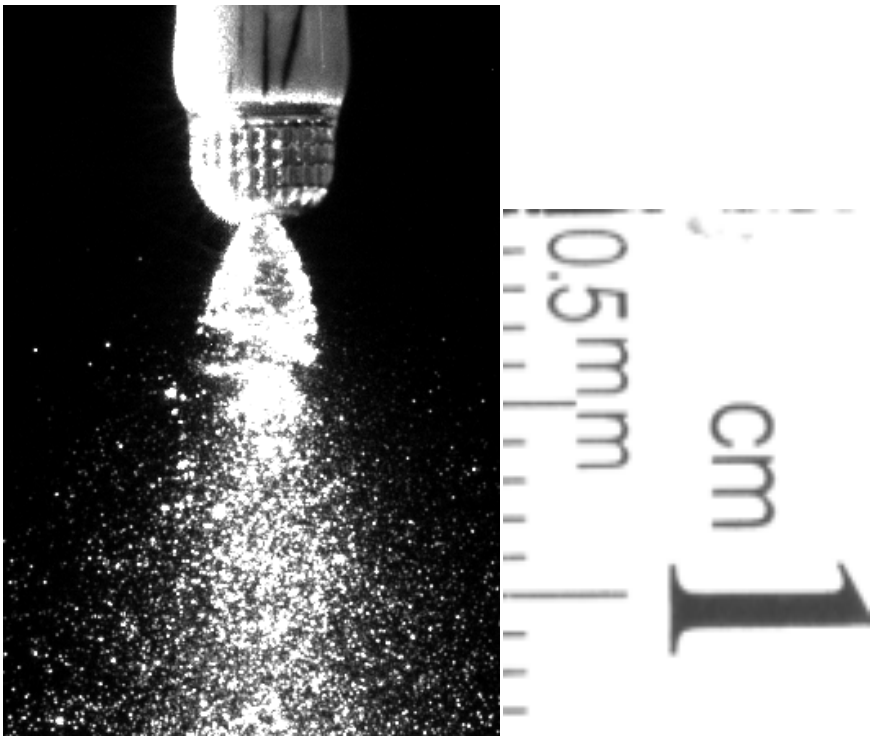

Appendix 7.3 Spray penetration against time for the new 4-hole injector. The injector nozzle is opened for 2 ms time period. A mean velocity of 20 ms^{-1} is calculated at P=5 bar. Smaller particles usually have smaller velocity.

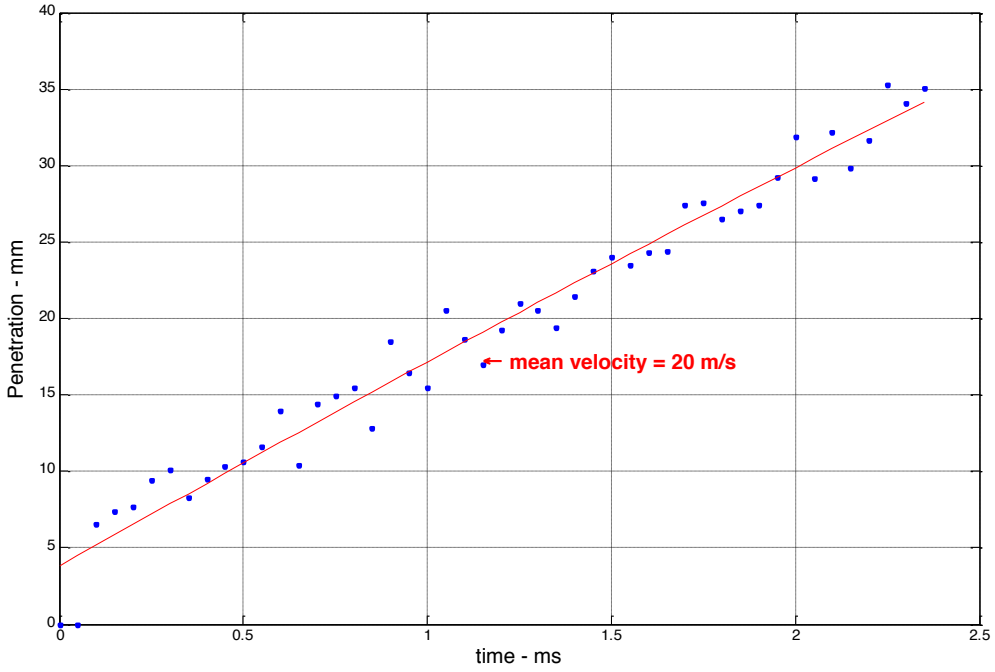

Spray penetration against time for the old 1-hole injector (IWP023). The injector nozzle is opened for 2 ms time period. A mean velocity of 28 ms^{-1} is calculated at P=5 bar.

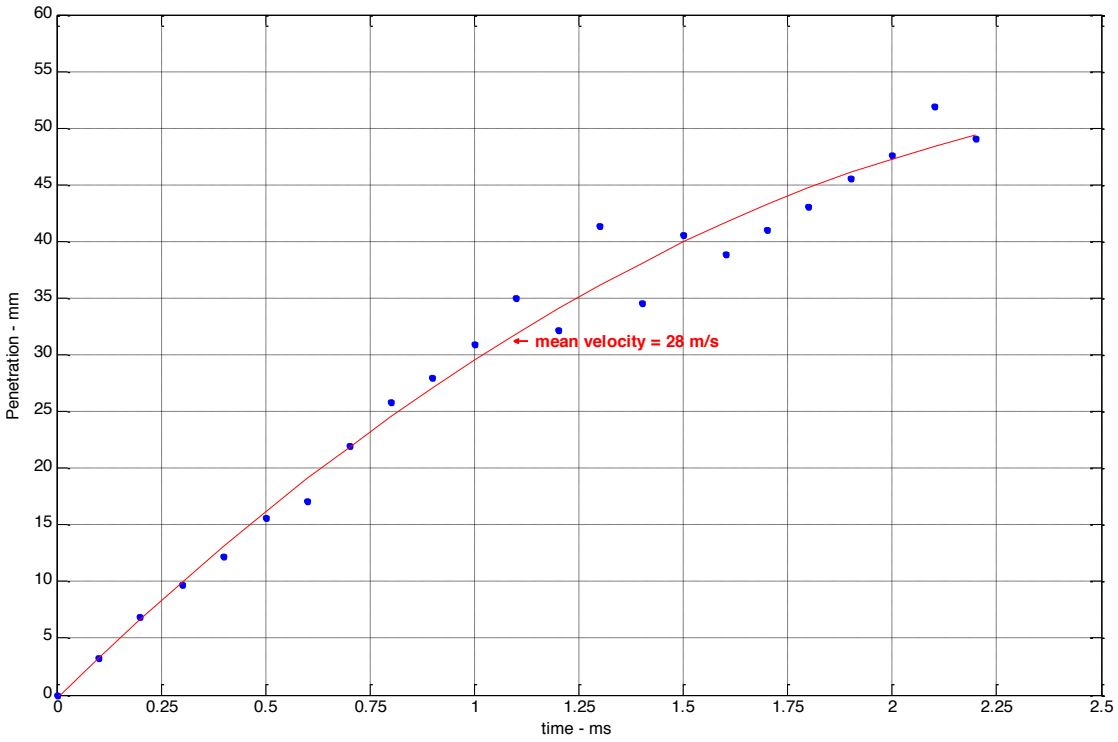

Appendix 7.4: Tip penetration during the first millisecond of a 2 ms injection pulse for both water and kerosene (JP-8).

The viscosity effect is not included in the Weber number mathematical expression, alternatively, it appears in another dimensionless number called "Ohnesorge number" $Oh = \sqrt{We}/\mathrm{Re}$.

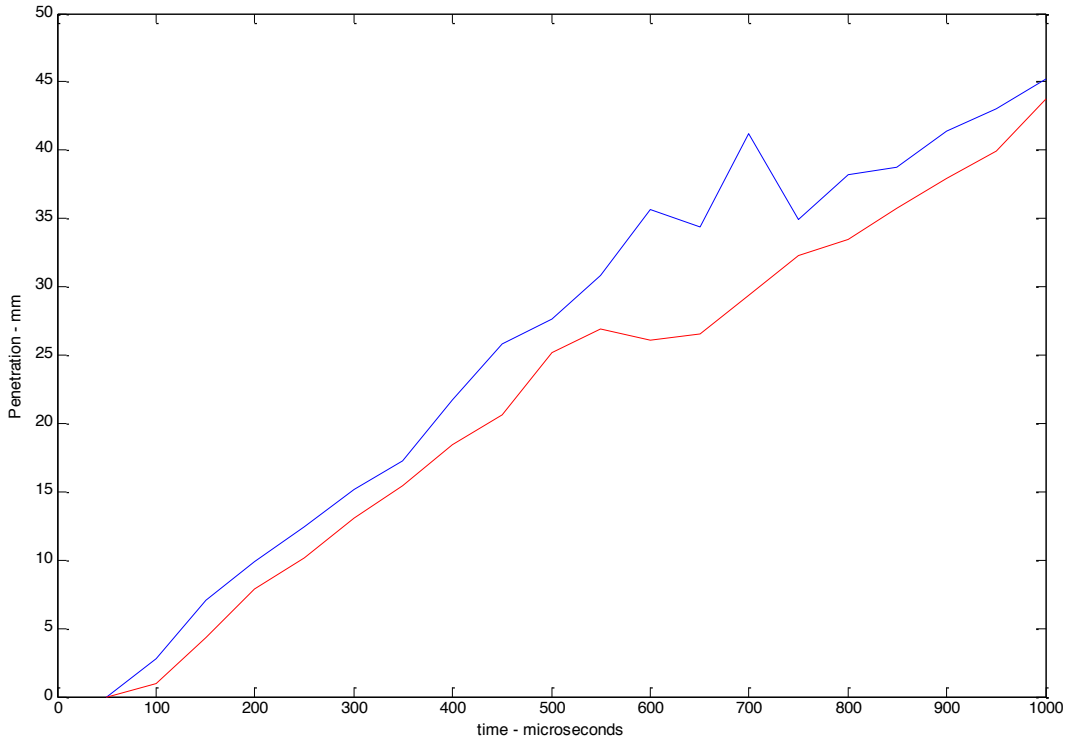

JP8 fuel (blue) against water (red) velocity.

	Dynamic Viscosity (N.s/m^2)	Surface tension (mN/m)
Water:	1.002 x 10^{-3}	72
Kerosene:	2.8 x 10^{-3}	27

Table 6.1 Transition *We* for Newtonian drops with $Oh < 0.1$ [4]

Vibrational (no breakup)	$0 < We < \sim 11$
Bag	$\sim 11 < We < \sim 35$
Multimode	$\sim 35 < We < \sim 80$
Sheet thinning	$\sim 80 < We < \sim 350$
Catastrophic	$We > \sim 350$

[Guildenbecher et al.(2011)]

Appendix 7.5: Two injection cycles using gasoline gasoline injector (2ms each with 1 ms interval between them)

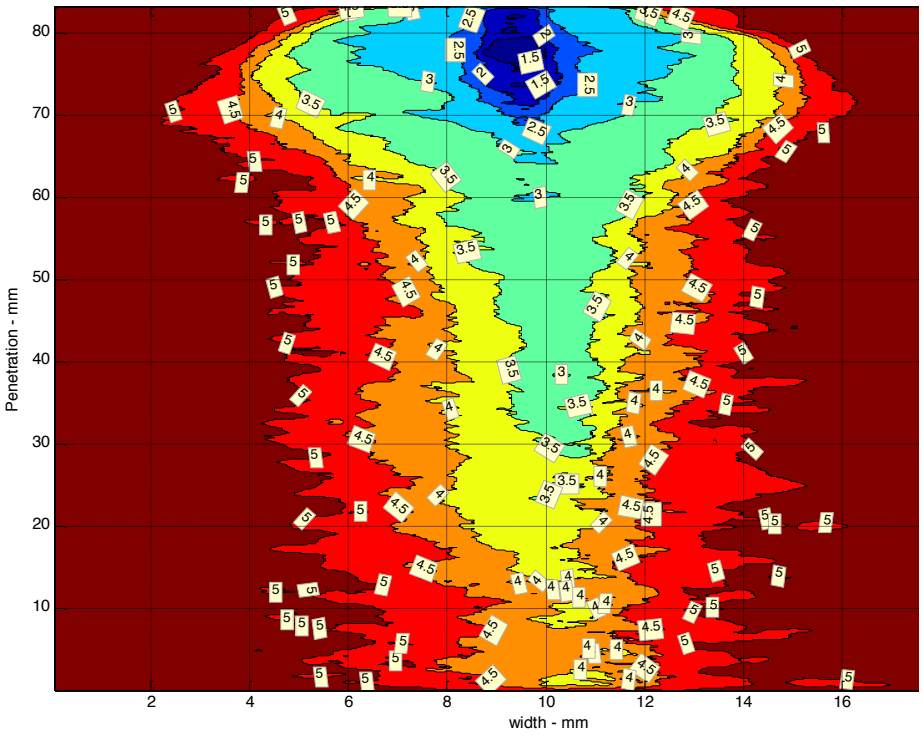

single-hole gasoline injector sprays.

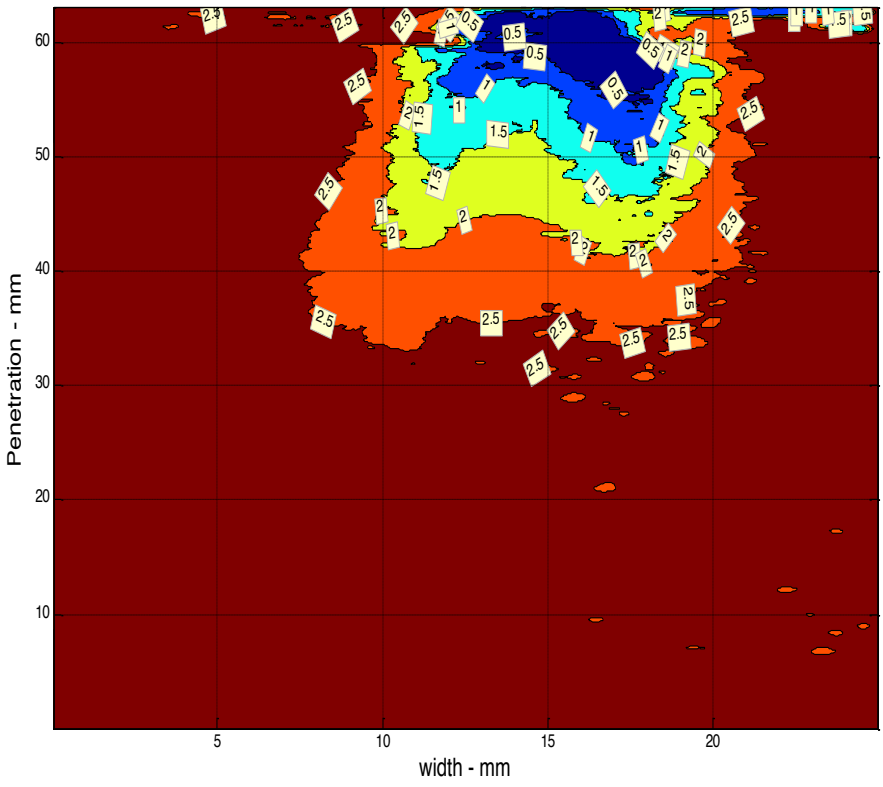

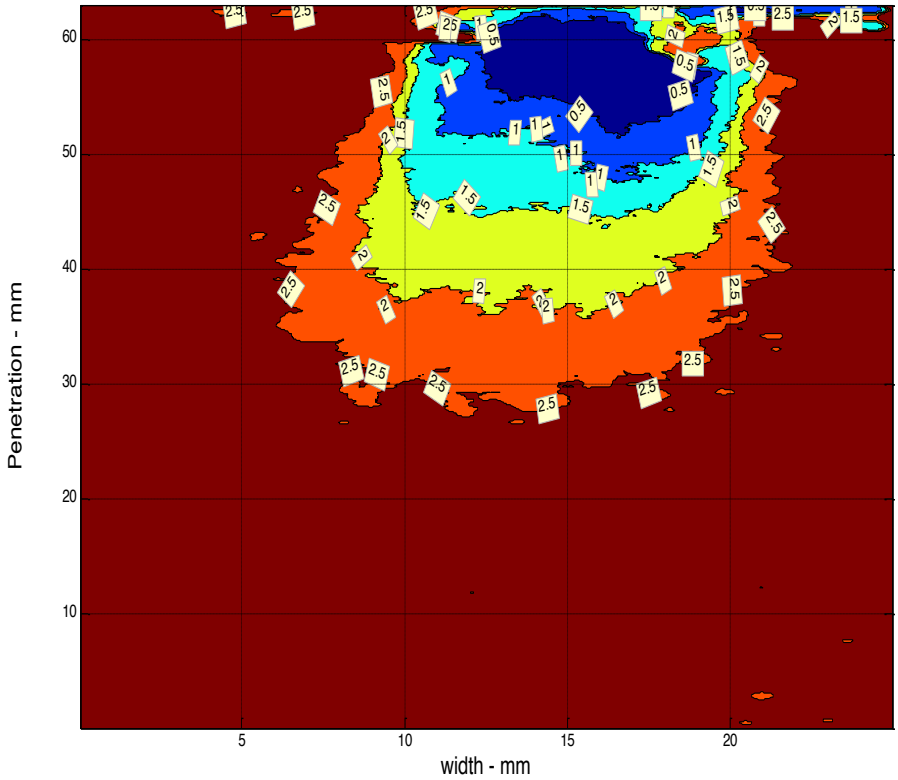

Four-hole gasoline injector sprays.

Appendix 7.6 The duty cycle effect on the flow rate of the Lee medical dispenser at P= 3 bar, f=500 Hz.

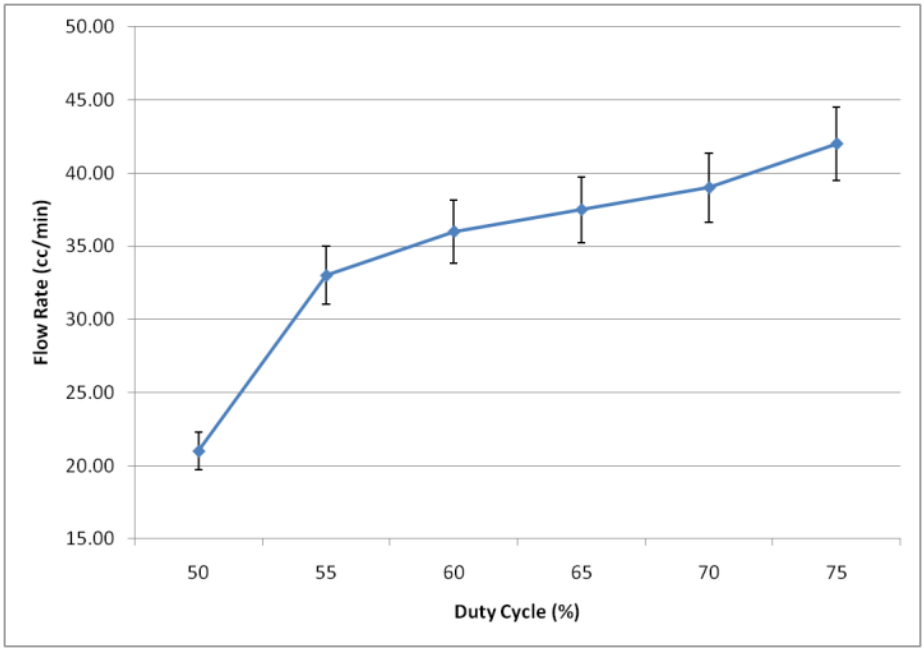

Appendix 7.7 : Samples of the PIV of a primary breakup 600 microsecond ASOI. Resolution: (1pixel=57 um). Time delay between double frames = 15 microsecond.

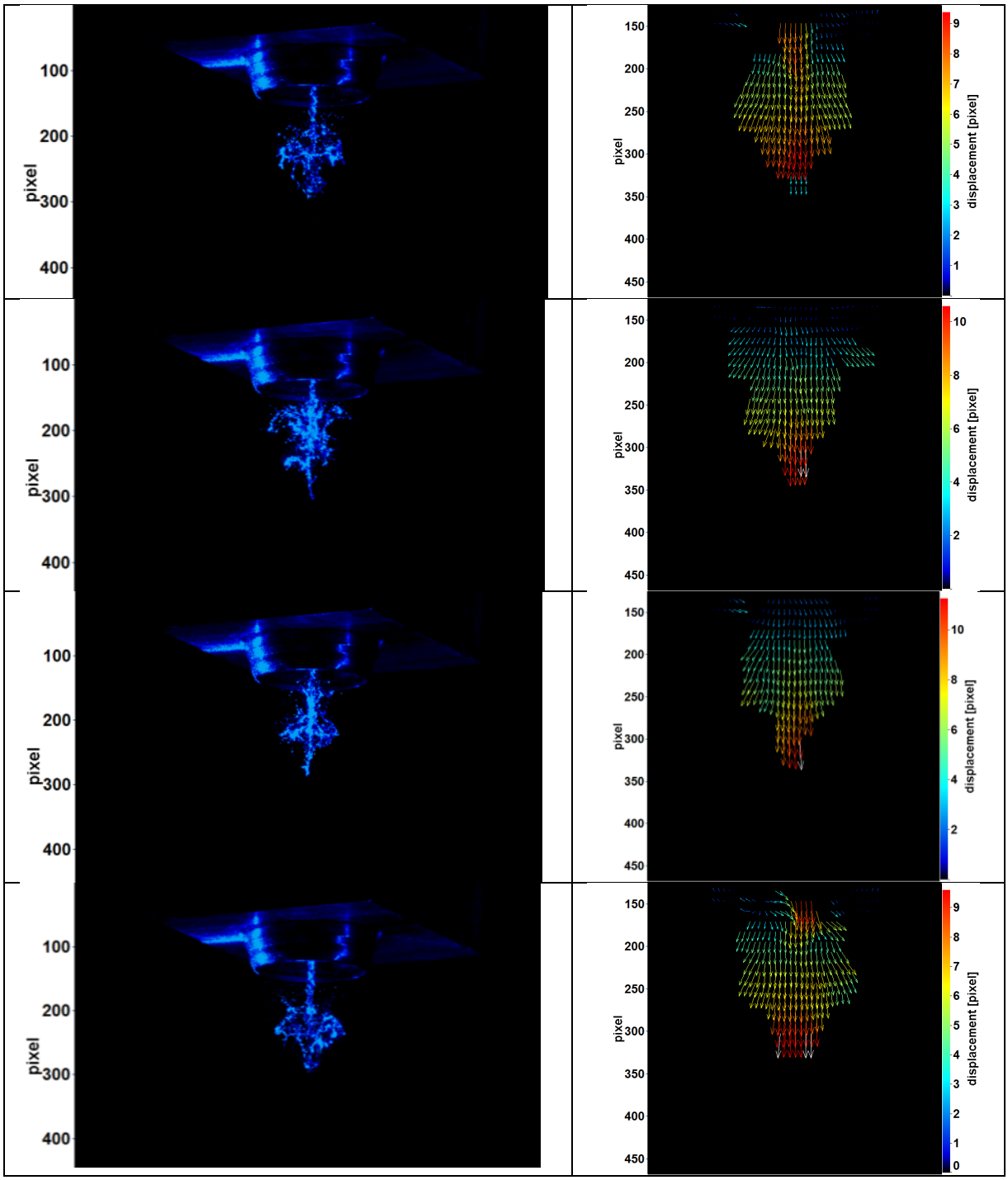

Appendix 7.8 : PIV for spray breakup on a surface

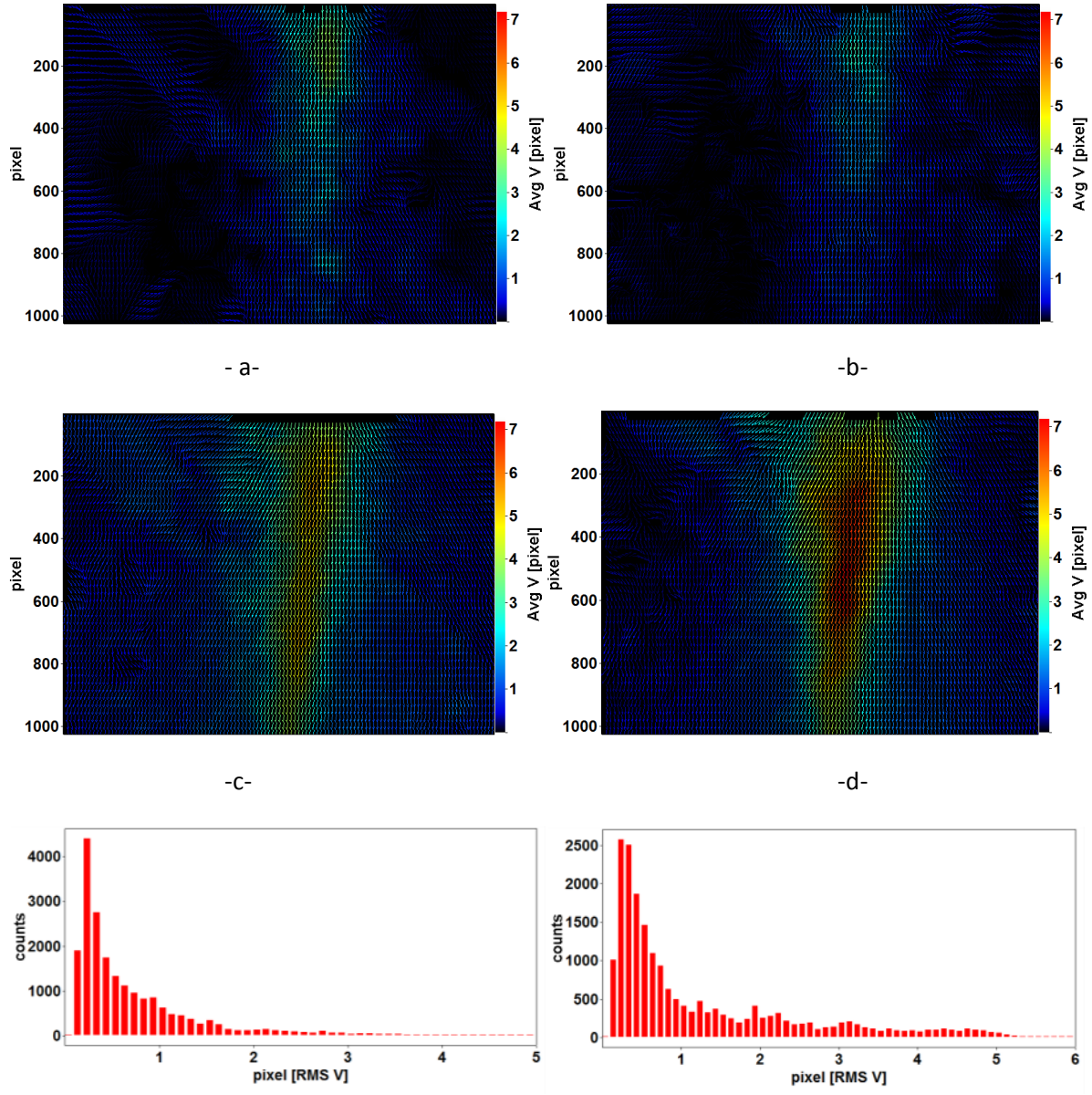

Resolution = 51 micrometer per pixel. Delay= 15 microsecond; a- at 3 bar without the surface, b- at 5 bar without the surface, c- at 3 bar with the surface, d- at 5 bar with the surface, e- the probability distribution of the velocity at 5 bar without the surface, f- the probability distribution of the velocity at 5 bar with the surface.

Appendix 7.9 PIV for kerosene against water

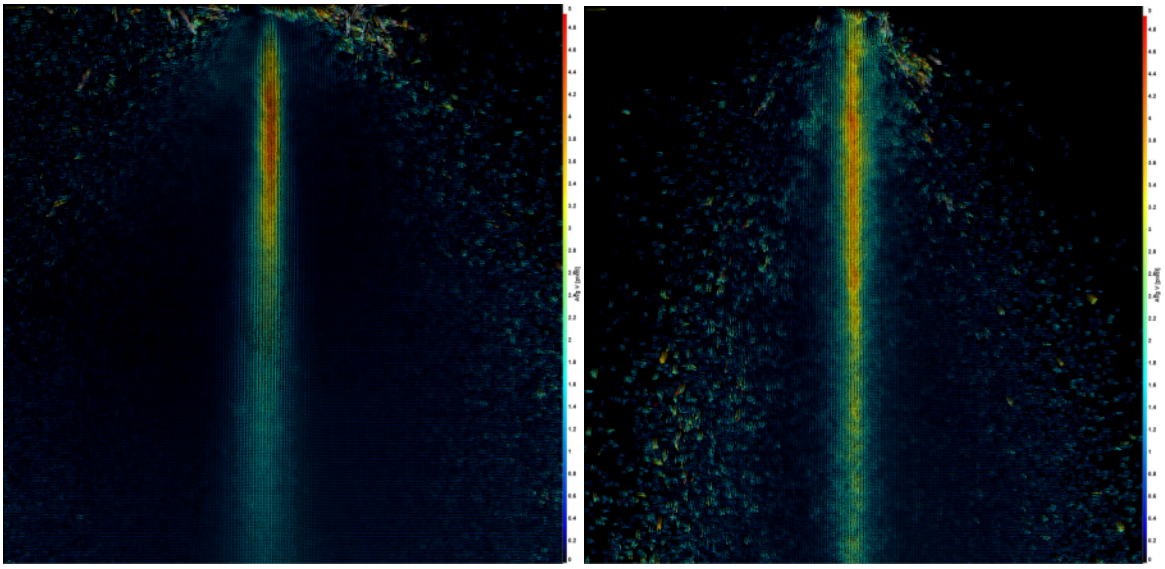

-a- -b-

Average velocity distribution ; a- kerosene, b- water.

Appendix 7.10 Injecting upward into an air stream.

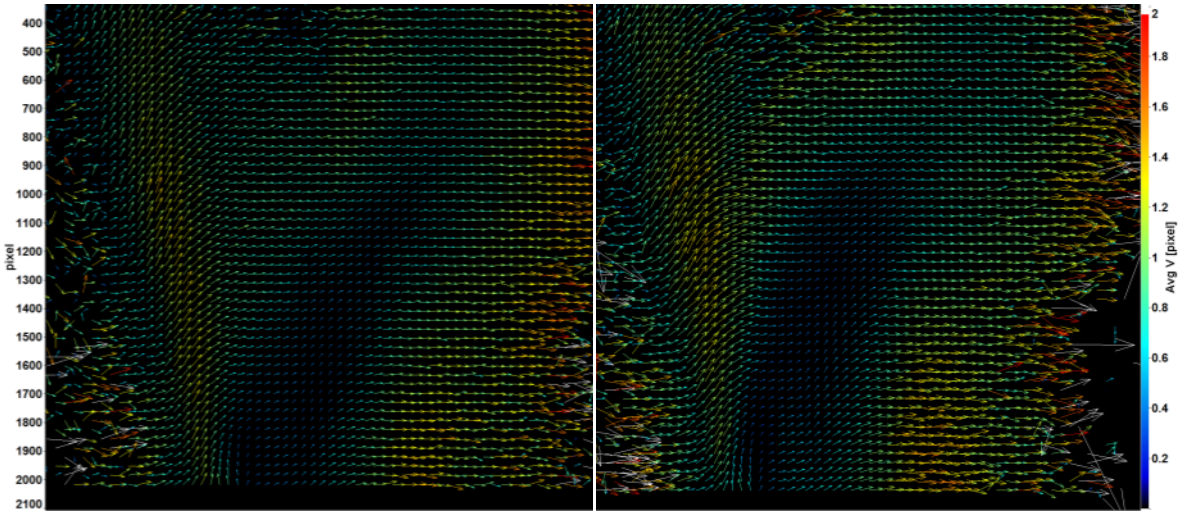

-a- -b-

The average PIV of fuel droplets injected upstream into air stream (the ventilation system nozzle is making around 30 degree with the vertical axis of the spray jet). (a) at 5 bar and (b) at 6 bar fluid pressure. 1 pixel displacement is equivalent to 1.63 m/s. The air steam velocity is estimated by (4-ms^{-1})

Appendix 7.11 top-bottom configuration; unbalanced intensity levels between 3C-PIV cameras using 0.3 microns (mean diameter) oil droplets.

Cam1: Top, Cam2: Bottom.

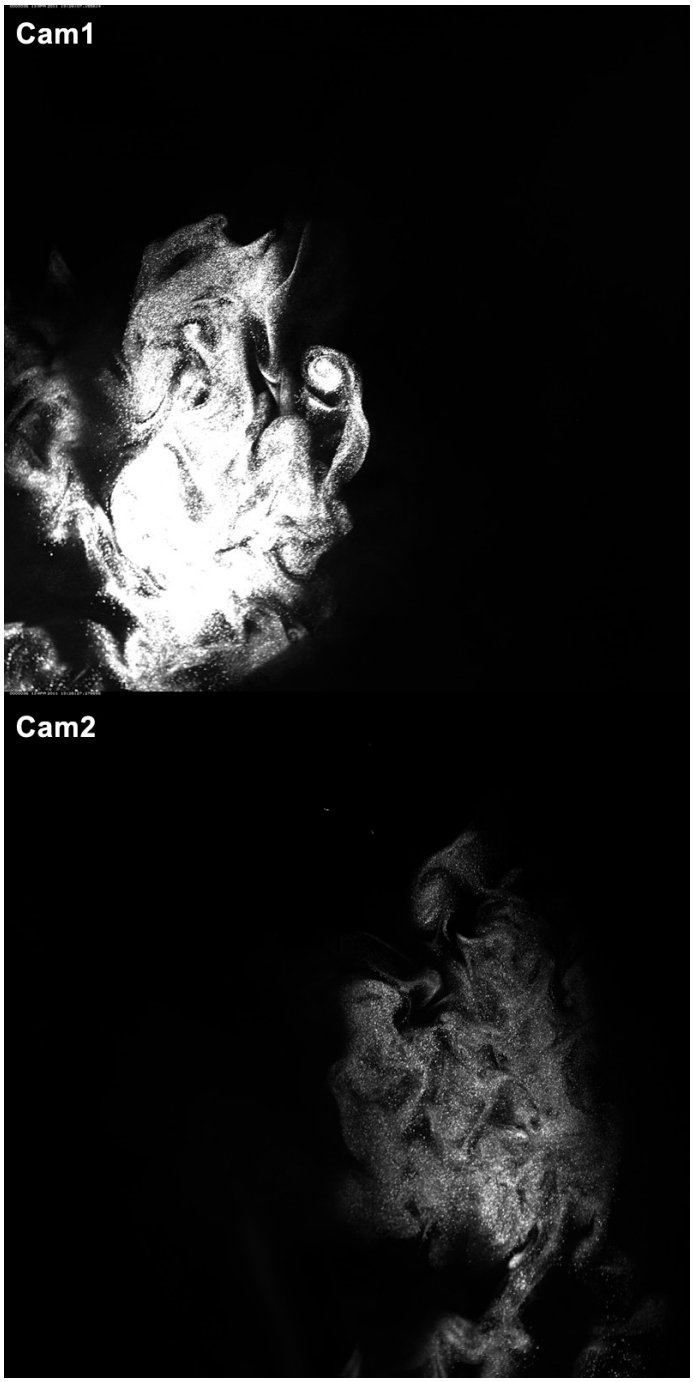

Top/bottom estimated difference in image energy= 72 % - 67 %

Appendix 7.12: Al_2O_3 (m= 1.66+0.001i) Mie scattering pattern for particles range (0.2 – 1 microns)

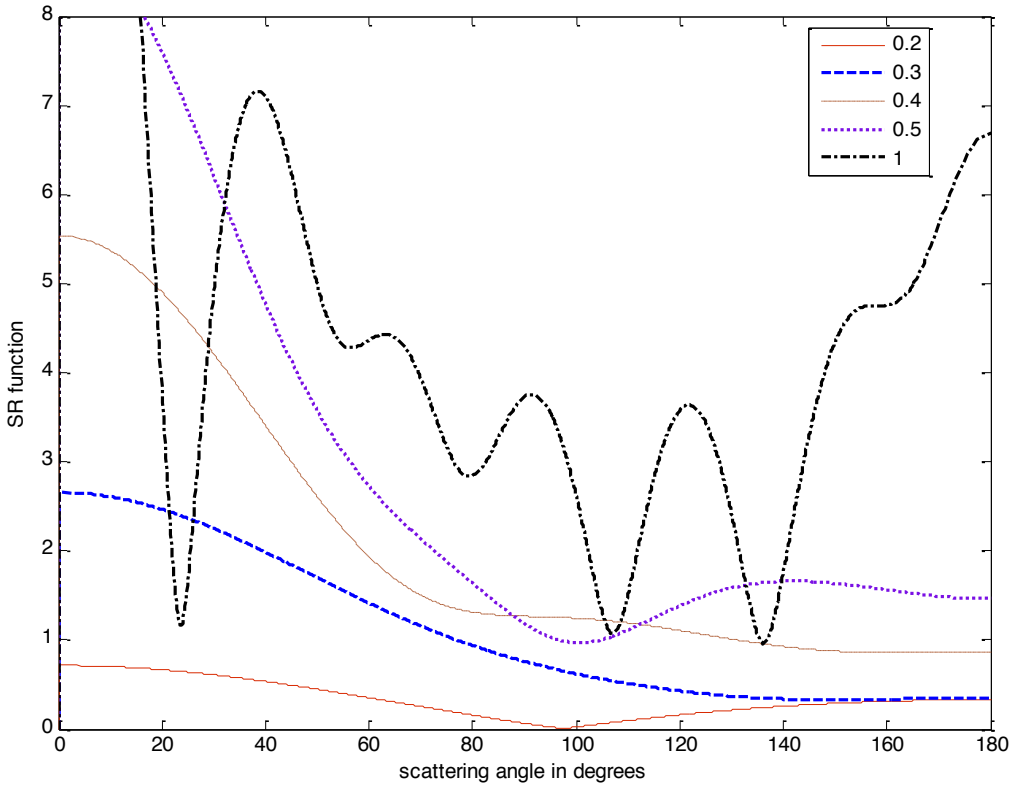

Appendix 7.13 TiO2 Mie scattering profile

D=0.25 µm

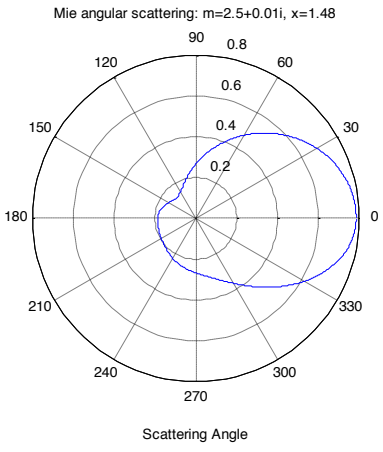

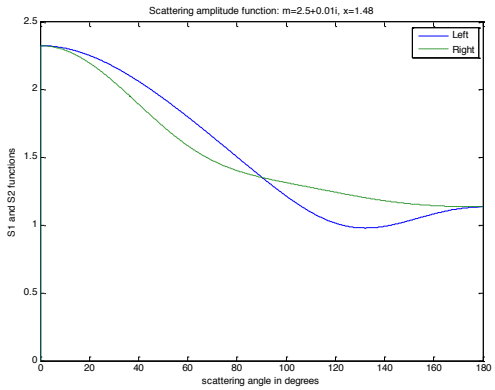

D=2 µm

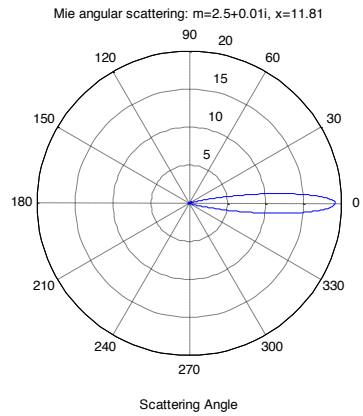

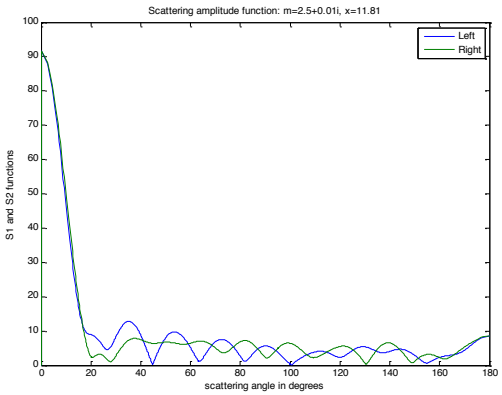

Appendix 7.14 Light scattering profile for oil seeding smoke and Al2O3 particles for 0.3 and 0.6 microns diameter.

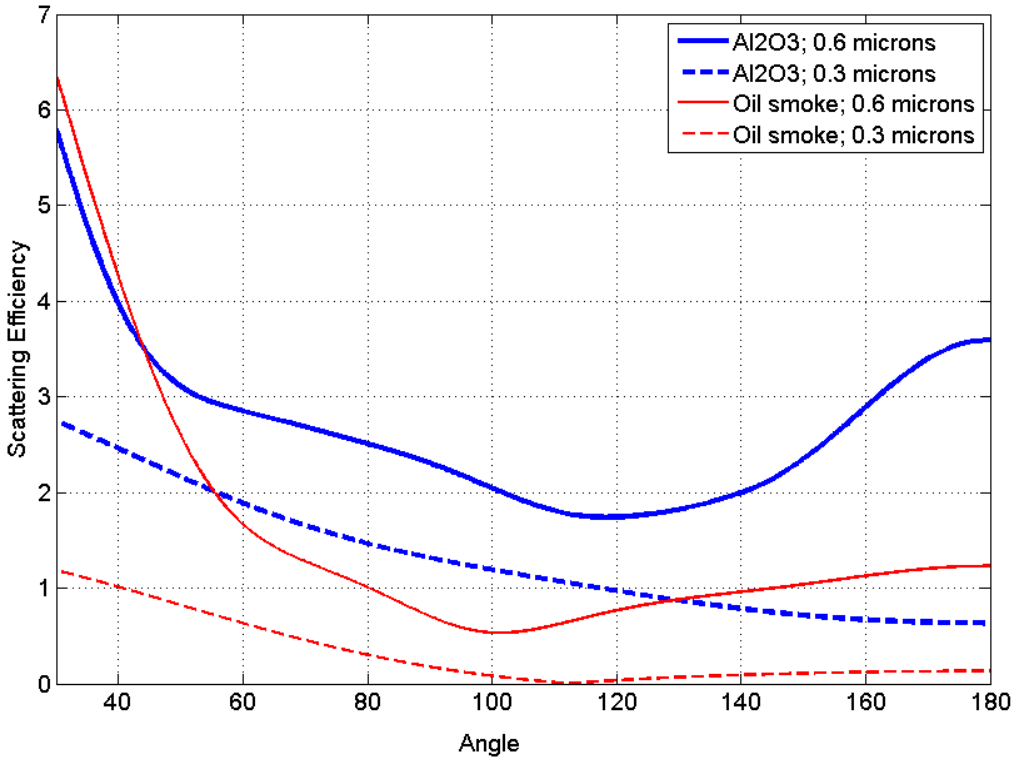

n= 1.77 – 0.001i (Al2O3), n= 1.35-0.000001i (Oil)

Appendix 7.15: Matlab code for image correlation calculation

```
%clear all;Peak_tot=0;st_tot=0;R_tot=0;clc
close all; clc
I=imread('C:\image_correlation\images\JetImage1.bmp'); %image path
imshow(I)
k=256;
t=32;

[m,n]=size(I);
I1=I(1:(m/2),1:n);
I2=I((m/2-1):m,1:n);

figure; imshow(I1)
[c]=round(ginput(1));

a=[c(1)+t/2 c(2)+t/2];
b=[c(1)-t/2 c(2)-t/2];
sec1=I1(b(2):a(2)-1,b(1):a(1)-1);
figure;
subplot(2,1,1); imshow(sec1)

d=[c(1)+k/2 c(2)+k/2];
f=[c(1)-k/2 c(2)-k/2];
sec2=I2(f(2):d(2)-1,f(1):d(1)-1);

subplot(2,1,2); imshow(sec2)

%%

v=normxcorr2(sec1,sec2);
figure;
v=abs(v);
imagesc(v);colorbar
P=max(max(v))

st=std(std(v))

mv=log(mean(mean(exp(v))));


r=P/mv % coefficient independent of t and k


title(['Peak Correlation= ', num2str(P), ', R=',num2str(r)])
 % the following variables need to be cleared in the beginning
Peak_tot=[Peak_tot P];
st_tot=[st_tot st];
R_tot=[R_tot r];
```

Appendix 8.1 CFD simulation for a gasoline conventional nozzle at 5 bar injection pressure

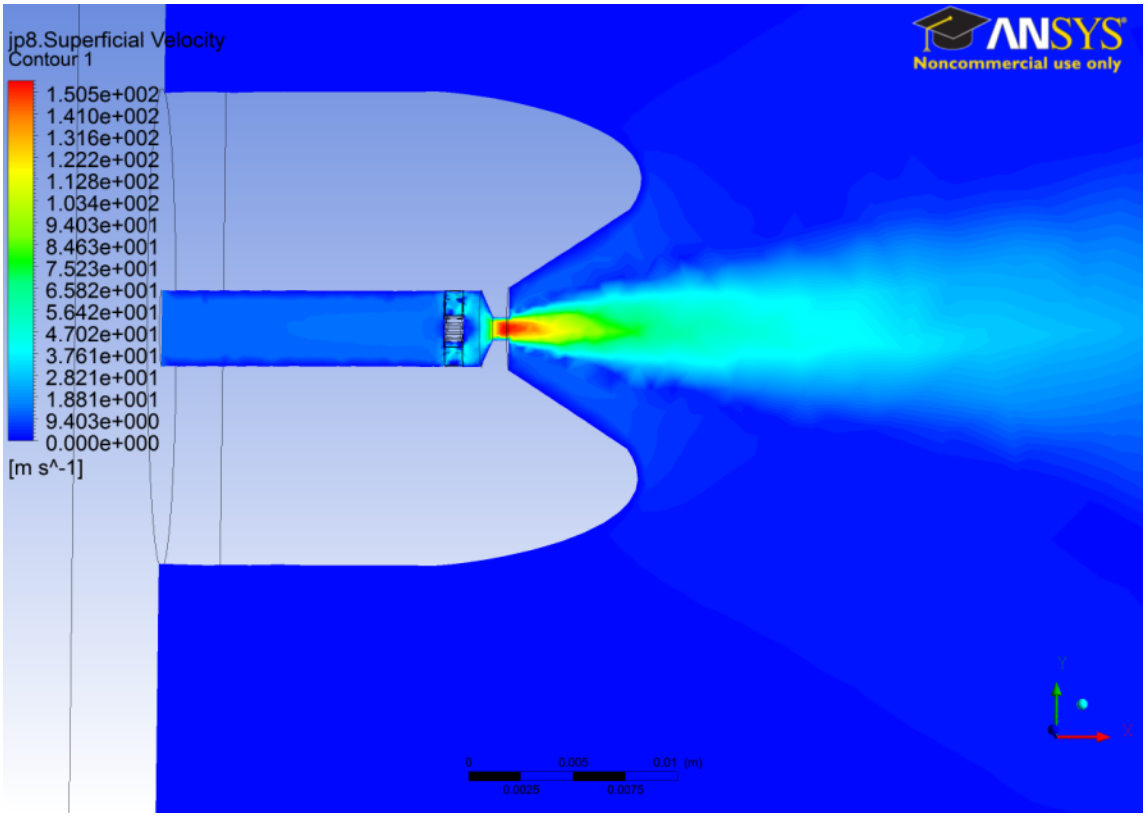

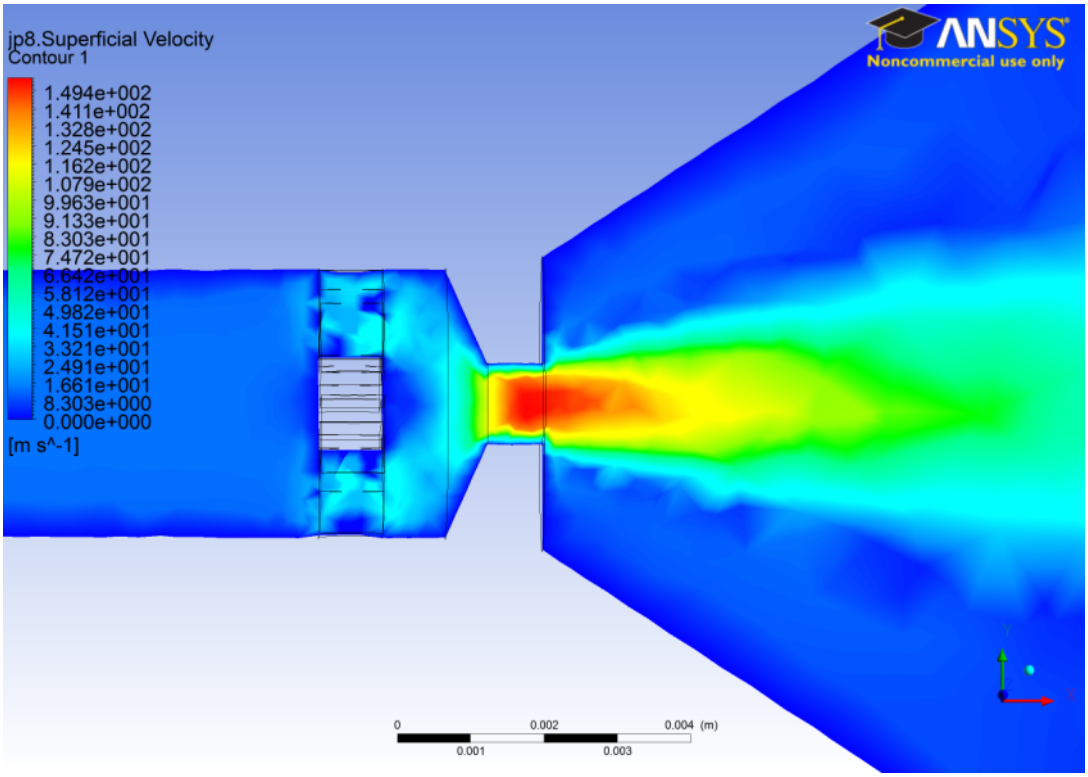

The velocity distribution for a kerosene injector nozzle (D_0=1 mm) static flow using Ansys.